ABSTRACT

Title of Dissertation: DETECTING HIGH-ENERGY EMISSION FROM GAMMA-RAY BURSTS WITH EGRET AND GLAST

David Nathan Wren, Doctor of Philosophy, 2005

Dissertation directed by: Dr. Steven M. Ritz
NASA's GSFC

The research described in this dissertation explores the detection of high-energy emission from gamma-ray bursts (GRBs) with EGRET and GLAST. Data from the EGRET experiment were searched for evidence of ∼1-250 MeV emission that preceded or followed gamma-ray bursts on a time scale of hours. This led to the discovery of a gamma-ray burst with high-energy, post-quiescent emission from the prompt phase that was coincident with lower-energy (keV) emission.

To do detailed event filtering studies for the GLAST Large Area Telescope (LAT), the flight software event filter was embedded in the standard science analysis environment. The event trigger rate, reasons why it must be reduced, and hardware-level methods of reducing it are studied. Much work was done to improve the performance of the prototype event filter, and additional work was done to develop algorithms to allow the LAT to distinguish Earth albedo photons from celestial gamma-rays, and to eliminate albedo events from the data stream. It is shown that it is possible to reduce the background rate to meet LAT mission requirements,

while simultaneously keeping the gamma-ray acceptance rate high enough to exceed the relevant LAT requirements for those events.

Using the onboard event filter, real-time, onboard, gamma-ray burst detection was then studied. A detection algorithm had been developed by members of the LAT collaboration, but the algorithm required a lower onboard background rate than the basic LAT requirement for downlink, in addition to knowledge of incident gamma-ray directions. Therefore, several methods of reducing the background rate to acceptable levels were provided, and onboard track reconstruction methods were created and tested. GRB detection was tested for two background filters and two track reconstruction methods for simulated bursts that had realistic light curves and spectral characteristics. With prototype background cuts, track reconstruction, and burst detection algorithms, the LAT burst detection requirements were exceeded. Suggestions were offered about how to enhance burst detection performance in the coming months before GLAST is launched.

DETECTING HIGH-ENERGY EMISSION FROM GAMMA-RAY BURSTS WITH EGRET AND GLAST

by

David Nathan Wren

Dissertation submitted to the Faculty of the Graduate School of the
University of Maryland, College Park in partial fulfillment
of the requirements for the degree of
Doctor of Philosophy
2005

Advisory Committee:

Dr. Steven M. Ritz, Advisor (NASA/GSFC)
Professor Gregory W. Sullivan, Chairman and Advisor (UMD)
Professor Jordan A. Goodman
Professor M. Coleman Miller
Professor Douglas A. Roberts

To "the girl behind the gamma rays"

ACKNOWLEDGMENTS

Completing a PhD has been a goal of mine since maybe 15 years ago, when I first picked up a copy of *Astronomy* magazine in the 9th grade and got hooked. Since then, I've had a lot of help making it to this point.

I'd like to thank the Laboratory for High Energy Astrophysics at Goddard for creating the fellowship that convinced me to come out here 6 years ago (and for giving it to me!). Working at NASA for the past few years has been a very rewarding experience, and the people I met were of the highest quality. I'm especially grateful to Bob Streitmatter and Elihu Boldt for familiarizing me with what LHEA does when I first learned of the opportunity to come here. I also thank Alex Moiseev, Dave Thompson, Bob Hartman, Jay Norris, and Jerry Bonnell for their council at various times. I owe a special thanks to Dave Bertsch for teaching me how to analyze TASC data. Without Dave, the ApJ Letter and the third chapter of this thesis would not have been possible.

None of this thesis would have been possible without the guidance of Steve Ritz, who took me on as a grad student, and allowed me to work on some substantial projects with GLAST. I've learned a lot from Steve, and he gave me the very fulfilling opportunity of contributing to the mission in significant ways. Much of the GLAST-related work would not have been possible without the help of many additional

members of the LAT collaboration, both at SLAC and at Goddard. Special thanks go to J. J. Russell, Heather Kelly, Navid Golpayegani, Toby Burnett, Sean Robinson, Julie McEnery, and Luis Reyes for help with the filter, software, fluxes, bugs, ROOT, and all the other things that come up when doing this kind of work. Julie and Luis, thank you for spending so much time reading drafts of thesis chapters, and for offering very useful suggestions on how to improve it.

My thanks goes to Greg Sullivan for acting as my official advisor at UMD, and for all the help that entails.

Special thanks to Jay Hauser at UCLA for allowing me to join his research group. The problem solving experience I gained during that time was great preparation for grad school.

To Mike Fiducia, Brian May, and Bill McGaugh from Temecula Valley High School, thank you for giving me the extra bit of confidence I needed to attempt an astrophysics major way back when.

Outside the academic sphere, there are many people who provided a lot of support through this process. I don't know what my parents, Tony and Sandy Wren, thought of the 14 year old kid who wanted to spend his money on telescope parts, and his weekends being shuttled all over the South Bay looking for instructional books, pieces of scrap yard laminate, and affordable optics. Whatever they thought, they consistently reminded me of my dreams when I was about to give up on them, always persuading me that though I couldn't make them happen by my own efforts, God would see His plans through to completion. Mom and Dad, without your

encouragement, I might have chosen an easier path to my later regret.

Jenn, thank you for always being available to talk when things were rough or when I needed advice, and for never telling me to stop complaining about the same old things that never seemed to go away. I also give my thanks to the other family and friends who prayed for me and took an interest in what I was doing. My grandfather reminded me recently that he prays for me daily, and I know my grandmother and Pastor Kuester provide the same kind of support. The Hensleys made my time at UCLA easier by giving me a place to live, and what would I have done without the nightly dinner-table math quiz? More recently, the 10-40 girls, the guys I'd meet with at Common Grounds, Tim and Greta, and *all* my other friends at NCC and DCV have been fantastic. I know you've all been holding me up at different times, because I've felt it and I've seen the many, many specific answers. Don't underestimate the role you played – I don't.

One thing I really wanted was to get married before the degree was finished, so my wife could be there to celebrate with me when I finally got it. Well, Selina will definitely be celebrating the completion of the goal, but I think she'll also be celebrating that she gets me back. No more nights and weekends with me sitting at the computer! Selina, thank you for being so understanding about the workload and the stress, and for making life so much easier on me in every way you could think of. Having you in my life has made this all the more significant, and your faith has helped to sustain me when mine gave out.

TABLE OF CONTENTS

LIST OF TABLES

LIST OF FIGURES

Chapter 1

Searching for High-Energy Emission from Gamma-Ray Bursts

Research in sub-TeV gamma-ray astrophysics has grown dramatically since space flight has allowed for the placement of scientific instruments above Earth's gamma-ray absorbing atmosphere. These experiments share much of their technology with the high-energy physics community, which had developed particle detection techniques that could be adapted for the purpose of detecting high-energy photons in a space environment.

Work done for this thesis relied upon archived data from the Burst and Transient Spectrometer Experiment (BATSE) (Band et al., 1992) and the Energetic Gamma-Ray Experiment Telescope (EGRET) (Kanbach et al., 1988) instruments onboard one such satellite, the Compton Gamma Ray Observatory (CGRO), which was deorbited in 2000 after 9 years of operation. Also described are efforts related to the design of CGRO's successor, the Gamma-Ray Large Area Space Telescope (GLAST), and the possibility of its use in detecting MeV-GeV emission from

gamma-ray bursts in real time.

Data from the EGRET experiment were searched for evidence of ∼1-250 MeV emission that preceded or followed gamma-ray bursts on a time scale of hours. This led to the discovery, which was published in ApJ Letters (Wren et al., 2002), of the first gamma-ray burst with significant high-energy, post-quiescent emission from the prompt phase that was coincident with lower-energy emission[1]. Possible evidence for delayed ∼1-250 MeV burst emission is also presented, but no firm conclusions regarding its existence can be postulated, so an upper limit is calculated.

GLAST observations of gamma-ray bursts on a wide range of time scales should contribute to our knowledge of high-energy GRB emission, prompt or delayed, so much of this thesis is dedicated to work that will allow GLAST's main instrument, the Large Area Telescope (LAT), to operate with good detection efficiency. Chapter 4 describes the particle background that GLAST will encounter in orbit, the resulting event trigger rate, reasons why it must be reduced, and possible hardware-level methods of reducing it. Chapter 5 discusses the use of a software event filter to further reduce the background rate before data are sent to the ground. Much work was done to improve the performance of the prototype event filter, and new filters were developed for the purpose of identifying and eliminating (from the data stream) Earth albedo photons. It is shown that it is possible to reduce the background rate to meet LAT mission requirements, while simultaneously keeping the gamma-ray acceptance rate high enough to exceed the relevant LAT requirements for those events.

[1]Lower energy spectra have been observed by COMPTEL (Winkler et al., 1992).

Those results were then applied to the problem of real-time, onboard gamma-ray burst detection. A detection algorithm had been developed by members of the LAT collaboration, but it required a lower onboard background rate than the basic LAT requirement for downlink, in addition to knowledge of incident gamma-ray directions. In Chapter 6, methods of reducing the background rate to levels at which the GRB detection algorithm can successfully function are presented. Onboard track reconstruction methods were also created and tested; these provide directional information regarding incident photons (and cosmic-rays) to the GRB detection algorithm. Virtual gamma-ray bursts were then generated with the GLAST Monte Carlo simulation, and these were used to test the background filters, track reconstruction methods, and GRB detection algorithm. Onboard GRB detection is shown to be possible, and suggestions for improving the sensitivity are presented. With GLAST, the future of gamma-ray astrophysics is indeed bright.

1.1 A Brief Introduction to Gamma-Ray Astrophysics

Astrophysics has long been a data-driven science, with explanations tending to follow discoveries, rather than hypothesis anticipating observation. The sheer scale and complexity of the universe ensure that discoveries are not easily foreseen, so it is advantageous to explore the astrophysical phase-space as thoroughly as possible. Historically, each foray into a new frequency regime has resulted in observations of previously unknown objects and phenomena, advancing our physical understanding of the universe. Much knowledge was only acquired in the past few decades when

technological advances made it possible to extend astronomical observations beyond the visual portion of the spectrum. The expansion into studies of gamma-ray astrophysics is one of the most recent, and it is providing insight into some of the most violent, energetic processes since the Big Bang.

1.1.1 Sources and Production Mechanisms

The processes that produce these high energy photons[2] include black holes at the centers of galaxies (active galactic nuclei), rapidly spinning neutron stars, the ejection of material from the surface of the Sun, the decay of elementary particles and possibly dark matter, particles interacting with the cosmic microwave background, and massive explosions from the collapse of stars, some of which result in intense bursts of gamma-rays.

The GLAST mission will observe many of the above, and expectations are that unforeseen phenomena will also be discovered, but there are also a few pre-defined questions that guide the mission. For instance, GLAST should measure many detailed spectra of active galactic nuclei (AGN) that can be compared to lower energy observations, and this will help determine characteristics of the source (McEnery, 2003; Ciprini, 2003). The acceleration of particles in jets at AGNs is also of interest, as is providing data that can be used to discriminate among theoretical models (Ciprini, 2003). It is hoped that GLAST's sensitivity and resolution will also help determine the origin of the extragalactic diffuse gamma-ray background (Stecker,

[2]Gamma-rays are typically considered to be those photons with energy $\gtrsim$10 keV.

1999; Totani and Kitayama, 2000). If it is due to previously-unresolved individual sources, GLAST will be able to resolve a large fraction of them, and GLAST will identify many of the unidentified sources in the EGRET catalog (Kamae et al., 2000; Zhang et al., 2000). It may also be possible to use years of GLAST observations to detect signs of dark matter annihilation as line and anomalous continuum features in a spectrum (Moiseev, 1999b). By observing pulsars that emit gamma-rays, the gamma-ray production mechanisms and particle acceleration mechanisms can be understood (Bulik et al., 2000; Rudak, 2001; Wang et al., 2002). Of particular interest for this thesis are gamma-ray bursts. By observing them at high energies in the LAT and lower energy in the GLAST Burst Monitor (GBM), it will be possible to compare the high and low energy spectra for the same bursts. Analysis of the high quality spectra may distinguish burst models (Lithwick and Sari, 2001; Zhang and Mészáros, 2002; Baring, 1999; Zhang and Mészáros, 2004), and it will open up an energy range not previously attainable.

Most of the sources listed above can be regarded as extreme astrophysical objects, and many of them create gamma rays through a limited number of physical mechanisms, the most common of which we describe here. One of the most relevant to our discussion is synchrotron emission, in which relativistic charged particles emit radiation as they spiral around magnetic field lines. The resulting energy spectrum for synchrotron emission in astrophysical sources is typically power-law. Another common method of gamma-ray production is bremsstrahlung, in which electrons are decelerated in collisions with nuclei. An astrophysical bremsstrahlung spectrum is

often thermal, because the photon energy is proportional to the thermal distribution of electrons in the gas. Also possible is the production of neutral pions from hadronic interactions. The $\pi^o s$ quickly decay into gamma rays. It is also possible for lower energy photons to be up-scattered to gamma-ray energies when photons are boosted by charged particles via the inverse-Compton mechanism (IC). Synchrotron-self-Compton (SSC) is the up-scattering of synchrotron photons to even higher energies by the same electrons that gave rise to the original photons.

1.1.2 Interaction with Matter

The primary gamma-ray interactions with matter are energy dependent. Primarily below a few 10's of keV, the photoelectric effect dominates. In this process, a gamma ray is absorbed by an atom and knocks loose an outer electron. At higher photon energies, the electron can be regarded as free because its binding energy becomes smaller relative to that of the incident photon. Therefore, the probability of photoelectric absorption falls off rapidly, and Compton scattering begins to dominate. The Compton process occurs when a photon scatters off of an electron, imparting some of its energy to that electron as the photon looses energy in the process.

Above a few MeV, the cross section for Compton scattering decreases, and pair-production is most important. Pair-production refers to a process by which a gamma ray will interact in the Coulomb field of a nucleus and convert to an electron-positron pair. This can happen when the center of mass energy is equivalent to at least twice the rest mass of an electron (0.511 MeV). The gamma ray then can

convert into the pair (Bethe and Heitler, 1934). Any energy beyond the 1.022 MeV required to create the pair goes into their kinetic energy.

Any of the above methods can be exploited in a gamma-ray experiment for the purpose of detecting a source, but in the energy regime important to two instruments important for this thesis, EGRET and the GLAST LAT, the pair-production mechanism is the most important. Of course, this is irrelevant if the gamma rays cannot reach the instrument in the first place.

1.1.3 Observing from Space

Gamma-rays that reach Earth are limited by our atmosphere from traveling the last few miles to the ground. It is possible to do some gamma-ray astronomy by observing the interactions of gamma-ray photons with the atmosphere, or by detecting the particles produced when they interact in the atmosphere. These methods are most effective at very high energies (beginning at $\sim$ 100 GeV), however, and lower-energy gamma-ray detections are only possible from space.

The solution to the atmospheric problem is to observe from above the atmosphere. The first gamma-ray experiments used high-altitude balloons, but the high background due to cosmic ray interactions makes any gamma-ray science within the atmosphere very difficult. For this reason, the modern era of gamma-ray astrophysics did not truly begin until the Small Astronomy Satellite (SAS-2) (Fichtel et al., 1975) was launched in 1972.

Once it was possible to make gamma-ray observations from above the atmo-

sphere, science proceeded rapidly, and additional satellite-based gamma-ray experiments were planned. The most fruitful of these was NASA's Compton Gamma-Ray Observatory (CGRO), which was launched in 1991 and was active for over nine years. It used four distinct experimental instruments to detect gamma rays over six decades of energy, from 30 keV to 30 GeV.

While CGRO was still in flight, the design of CGRO's successor telescope, GLAST, was proceeding. In addition to other advances described in Chapter 2, GLAST has been designed to extend the detection range an order of magnitude beyond EGRET's upper limit of 30 GeV.

1.2 High-Energy Gamma-Ray Burst Observations

One of the expectations for the GLAST mission is that its wide window in the MeV-GeV energy range, and its unprecedented sensitivity in that range, will allow for the discovery of new astrophysical phenomena, in addition to providing a better understanding of phenomena already observed at different energies. The pattern of new instruments leading to unanticipated discoveries is well established in astrophysics, and was confirmed with EGRET's many surprises.

For example, some of the most exciting results in gamma-ray burst science came from EGRET at MeV-GeV energies, at the same time that BATSE worked onboard the same satellite to collect burst data at a high rate at lower energies (20 keV to 1.9 MeV). BATSE consisted of eight detectors that were placed around CGRO in such a way that GRBs from anywhere on the non-occulted sky could be

detected at any time. This allowed BATSE to detect over 2700 bursts (Paciesas et al., 2000), and much of our current knowledge of bursts is the direct result of BATSE observations. However, the few bursts that were detected by EGRET showed that MeV and GeV burst emission is possible, and that the emission can arrive minutes, or possibly hours after the burst appears to end at lower energies (Hurley, 1994). There was also a recent discovery of high-energy emission that appeared to evolve separately from lower-energy emission (González et al., 2004). These observations are detailed in the coming sections. High-energy EGRET observations provide what little is known about gamma-ray burst emission in this energy range, and GLAST will greatly expand the catalog of high-energy burst detections. A greater number of detailed observations of burst emission at MeV and GeV energies should give us a better understanding of bursts and the environment in which they occur, and should allow for the testing of gamma-ray burst models that make predictions regarding high-energy emission.

In order to provide some background on gamma-ray bursts, and to give context that is useful for understanding the rest of the thesis, the next section (1.3) is a brief review of gamma-ray burst astrophysics. Because most burst observations were in the keV to low-MeV range, most of the discussion focuses on observations made at those lower energies. In section 1.4, the discussion shifts to high-energy and delayed emission, which are main topics of this dissertation. The high-energy burst section discusses both the few high-energy observations that do exist, the physical mechanisms and astrophysical processes that might produce the emission, and why

observations of high-energy burst emission are important.

1.3 Gamma-Ray Bursts

The discovery of gamma-ray bursts was announced in the 1973 after the US Department of Defense revealed that bursts of gamma rays were detected with the VELA satellites between 1969 and 1972. The satellites were designed to detect the testing of nuclear weapons in space, but instead of detecting violations of the Nuclear Test Ban Treaty, the satellites had detected bursts of celestial gamma-rays (Klebesadel, Strong, and Olsen, 1973; Mazets, Golenetskii, and Ilinskii, 1974).

Since the first papers were published, our understanding of gamma-ray bursts has increased substantially, but a basic definition has remained essentially the same as that reported in the original literature. A gamma-ray burst is an intense flash of gamma-rays with energy greater than 50 keV that lasts between a fraction of a second to several seconds. It is sometimes followed by a multiwavelength afterglow (x-ray through radio) that quickly rises, but then slowly fades over a period of days. It is believed with some confidence that bursts are of cosmological origin (Metzger et al., 1997; Kulkarni et al., 1998), isotropically distributed (Meegan et al, 1992), last from milliseconds to many 10s of seconds (Kouveliotou et al., 1993), have non-thermal spectra (Band et al., 1993), beam their emission in jets (Rhoads, 1998, 1999), have a peak energy centered around 250 keV (Preece et al., 2000), have x-ray, optical, and radio afterglows (Costa et al., 1997; van Paradijs et al., 1997; Frail et al., 1997), emit about the same energy as a supernova (Frail et al., 2001), and

may be caused by the collapse of a massive star (Woosley, 1993; Vietri and Stella, 1998) or the merger of compact objects (Eichler et al., 1989; Narayan et al., 1992).

Here, a common pattern in burst reviews is followed (Piran, 2005; Zhang and Mészáros, 2004; Hurley, Sari, and Djorgovski, 2002). The discussion begins with the observational evidence, and then moves to the physical processes inferred from the observations, and finally to some models that attempt to explain most of what has been observed.

1.3.1 Prompt Emission

Most burst emission can be divided into two parts: the prompt emission that lasts up to a few 10s of seconds, and the days-long *afterglow* emission that follows. When the term "gamma-ray burst" is used without any qualification, it is typically being used to describe the prompt phase, when the detectable emission is in the form of gamma rays. As stated earlier, most of what we know about prompt emission comes from BATSE observations, which told us, among other things, that bursts are isotropically distributed, have unique time profiles (in that each burst's light curve looks very different), are very energetic, and have power-law spectra that appear to peak in a narrow energy range.

Temporal Properties

The light curves from GRBs vary not only in duration, but in shape; there is no characteristic gamma-ray burst light curve (see Figure 1.1). On the contrary, most

(about 80% (Piran, 2005)) GRBs show considerable variety in their substructure. Larger pulses within the curves are made up of many smaller pulses of much shorter duration. The smaller pulses average about 1 s in duration, and are separated on average once every 1.3 s (Piran, 2005). These small pulses are characterized by a fast rise and an exponential decay (FRED) (Norris et al., 1996), which is also a common shape for the shortest gamma-ray bursts. For longer bursts, even periods of inactivity for 10s of seconds – known as quiescent periods – while not the rule, are not uncommon (Ramirez-Ruiz and Merloni, 2001).

Gamma-ray burst duration is often described in terms of the length during which the middle 90% (5% to 95%) of the emission is detected, T_{90}, and in terms of the length in which the middle 50% of the emission is detected, T_{50}. The largest repository of gamma-ray burst data (Paciesas et al., 2000), from the BATSE experiment on CGRO, has T_{90} durations that range between milliseconds to several hundreds of seconds.

Spectral Properties

The observed spectra of gamma-ray bursts are well characterized by a so-called Band function (Band et al., 1993), a phenomenological formula in which two power-laws meet at a break energy, E_p. This peak energy tends to be lower for bursts with lower flux, and the lognormal peak energy distribution is narrowly centered at $\sim$250 keV (Preece et al., 2000). It is not clear whether the narrow peak is due to a selection effect or whether it is real. If there exist a class of bursts that peak at higher

energies, the bursts could be difficult to detect at lower (keV) energies, because the lower-energy emission (whose flux increases until E_p) might be below detection thresholds (Piran and Narayan, 1996; Cohen et al., 1997; Higdon and Lingenfelter, 1998; Lloyd and Petrosian, 1999). However, GLAST, which is sensitive to the high-energy emission, may be able to detect these bursts, if they exist. Observations of a cutoff in the high-energy spectrum, when combined with redshifts obtained from afterglow observations, may help to constrain models that attempt to explain the peak energy distribution (Lithwick and Sari, 2001; Zhang and Mészáros, 2002; Baring, 1999).

If the narrowness of the peak (the full-width at half-max is only about a decade in energy (Zhang and Mészáros, 2004)) is not due to a selection effect, there may be a correlation between redshift and hardness[3] (Piran, 2005). Redshift would tend to spread out the distribution, so its narrowness implies that a competing factor – such as increasing hardness with distance – is working against that tendency. Observational evidence suggests that hardness (E_p) does increase with redshift (Amati et al., 2002), that the peak flux corresponds to the peak energy (Mallozzi et al., 1995, 1998), that the isotropic equivalent energy corresponds to the peak energy (Amati et al., 2002), and that more energetic bursts tend to be at greater distances (Amati et al., 2002). Taken together, these observations point to the interesting conclusion that more distant bursts emit more energy or are more strongly beamed, though selection effects may be present, and the evidence is not conclusive (Zhang

[3]Hardness is a term used to describe the energy of a spectrum. Higher energies are considered to be harder than lower energies, so a hard spectrum is one that has a relatively high fraction of high energy emission, i. e. smaller β for $dN/dE \sim 1/E^{\beta}$.

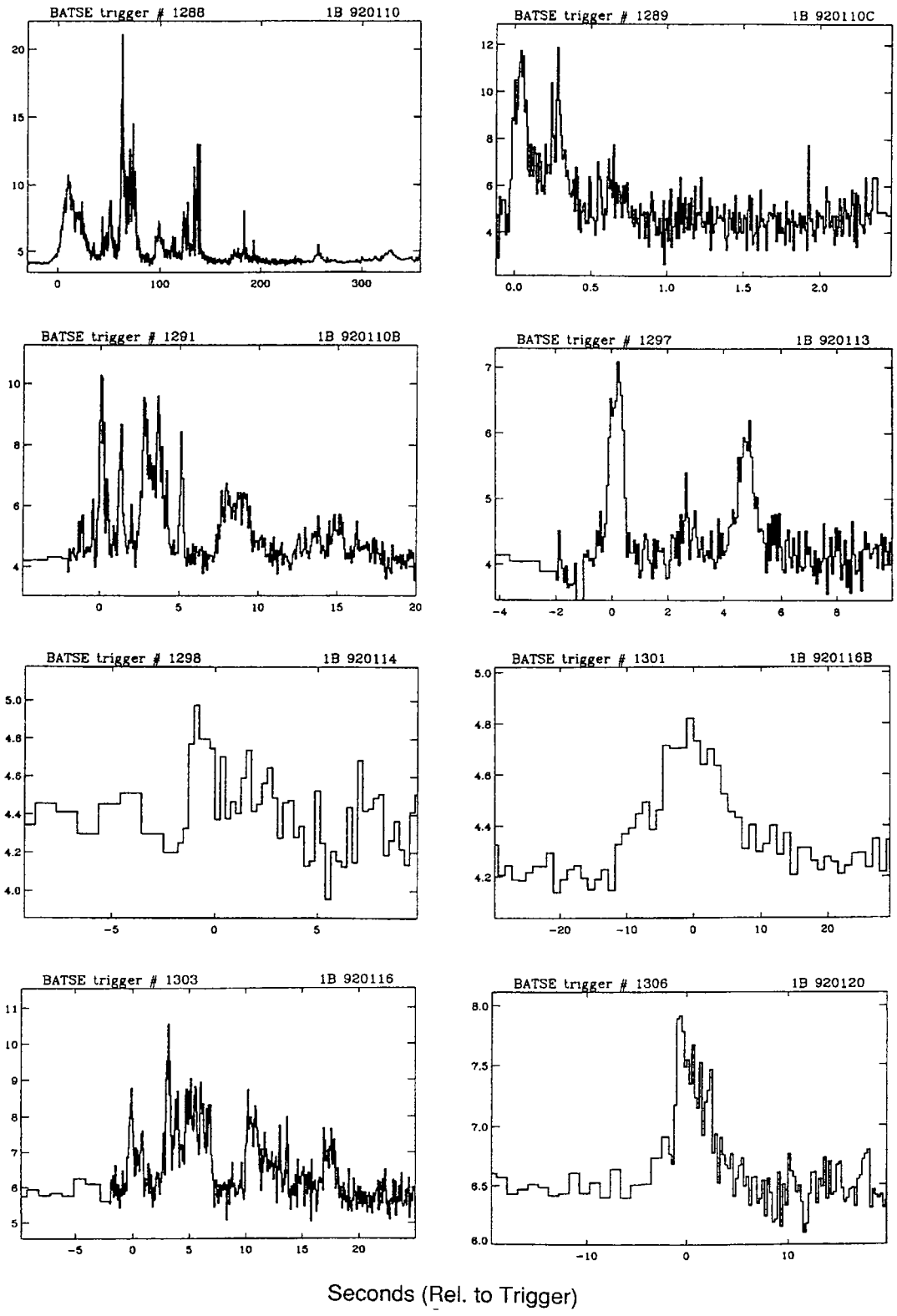

Figure 1.1: An assortment of BATSE light curves illustrating the variety evident in burst temporal behavior. The Y-axis is in thousands of counts per second. From Fishman and Meegan (1995).

and Mészáros, 2004).

For bursts that do not have measured redshifts (see Figure 1.2 for a distribution of measured redshifts), it may be still possible to derive an estimate of luminosity, because there exists a possible correlation between variability and luminosity (Fenimore and Ramirez-Ruiz, 2000; Reichart et al., 2001). For variability on a shorter time scale, within individual burst peaks, the spectrum has been observed to often evolve from hard to soft (Ford et al., 1995; Liang and Kargatis, 1996; Norris et al., 1996). Within the prompt phase, emission of up to 300 keV in the highest BATSE energy bins has been observed to arrive before lower-energy BATSE-detected emission (energy beginning at 20 keV), and in those cases, the more luminous the burst, the longer the lag between higher-energy and lower-energy photons (Norris et al., 1996). The lag-luminosity relationship also provides a means of estimating the redshift of a burst because of the relationships between luminosity and E_p, and E_p and redshift (Norris et al., 2000). Higher BATSE-level energy emission is often shorter in duration than lower-energy emission, an effect visible when multispectra light curves are superimposed. It is important to distinguish the above observations from those at EGRET energies, because the above cited results were limited to energies of a few hundred keV. Described later are EGRET observations that do not necessarily adhere to these patterns.

Populations

Bursts can be divided into two classes based on their T_{90} duration: those that last longer than 2 s, and those for which T_{90} is less than 2 s (Norris et al., 1996). (See Figure 1.3 for a plot of the bimodal duration distribution.) The spectra of shorter bursts are also known to be harder than those of longer bursts, and short-hard bursts are hypothesized to have a completely different type of progenitor. Until 2005, with the detections of the afterglow of a short-hard burst (Bloom et al., 2005; Gehrels et al., 2005), it had not been possible to determine the distance of a short-hard burst, as has been possible for long bursts (this is discussed later). Without the afterglows that make it possible to observe a burst for extended periods in longer wavelengths, it is not possible to find, localize, and determine the redshift of the host galaxy. With only one afterglow observation for a short-hard burst, not much is known much about their distances or their environment (Piran, 2005).

Another class of bursts exist that emit most of their energy in X-rays rather than gamma rays, but have similar time profiles and distributions. These are called *X-ray flashes (XRFs)*, and they have more emission from 2-30 keV than from 30-400 keV. There appears to be a continuum between X-ray flashes and gamma-ray bursts (Barraud et al., 2003), but the suggestion that XRFs are just highly redshifted GRBs does not hold, as XRFs have been detected as close as $z = 0.25$ (Soderberg et al., 2002). XRFs are a notable exception to the narrow GRB energy peak at 250 keV.

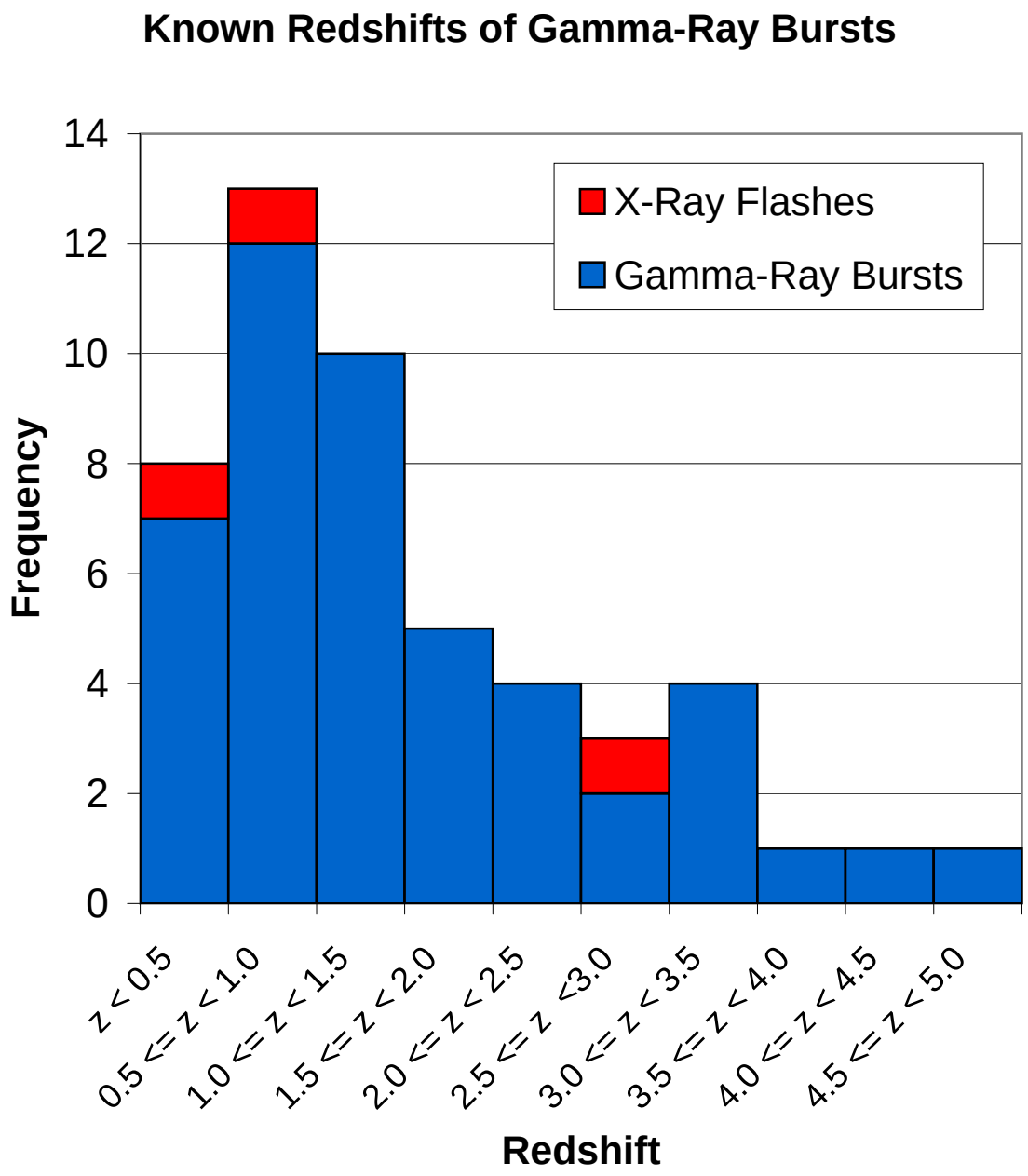

Figure 1.2: Distribution of known redshifts for gamma-ray bursts and X-ray flashes. Blue corresponds measured gamma-ray burst redshifts, and red corresponds to measurements X-ray flash redshifts. Unconfirmed measurements or those for which only upper limits were possible are excluded from this plot. Data from Greiner (2005).

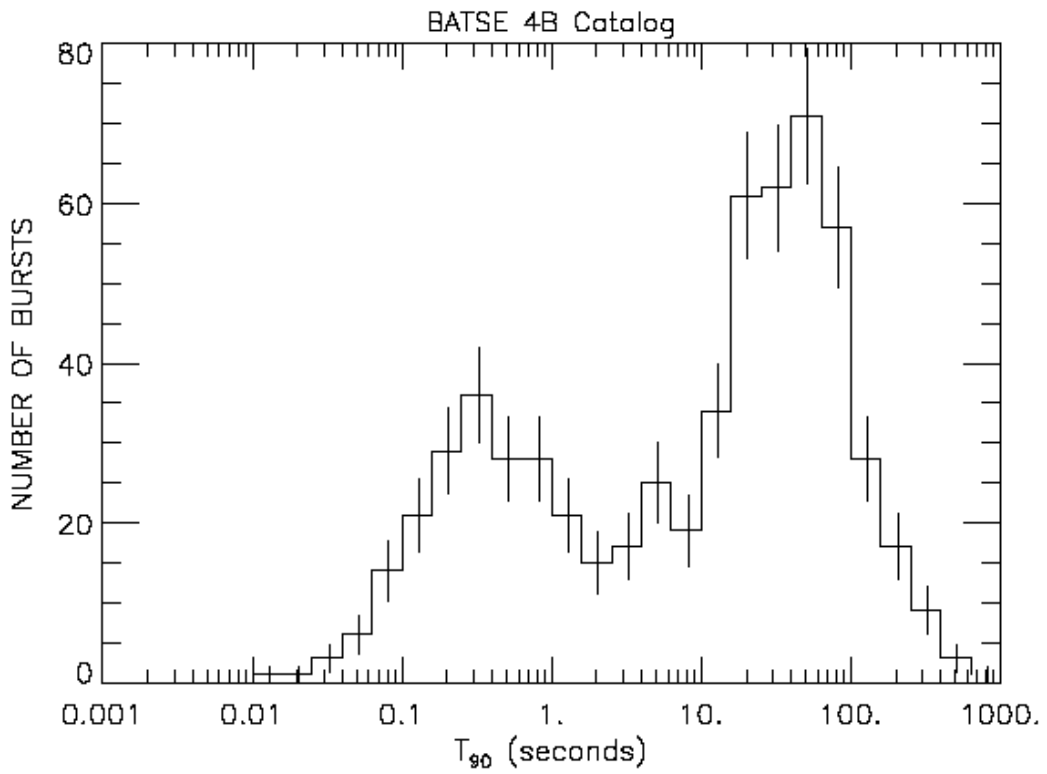

Figure 1.3: Bimodal burst distribution created with the BATSE T_{90} times from the BATSE 4B Catalog. This kind of distribution led to speculation that bursts are divided into short and long classes, and that two different progenitors existed. From Paciesas et al. (2000).

1.3.2 Afterglow

Prompt emission is short lived, so follow-up observations of afterglow emission in other wavelengths is helpful for obtaining precise localizations of bursts. In 1997, the Itailan-Dutch BeppoSAX satellite (Piro, 1997) was able to do this within hours of a burst trigger. This ability led to observations in longer wavelengths that in turn led to the discovery that long gamma-ray bursts reside in star forming galaxies at cosmological distances (determined from redshifts of host galaxies). Knowledge of their distance allowed calculation of the total energy budget, which was initially estimated to be 10^{53-54} ergs (Kulkarni et al., 1998), but is now understood to be much

less because the emission is likely beamed (more on this later). In this section, some characteristics of the afterglow in different wavelengths are described (see Figures 1.4–1.6), beginning with the most energetic. Until recently, afterglow observations were lacking for short bursts, so most of the following is only certain for long bursts. However, at the end of the section, the localization of a short burst via its afterglow detection is described.

X-ray

Even while gamma rays are still being emitted from the prompt phase, an X-ray afterglow begins (Burenin et al., 1999; Giblin et al., 1999; Connaughton, 2002). It has a power-law decay in flux over time, fading below sensitivity limits after days or a few weeks (Cheng and Lu, 2001). The afterglow has also been detected flattening out later in time (Harrison et al., 2001). The X-ray afterglow does not appear to be an extension of the gamma-ray emission, but rather a discontinuous emission that is caused by a different physical process. X-ray emission and absorption lines may have been seen in some afterglows (Piro et al., 1999; Amati et al., 2000; Piro et al., 2000; Antonelli et al., 2000; Reeves et al., 2002). The emission lines are attributed to Fe, Si, S, Ar, and Ca (Piran, 2005), but some have claimed that a detailed statistical analysis shows that the absorption lines are not significant (Rutledge and Sako, 2003). If the absorption lines are significant, they would imply a burst energy 4-50 times larger than the currently accepted value (Ghisellini et al., 2002). The X-ray afterglow typically lasts up to a few days before fading below instrument sensitivity

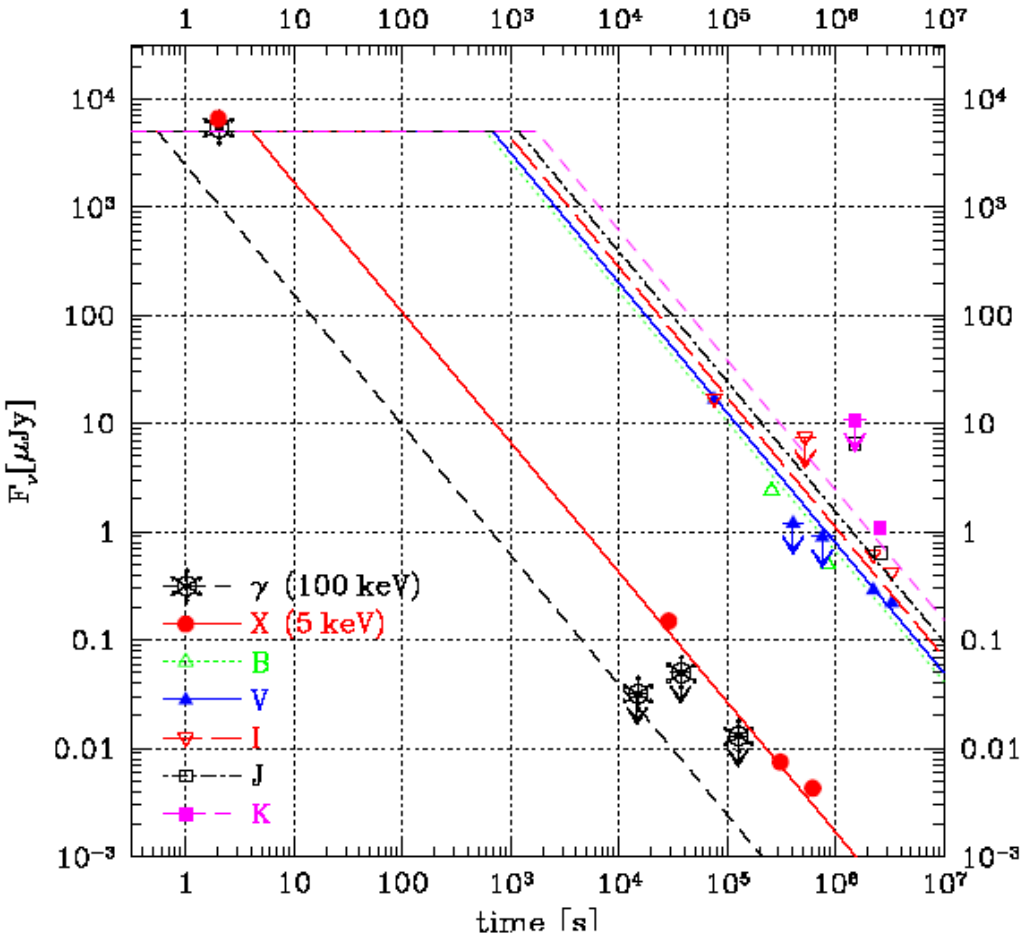

Figure 1.4: Gamma-ray, X-ray and optical afterglow light curves from GRB 970228. Shown are 100 keV gamma-ray fluxes, 5 keV X-ray fluxes, and optical to near-infrared fluxes in the B, V, I, J, and K bands. The fluxes decay over time, and the lines are a prediction from a model of a relativistic blast wave that precedes the decelerating fireball of a gamma-ray burst as it encounters external matter. The temporal flux decay is consistent with power-law fits, except for one data point in the J-band more than 10^6 s after the burst. The authors drew no conclusions from that deviation. From (Wijers et al., 1997).

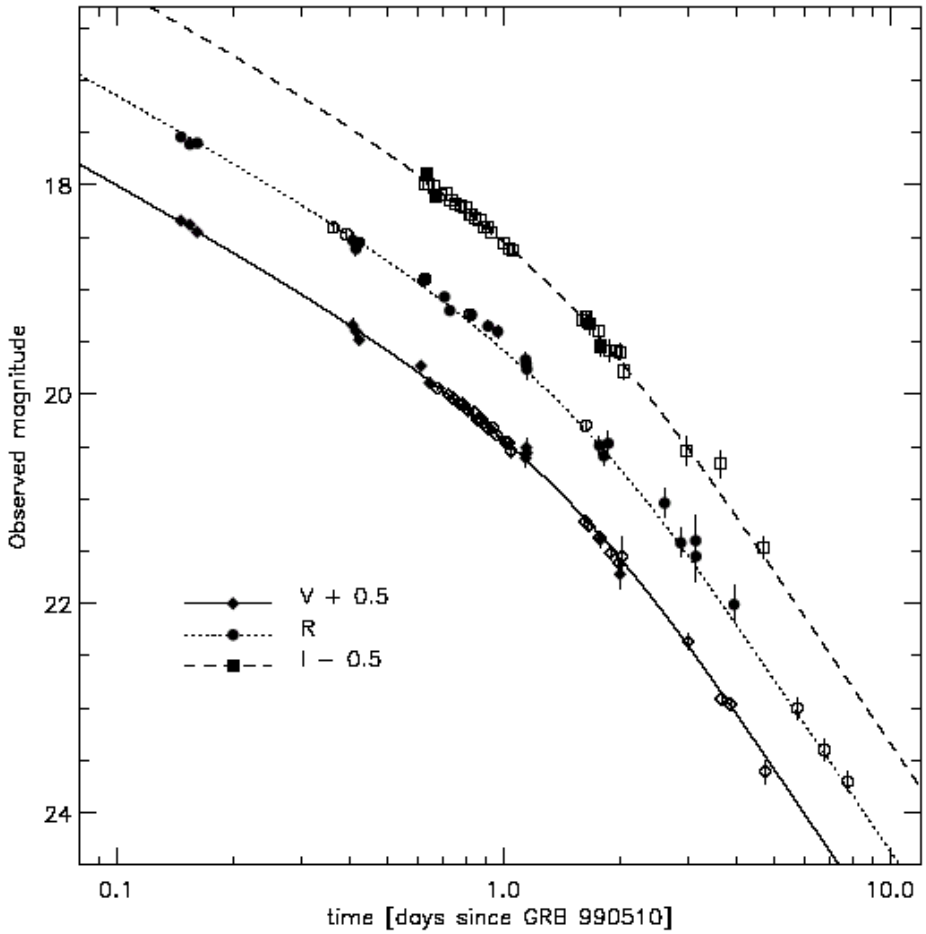

Figure 1.5: Optical afterglow light curves from GRB 990510 in the V, R, and I bands, showing the decay in observed magnitude vs. the time in days passed since the gamma-ray burst. These light curves show evidence of a jet break between 1 and 2 days after the burst. The lines are functional fits to the data, and do not arise from a theoretical model. The authors interpret the break in the curves as evidence for a jet. This reduces the energy of the burst by a factor of 300 relative to what it would be if the geometry were spherical. From Wijers et al. (1997).

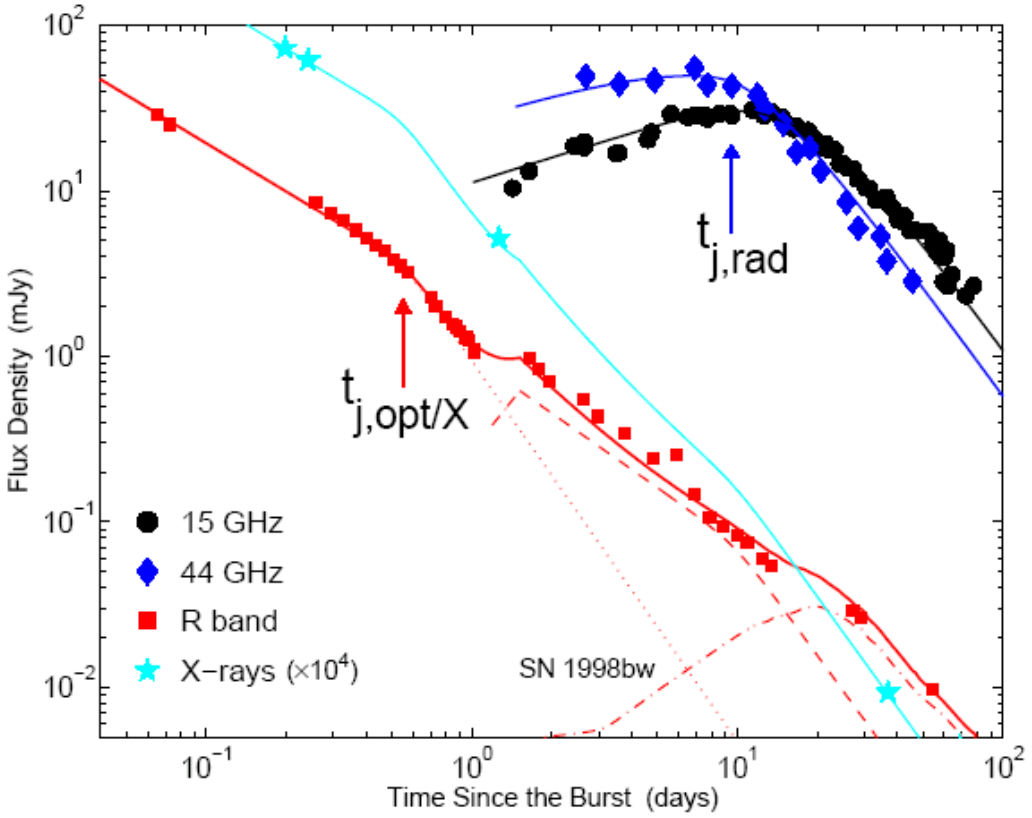

Figure 1.6: X-ray to radio light curves from GRB 030329 showing the flux density vs. time in days since the burst. The dotted and dashed lines are from models of optical afterglow emission. The solid line connecting X-ray data points is also from a model. It is based on the optical to X-ray spectral slope. The increase in the optical emission near t=1.5 days is interpreted as evidence of the deceleration of one of two jet components used to model the burst. The dot-dashed line is the emission from supernova 1998bw. It coincides with a bump in the optical afterglow light curve, suggesting a supernova-grb connection. From Berger et al. (2003).

limits (see Figures 1.4 and 1.6).

Optical and IR

An optical and infrared afterglow has been detected in a few dozen bursts hours to days after the burst. They tend to rise in intensity before peaking and falling off as a power-law in time and energy (Harrison et al., 1999; Stanek et al., 1999), and they usually last a few weeks before they fall below the brightness of the host

galaxy, though some have lasted much longer (Fruchter et al., 1998). From the time of the peak in the light curve, one can estimate the opening angle of the jet from which the burst emission is thought to come (Rhoads, 1999; Sari et al., 1999). (The evidence for and physics of jets are discussed shortly).

The optical light curves do not exhibit completely smooth power-law time decay, and instead show absorption and emission lines in addition to bumps at later times in the curve (see Figures 1.4 and 1.6). Absorption lines are due to matter anywhere along the line of sight to the burst, including in the host galaxy. Emission lines, not seen in many bursts, are thought to be from excited gas between the burst and the detector. The bump seen in some curves is the more interesting feature (see Figure 1.7), because it appears to be evidence for the brightening light curve of a supernova explosion. Several bursts have been detected with these bumps (Bloom et al., 1999; Reichart, 1999; Bloom et al., 2002; Garnavich et al., 2003; Hjorth et al., 2003; Stanek et al., 2003), and the GRB-supernova connection is considered to be well established, though there is no evidence that supernovae are associated with all or most bursts. Finally, polarization of the optical afterglow has been detected with confidence from some bursts (Covino et al., 1999, 2002; Wijers et al., 1999; Rol et al., 2000; Bersier et al., 2003; Greiner et al., 2003), but only on the order of a few percent.

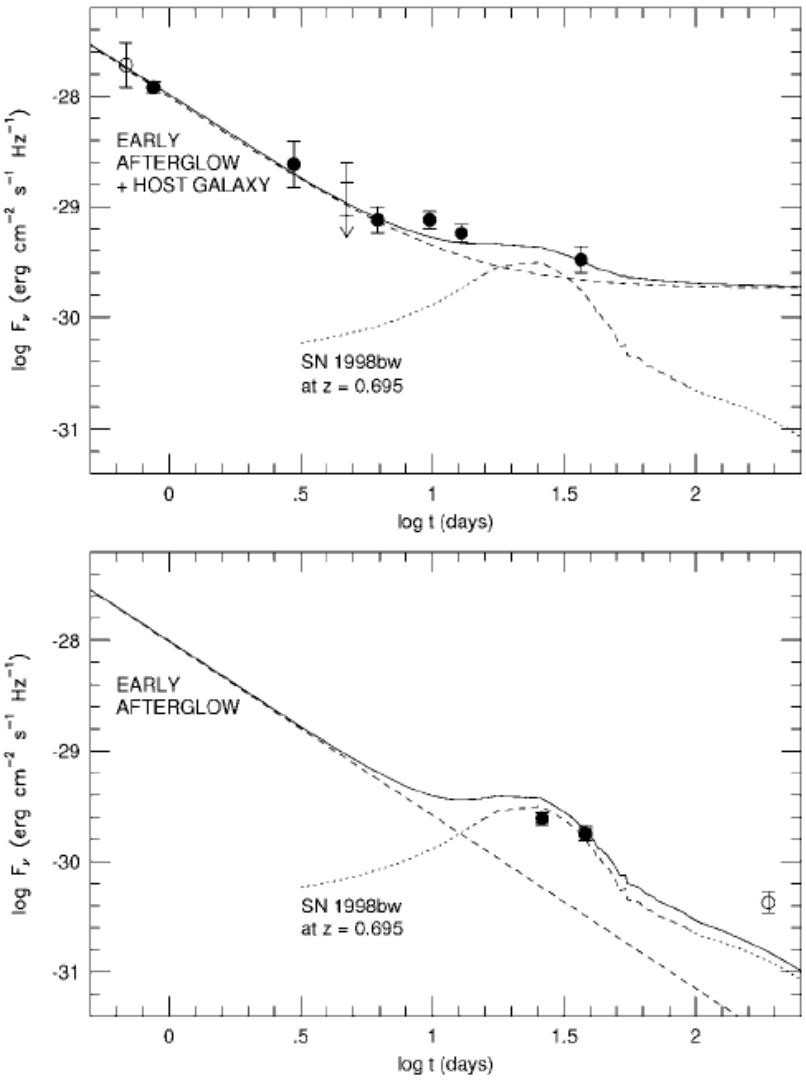

Figure 1.7: Optical light curves from SN 1998bw and the GRB 970228 afterglow. The top plot has R-band light curve of the burst and its host galaxy from ground based measurements, along with a fit. The bottom plot has a space-based measurement of the same event. Superimposed on both plots is the fit to the light curve of SN 1998bw when transformed to the GRB redshift. From Reichart (1999).

Optical Flashes

Distinct from optical afterglow, in a few bursts, short lived optical emission has been detected 10s of seconds to 1.5 hours after gamma-ray burst emission has subsided (Akerlof et al., 1999; Fox et al., 2003; Li et al., 2003; Price et al., 2003), but before a traditional afterglow begins. Observations of these *optical flashes* show that their peaks do not occur in coincidence with the peak gamma emission, so it is clear that they are not simply a low energy tail of burst emission (Piran, 2005), but are produced by a different post-burst mechanism. See Figure 1.8 for the light curve from an optical flash.

Radio

Monitored for longer times than the optical afterglow is the radio afterglow (Figure 1.6), which has been observed for years after some bursts before the spectra flatten out and decay below detection sensitivity. Most detections do not begin until about one day after a burst, and the earliest was at about 0.8 days after a burst (Taylor et al., 2001). Fluctuations in the emission have been interpreted as interstellar scintillation[4], and this was used in one case to calculate the size of the emitting region (Frail et al., 1997). This showed that the emission came from a region the size of 10^{17} cm only four weeks after a burst, which is a clear sign of relativistic expansion. The long life of radio emission has made possible measurements of the total burst energy (Waxman et al., 1998), because after a time the emitting region

[4]Fluctuations in emission intensity due to variations in the density of interstellar material.

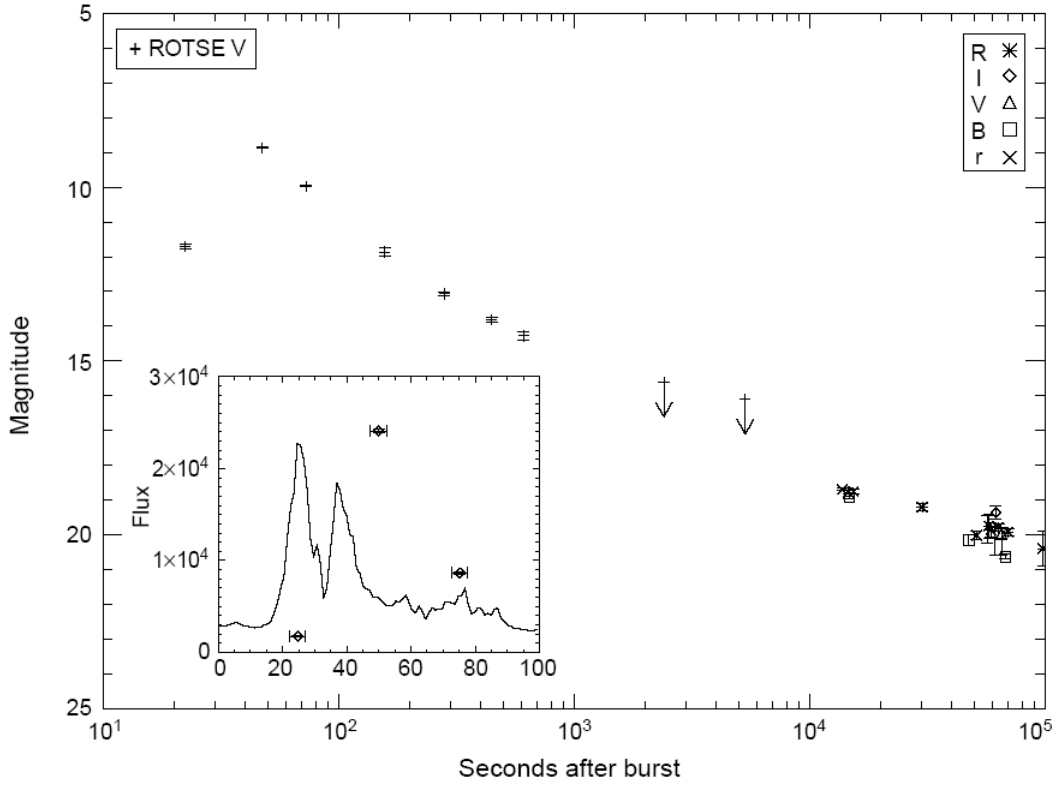

Figure 1.8: Light curve from the optical flash of GRB 990123 (Akerlof et al., 1999). This flash was detected by the Robotic Optical Transient Search Experiment (ROTSE) (Marshall et al., 1997). The main plot shows the magnitude of the optical emission versus time after the BATSE trigger. The inset is a 100-300 keV BATSE flux with the superposition of the first three ROTSE optical fluxes (in arbitrary units). Note the rise and decay of the optical flash, which peaks before the BATSE emission subsides. From Akerlof et al. (1999).

spreads out and becomes spherical. Radio afterglows are not to be confused with radio flares, which are of much shorter duration and have also been detected after gamma-ray bursts (Kulkarni et al., 1999; Frail et al., 2000). These may be caused by the same process that causes optical flashes.

The Localization of a Short Burst

It was mentioned above that a short-hard burst had finally been localized and its distance determined. Because most of the discussion above is based on that of long bursts, this short burst deserves special mention.

On May 9, 2005, GRB 050509b, with duration of $\sim 0.4s$ and 15 to 150 keV fluence of $(9.5\pm2.5)\times10^{-9}$ergs cm^{-2} was detected by the Swift Burst Alert Telescope (BAT) (Gehrels et al., 2005). Swift was able to localize an associated X-ray source after ground-based processing of data from its X-ray telescope (XRT), but optical and *Chandra* X-ray telescope (Martin, 1999) observations were not able to find any sources. The Chandra observation was not until two days later.

The center of a giant elliptical galaxy, 2MASX J12361286+2858580, is 9.8" from the center of the XRT error circle. The probability that this is due to a random occurrence is $\sim 10^{-4}$, so it is believed that the galaxy is the host for this burst (Bloom et al., 2005). The redshift for this galaxy is z=0.225. Giant ellipticals are thought to be good candidate sites for binary pairs in which one star is a compact object (neutron star or black hole). This is consistent with the model (explained below) that short-hard bursts are caused by the merger of compact objects.

1.3.3 Global Properties

Details of the prompt emission and afterglows were discussed above, but little has been said about the burst environment and properties as a whole. To begin with, studies of BATSE data showed that the burst distribution is spatially isotropic (Meegan et al, 1992) (see Figure 1.9). More recently some have suggested that shorter bursts may not be evenly distributed, which would imply that they are closer than longer bursts (Mészáros et al., 2000a,b; Magliocchetti et al., 2003; Cline et al., 2003). This could be a selection effect since it may be more difficult to detect distant short bursts.

From redshifts of long bursts we know that they are at cosmological distances. They appear to reside in star-forming host galaxies (Fruchter et al., 1999), and within star forming regions within those galaxies. The distribution of GRB host galaxies at a given redshift could be consistent with the distribution of star forming galaxies at the same redshift, but some argue that the galaxies in which GRBs are found are of a different population (Piran, 2005). If one assumes that it is possible to extrapolate from the known redshift distribution, one can argue that the rate and luminosity of GRBs was higher in the past, and that there is a hardness-luminosity correlation (Lloyd-Ronning et al., 2002). However, this means that the inner burst inner burst engine, or physics therein, had to be different, which make this method of estimation difficult to accept. A better determination of the redshift distribution should become possible with an increased data set.

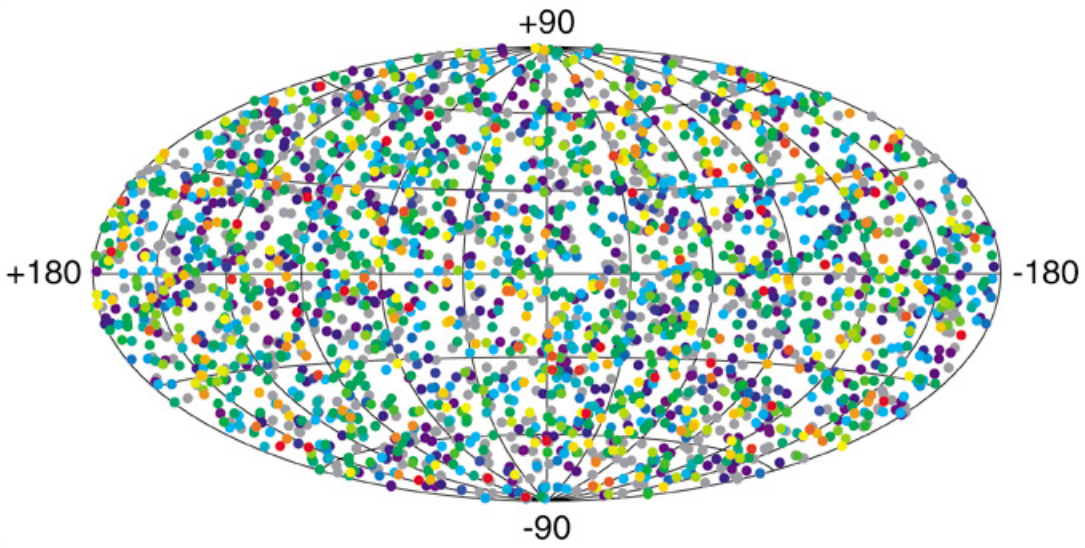

Figure 1.9: Isotropic distribution of 2704 BATSE bursts. This was one of the major results from BATSE. From Paciesas et al. (2000).

Early estimates of burst energy, which were at about 10^{53-54} ergs[5] presented a problem until it was suggested that GRBs are beamed (Rhoads, 1999; Sari et al., 1999). It was proposed that if the energy is constrained to a beam of width θ, the total energy could be lower by a factor of $\theta^2/2$ (Sari et al., 1999). A burst is only seen if its beamed emission is pointing at the detector. When beaming is taken into consideration, estimates of burst energy are lowered to about 10^{51} ergs (Frail et al., 2001), or about the same as a Type Ia supernova.

1.3.4 Physical Processes and Models

Before explaining the arguments in favor of beaming (in addition to the energetics), it is necessary to describe some of the physical processes that follow from observations and theoretical arguments.

[5]Compare this with the 10^{51} ergs of a Type Ia supernova.

The Compactness Problem

Shortly after bursts were discovered, the *compactness problem* arose (Ruderman, 1975). It was clear that the burst spectra were non-thermal, and the size of the emitting region could be inferred from the time scale of the fluctuations. Calculations were made in which the estimated total energy was put into the small emitting region, and there was no way to avoid the fact that the density of gamma rays would lead to e^+e^- pair creation at a prodigious rate, which would produce a very high optical depth for the remaining gammas. A non-thermal spectrum did not look possible.

The solution to the compactness problem was to move the emitting material at relativistic speeds towards the observer. If this is the case, the photons can be assumed to be blueshifted from their source frame energy, which means that they are less energetic and less likely to pair produce. The density of material is also much less than initial estimates, and the optical depth decreases by the square of the Lorentz factor, Γ, which is estimated to be at least 100. EGRET observations of high-energy photons contributed to this conclusion. Observations of radio scintillation are also supporting evidence for relativistic motion if the scintillation is due to scattering off of interstellar gas. In that case, the inferred size of the emitting region and the measured elapsed time lead to an estimate of the bulk velocity (Frail et al., 1997). Another means of determining the size of the emitting region can be inferred from measurements of the radio flux-density and the distance to the burst (Katz and Piran, 1997). These measurements confirm that motion has to be relativistic.

Thirdly, the synchrotron frequency of the optical flash from GRB 990123 allowed for the estimation of a Lorentz factor of about 200 for that burst (Sari and Piran, 1999).

Jets, Relativistic Beaming, and energetics

It was stated that energetic arguments suggest that the emission from bursts is beamed. In this model, the geometry of the burst is such that two collimated jets of material are ejected from the central engine in opposite directions. Jets are not unique to gamma-ray bursts; jets, however, are to be distinguished from relativistic beaming, in which radiation moving with a large Lorentz factor appears to be beamed into a smaller region along the line of sight, with a width of $1/\Gamma$.

The argument in favor of jets relies upon more than burst energetics. The breaks observed in afterglow light curves suggest the presence of a widening jet (Rhoads, 1998, 1999). Either the beamed energy exits sideways as the jet spreads hydrodynamically, so we do not observe it, or a decreasing Lorentz factor causes the size of the beamed region to expand such that a portion of the radiation that was once directed at the observer is then beamed away. Both of these effects are likely, and they are observed in the light curves as jet breaks (Sari et al., 1999; Panaitescu and Mésáros, 1999). If gamma-ray bursts are indeed beamed, a fixed observer only sees a small fraction of the total number of bursts, which suggests that the true burst rate is a factor of 75-500 times higher than the isotropically estimated rate (BATSE detected $\sim$1/day) (Frail et al., 2001; Guetta et al., 2005).

There are at least three empirical reasons for believing that long gamma-ray bursts have a standard energy reservoir (or at least most of them, in light of the previous paragraph). The opening angle of the jet can be derived from the jet break time, and the energy of the prompt emission phase of a burst can be calculated if a redshift is obtained from the afterglow. With this information, it has been shown that when the prompt energy of a burst is corrected for geometrical factors (the opening angle of the jet), it is nearly a constant (Frail et al., 2001; Bloom et al., 2003). It can also be shown that the energy contained in the afterglow is a standard value (Panaitescu and Kumar, 2000, 2001; Freedman and Waxman, 2001; Piran et al., 2001; Berger et al., 2003).

If the energy of the prompt emission and the energy of the afterglow are both approximately constant, the total energy of a long burst is constant – a remarkable statement. This is further bolstered by a combination of relationships. The first is between the jet opening angle and the spectral lag (high energy emission precedes low energy emission), and the second is between the spectral lag and the luminosity. Taken together, these imply a relationship between luminosity and jet opening angle (Norris et al., 2000; Salmonson and Galama, 2002; Frail et al., 2001) that is consistent with the first argument regarding jet geometry and energy (Zhang and Mészáros, 2004).

The Fireball Shock Model

Much of the above describes features of what is known as the fireball shock model (Rees & Mészáros, 1992; Mészáros & Rees, 1993), which says nothing about the burst's central engine, yet explains many observations and solves theoretical problems. The compactness problem and concerns regarding energetics are solved by relativistic motion and geometrical beaming, and relativistic expansion is also supported by radio afterglow observations and the optical flash.

Both the afterglow and the optical flash do not directly arise from collimated flow and relativistic beaming effects. Neither are the power-law spectra from either the prompt gamma-ray or later x-ray and optical explained. All of these observational features require a different physical process that is consistent with the jets and beaming, star forming regions, the collapse of massive stars, and the creation of compact objects.

The fireball shock model is compatible with the above constraints, though questions about its details are yet to be worked out. (See Figure 1.10 for one artist's conception.) In the model, material and radiation consisting of photons, e^+e^- pairs, and some baryons are ejected in shells on the time scale of ms in the observer's frame (Zhang and Mészáros, 2004). These shells are not spheres centered around the core of the explosion, but are more like "flying pancakes" constrained to jets. In order to convert the kinetic energy of the shells into the photons observed, the shells must collide with something. Either they have different Lorentz factors that leads to collisions with each other (the internal shock scenario), or they collide

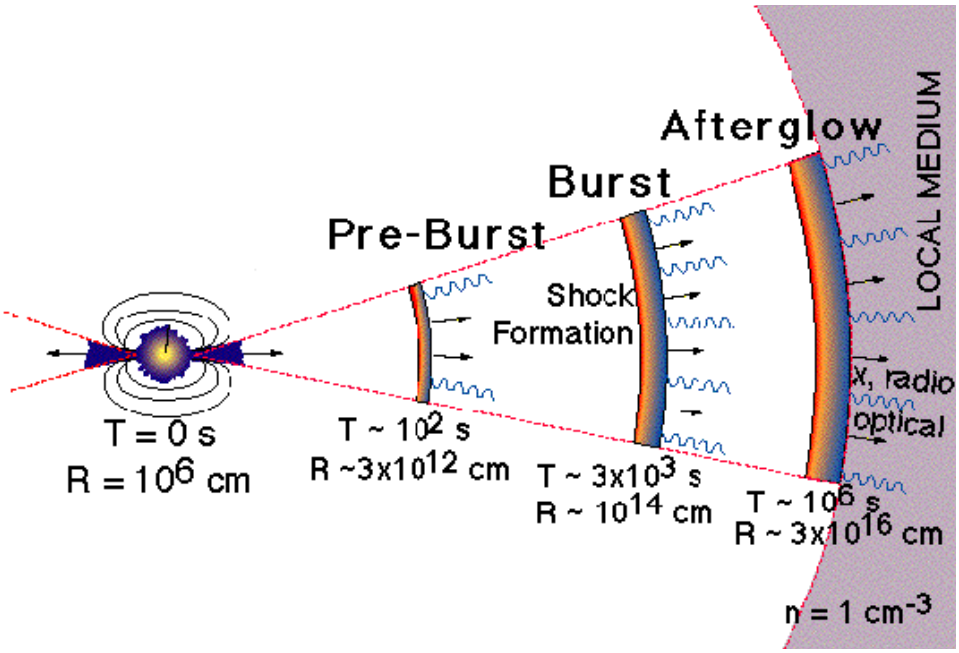

Figure 1.10: Schematic diagram of the fireball shock model. Jets are shown exiting from a central engine. Shocks form as shells of different Lorentz factors collide. The forward shock eventually interacts with the local medium to cause an X-ray through radio afterglow.

with other material (the external shock scenario).

External shock models require very dense, small clouds in order to efficiently convert energy with the observed time scales. Large gaps in emission – the quiescent periods observed in some bursts – are also troublesome for the external shock model. Conversely, internal shocks do not require a complicated environment. Instead, they require a source that varies on a short time scale, which is discussed in the following section on central engines. If the difference between the Lorentz factors of different shells is significant, the efficiency of conversion will be high (Hurley, Sari, and Djorgovski, 2002). One thing do keep in mind when thinking about the timing of burst emission is the relativistic time dilation effect. Though bursts are observed to fluctuate on the order of ms, in the rest frame, the fluctuations are spread over

much longer periods due to the high Lorentz factors, and the time scales are hours and days rather than milliseconds and seconds. Here, all discussions of time scales are in the observer's frame.

When shells collide, they create relativistic shocks that are believed to produce synchrotron emission that is responsible for some of the observed gamma rays (Rees & Mészáros, 1992; Mészáros & Rees, 1993). In shell collisions, densities are still low enough that individual particle collisions are not probable (Piran, 2005). These particles are repeatedly scattered back and forth across the shock by magnetic fields, gaining energy each time in a process known as *Fermi acceleration*. They can eventually get upstream of the shock, having been greatly accelerated, and produce power-law synchrotron radiation.

BATSE observations were not able to probe the fundamental energy scale of bursts and determine the true range of Lorentz factors. High-energy (GeV) observations by GLAST will be able to answer questions about a largely unexplored energy regime, and determine properties of internal and external shocks (Zhang and Mészáros, 2004; Lithwick and Sari, 2001; Zhang and Mészáros, 2002; Baring, 1999).

Synchrotron emission may only be responsible for part of the burst emission. Many variations on the fireball shock model predict inverse-Compton scattering of photons to high energies (possibly GeV-TeV). This would happen when a shock accelerated electron (or perhaps even a proton, as is discussed later) up-scatters a synchrotron photon. The resulting energies would be so great that they would be higher than the portion of the burst spectrum commonly observed in past experi-

ments.

The scenario just described is simplistic, ignoring the combinations of shocks and reverse shocks that can give rise to different features in the emission, but the basic mechanisms for particle acceleration and radiation are valid. As the burst continues to expand and radiate, it eventually reaches the point where it encounters the interstellar medium. External shocks form when this happens, and an external reverse shock is believed to lead to the observed optical flash. As the ejecta continue into the medium, continually slowing down, external shocks produce the observed afterglow. Eventually, the jets slow down and a break in the light curve is visible. After a time, the emission slows enough that it can be described in non-relativistic terms, and it spreads out to the point of being spherical.

1.3.5 The Central Engine

The fireball shock model has been studied extensively, and it continues to be refined. The natural question to ask is what might give rise to this scenario. There is no need to revisit arguments for a small emitting region, and we already suspect that these bursts come from star forming galaxies and at least some are associated with supernovae. Other constraints are the energies, rates at which they happen, the long and short populations, and collimated jets. Several types of progenitors have been proposed, and a few of the more popular candidates are described here.

One compact object that can emit great energy is a black hole that is accreting matter. Such a situation might arise when compact objects merge, such as some

combination of white dwarfs, neutron stars, or black holes (Paczynski, 1991; Fryer et al., 1999; Fryer and Woosley, 1998). This is the favored cause of short bursts (Narayan et al., 2001). For long bursts, the collapse of a massive star is thought to be a likely cause (Woosley, 1993; Paczynski, 1998; MacFadyen and Woosley, 1999).

Collapsars are speculated to begin as rapidly rotating massive stars. Their iron core collapses into a black hole, and an accretion disk forms. Then stellar material funnels in along the rotation axis and its energy is ejected into the surrounding stellar material, giving rise to jets that penetrate the material and produce the prompt emission phase of the burst (Piran, 2005). The Lorentz factors produced by this method would be greater than 100, with variation provided by the stellar envelope still enshrouding the core (Aloy et al., 2002; Zhang et al., 2003).

With the collapsar mechanism, it is conceived that the collapse can happen in one or two distinct stages. If it happens in one stage, a black hole is formed from the initial collapse in a *hypernova* scenario (Paczynski, 1998). Alternatively, long bursts may also be produced by a two-stage version of collapse known as the *supranova* model (Vietri and Stella, 1998). In this case, first a hyper-massive neutron star is formed by a supernova. The neutron star is only sustained by its rotational energy, so it loses angular momentum and collapses into a black hole. Accretion leads to a burst as described above. The burst ejecta, in this case, would not have to penetrate a stellar envelope, as the envelope has already been blown away by the supernova that preceded the burst. The ejecta would possibly pass through a strong magnetized medium produced by a pulsar wind produced by the neutron star, and

inverse-Compton scattering of associated photons might have produced the delayed GeV emission detected once by EGRET (Hurley, 1994).

Additional GeV observations may be able to determine the likelihood of the one-step and two-step models, since the supranova model does predict delayed GeV emission due to the fireball-SN shell interaction (Wang et al., 2002; Guetta and Granot, 2002; Inoue et al., 2003). In contrast, the one-stage collapsar may cause X-ray and gamma-ray precursor emission (Ramirez-Ruiz et al., 2002; Waxman and Mészáros, 2003).

Some have also thought that a pulsar-type mechanism *not* related to supranovae could be the central engine for bursts (Usov, 1992). In this case, an accreting white dwarf collapses into a neutron star whose magnetic and electric fields would produce a plasma from which energy is dissipated (Usov, 1994; Thompson, 1994). A variation on this involves the extraction of rotational energy from a black hole, also using a pulsar-type mechanism (Katz, 1997).

1.4 High-Energy Burst Emission and Quiescence

1.4.1 Previous Observations of High-Energy Emission from Gamma-Ray Bursts

This thesis is primarily concerned with detection of high-energy (MeV-GeV) emission from bursts, a topic about which there has been a great deal of speculation. In this section, some particularly interesting high-energy burst observations are sum-

marized, followed by a discussion of some problems that future GLAST and ground-based telescope observations may help solve. As described below and in Chapter 3, most observations of MeV and greater emission have been with EGRET, and some of those only with the EGRET calorimeter, known as the Total Absorption Shower Counter (TASC), which was sensitive in the ∼1-250 MeV range. The few high energy observations are dwarfed by lower energy observations, especially by BATSE's detection of over 2700 bursts. However, the scarcity of higher-energy observations makes each one all the more valuable for the window they provide.

Most observations made with EGRET used its spark chamber, which was able to detect individual photons and determine their energy and direction. The TASC calorimeter aided in the energy determination, and could also be used to take spectra independently of the spark chamber's operation. TASC data were used to study several bursts in the ∼1-250 MeV range, using BATSE triggers as a guide as to when to look in the data. Because the TASC is not shielded and thus has to contend with a high cosmic-ray background, and perhaps because of the narrow peak energy distribution at an energy lower than the TASC's range, only some of the most fluent BATSE bursts were observed in the TASC. However, some of these produced detectable emission up to 100 MeV or more (Schneid et al., 1995; Catelli et al., 1995; Schneid et al., 1992). Some of the emission showed the hard to soft spectral evolution that is commonly seen in bursts at lower energies (Schneid et al., 1995; Catelli et al., 1998, 1995; Schneid et al., 1992), and the high-energy emission observed was coincident with lower energy BATSE emission except in one

case (Dingus et al., 1998). A particularly bright burst, GRB 990104, had emission definitely past 50 MeV and perhaps beyond 100 MeV that was coincident with lower-energy emission after the burst did not emit for ∼100 s (Wren et al., 2002). Details of this burst are presented in Chapter 3.

There was also a report of early gamma-ray afterglow (Giblin et al., 1999), in which 25-300 keV emission was detected beginning at the tail end of a burst. More recently, emission up to 200 MeV was detected from GRB 941017 (González et al., 2004). Within statistical uncertainties, the high-energy emission from this burst was constant in flux and spectral index over time, and it is difficult to explain in terms of the synchrotron shock model. This is especially interesting because EGRET detected an 18 GeV photon from another burst, GRB 940217, some 75 min after the end of BATSE-detected emission (Hurley, 1994). Another intriguing high-energy observation is the possible detection of near-TeV emission from a burst by the Milagrito (Atkins et al., 2000a) ground based air-shower detector. It may have detected photons of at least 650 GeV from GRB 970417a coincident with the BATSE T_{90} time (Atkins et al., 2000b). The high-energy burst observations listed here are notable for their uniqueness. They are too few to reveal definitive patterns, and each one hints at distinct and varied mechanisms that will only be understood with more high-energy observations.

1.4.2 Motivation for Future High-Energy Burst Observations

Observations of 200 MeV emission that evolves independently, GeV photons thousands of seconds after a burst, or near-TeV emission closely following a trigger all require processes that are possible within the fireball shock model. However, many unknowns remain, and detections of high-energy emission are highly desired for their potential to solve problems that lower-energy detections cannot. GLAST and ground-based ($\gtrsim$100 GeV-sensitive) missions will be able to make many of the high-energy observations required for these solutions.

The few EGRET detections of high-energy gamma-ray emission from the prompt phase require high bulk Lorentz factors. The single detection of GeV photons from the prompt phase ($\sim$3 GeV from GRB 940217) requires a Lorentz factor of at least several hundred (Guetta and Granot, 2002) due to the lower bounds imposed by the compactness problem described in section 1.3.4. The lack of observations of GeV emission from other bursts means that it is unknown whether emission in this energy range is common from the prompt phase. However, fast detections and observations of bursts by GLAST in the GeV to 100s of GeV energy range will provide an answer to the question of whether emission in this range is common. If prompt GeV emission is common, bulk Lorentz factors of at least several hundred are also common. Burst models also predict that high-energy acceleration processes in jets could produce emission that extends into the TeV range (Mészáros et al., 1994; Pilla and Loeb, 1998; Dermer et al., 2000; Zhang & Mészáros, 2001), so high-energy observations are important. With an energy range that extends up to

100s of GeV, GLAST should be able to provide a large sample of cutoff measurements that will help to determine Lorentz factors, thereby constraining models that attempt to explain how and where prompt burst emission is produced.

GLAST, with the lower-energy (10 keV – 25 MeV) GBM and the higher-energy (20 MeV – >300 GeV) LAT, will have wide enough energy coverage both to measure the distribution of peak energies directly, and to help determine the burst energy budget with measurements of the spectrum over the wide GLAST energy range. By extrapolating the GeV burst spectrum to higher-energies, it would be possible to estimate more reliably the expectations for ground-based TeV observations of burst emission. The GLAST upper-energy range may overlap with the lower-energy range of ground-based observatories, providing continuous energy coverage of burst emission over an even wider range than could be accomplished with a single mission.

GLAST observations of high-energy emission will be able to help distinguish among many possible emission mechanisms beyond the standard synchrotron shock scenario. While synchrotron emission is believed to be a strong component of prompt burst spectra, the inverse-Compton (IC) mechanism is also thought to be responsible for some of the highest-energy prompt emission. It is also possible that π^o decay due to proton-proton, proton-neutron, or proton-photon interactions, or synchrotron emission from π^+ or protons could be responsible for a high-energy hadronic component. Both hadronic and IC high-energy emission components could be enhanced by the presence of a supernova shell or a pulsar wind nebula (Wang et al., 2002; Guetta and Granot, 2002; Inoue et al., 2003). GLAST-observed characteristics of

high-energy emission may provide insight into the burst environment, because each emission mechanism is predicted to have specific spectral features.

Observations coupled with detailed theoretical studies might also answer questions about the high-energy component that evolved separately from lower-energy emission for burst 941017 (González et al., 2004). The high-energy emission from this burst had a constant flux and constant spectral index, within statistical uncertainties, from 14 s to 211 s after the BATSE trigger (see Figure 1.11). The high-energy component contained more than three times the energy of the lower-energy component, and there is no high-energy cutoff visible. GLAST observations of bursts of this type are necessary for determining the location of a cutoff and the total energy emitted.

GLAST observations of delayed GeV emission are also important for the understanding of bursts. Attempts to explain the detection of the 18 GeV photon over an hour after the prompt phase of burst 940217 have involved many theories (Mészáros & Rees, 1994; Katz, 1994; Vietri, 1997; Totani, 1998a,b; Wang et al., 2001), but because sensitive, high-energy measurements are few, the commonality of the phenomena seen in bursts like 940217 and 941017 is unknown. However, GLAST observations of both prompt and delayed high-energy emission may be able to reveal whether the phenomena are rare, or whether such occurrences are common.

There may be other mechanisms by which delayed emission can occur. The spectral cutoffs mentioned above may be caused by the absorption of high-energy photons that interact with lower-energy photons to create electron-positron pairs.

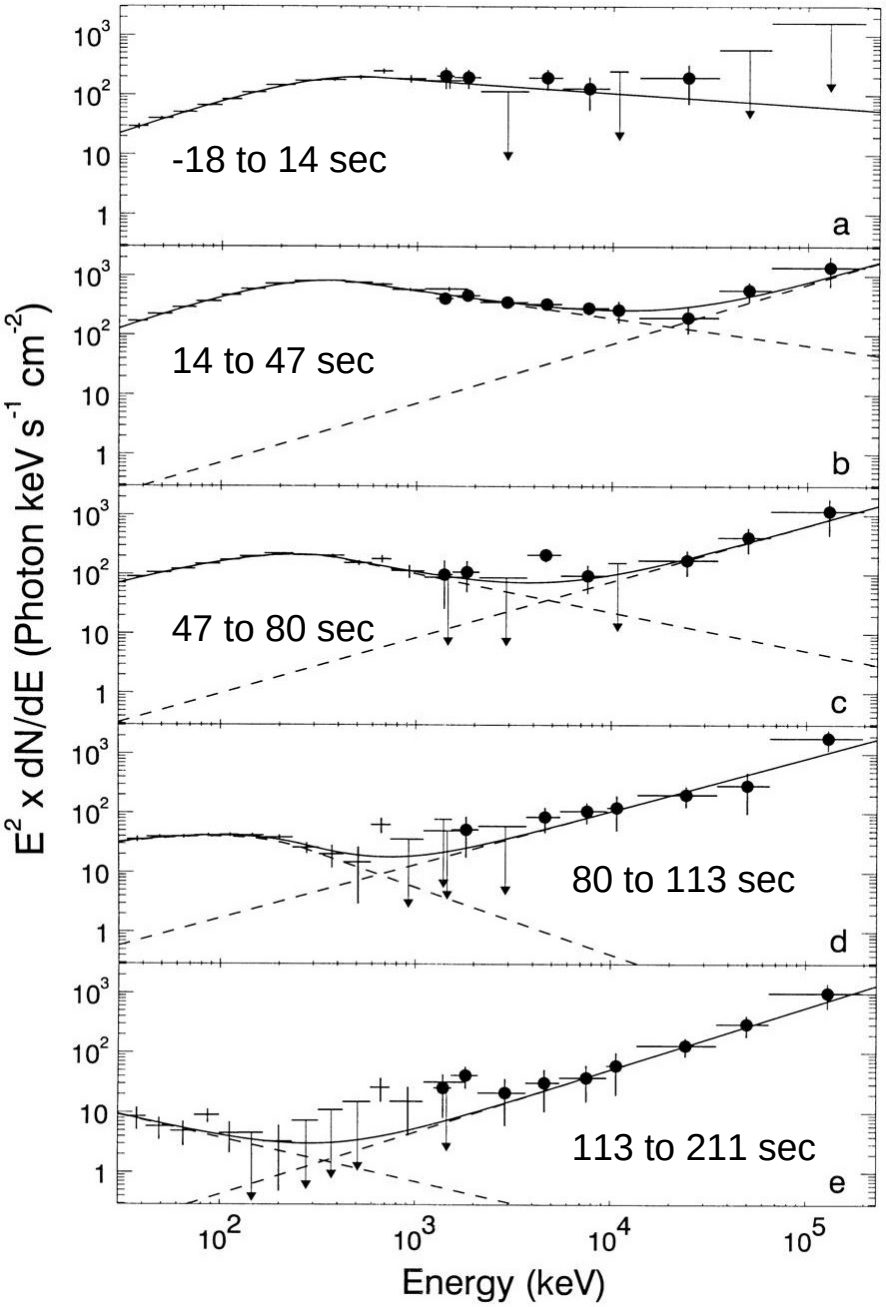

Figure 1.11: Energy fluxes from GRB 941017 with BATSE and EGRET (calorimeter) data points for five time intervals, noted on the figure. The times in seconds are relative to the BATSE trigger time. The crosses correspond to BATSE data, and the solid circles correspond to EGRET calorimeter data. The solid curves are model fits to the data, and the dashed lines are the low- and high-energy power-law spectral fits. From (González et al., 2004).

Through the pair creation process would cut off the high-energy spectrum, the pairs would be expected to synchrotron radiate and alter the spectrum (Pilla and Loeb, 1998; Mészáros et al., 2002). On the contrary, if high-energy photons are not absorbed, they could be scattered by pairs or by the baryon-associated electrons (Lithwick and Sari, 2001). The highest energy (TeV) photons, which are most likely to be absorbed, may only escape the source if it is compact. Even those that do escape may still be absorbed by interactions with the infrared (IR) background (de Jager and Stecker, 2002), producing pairs that could up-scatter cosmic microwave background (CMB) photons to the MeV-GeV range. It has been suggested that the attenuation of very-high-energy photons makes detections of TeV sources with redshifts greater than 0.1 unlikely (de Jager and Stecker, 2002). Any observations of TeV emission from bursts with $z > 0.1$ could pose problems for attenuation models. Likewise, it may be possible to measure the strength of the intergalactic magnetic field, which would change the trajectory of the e^+e^- pairs within a few Mpc of bursts (Guetta and Granot, 2002).

In the above scenario, the resulting emission would be delayed due to the multiple scattering of the e^+e^- pairs off CMB photons. As this happens, the $e^\pm$ would lose energy with each interaction, and the resulting photon energy would follow a power-law. A notable feature is that it would take longer for the creation of lower-energy photons than high-energy photons (Plaga, 1995; Cheng and Cheng, 1996; Dai and Lu, 2002), such that the delay for 1 GeV photons could be up to 1 day, and 100 MeV photons could be delayed several days (Cheng and Cheng, 1996). This

is considered a maximum delay, and there is the probability that MeV photons could arrive earlier. It might even be possible to measure the strength of the intergalactic magnetic field through high-energy observations (Zhang and Mészáros, 2004; Dai et al., 2002).

It is possible that time-extended observations at MeV-GeV energies could detect up-scattered background photons with a power-law spectrum. The cited model may overestimate or underestimate the power-law index and the time delay, but higher-energy emission would be expected to arrive before lower-energy emission. At the present time, delayed MeV emission might be found in EGRET data, and in the future, GLAST may be able to detect very high-energy GeV emission that is later followed by lower energy emission. A later chapter describes work done for this thesis to search for delayed MeV emission in EGRET's TASC.

GLAST will also have very low deadtime ($\sim$26 μs), which will allow for the measurement of very short time scale light curves at very high energies, which is something that has not been modeled before. GLAST's temporal resolution will also allow for measurements of different arrival times for photons of different energies. Spectral lag was discussed in section 1.3.1, but lag has only been measured in the keV energy range. GLAST will be able to determine whether the lag is evident as the energy increases into the MeV and GeV. In addition, if there is an energy dependence on arrival time that can be correlated with redshift, it might provide evidence for theories of loop quantum gravity that predict that higher-energy photons will travel faster than those of lower-energy (Alfaro et al., 2002). With its wide energy

range, sensitivity, wide field of view, and low deadtime, GLAST has the potential to contribute much to gamma-ray burst science.

1.4.3 Quiescence

Instances of quiescent periods in burst light curves were briefly mentioned above. These are periods during which the prompt phase of a burst appeared to go quiet for significant amounts of time (relative to the total length of the burst) before engaging in a second emission episode. The first comprehensive study of bursts with quiescent episodes labeled the pre-quiescent emission as *precursor* emission (Koshut et al., 1995) because it was not as intense as the second emission episode. Later, it was argued that the precursor categorization was too restrictive and singled out a small class of bursts, while there were other bursts that had pre-quiescent emission more intense or equal to that of later emission episodes (Ramirez-Ruiz and Merloni, 2001; Ramirez-Ruiz et al., 2001). The authors of the latter study did not distinguish among bursts depending on the intensity of different emission episodes, but just singled out bursts that had quiescent periods of any length, where the definition of "quiescent" was that the emission dropped to a level within 2σ of background.

That study examined bursts longer than 5 s, and found that about 15% of them had a quiescent period. The longer bursts were not more likely to have a quiescent period than the shorter bursts, and the post-quiescent emission episodes were found to be the same length as the quiescent period that preceded them. Detailed studies were performed of different scenarios involving the central engine and the shells it

ejects. The models showed that if the central engine goes quiet, the gamma-ray light curve will always also have a quiescent period.

All but two observations of a single burst with a quiescent episodes used BATSE energies. One EGRET observation of a high-energy pre-quiescent episode from GRB 910503 showed hard to soft spectral evolution, and spectral data were not available for the second, much less intense episode (Schneid et al., 1992). Observations of the same burst with the imaging Compton telescope COMPTEL onboard CGRO led to a measurement of a spectrum with energy up to 10 MeV for the post-quiescent emission episode (Winkler et al., 1992), but the measurement was weak above 5 MeV. No observations of >10 MeV, post-quiescent emission coincident with lower-energy emission had been made until emission of this type was found, as part of the work reported here, in GRB 990104. Detections of high-energy emission from bursts with quiescent periods were rare, because only the brightest bursts would produce EGRET-detectable high-energy emission.

When the spectral properties of BATSE bursts were examined, the focus was often on spectral lags, spectral evolution, and how the luminosity evolved. These made use of the relatively high time resolution of BATSE data. The high-energy data available from EGRET does not have nearly as good a time resolution as BATSE data, but it is possible to use it to study spectral evolution by looking at spectra from different time periods within bursts. Studies of this kind have not been performed on high-energy emission from bursts with quiescent episodes. At BATSE energies, hard to soft evolution was observed within post-quiescent emission episodes, but

no clear signs of spectral evolution were observed between pre and post-quiescent emission episodes when precursors were compared to the emission that followed. Any information on the spectral evolution either within or between pre and post-quiescent emission episodes would be valuable for its possible use in constraining models of the central engine and its prompt emission.

1.5 Detecting High-Energy Gamma-Ray Burst Emission with EGRET and GLAST

Past research on high-energy gamma-ray bursts mainly focused on the prompt emission, with the few notable exceptions described earlier. TASC data was only searched during the prompt-emission phase of bright bursts, and then only for a few seconds after a trigger. For this thesis, an attempt was made to minimize assumptions regarding when high-energy emission can occur. Results of a search through archival EGRET data for signs of high-energy emission for a period of several hours surrounding known BATSE triggers are described. The models described in the previous section suggest that a search is warranted, but in light of a desire to not restrict investigation of unexplored phase space, it would be a worthy endeavor even without theoretical justification. The search was fruitful, resulting in the first discovery of MeV emission from a post-quiescent emission episode, and other possible detections of high-energy delayed emission. The post-quiescent emission detected is among the strongest detected in the $\sim$1-250 MeV range, and was only found because assumptions regarding when high-energy emission might be found were relaxed. The time

profile of the burst is consistent with the internal shock scenario, and the detection of high-energy emission may be the first evidence that high-energy, post-quiescent emission is possible from internal shocks. A calculation of an upper limit on ∼1-250 MeV emission in the hours surrounding especially bright bursts is also presented.

The chapters that follow will describe the EGRET and GLAST instruments and their capabilities. The focus is then turned towards efforts to characterize and improve the performance of the GLAST satellite with regard to onboard triggering, event filtering (distinguishing between background events and gamma-rays), and real-time track reconstruction, which is essential for determining the location from which gamma-rays arrive. GLAST has the potential for great contributions to high-energy gamma-ray burst physics and many other important topics. The final chapter shows how careful onboard filtering and track reconstruction can be used to detect and localize gamma-ray bursts onboard GLAST in real-time. Recommendations on how to continue development in this area are also offered.

Chapter 2

Gamma-Ray Satellite Experiments: EGRET and GLAST

2.1 The Pair-Conversion Telescope

Solving the problem of detecting high energy photons in space, determining their direction and measuring their energy, while also screening out the cosmic-ray background, has led to the development of a standard approach called a pair-conversion telescope (Figure 2.1).

When a gamma ray interacts with the strong electric field of an atomic nucleus, and their center of mass energy is equivalent to at least twice the rest mass of an electron (0.511 MeV), the gamma ray can convert into an electron-positron pair (Fichtel and Trombka, 1997). Any energy beyond the 1.022 MeV required to create the pair goes into the kinetic energy of the pair. A pair-conversion telescope uses this interaction mechanism to convert gamma rays into e^+-e^- pairs that can be tracked as they pass through a charged particle detector system. Because momen-

tum conservation allows the pair to retain much of the information about the initial direction of the gamma ray, tracking the path of the pair through the instrument and projecting it back to the celestial sphere can reveal the location of the gamma ray's source. For a 30 MeV gamma, the root mean square angle between the parent gamma ray and a secondary lepton in the lab frame is about 4^o; at 100 MeV it decreases to 1.5^o, and at 1 GeV it is only 0.2^o (Fichtel and Trombka, 1997). Important additional deflection occurs when the electron and positron undergo multiple scattering as they pass through instrument material.

Each mission is different in its specific requirements and science goals, so there are carefully-determined variations on the basic approach to pair-telescope design. The common design elements can be outlined here and later the details that are unique to the EGRET and GLAST missions are described. This is done by following the path of a particle through a pair-conversion telescope, and explaining the detector response along the way. After describing the general case, separate sections on EGRET and GLAST will draw attention to the different approaches each of these missions took towards accomplishing their goals.

2.1.1 The Micrometeoroid Shield and Thermal Blanket

As an incoming particle encounters a pair-production telescope, it first must pass through a micrometeoroid shield and thermal insulator known as a blanket. This shield is designed to protect the instrument from high-speed meteoroids that would otherwise impact and damage the detector systems, and it protects the detectors from the temperature fluctuations in space. Without compromising its insulating

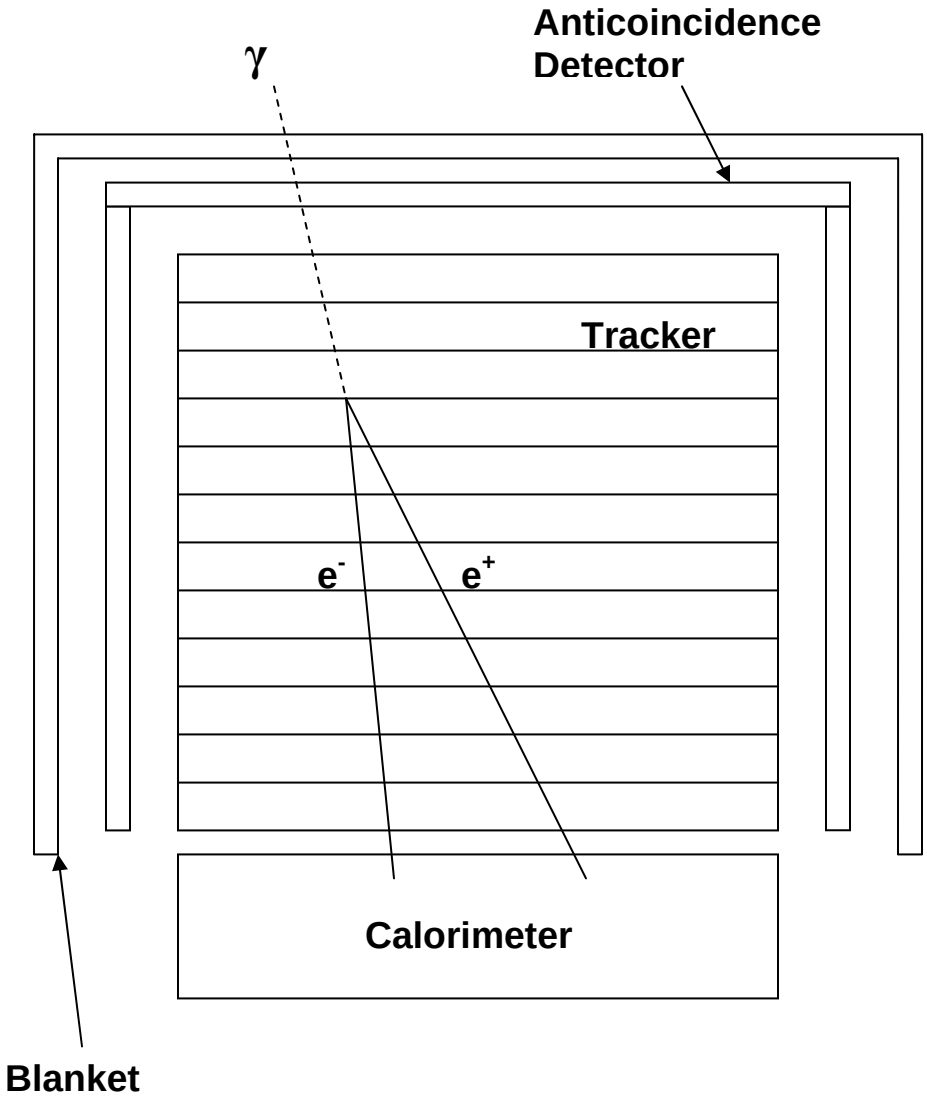

Figure 2.1: Diagram of a pair-conversion telescope. The three main detector systems of a pair-conversion telescope are shown: anticoincidence detector, tracker, and calorimeter. The thermal blanket and micrometeoroid shield are also shown. A gamma ray converts into a e^+e^- pair in the tracker, and the pair passes through several layers before entering the calorimeter.

and shielding capabilities, the blanket must remain transparent to gamma rays. Minimizing the thickness of the blanket (as measured in units of radiation lengths (r. l.)[1]) minimizes the probability of gamma-ray conversion. The GLAST blanket is only about 0.8% of a radiation length thick, or $<0.3\ g/cm^2$. On EGRET, the blanket was even less dense at $0.17\ g/cm^2$. It is also possible for cosmic rays to interact with blanket material to create π^os that decay to gammas, but the interaction probability is low. The EGRET mission investigated this possibility in a Brookhaven beam test(Edwards et al., 1991), in which protons between 1.3 and 8.1 GeV were targeted tangentially at the blanket covered dome of the telescope. The upper limit on the instrument background rate due to gamma-ray production was calculated by a Monte Carlo simulation to be $5.3(3.2) \times 10^{-7} cm^{-2} sr^{-1} s^{-1}$, which was verified by the proton beam test. This amounted to about 4% of the gamma-ray background due to the extragalactic diffuse emission[2].

2.1.2 The Anticoincidence Detector

After the blanket, the incoming particle would encounter the first detector system, which is known as an anticoincidence detector (ACD). The primary purpose of an ACD is to detect cosmic rays, which are energetic nuclei and electrons that travel

[1]Radiation length is the average length in a specific material in which a relativistic charged particle will lose 67 percent of its energy by bremsstrahlung. The radiation length of a material is given by $1/X_o = (4\alpha N_A Z(Z+1) r_e^2 log(183 Z^{-1/3}))/A$, where α is the fine structure constant, N_A is Avogadro's number, Z is the atomic number of the traversed material, A is the atomic weight of the traversed material, and r_e is the electron radius in cm. The average energy loss due to bremsstrahlung for an electron of energy E is related to the energy length by $-(dE/dx)_{brems} = E/X_o$(CERN web page, 2005)

[2]The extragalactic diffuse is a gamma-ray background that is likely caused by numerous unresolved blazars (Stecker et al., 1993).

through space. Because they interact in the type of detector systems found on pair-conversion telescopes, they must be identified as background and eliminated from the data stream so their signal is not interpreted as coming from a gamma ray. GLAST, for example, requires that the contamination of the gamma-ray extragalactic diffuse gamma-ray emission due to charged particle background be less than 10% (Ritz, 2003). The ACD is used to look for the absence of a coincidence with a signal in the particle tracker. A signal in the particle tracker can indicate the passage of either a cosmic ray or the e^+-e^- produced by a gamma-ray conversion, but a signal in the ACD is almost always due to a charged particle originating outside the instrument. Therefore, an anticoincidence between the ACD and the tracker indicates that a gamma ray may have been detected by the telescope.

ACDs use scintillator detectors, commonly made from an organic plastic. When an incident cosmic ray passes through the organic plastic scintillator, it excites molecules in the scintillator; as the exited molecules return to lower states they fluoresce, releasing ultraviolet light that propagates through the plastic via total internal reflection until it is detected by a set of photomultiplier tubes (PMTs). About 18,000-20,000 photons are produced by a minimum ionizing particle (MIP) as it traverses 1 cm of plastic (Bicron, 2003). This light is detected by the photomultiplier tubes and converted into an electronic signal in the following manner. When a photon hits a photosensitive cathode at the face of the tube, an electron is knocked loose by the photoelectric effect. The electron is accelerated towards the first of a series of plates at high voltage (dynodes) within the tube. When it hits

the first dynode, it knocks loose additional electrons, which are accelerated to the next dynode. The process repeats, causing a shower of electrons to develop as they accelerate from plate to plate. The resulting current collected at the anode indicates the number of photons detected. The typical photon detection efficiency is 15-20%, mainly due to the properties of the photocathode. There are different techniques for ensuring that the light is delivered to the phototubes, and the techniques that EGRET and GLAST used are discussed in the coming sections.

Beyond a threshold of a few MeV the scintillator becomes mostly transparent to gamma rays (Fichtel and Trombka, 1997), but there is a small probability that gammas will interact and produce a signal. If enough gammas are present, the signal from the photons can even be used to generate light curves during gamma-ray bursts. The lower energy gammas do not have enough energy for pair-production in the tracking portion of the telescope, however, so a pair-conversion telescope cannot detect them.

2.1.3 The Particle Tracker

After passing through the ACD, a gamma ray or cosmic ray would then enter the detector system known as the particle tracker. Regardless of the specific implementation, this detector consists of several layers of high-Z material, like tungsten, lead or tantalum, in between layers of position sensitive charged particle detectors. Enough layers of dense metal are arranged such that the total radiation length will give a good probability of the conversion of a gamma ray into an e^+-e^- pair. The pair is then tracked in three dimensions by the layers of charged particle detectors.

As the particles pass through layers of dense converter, multiple instances of Coulomb scattering take place, and the trajectory upon exiting the layer is different than the trajectory upon entering. When designing a detector, one must balance a desire for high probability of conversion (thick converter) with a minimization of the multiple scattering effect. The particles produced by higher energy gammas are not deflected as much as those with less momentum, so their tracks tend to wander less from layer to layer (they are straighter), and their overall direction aligns more with the initial direction of the gamma ray. Another interesting feature of higher-energy events is that their e^+-e^- pairs have less separation (smaller opening angle) than lower energy pairs on average. Low energy pairs will not necessarily show an immediate separation, because the probability distribution of the opening angles allows for the pair to move along a similar trajectory, but the initial separation can be noticeable, and multiple scattering will eventually cause the angle between the pair to increase. For low energy events, determining the direction of the initial gamma ray can involve reconstructing the vertex of the e^+-e^- tracks if the pair does not follow nearly the same trajectory. For high energy gammas, unless the resolution of the charged particle detectors is very high, the e^+-e^- pair will appear to make one track that points back along the direction of the initial gamma ray. The particle tracker is an area where GLAST and EGRET differ most markedly in their respective implementations, and the different approaches are described below.

2.1.4 The Calorimeter

Depending on the trajectory of the incident gamma ray, the e^+-e^- pair, or any additional secondary charged particles or photons resulting from its passage through the tracker will enter the calorimeter located at the base of the telescope. The type of calorimeter commonly used in gamma-ray telescopes provides an energy measurement of the event by causing a cascading shower of photons and secondary particles that deposit their energy in the material. This provides a count of the number of particles in the shower, which in turn allows an energy measurement because the count is proportional to the total energy. Different materials can be used to build a calorimeter, but the usual choices are restricted to a few types of crystals that are then doped with an impurity. Sodium Iodide (NaI) and Cesium Iodide (CsI) are two common materials with good light yield, fast response, and good particle stopping power, and they were the choices for EGRET and GLAST, respectively. The e^+-e^- pair or secondary particles are decelerated by the high Z nuclei in the crystal, losing their energy by bremsstrahlung radiation. The created photons will convert to e^+-e^- pairs that will in turn radiate via bremsstrahlung, creating yet more photons and pairs. This process creates a shower that increases exponentially until a maximum as the shower depth increases. Coulomb scattering of the charged particles also causes the shower to spread out, and Compton scattering of the photons allows for the generation of some secondaries that splash upward into the tracker and ACD (Moiseev et al., 2004). If the calorimeter is deep enough, the energy of secondary particles will eventually be low enough that it is comparable

to the ionization energy of the crystal. At this critical energy, the bremsstrahlung photons can be completely absorbed by the photoelectric effect, and the shower reaches its maximum and begins to decrease (Perkins, 1987). The depth of the shower maximum is a function of energy because higher energy events will have greater depth before the secondary particles reach the critical energy.

Impurities introduced into the crystal, e. g. Thallium (Tl), enhance the ability of ionizing charged particles passing through the calorimeter to create electron-hole pairs (Fichtel and Trombka, 1997). As the excited electrons fall back to their valence energy level, scintillation light of wavelengths that can easily can be detected by the PMTs or photodiodes is produced. Thoughtful design of a segmented calorimeter can improve the energy resolution and allow it to be used for crude direction finding by providing an image of the shower.

2.1.5 Self-Veto

ACD scintillator material must be sensitive to charged particles in order to reduce the background. However, the primary design concern besides maximizing the detector efficiency is minimizing what is called self-veto. Although the ACD is in place to veto, or eliminate background events by detecting their passage through its material, it is also susceptible to the backsplash of electrons and soft gammas that are created when the e^+-e^- pair interact in the calorimeter (Moiseev et al., 2004). The Compton scattering can cause the lower energy scattered photons to splash upward through the calorimeter and hit the ACD, which may cause a signal in the scintillator (though the probability of this is low). It is mostly higher energy

gamma rays that tend to produce large electromagnetic showers with backsplash, because more energy is available for conversion into secondary particles. If care is not taken, the ACD signal can be mistaken for a cosmic ray and cause a self-veto, thus eliminating the desirable gamma-ray event. The different approaches EGRET and GLAST take to the backsplash problem are described later.

2.2 EGRET Instrument Design

The EGRET instrument (Fig. 2) (Thompson et al., 1993), one of four experiments onboard CGRO, was specifically designed to detect gamma-ray photons in the 20 MeV to 30 GeV energy range, and localize high-energy sources to 0.1^o-0.2^o (Kanbach et al., 1988). CGRO's orbit placed it at an inclination of 28.5^o (from the equator), and at an altitude of approximately 450 km. EGRET had to identify and suppress a background of cosmic rays, including upward going cosmic rays and albedo gamma rays from the Earth's atmosphere, that was approximately 10^4 times greater than the diffuse gamma-ray background emission (Kaluzienski, 2004).

2.2.1 EGRET Anticoincidence Detector

The EGRET ACD consisted of a dome of 2 cm thick plastic scintillator material that covered the upper half of the EGRET telescope. Coupled to the bottom edge of the dome were 24 photomultiplier tubes which collected the light. The distance from a light emittance to a phototube would vary depending on the location of the particle's passage through the ACD. Because there was light loss due to imperfect internal reflection, the transmissivity of the scintillator, and incomplete coverage

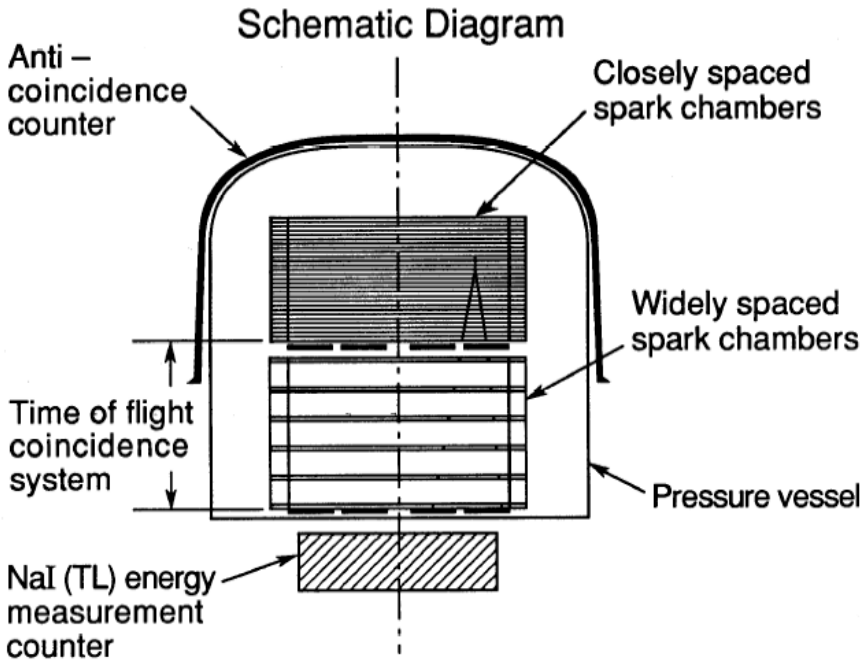

Figure 2.2: EGRET schematic diagram. The thermal blanket is shown covering the anticoincidence dome, under which are the upper and lower spark chambers and the TOF system. Under the spark chambers, the calorimeter is depicted. The pressure vessel is filled by tanks (not shown) of neon, argon, and ethane which were used to replenish the spark chambers as necessary. From Thompson et al. (1993).

of the scintillator edge by phototubes, a 4 MeV charged particle was expected to produce 150 detectable photons if the particle hit the apex of the dome (EGRET PDR Document, unpublished, 1982). If it hit closer to the edge of the ACD, more photons would be detectable because that is where the phototubes were attached. Assuming a quantum efficiency of 20% for one PMT, it was calculated that 62 photons were necessary for an event detection, so the ACD performance was initially thought to be more than twice as efficient as necessary. Both Monte Carlo simulations and beam test calibration runs were used to confirm these calculations and determine where to set the PMT threshold (Thompson et al., 1993). By setting the threshold correctly, it was possible to ensure high detection efficiency, but still reduce the probability of self-veto from backsplash. Even so, EGRET still suffered from a >50% drop in effective area above 10 GeV, something GLAST will minimize (as described in subsection 2.3.2).

2.2.2 EGRET Spark Chamber and Time of Flight Coincidence System

The EGRET implementation of a particle tracker used a detector system that was common in high energy physics experiments, known as a spark chamber, a type of gas-based charged particle detector. It consisted of stacked modules that each had two parallel planes of perpendicular wires. A particle passing through the spark chamber would enter one of the 28 closely-spaced spark chamber modules in the upper portion of the chamber. Between each pair of adjacent modules was a 90 μm thick layer of tantalum, for a total of 0.54 radiation lengths along the vertical

axis (Kanbach et al., 1988). Any charged particles, be they e^+e^- pairs or cosmic rays, would proceed to pass through the neon, argon, and ethane gas that filled the spark chamber modules, ionizing the mixture and producing free electrons. When a fast high voltage pulse was applied to the wires, the free electrons would accelerate through the gas and become ionizing. This would create an avalanche of rapidly increasing ionization in the gas before the charge would collect on the wires. The large potential difference could not be maintained in the ionized gas, and a spark would occur. Wires that had collected charge were read out, and a three dimensional image of the track was formed by the orthogonal wires. Until the tracker was finished reading out, it could not detect another event. This deadtime was on the order of 100 ms (Atwood, 1993). The readout itself was initiated by an external signal; the tracker had no way to self-trigger and initiate the collection of charge on its wires because it had no mechanism by which it could tell when a particle had passed through its modules.

In order to trigger and read out the data, the charged particle had to pass through some or all of the 28 closely spaced spark chamber modules, and then through the first of two arrays of scintillators spaced 60 cm apart. Between the scintillators were more spark chamber modules, not spaced as closely as those above, which were used for additional direction determination. Before exiting the bottom of the spark chamber, the particle would pass through the second of the two scintillators, providing that its trajectory did not cause it to miss and pass out the side. Each scintillator detector was attached to a PMT, and the difference in arrival time

could be determined. Depending on which of the scintillators detected light first, the particle was determined to have come from above or below. Because it was the difference in time that provided the information, this detector was known as a time-of-flight (TOF) trigger telescope. If an event came from above, and if there was no charged particle detection in the ACD, EGRET would trigger and apply the high voltage to the wires of the spark chamber, initiating the ionization process described earlier.

The trigger logic was actually considerably more complicated than a simple anticoincidence between the ACD and the trigger telescope because the two (TOF) scintillation planes were not monolithic, but composed of a 4×4 array. Examining which of the scintillation tiles emitted light allowed an EGRET analyst to disregard events that originated from a particular portion of its field of view. This could be used to screen against particularly strong sources of background, including albedo from Earth.

2.2.3 EGRET Calorimeter: Total Absorption Shower Counter

EGRET was able to measure photon energies up to tens of GeV with a large calorimeter composed of sodium iodide crystal doped with thallium (NaI(Tl)). This massive detector, weighing 435 kg, was dubbed the Total Absorption Shower Counter (TASC). There were 16 photomultiplier tubes of 12.7 cm diameter attached to the bottom of the TASC, which was a full 8 radiation lengths thick.

In addition to reporting single event energies, an important function of the

TASC was its ability to also accumulate spectra using multiple events over different time scales, independent of the tracker. The energy range for TASC spectroscopy is $\sim 1 - 250$ MeV, however, the energy range depends on the gain of the phototubes, which changed over the course of the mission. The next chapter contains more information on how to calculate the gain and determine the energy range of the 256 channel spectrum. These spectra were most often accumulated over a time span of 32.768 s, which was also known as either the "normal mode" or "solar mode," because of their potential use in studying solar flares. However, if the BATSE experiment also onboard CGRO detected a gamma-ray burst, the TASC would go into "burst mode," and take four consecutive spectra of 1 s, 2 s, 4 s, and 16 s. These intervals were programmable, but were left at these values for most of the mission. This thesis will show how fruitful the spectroscopic function of the TASC was when searching for and studying gamma-ray bursts.

2.3 LAT Instrument Design

The Gamma Ray Large Area Space Telescope owes much of its design inspiration to other gamma-ray instruments, such as EGRET and earlier pair-conversion telescopes. However, GLAST is more than simply a larger version of previous space telescopes. GLAST was specifically designed to avoid some of the limitations of EGRET, and it incorporates new technology and advanced onboard software that will allow it to achieve scientific goals greater than previous space experiments. Table 2.1 shows some of the performance characteristics of GLAST as compared to

EGRET (GLAST Proposal Study, 2005).

Although much more massive than EGRET, GLAST will have a similar orbital inclination of 28.5^o, in the slightly higher orbit of 565 km. It is still small enough[3] to be launched on a Delta II rocket. Figure 2.3 is a rendering of the GLAST Large Area Telescope showing the tracker, ACD, and calorimeter. The following sections contain a detailed description of the LAT.

2.3.1 GLAST Large Area Telescope

The LAT consists of an anticoincidence detector for the purpose of screening out cosmic-rays, a tracker for tracking the passage of charged particles, and a calorimeter for energy measurement. It does not, however, have a time-of-flight triggering telescope like EGRET did, the ACD design is designed to reduce self-veto, and the tracker is based on different technology. In addition, while EGRET had one tracker, the LAT is made of 16 identical towers – tracker on top, calorimeter on bottom – in a 4x4 array, and the tracker is solid state, which means that it does not require gas. The LAT will have a field of view (about 2.4 steradians) that will be over 10 times as wide as that of EGRET, a peak effective area at least 8 times that of EGRET, and better ability to resolve sources, with a point source localization (also known as "point spread function") between 0.086^o and 0.115^o above 10 GeV, compared to the 0.5^o of EGRET.

[3]GLAST will weigh 4527 kg and will have a volume of $< 3\,m^3$. The LAT contributes 3000 kg to the total mass.

	EGRET	*GLASTLAT ScienceRequirement*	*GLASTLAT PredictedPerformance*
Energy Range	20 MeV - 30 GeV	20 MeV - >300 GeV	LAT: 20 MeV - >300 GeV
Field of View	0.2 sr	>2 sr	2.4 sr
Effective Area at Normal Incidence (1-10 GeV Range)	1500 cm^2	>8000 cm^2	>9000 cm^2
Energy Resolution			
100 MeV on-axis	10%	<10%	9%
10 GeV on-axis	10%	<10%	8%
10-300 GeV on-axis	...	<20%	<15%
10-300 GeV off-axis (>60^o)	...	<6%	<4.5%
Point Spread Function 68% on-axis			
100 MeV	5.6^o	<3.5^o	3.37^o (front), 4.64^o (total)
10 GeV	0.5^o	<0.15^o	0.086^o Front), 0.115^o (total)

Table 2.1: EGRET performance and GLAST LAT requirements (Ritz, 2003)

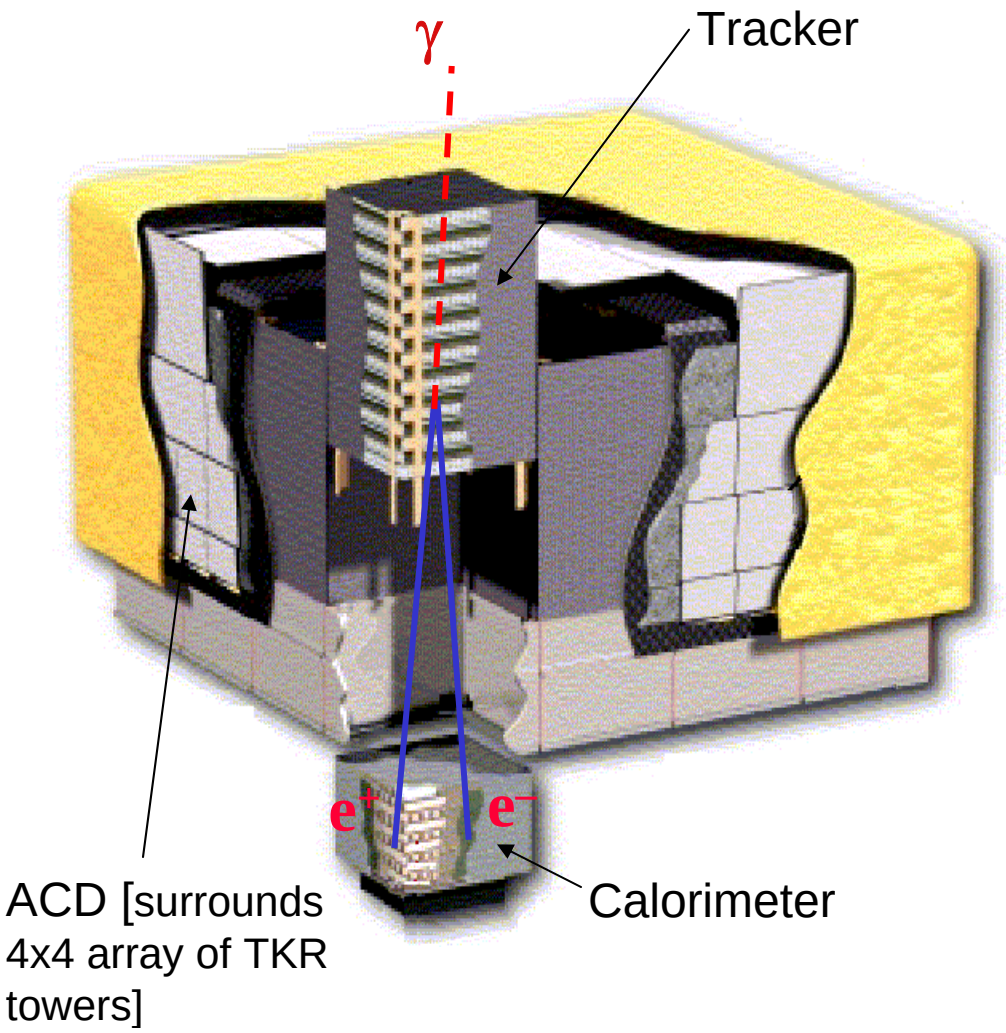

Figure 2.3: Cutaway view of the GLAST Large Area Telescope (LAT). Shown are the anticoincidence detector covered by the micrometeoroid shield and thermal blanket, a tower module with an 18 layer tracker on top of a hodoscopic calorimeter. A gamma ray converts into an electron positron pair in the tracker module. From Ritz (2003).

2.3.2 LAT Anticoincidence Detector

As described earlier, EGRET suffered from self-veto when high energy gammas would interact in the rest of the instrument (most notably, the TASC), producing a shower of secondary particles that would splash back up into the ACD, causing the event to be mistaken for a background cosmic-ray. Because the EGRET veto conditions were hard-wired into the triggering system, they could not be changed after launch. In contrast, if it is necessary to alter GLAST veto conditions, it will be possible to update the onboard software. The EGRET self-veto problem caused a 50% drop in detection efficiency at 10 GeV, as compared to 1 GeV, and was something that had to be addressed if GLAST was not to suffer in the same way.

The solution developed for GLAST was to segment the ACD into 89 separate tiles that are read out individually (Fig. 2.4). The ACD tiles are arranged in a 5×5 grid on the top, or "front" face, and then in 3 rows of 5 columns on each side face, with one long tile at the bottom. Attaching a phototube to each of 89 ACD tiles would have presented difficulty, so waveshifting fibers were embedded every 0.5 cm in each tile and then run to phototubes located along the base of the ACD. Each tile has two phototubes for redundancy. Besides making it possible to transmit the light to the phototubes, an advantage of the fibers is that they ensure that the detection efficiency is uniform throughout the tile (Moiseev, 1999a). See Fig. 2.5 for a photo of a prototype ACD tile with embedded wave shifting fibers.

By segmenting the ACD and associating a track with a specific set of tiles that are checked for hits, GLAST minimizes the self-veto problem. Events are

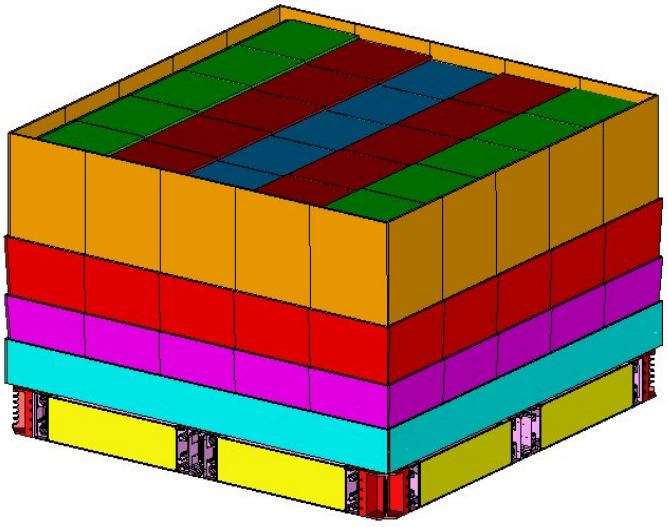

Figure 2.4: GLAST ACD (false color). The top, or front, is composed of 25 tiles in a 5x5 grid, and each side is composed of 4 rows of 5 tiles, except for the bottom row, which is monolithic. Some of the mechanical and electrical assembly is visible at the base. From Thompson and Thompson (2003).

generally not vetoed, particularly at high energy, if any single tile goes over veto threshold. Rather, events are vetoed if a tile and a track could be associated, which is a signature of a charged particle background event. Self-veto can still occur if a secondary particle scatters back up through the tracker and produces a signal in an ACD tile. However, onboard event filtering software employs checks to guard against this, such as only rejecting events if there is evidence that a track starts at or below a hit tile (on a side face), not above. If evidence suggests a track starts above a hit tile, it may be because a gamma converted and the resulting e^+-e^- pair exited out the side.

The ACD will output two basic types of signals from each tile. Logic signals indicate whether a condition has been met, while pulse height analysis (PHA) signals indicate the magnitude of the energy deposition. Each type of signal comes in

pairs of two because of the two PMTs per tile. The logic signals include two veto discriminator signals (VETO) that indicate that a tile has absorbed the energy equivalent to roughly 0.3 MIPs, and two high-threshold discriminator signals (HI), which indicate whether the tile has detected the equivalent of $\sim$ 25 MIPs (Ormes, 2002). The PHA signals are two low-level signals if the deposit was less than 10 MIP, and two high-level values if the signal was over 10 MIPs.

The ACD veto signals are ORed together in several ways to create different types of "trigger primitive" signals (low level, basic signals) that are sent to the LAT trigger system (described later). Sixteen primitives indicate whether a veto tile on the top shadows one of the towers. Fifteen primitives come from a total of 3 signals from each of the 5 ACD planes. One says whether one or more VETO discriminator signals occurred in the plane; one says whether 2 or more VETO signals occurred; and one says whether 3 or more LO signals occurred. Finally, there is one signal that tells if any of the front 25 tiles were over the HI discriminator threshold, and one signal says whether any of the side tiles were over the HI threshold. These HI primitives can be used as a CNO (carbon, oxygen, nitrogen) trigger, which indicates the passage of a heavy ion cosmic ray that is useful for calibration of the calorimeter.

2.3.3 LAT Tracker

The LAT tracker design uses orthogonal planes of silicon strip detectors interleaved with tungsten converter, to provide precise determination of a charged particle's direction, when the information is analyzed with onboard and ground based algorithms (Johnson, 2001). The basic concept behind the LAT tracker (Fig. 2.6) is the

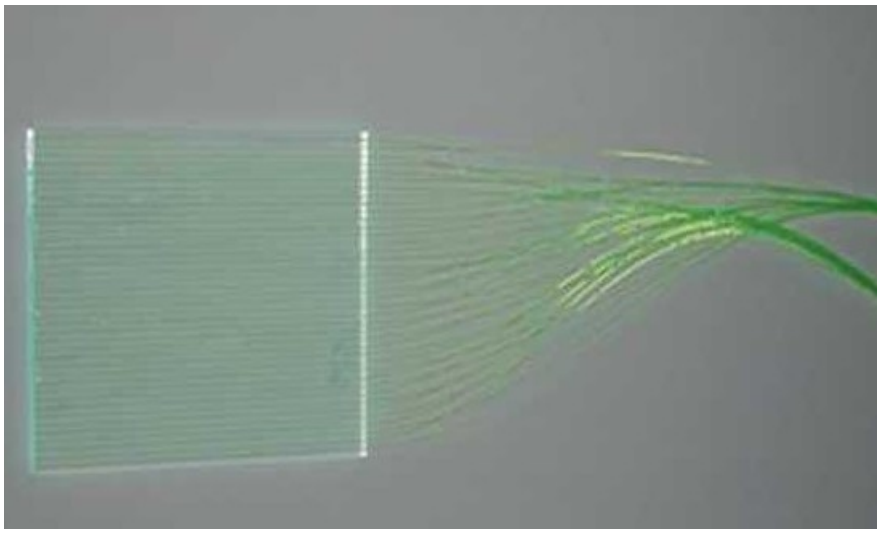

Figure 2.5: ACD tile with wave shifting fibers. The tile is 1 cm thick organic plastic scintillator, with embedded waveshifting fibers to collect the light. Two sets of fibers transmit scintillation light to separate PMTs. From Thompson and Thompson (2003).

same as those used in modern particle physics detectors on the ground, and even some experiments in space (AMS) (Johnson, 2000). The use of silicon-strip detectors instead of a gas filled spark chamber gives the LAT tracker several benefits.

One of the disadvantages of the EGRET spark chamber was that it periodically had to be refilled with gas, which limited its lifetime. This problem of "consumables" is eliminated with a silicon-strip detector, which uses solid state technology to detect the passage of a charged particle. Other disadvantages of EGRET's system were that it required an external trigger to tell the chamber when to turn on the high voltage, it had limited spatial resolution, and it had relatively high dead time of 100 ms after reading out an event (Atwood, 1993). The LAT's tracker, however, will self-trigger, has low dead time ($\sim$26 μs), has very good resolution (the strip pitch, or separation, is 0.228 mm), high efficiency, and a long lifetime. The high resolution of the tracker makes it possible to resolve multiple tracks, which allows for

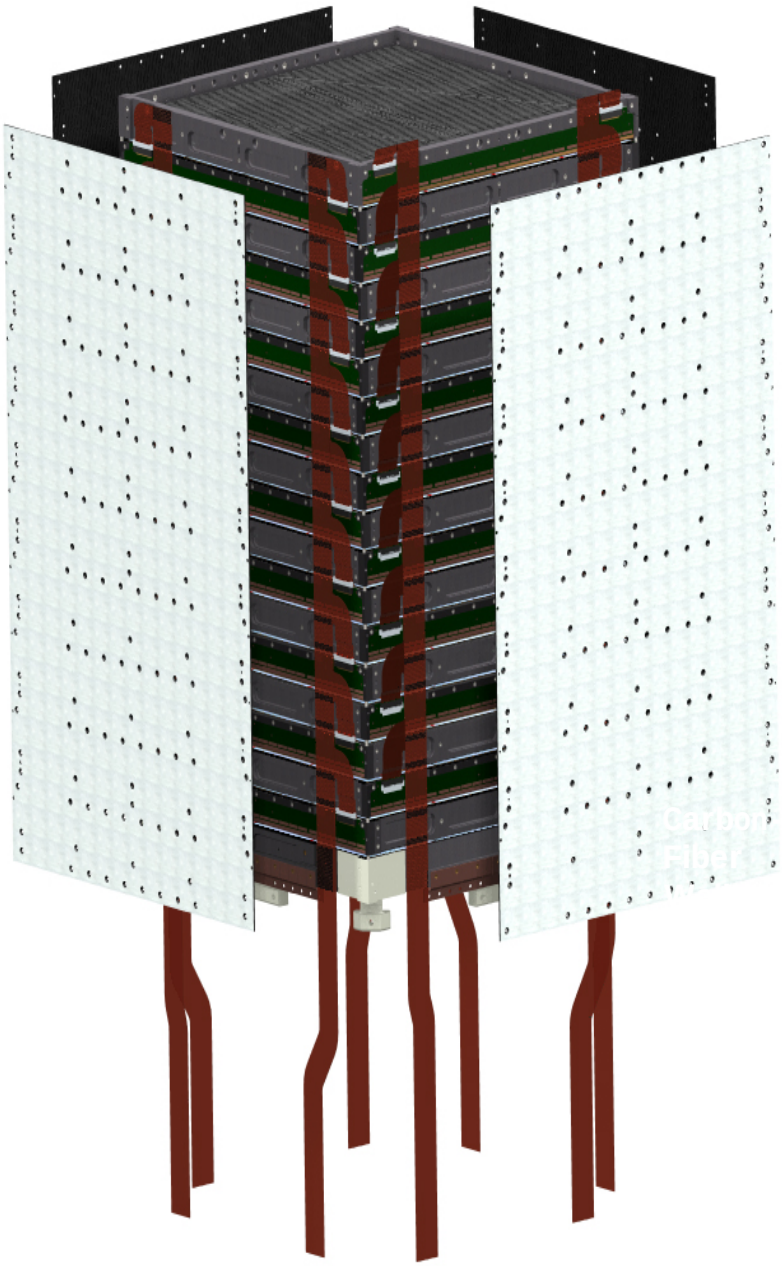

Figure 2.6: LAT Tracker Tower. Consists of 19 carbon-fiber trays with tungsten foil on the bottom face, and silicon-strip detectors (SSDs) on the top and bottom faces. The exposed top face and the bottom face do not have SSDs, so there are 18 layers of SSD, each composed of a sandwich of one X and one Y plane of SSD, and one layer of tungsten. Electronics are on the tray edges, and readout cables go down the side. Aluminum covered carbon fiber walls give vertical support. From Johnson (2003).

the reconstruction of the e^+-e^- pair vertex for lower energy events, which indicates which direction the incoming gamma came from. The tracker is also shorter than it is wide, which gives it a large field of view. This is made possible in part by the segmented calorimeter (more on this below), which allows the analyst to determine from an energy deposit whether the responsible particle shower started towards the top or the bottom. Because one can distinguish between showers that start above and those that start below, this eliminates the need for a widely spaced time-of-flight system, so the LAT does not need to be tall.

The LAT is constructed of a 4×4 array of identical towers, and each of these towers has 18 layers of X and Y planes of silicon-strip detectors that mechanically consist of sandwiches of 19 carbon fiber reinforced trays. Each tray consists of two planes of silicon – one on the top, one on the bottom – and a layer of tungsten converter, which converts incoming gammas into e^+-e^- pairs that can be tracked by the remaining layers. The tracking is accomplished by orienting alternating trays 90^o from each other, such that when the trays are stacked up, the outer faces of silicon strip material are orthogonal. This allows a passing particle to be tracked in both the X and the Y direction. The top, or front (see Figure 2.7), 12 planes differ from the bottom, or back, in that the front planes have 3% r.l. of tungsten converter, while the next 4 back planes have 18% r.l. of converter, and the last two, just used for tracking and self-triggering, have no converter foil at all. These 18 layers are spaced approximately every 3 cm, which makes the towers about 60 cm tall. They are 37 cm wide, and contain 55,296 channels each (36 planes, 1536 strips

per plane), for a total of 884,736 channels to read out in the tracker. The small strip pitch gives the tracker a potential single photon resolution of $\tilde{4}0$ arcsec over the height of one tower (Haller, 2003). Typical source localization will not be as good (within 0.5 to 5 arc minutes) because it is based on multiple events of varying energy whose tracks must be reconstructed. Because of multiple scattering and less than perfect track reconstruction, the accuracy of source localization varies.

Silicon-strip detectors (SSDs) use a p-type material with a deficiency of electrons for the strips, and an n-type material with an excess of electrons for the base. An aluminum backplane is bonded to the n-type material, and the p-type strips are covered with aluminum strips, but separated from them by a thin insulator. When a charged particle passes through the detector, it ionizes the n-type material, creating free electrons that drift towards the positivity biased (100V) aluminum plane (Bloom et al., 2001). The "holes" that they leave behind also drift, but towards the p-type strip and induce a charge on their corresponding aluminum strips. The charge can be measured by converting the current into a voltage (Baldini et al., 2003). The voltage is amplified and shaped, and if it is over a predetermined threshold, the time-over-threshold (TOT) is measured. This time over threshold is linear with charge all the way up to 50-60 fC (equivalent to the charge deposited by 10-12 normally incident MIPs) (Brigida et al., 2002), and because the charge is proportional to ionization, as governed by the Bethe-Block formula (Barnett et al., 1996), it is possible to infer information about the incoming particle. For instance, a slow moving proton will experience increasing energy loss, and deposit increasing

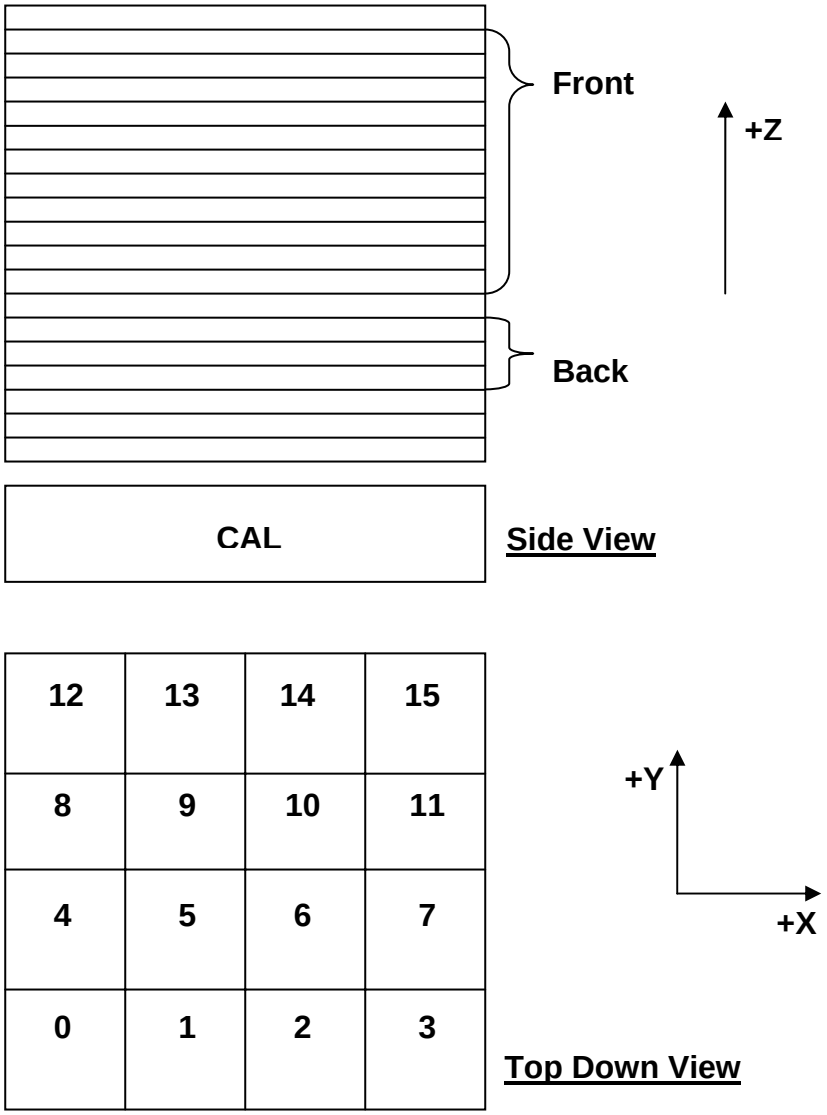

Figure 2.7: The LAT coordinate system and tower numbering (not to scale). The side view shows the tracker above the CAL, with the front 12 layers farthest from the CAL, and the 4 back planes closest to the CAL. The two planes next to the CAL do not have tungsten converter foil. The top down view (Z pointing out of the page) shows the tower numbering relative to the X and Y axes.

charge, as it passes through layers of silicon. In contrast, a minimum ionizing particle will deposit a much smaller amount of energy in each layer. e^+-e^- pairs have yet another signature, because near their point of conversion they are close together and can strike the same strip, causing a TOT twice as large as that from a single electron.

Though the TOT allows one to infer analog information via a Bethe-Block curve parameterization, the digital patterns of strip "hits" provide the most important information. Hits allow for the precise tracking of particles as they pass through the LAT. Strip hits also allow any tower of the LAT to self-trigger, because the tower never requires that a voltage suddenly be applied globally, as was the case with EGRET (ATLAS web page, 2005).

When a coincidence of 6 sequential planes of silicon is detected in a tower, a tracker primitive – a very simple logic signal that indicates the existence of the coincidence – is sent from the tower to the trigger system. Because the coincidence of 6 planes constitutes a select group of 3 X-Y pairs, the coincidence is known as a 3-in-a-row tracker trigger.

2.3.4 LAT Calorimeter

Directly below each tracker module is the CsI(Tl) calorimeter (CAL). See Figure 2.8 for a diagram of the CAL. Each module of the GLAST calorimeter is composed of 8 layers of 12 CsI(Tl) logs, and is 8.5 r. l. deep. Like the TASC of EGRET, the GLAST calorimeter will measure the energy of passing particles, but its segmented design also allows it to be used for background rejection. CsI(Tl) has very good

stopping power, a fast response, and a little less light output than the NaI(Tl) used in EGRET. Even though the light output is slightly less, Cesium Iodide has peak emission near 550 nm, which allows for the use of photodiodes to detect the light, instead of the bulkier and heavier photomultiplier tubes. It would be very difficult to arrange the 1536 crystal logs that give the CAL its spatial resolution, and read them out with a corresponding number of PMTs. Instead, using photodiodes makes the LAT CAL a smaller, lighter system that draws less power, which are important considerations for space flight. GLAST's CAL logs are stacked in alternating orthogonal layers in an arrangement known as hodoscopic stacking (Johnson et al., 2000). It not only allows the CAL to measure energy, but also allows for the measurement of the position of the energy centroid. This information is very useful for guiding the track finding algorithms on the ground, especially for higher energy events that create large showers of secondary particles, because one can anchor one end of a track in the CAL.

Equally important is the depth of the shower maximum, which increases with the log of the energy. This feature of showers, combined with the segmented design of the CAL, allows one to determine whether the incident particle was upward or downward moving, which allows one to reject particles coming from below. The segmentation and the shape of the shower also allows one to accurately determine the energy of the particle. In the case of a higher energy photon, the shower will not be completely contained within the CAL. In other words, it will start in the CAL, but secondary particles, carrying a large amount of energy, exit out one face of the

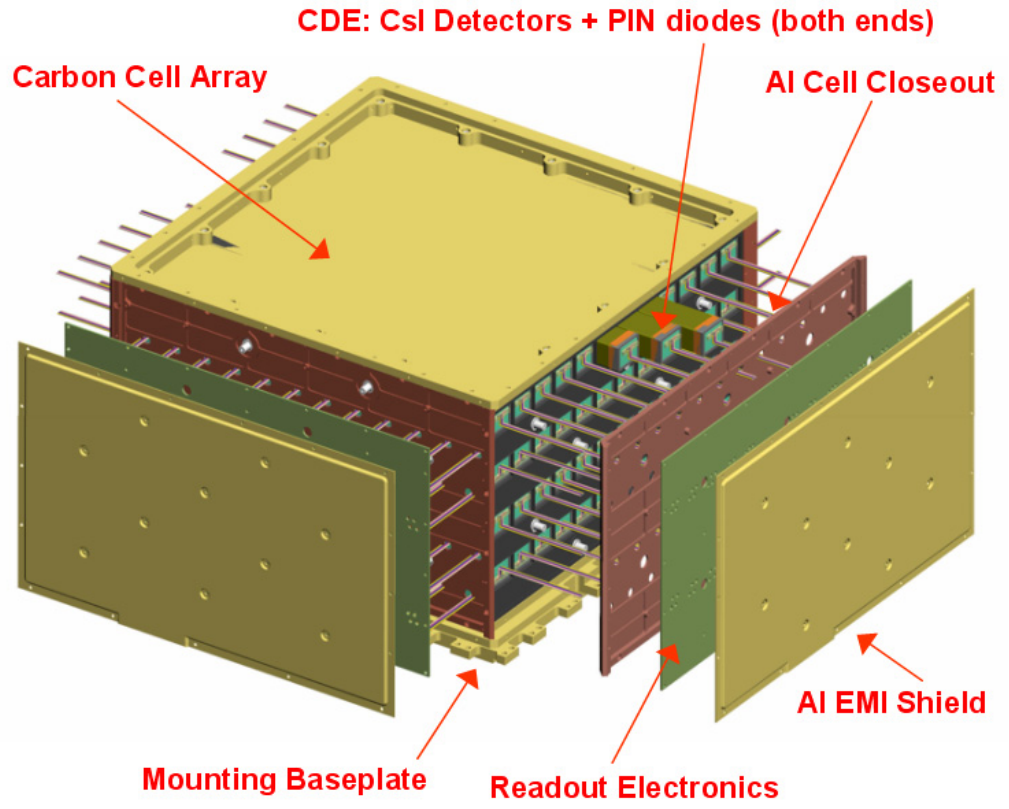

Figure 2.8: GLAST calorimeter module. Visible is the carbon cell holding the hodoscopic arrangement of 96 CsI detectors in 8 layers, with two PIN diodes at each end. Readout electronics and the aluminum shield are also shown. From Johnson (2003).

crystal array. That means that a portion of the energy is not deposited in the CAL, and a simple sum of the crystal signals underestimates the energy. This is known as leakage, but the CAL design allows for leakage correction. Because the shower increases in intensity as it progresses through CsI(Tl), it is possible to characterize a profile for a shower. When a profile is known in advance (through ground based testing and a detailed understanding of electromagnetic showers in general), it is then possible to look at the part of the shower that is contained in the CAL, fit its characteristic curve to a known profile, and thereby determine the energy and correct for the energy leakage.

Before sending digitized data to the Data Acquisition System (DAQ, described in section 2.3.6), the CAL sends its trigger primitives to the trigger system. These primitives consist of two logic signals from each tower. A CAL LO discriminator signal indicates whether the CAL had more than 100 MeV deposited in any single log, and a CAL HI signal indicates whether the CAL had a 1 GeV deposit in each of three consecutive layers. These signals are also known as CAL triggers.

2.3.5 LAT Trigger System

The LAT trigger system takes primitives from each of the detector subsystems as input and determines when the LAT will trigger in order to digitize the signals and read out an event. There are a few functional elements in the trigger system, and they work as follows.

Trigger primitives are received by the Algorithm Engine, which determines whether to create a named trigger (Russell, 2001). A named trigger specifies whether

a triggering command should be issued, which digitization to read out, and where to send the data. Before issuing any requests, the algorithm engine reduces the 97 trigger primitives (33 ACD + (2 CAL + 2-bit TKR)×16 towers) into a refined list. This list includes whether there was a CAL LO, a CAL HI, an ACD HI, a 3-in-a-row in any tower, a 3-in-a-row under (shadowed by) a hit ACD tile, and opposite sides of the ACD with more than one hit. These logical quantities can be combined in any way to form named trigger requests, which are the requests that the trigger system can send to the front end electronics in order to initiate a readout. For example, if trigger primitives from the CAL indicated that the OR of the CAL LO discriminators went over threshold, and the tracker primitives indicated that one or more towers had a 3-in-a-row, the trigger request might be named "3-in-a-row and Lo Energy CAL," in which case the tracker and CAL signals would need to be digitized and read out. Depending on which primitives are active, it is possible for the trigger system to issue more than one named request.

Just because a named request is initiated does not mean that it is automatically sent to the front end electronics of each detector system. The trigger requests can be inhibited if the electronics are not able to accept another request because their buffers are not yet read out due to a previous event (this is known as dead time). When requests are not blocked, they are combined into an acknowledge message, which contains instructions to the electronics on what to read out, and to which CPUs to send the data. When the acknowledge message is received by the detector electronics, they latch (save) their current data, and send it on for processing.

2.3.6 LAT Data Acquisition System

The Data Acquisition System (DAQ) is what makes the different detector systems of the LAT work as one coherent unit. The triggering system is just one part of the DAQ, which is also responsible for packaging the data into an event, and analyzing the event to determine if it is more likely background (reject it), or a gamma (keep it). The DAQ must package and send the data to the onboard filter while monitoring the performance of the spacecraft and its subsystems. Each tower has its own power supply and electronics module (TEM), which all must feed into the same DAQ along with the data from the ACD. See Figure 2.9 for a diagram of the basic data flow.

All of the DAQ tasks are taken care of by a few dedicated components: the Spacecraft Interface Unit (SIU), the Global-Trigger/ACD-EM/Signal-Distribution Unit (GASU), the Power Distribution Unit (PDU), and the Event-Processing Units (EPU). All the GLAST electronics are radiation hardened and certified for space flight.

Two of the processing units are of special interest for the purposes of this thesis: the GASU, which handles triggering, and the EPUs, which do the event processing and onboard science. The types of event triggers are discussed in a bit more detail in Chapter 4, and event processing (or filtering) is the subject of Chapter 5. The EPUs (there are two, plus one spare), have the crucial task of running an algorithm to reduce a background rate of several kHz down to less than 400 Hz. They also are responsible for running onboard science algorithms, most notably the gamma-ray burst detection and localization programs. Both the onboard filtering

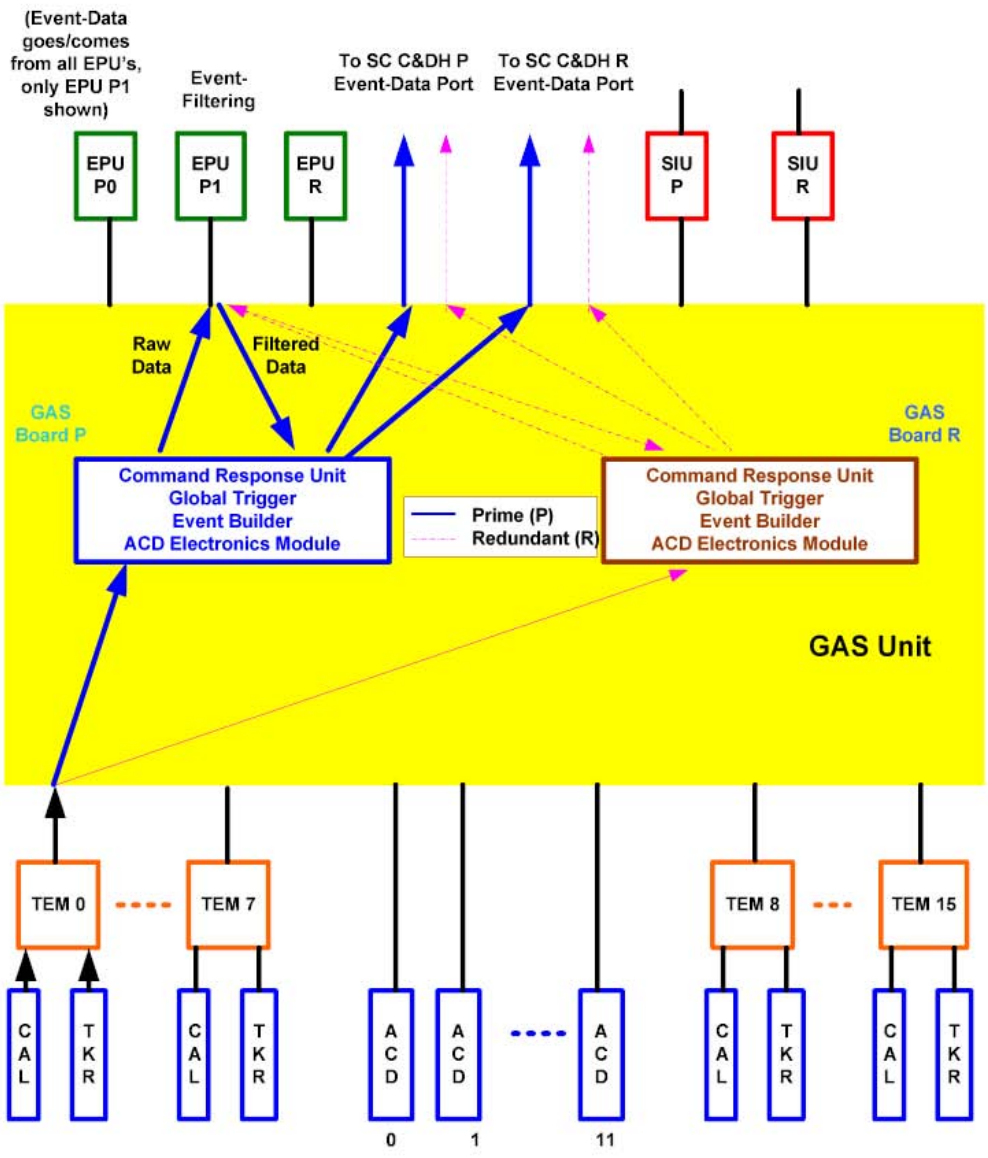

Figure 2.9: Basic data flow in LAT electronics and data acquisition system (DAQ). Each CAL-tracker module (the 16 towers) feed their data to a tower electronics module (TEM), which packages the data and sends it, with data from the ACD, to the global triggering system (GASU), which determines if there is an event trigger. The raw data are sent to Event Processing Units (EPUs) for onboard filtering (the subject of Chapter 5), which send filtered data back to the GASU for packaging and compression before it is telemetered to the satellite that sends it to the ground. The redundancy of the system is also shown, as are the Spacecraft Interface Units (SIUs) that provide an interface between the LAT electronics and the spacecraft control. From Haller (2003).

and its relationship to onboard GRB science are major focuses of this dissertation.

2.3.7 LAT Flight Software

The LAT has both onboard and ground system software. The flight software runs on the EPU and SIU, and is tested and developed on ground-based testbeds and simulators. The EPU runs the event filtering and science algorithm software, and the SIU runs software to control and monitor the LAT as a whole. Some of the functions that the SIU software serves are to transmit and receive telemetry packets, send data to the spacecraft's persistent storage, distribute commands, notify the LAT when a trigger comes in from the GLAST Burst Monitor, and keep track of housekeeping information, such as temperatures, currents and voltages. It also controls diagnostics and calibration, provides low level access to hardware interfaces, reports spacecraft time and orientation, and can automatically force the system to reset itself if necessary (GLAST flight software web page, 2005).

Much of the research done for this thesis involved and depended on the integration of the event filtering software into a high-fidelity Monte Carlo simulation of the GLAST experiment, known as GlastSim. The reasons for event filtering and the integration of the filter into GlastSim are described in the following sections.

2.3.8 Transmitting Data to the Ground

The LAT will sustain high trigger rates in orbit (see Chapter 4), and must run onboard filtering software to reduce the data rate to a level that can be transmitted to the ground. By putting the burden of distinguishing gamma rays from background

on a software filter, the LAT can use hardware triggering that is less stringent than previous gamma ray missions like EGRET. This prevents the hardware from rejecting a large fraction of gamma rays at the triggering stage, and instead gives the mission the flexibility of using sophisticated filtering algorithms that can be upgraded if necessary. However, as described in Chapter 5, it is not necessary to distinguish background events from gammas with 100% certainty. Though the flight software performs well using the limited processing power available onboard the instrument, simulations demonstrate that one can do a better job inferring the type of event with more complicated ground based software algorithms and essentially infinite computing resources. A valid question, then, is why not send all the data to the ground and process it there? There are two reasons why this strategy is not viable.

One reason for doing a first filtering of events onboard is the science goal of fast onboard gamma-ray detection. The gamma-ray burst detection and localization method under consideration requires a reduced background, or the signal from any burst is likely to be overwhelmed by the 10kHz of cosmic rays. Therefore, some onboard filtering is necessary. But this reason is not completely prohibitive, because the GRB algorithms could, after all, include their own filters to get the background rate low enough for them to be effective, and the satellite could still telemeter every event to the ground for further processing. In fact, the GRB detection scheme studied for this thesis does include additional filters of its own (see Chapter 6).

The main reason for an onboard filter is that bandwidth to ground is limited,

a restriction on any space-based experiment. The data are telemetered via a system of relay satellites known as TDRSS, and the data rate that GLAST is restricted to is an average of 1.2 Mbps. A compressed event package is expected to be about 3000 bits in size, and Chapter 4 will show that the LAT trigger rate will be up to 4000 Hz on average, for a total of 12 Mbps of data. The rate must be reduced by a factor of 10 to 1.2 Mbps, which means that no more than 400 events can be transmitted each second. Chapters 4 and 5 discuss the trigger rates and onboard filtering in detail.

2.3.9 LAT Ground Software and Data Analysis

The ground software is an important complement to the onboard algorithms, but cannot be considered part of the GLAST instrument in a direct physical sense. However, without it GLAST would not have been developed, and its data would be difficult to interpret correctly.

The GLAST Simulation

A major component of the ground software suite is the GlastSim Monte Carlo simulation. It has a 3-D description of GLAST in fully configurable XML files. The description includes the materials that GLAST is built of, and the simulation makes use of standard high-energy physics code (GEANT 4[4]) to model the particle propagation through the instrument (GEANT4 web page, 2005). The incident particles are provided by a source engine that can produce a wide range of incoming fluxes to simulate background and gamma-ray sources of different types. Each of these fluxes

[4]The collaboration made fixes to the GEANT 4 multiple scattering routines to make them more accurate.

is based on physical data, and some of them draw upon well established software packages developed by the space physics community. GlastSim outputs a summary Ntuple that can be analyzed event by event, or in aggregate, using analysis methods developed by the GLAST collaboration. The main tool for Ntuple analysis is the C++ based ROOT analysis framework developed at CERN. GlastSim also outputs detailed information on the incoming flux, the detector response, and the ground software's reconstruction of the event. The accuracy of GlastSim's Monte Carlo modeling was tested by placing an anticoincidence shield, silicon strip detector, and calorimeter in beams of tagged photons, electrons, and protons at the Stanford Linear Accelerator Center (do Couto e Silva & GLAST Collaboration, 2000; Handa & GLAST Collaboration, 2000; Johnson et al., 2000; Atwood, 2000). The simulation was successfully verified.

Event Reconstruction

One of the primary goals of the ground software is to reconstruct tracks from the pattern of strip hits in the tracker and the energy centroid in the CAL. Reconstructing tracks from hits on the X and Y oriented strips is necessary in order to determine the incident direction of the photon. This is not a simple task, but sophisticated methods have been developed by a tracker reconstruction team. The basic idea is to start by grouping nearby strip hits into clusters, beginning with hits in the uppermost layer of a tower that has triggered. If there is information in the CAL (an energy centroid), it is used as an anchor, and a line is drawn from the uppermost cluster to the centroid. This line is used as a guide as the algorithm steps down a

layer closer to the CAL, and looks for a cluster near the line. If an energy centroid is not available, the algorithm just steps down a layer and looks for the next cluster. Of course, there are often multiple clusters on a given layer, so the algorithm has to cycle over combinations and build up a list of possible tracks as it continues to step down through additional layers. When it steps down, it uses the vectors defined by previous clusters as a guide as to where to look for the next one. Once a list of tracks is developed, they are ordered by a quality parameter. This parameter looks at the number of hits in a track (the more the better), the chi-squared fit, how high the track started (the higher the better), how much the track kinks versus an estimation of the multiple scattering angle, whether charge was "shared" between strips, and whether there were stray X or Y strips that were not paired with an orthogonal counterpart at the beginning of a track (Atwood, 2004). Each of these factors had to be weighted by examining the performance of the reconstruction for different weights.

Once the tracks are found and ordered for quality, the best tracks are fit with a Kalman Filtering method (Kalman, 1960; Fruhwirth, 2000). This method steps down the track length taking into account information in previous hits, including the noise of multiple scattering, in order to predict where the next hit should be. Once the filter has information on all of the hits and noise in the track, it is run backwards in a smoothing mode to propagate the information back to the start of the track. When the Kalman Filtering process includes an estimate of Bethe-Block energy loss, in addition to some other energy corrections, and is then run through a

second pass, it provides good track fits. It is possible to combine tracks into vertices for lower energy events in which the tracks of the e^+-e^- pair can be well resolved.

The CAL reconstruction of an energy centroid is not as complicated, and mainly involves weighting the response of individual crystals in order to find both the centroid and the likely trajectory of the incident particle. To resolve the energy, shower fitting is done, as was described above. Corrections using a correlation between energy leakage and the energy deposited in the last layer improve this further (Usher, 2003).

Onboard Filtering in Offline Software

Ground reconstruction efforts are not a focus of this thesis, but the related goal of evaluating the onboard filter is relevant to this discussion. Incorporating the onboard filter into GlastSim allows one to pass simulated data through it. The flight code can then process the data and return the output that it will generate onboard. Because it is important to maintain the accuracy of the simulation and test the flight software itself, the desire was not merely to include emulation of the code (though that was also done later - see Chapter 5), but to run the actual code that will be embedded into LAT EPUs when the experiment is launched. Accomplishing the integration involved taking the embedded C code and writing a C++ wrapper around it that would take the digitization data from the digi part of GlastSim, package it exactly as it would be packaged in flight, and then feed it into the flight code via a function call. The primary output is a status word that indicates whether the filter rejected the event or determined that it was a gamma

ray. In order to make this determination the filter does some rudimentary track finding. Whether the crude track reconstruction can be extracted from the code and used for onboard science is a primary subject of this dissertation.

2.4 Dedicated Gamma-Ray Burst Detectors on CGRO and GLAST

Pair-conversion telescopes have been the focus thus far, but a discussion of EGRET and GLAST would be incomplete without mention of the dedicated gamma-ray burst detectors that complement the telescopes.

EGRET was one of four instruments onboard the Compton Gamma-Ray Observatory. Another was the Burst and Transient Source Experiment (BATSE), which was designed to observe the unocculted sky at once in order to detect and localize gamma-ray bursts. It consisted of eight identical detector modules placed around CGRO, each made of the same NaI(Tl) material as the EGRET calorimeter. There were two instruments in each module, one used for detection and direction finding, with a typical energy range of 20 keV to 1.9 MeV, and one used for spectroscopy, with a programmable range between 10 keV and 100 MeV. BATSE discriminator levels were significantly lower than the 30 MeV lower limit of the EGRET energy range. When BATSE detected a significant rise in count rates (5.5 sigma in two detector modules, in the 60 keV to 325 keV range), it would trigger and begin recording data for up to 105 minutes. When a trigger was detected, BATSE would send a signal to the other instruments onboard CGRO so that they could respond.

EGRET would go into a special burst mode in which the calorimeter would stop accumulating 32.768 s spectra, and instead go into a burst mode in which it would accumulate successive spectra of 1, 2, 4, and 16 seconds. Few gamma-ray bursts were detectable in the EGRET tracker, but the calorimeter, with its energy range of approximately 2-200 MeV, was able to accumulate spectra for some of the stronger bursts.

GLAST has a detector system that is similar to BATSE, and serves some of the same functions. The GLAST Burst Monitor (GBM), enhances GLAST's performance by extending the detectable energy range down to 10 keV - 25 MeV over a large field of view (8-10 steradians) specifically for the purpose of detecting gamma-ray bursts. Consisting of 12 NaI scintillator detectors and two bismuth germinate (BGO) scintillation detectors, the GBM will localize gamma-ray bursts to within 10^o-15^o within 2 s, or within 3^o-5^o within 5 s on the ground. BATSE was able to localize strong bursts to within 4^o. Like BATSE, the GBM will notify the LAT when it triggers, so that the spacecraft can slew towards the burst for higher-energy observations with the LAT. The GBM is not the only means that GLAST will have of detecting and localizing gamma-ray bursts, however. Unlike EGRET, the GLAST LAT will be able to detect and localize high-energy gamma-ray bursts without an external trigger provided by an instrument such as the GBM. This is made possible by the ability to run onboard software in the background that analyzes LAT data in real-time. The software will be able to discern whether a temporal and spatial pattern suggests that a gamma-ray burst is being detected.

Efforts to develop a method of detecting and localizing gamma-ray bursts in the LAT are described in Chapter 6.

Chapter 3

High-Energy, Post-Quiesecent Emission from Gamma-Ray Bursts

3.1 Motivation for Using the EGRET TASC to Search for Time-Extended, High-Energy Burst Emission

In Chapter 1, gamma-ray burst observations and theories were reviewed, with special attention paid to the possibility of high-energy emission, prompt and delayed, and the phenomenon of quiescent periods. The chapter described how MeV and higher-energy detections of both prompt and time-delayed emission could constrain parameters of burst physics related to the central engine, fireball shocks, and interaction with the local and extra-galactic media. It was stated that gains in the understanding of burst physics are expected to be possible with an increasing body of high-energy observations. Therefore, the relative scarcity of MeV-TeV burst detections makes each additional observation especially valuable. The common understanding has been that it will be necessary to wait for the launch of GLAST in order to make observations with the sensitivity required for the investigation of the aforementioned speculation. However, analysis of EGRET data has already led

to very significant high-energy burst discoveries, and its archived data need not be neglected.

EGRET burst detections cited in Chapter 1 were made possible through the use of BATSE triggers that acted as a guide for where to look for emission. Because of this, the high-energy emission thus found was coincident in time with lower energy BATSE emission, or followed shortly thereafter. One search that did not use BATSE triggers as a guide looked through EGRET spark chamber data independently of BATSE triggers, and uncovered one possibility of a burst that was not correlated with a BATSE trigger (Jones et al., 1996). However, by focusing on spark chamber data only, the search did not use all available EGRET data types, and it only covered a period of 40 months. For this thesis, it was hypothesized that a search through another EGRET data type and over a different period of time might be fruitful.

Though the spark chamber was the primary detector system on EGRET, several EGRET-detected bursts were studied using data from the TASC alone, which was often active even when the spark chamber was not. The TASC also took data in a lower energy range than the spark chamber (though there was overlap), but higher than the main data products of BATSE, and thereby provided data in an intermediate range. Furthermore, the TASC had the advantage of detecting emission from all incident directions, so its field of view was not limited in the way that the spark chamber's was. Despite these benefits, no comprehensive search for high-energy afterglow emission in TASC data products had been performed. Any evidence of time-extended emission in the TASC energy range, whether it be regarded afterglow

or a repeating event, would be valuable in its own right, and would also be very useful for determining the length of GLAST post-burst observations. In this chapter, such a search and its particularly exciting results are described.

3.2 Search Purpose and Method

Described in this chapter is a search through TASC data for delayed high-energy burst emission that may have been overlooked by previous analyses. The goal was not to find every possible instance of overlooked emission, to do comprehensive population studies, or to calculate a well-measured upper limit on gamma-ray emission in the TASC energy range. TASC data had previously searched only during the few seconds immediately following BATSE triggers for many brighter bursts, and TASC detections of prompt burst emission had already been analyzed (Schneid et al., 1992; Hurley, 1994; Catelli et al., 1995; Schneid et al., 1995; Catelli et al., 1998; Dingus et al., 1998). Therefore, there was no desire to find a few more cases of that kind for this thesis. Rather, the goal was to find some interesting cases of delayed high-energy burst emission for further analysis. Because a search for TASC detected emission after the BATSE T_{90} time had not been conducted, any search resulting in a discovery of delayed high-energy emission would be regarded as a success. The search reported in this chapter did result in at least one very significant detection (Wren et al., 2002). Because the goal was to look over large time periods surrounding bursts, a simple method of locating possible periods of burst emission was developed. Necessarily, some practical considerations were taken into account, and

some purposeful assumptions were made. These are discussed as they arise in the following sections, along with a description of the data type used and the method developed to search for periods possible high-energy burst emission that could be examined more closely. An assessment of the resulting search procedure sensitivity is given in Appendix B.

3.2.1 The Primary TASC Data Type

The primary TASC data type consisted of the constantly accumulated 32.768 s, *normal mode* or *solar* spectra, which were only interrupted when a signal indicating a burst trigger was received from BATSE. Consecutive 1.024, 2.048, 4.096, and 16.384 s *burst mode* spectra that resulted from a burst trigger were also available for analysis. These would interrupt the continual accumulation of normal mode spectra until the 23.552 s of burst mode spectral accumulation was complete. At that point, the accumulation of normal mode spectra would continue.

The choice of 1, 2, 4, and 16 s burst mode spectra illustrates a bias in the approach to detecting high-energy burst emission in the TASC. The increasing integration periods and the length of those periods may indicate that it was thought that high-energy burst emission would be initially intense, requiring a short integration period, and then fall off exponentially. Burst mode spectra were also taken for less than 24 s, which perhaps indicates that high-energy emission was not expected to be detectable for more than a few seconds. In contrast, the work described in this chapter is not based on an assumption that high-energy burst emission is only detectable in the TASC for less than two-dozen seconds, or that the emission will

be most intense immediately following a BATSE trigger, and will then decay in an exponential fashion. Instead, TASC emission is searched for a period of hours surrounding a burst.

Each spectrum, regardless of its period, was accumulated by a 16 MHz, 12-bit analog to digital converter (ADC). When an event's energy was measured, it was recorded as one count in a channel of the ADC; each channel corresponded to an energy bin. Higher energy events were recorded in higher numbered channels. The channels were grouped into 256 bins, and their contents were summed before transmission to the ground. This was efficient, because high energy events were uncommon, and the upper end of the 4096 channels was sparsely populated.

Recording an energy measurement in an ADC channel required the conversion of the analog signal to a digital count, and this introduced some instrument deadtime. For each event, there was a fixed 0.18 ms deadtime in addition to the 0.000063 ms/channel it took the ADC to increment a bin (0.000063 ms = 1/16MHz). The amount of time that the instrument was active and available to take data, the *live-time*, is derived from the deadtime by subtracting the deadtime from the length of the accumulation interval.

In order to convert the count spectra to energy spectra, one must know the *gain* of the TASC photomultiplier tubes, which tells how each bin corresponds to energy. Calculating the gain is a matter of looking at the raw spectral counts for a given accumulation period, and then locating a small peak in rates in the first few channels. This peak is due to radioactive potassium found in the spacecraft itself,

and its emission is at a constant 1.46 MeV. One can fit a parabola to the peak, and thereby derive the channel that corresponds to 1.46 MeV. The gain is then known in units of MeV/channel, and it is straightforward to extrapolate that to determine the energy of the other bins.

3.2.2 Development of TASC Spectral Rates

To use TASC spectra for the purpose of a temporal search for emission, it is necessary to convert them into a type of rate that can be examined for significant rises. Each TASC spectrum is a count of events that are binned according to energy. One can sum the raw data counts, ignoring the energy of the bin that a particular count belongs to, and get an integrated count of the number of detections. The integrated count can then be divided by the amount of time measurements were being taken for that spectrum, the livetime, and the resulting number is a *spectral rate* that changes every 32.768 s. After applying the livetime correction, this rate is a measure of the average activity of the TASC during the 32.768 s spectral accumulation period.

Creating Light Curves

Because this search was more general than previous searches, use of the standard EGRET analysis toolset was adapted. Using the existing tool for creating TASC spectra, a program known as *TBurst*, the desired number of spectral intervals for which to create spectra is entered. In TBurst, it was specified that no background subtraction is necessary (because only the raw count rate is desired), and then the program extracts data from up to 20 normal mode spectrum accumulation periods,

or a total of about 11 minutes. In order to get light curves over a period of hours, this process was repeated multiple times.

The program output contained the raw spectral counts for the accumulation interval. It was necessary to write a program to process the files. It went through each spectrum, found the sum of the raw counts, the TBurst-computed livetime for that accumulation period, and the midpoint time for that period. It would then compute the spectral rate by dividing the sum of the raw counts by the livetime, and also calculated the beginning time of the spectral period. For each set of 20 spectra, the spectral rates and their corresponding start time were output to a text file. After processing all the spectra associated with one search interval, these spectral rates were combined into one file that could then be used as input to an automated peak finding program.

3.2.3 Determining Where to Search

Since the primary interest was in delayed emission, BATSE triggers were used as a starting point. Because previous detections of TASC emission were for bursts with high >300 keV BATSE-deteced fluence[1], the >300 keV fluence was chosen as the indicator of whether emission was likely to be found in a higher energy range. Another program was written to scan the BATSE catalog (Paciesas et al., 2000) and extract the fluence information in the highest energy bin, which was anything above 300 keV. After ordering this list from greatest to least >300 keV fluence, the

[1]Bursts 910503, 910601, 910814, 920622, 930131, 940217, 940301, 940921, 950425, and 990123 were detected in the TASC and were among the top 64 most fluent bursts in the BATSE >300 keV range.

most fluent 100 bursts were selected as a first sample (Table 3.1).

It was decided to search one hour before and six hours after each BATSE trigger for the candidate bursts. One hour before, because the possibility of a high-energy precursor is also interesting, and six hours after, because the detection of GeV emission 75 min after GRB 940217 (Hurley, 1994) indicates that a 1.25 hr search is minimally necessary, and a search a few times that length is prudent.

3.2.4 Using TASC Spectral Rates to Search for Emission

Energy spectra were calculated for each burst during the period covered by the BATSE T_{90} time. As discussed below, this led to a reduction of the original list to a final sample that was searched for seven hour periods.

Creating Energy Spectra

The process of generating and examining spectra involved several steps. The first step was to use TBurst to generate a raw (no background subtraction) spectrum for the time interval so that the gain could be computed. Once the gain was calculated, it was entered into TBurst along with the time periods of the background intervals, which were usually chosen to be two intervals before the interval under study, and two intervals after, with a one interval gap before and after the studied interval so that the background records did not directly precede or follow the possible burst. Attention was also paid to the local spectral rate light curves when picking background intervals, and the standard selection was adjusted if it would have resulted in a poor choice. TBurst would then use the background records before and after

the studied interval to interpolate a background spectrum to subtract from that interval's spectrum. The resulting background subtracted spectrum was still in the 256 channel format, and uncertainties in each bin were also computed. These were based on the square root of the counts in each bin, a simple statistical calculation.

Background subtracted spectra did not reflect the fact that incoming events had to pass through varying configurations of spacecraft material before entering the TASC. In order to get the spectrum of the incoming burst, the measured spectrum had to be deconvoluted by multiplying it by a large *response* matrix that contained the probabilities that events of a given measured energy would have resulted from events of a particular incident energy. The accuracy of the mass model was tested using a gamma-ray source, and it was concluded that the mass model alone accurately described the instrument performance for gamma rays incident from the EGRET pointing direction, but for other directions it was necessary to make corrections using an instrument response function (Thompson et al., 1993). The application of a response matrix to the measured spectrum therefore converted it into a reliably determined incident energy spectrum. Generating the matrix required use of a standard program that used the EGRET mass model and Monte Carlo code, and it typically took several hours of computing time to run. It required the user to input the orientation of the spacecraft, which was available in an EGRET summary timeline file, and the location from which the incident emission came. Unfortunately, the TASC does not provide directional information, so it is impossible to generate an accurate response matrix unless the direction of incident emission is known by some

other means. For rises in rates that were coincident with BATSE-detected emission, it was assumed that the TASC-detected emission was from the same direction.

Before devoting several hours of computing time for each burst to generate a matrix corresponding to a specific direction, a faster method was used to determine whether emission was present to begin with. The standard EGRET toolkit required the generation of an instrument response matrix for the creation of any energy spectrum. Therefore, a single response matrix was generated for emission that entered along EGRET's zenith – straight through the top of the tracker and into the TASC. The material encountered coming through the top of EGRET was less than for many other configurations, because other instruments and spacecraft components were along other lines of sight. The area×efficiency of the TASC could thus vary by as much as a factor of 3, but this was taken into account by the instrument response function (Thompson et al., 1993). If the *zenith matrix* were applied to any raw count spectrum, the conversion process would alter the spectrum minimally as it was converted to an energy spectrum. Once the energy spectra had been calculated, it was possible to bin and plot them.

Refining the List

It was decided to focus on those bursts that had the greatest potential to provide information on delayed high-energy emission – if present. Although gamma-ray emission found minutes or hours after a BATSE trigger would be valuable and a significant discovery in itself, it would be even more valuable if its properties could be compared with the prompt burst emission. It was also a reasonable assumption

that any delayed emission episodes would be weaker than the prompt emission. Therefore, if it was not possible to detect intense high-energy emission during the BATSE T_{90} time, it was not believed likely that afterglow emission could be detected.

A standard EGRET program was used to bin and plot TASC energy spectra whose accumulation periods overlapped with the BATSE T_{90} time period. The plotting program required a fit to the data points, and as stated in Chapter 1, the synchrotron and IC mechanisms believed to be responsible for burst emission, both prompt and delayed, produce emission that is consistent with a power-law. Therefore, each spectrum was fitted with a single power-law over 1-10 MeV. It was found that TASC spectra for bursts with a BATSE >300 keV fluence that was less than 6×10^{-5} ergs cm^{-2} were usually empty or too weak for a fit, so the 47 bursts with less than 6×10^{-5} ergs cm^{-2} were removed from the list. Of the remaining 53 bursts, it was necessary to remove another 21 because of corrupt spectral records that could not be processed.

The remaining 32 bursts all had some evidence of emission in at least one of their prompt burst TASC spectra[2]. This does not necessarily mean that a power-law fit was successful for any of the spectra, but only that the combination of high BATSE >300 keV fluence, and the possibility of TASC detected emission in at least one spectrum made the burst worthy of a closer look. It was for these 32 bursts that light curves were generated for a seven hour period beginning an hour before each BATSE trigger. None of the light curves were continuous over the seven hour

[2]More than one prompt burst spectrum was possible for some bursts depending on the length and where the emission fell relative to the start and stop times of the TASC 32.768 s spectral accumulation periods.

period, because the TASC did not take data when EGRET passed through a region of high cosmic ray flux known as the South Atlantic Anomaly (SAA), and there were occasional gaps in the telemetry. The search method described below was able to recognize and skip gaps in the light curves.

Automated Light Curve Scanning

The search through light curves for high energy pre or post-burst emission was twofold in process. The primary method was to use a consistent background selection method to determine whether a peak was sufficiently statistically significant to examine more carefully. The secondary method was a visual scan of the light curves to determine whether the automated method had missed any peaks.

To automatically scan the light curves for rises in rates, a simple method that would minimize issues related to background subtraction was desired, and it was necessary to make a choice about what length of emission to look for. Most BATSE-energy prompt-phase emission and that previously detected by EGRET was on the order of a few seconds to few tens of seconds long. It was decided to focus the search on emission periods of similar length, because background subtraction over longer periods could be unreliable. The background spectra could change significantly over periods of more than a few minutes as CGRO passed through regions of different geomagnetic cutoff. Searching for slow rises over periods of minutes or more would therefore decrease confidence in the background subtraction and the interpretation of results. A shorter time scale would be most sensitive to faster temporal variation, but the corresponding spectra would be measured with greater certainty.

The time scale chosen was one 32.768 s accumulation period. The search software would compare the magnitude of the spectral rate in a given accumulation period to that in surrounding time periods, and then determine how significant the peak was relative to the standard deviation in the count rate of the local background. This was done by selecting background records before and after the accumulation period under examination, interpolating in order to get an estimated background during that period, and then computing the standard deviation at that time (the square root of the estimated rate). The strength of a rise in rates, a peak, was described in units of the number of standard deviations above the local background.

Several choices of background were tested. The first method used one spectral period directly before and one directly after the period under examination. If "X" is used to denote the interval was used for background, "_" for a one interval gap, and "*" for the period under examination, method one looks like: X*X. The second method used two periods directly before the possible peak, and two periods directly after: XX*XX. The third method used two periods before and two periods after, but the *after* periods were separated from the period under study by one accumulation interval: XX*_XX. The fourth method used two before and two after, but the two periods before were separated from the period under study by one interval: XX_*XX. The fifth and final method used two periods before and two after, but each set was spaced from the period under study by one accumulation interval: XX_*_XX. Choosing intervals shortly before and after an interval under study was a standard approach for TASC background analysis that had previously been used in EGRET

analyses. No background selection covered a period of more than 230 s.

Each of the above background selections were programmed into the peak finding program, and a threshold for the rise in *spectral rate strength* was set at a confidence threshold of 95% above background, or 1.96σ. The program was run on several of the brightest BATSE bursts, and it output the rate strength in units of σ for each accumulation interval. Any intervals that had a rise in count rates that was at or equal to the 95% confidence threshold were distinguished in the program's output. After running each of the methods on several bright bursts, it was clear that count rates did indeed rise after BATSE triggers, and all five methods detected the rises. The choice of a 95% confidence threshold was based on a desire to have a high degree of certainty in the significance of a rise in rates, yet not be so high as to exclude peaks that might be of interest. Lower thresholds (80%, 85%, and 90%) were tested, but they yielded many peaks that corresponded to statistical fluctuations and empty spectra.

It was possible that GRB emission would cross boundaries between accumulation intervals, beginning in one interval and ending in the next. This was the reason for putting in one interval gaps between the background selection and the interval under study. The final factor to consider was the statistical fluctuations (typically 0.5-1.0%) of the background spectra from one interval to the next. For this reason, two background spectra before each possible burst, and two after, were averaged. A consistent method of finding peaks and of selecting background intervals to be used for additional spectral analysis had thus been developed. As shown in Appendix

B, the uniform method for peak finding is used for an estimate of the search sensitivity. The method was estimated to detect any 32.768 s burst fluence of at least $4 \times 10^{-5}\, ergs/cm^2$.

Table 3.1: Summary of Initial Search Through 100 Gamma-Ray Bursts. The BATSE T90 is the time during which 90% of BATSE emission was detected. "Evidence for Emission" indicates that at lease one burst-time spectrum was not empty or obviously background. "Corrupt or Empty Spectra" indicates that the spectra for that burst were either empty after background subtraction, or were corrupted in some way.

Rank	GRB Designation	BATSE Trigger Number	BATSE Trigger Time (UT s)	BATSE >300 keV Fluence (ergs cm^{-2})	BATSE T90 Duration	Notes
1	940703	3057	16846.51	6.0757e-04	34.88	Corrupt or Empty Spectra
2	940217	2831	82962.07	4.9183e-04	150.144	Evidence for Emission
3	990104	7301	57753.7214	4.1220e-04	174.464	Evidence for Emission
4	990123	7343	35216.1214	3.7433e-04	63.36	Evidence for Emission
5	950425	3523	919.218	3.4639e-04	59.072	Evidence for Emission
6	930506	2329	53571.461	3.1066e-04	22.144	Corrupt or Empty Spectra
7	980923	7113	72647.5214	2.8794e-04	33.024	Evidence for Emission
8	910503	143	25452.65	2.3324e-04	50.816	Corrupt or Empty Spectra
9	910814	678	69273	2.2764e-04	53.888	Evidence for Emission
10	990323	7491	62977.0814	2.1686e-04	49.472	Corrupt or Empty Spectra
11	990518	7575	62325.4974	1.7858e-04	195.2	Corrupt or Empty Spectra
12	971110	6472	68006.8815	1.7339e-04	39.808	Corrupt or Empty Spectra
13	941017	3245	37173.938	1.6888e-04	77.056	Evidence for Emission

Continued on Next Page...

Table 3.1 – Continued

Rank	GRB Designation	BATSE Trigger Number	BATSE Trigger Time (UT s)	BATSE >300 keV Fluence (ergs cm^{-2})	BATSE T90 Duration	Notes
14	970202	5995	25844.4255	1.6476e-04	26.688	Corrupt or Empty Spectra
15	981203	7247	3552.9934	1.5577e-04	180.736	Evidence for Emission
16	940206	2798	517.79	1.4808e-04	49.152	Corrupt or Empty Spectra
17	991216	7906	58021.3694	1.4756e-04	15.168	Evidence for Emission
18	990915	7766	83722.5534	1.4645e-04	77.952	Evidence for Emission
19	960924	5614	42110.6655	1.3837e-04	5.312	Corrupt or Empty Spectra
20	930916	2533	73163.422	1.3834e-04	74.304	Corrupt or Empty Spectra
21	970411	6168	35545.8015	1.3245e-04	25.984	Corrupt or Empty Spectra
22	981021	7170	83292.3214	1.2526e-04	99.584	Evidence for Emission
23	990506	7549	41010.9374	1.2484e-04	130.048	Evidence for Emission
24	920622	1663	25504.49	1.1951e-04	35.968	Corrupt or Empty Spectra
25	980203	6587	82028.2575	1.1767e-04	23.04	Evidence for Emission
26	940302	2856	18511.51	1.1126e-04	119.872	Evidence for Emission
27	960529	5477	43665.098	1.0147e-04	17.088	Evidence for Emission
28	990803	7695	23375.9294	9.9388e-05	19.3925	Evidence for Emission
29	930201	2156	60115.59	9.2034e-05	154.432	Corrupt or Empty Spectra
30	910601	249	69734.508	8.9605e-05	28.544	Evidence for Emission
31	950117	3360	5761.713	8.9147e-05	NA	Corrupt or Empty Spectra
32	951203	3930	3987.634	8.7050e-05	172.739	Corrupt or Empty Spectra

Continued on Next Page...

Table 3.1 – Continued

Rank	GRB Designation	BATSE Trigger Number	BATSE Trigger Time (UT s)	BATSE >300 keV Fluence (ergs cm^{-2})	BATSE T90 Duration	Notes
33	920311	1473	8424.04	8.6820e-05	NA	Corrupt or Empty Spectra
34	000101	7929	4799.2254	8.4162e-05	51.776	Evidence for Emission
35	980724	6944	74080.9934	8.3209e-05	NA	Corrupt or Empty Spectra
36	940323	2891	79478.43	8.3182e-05	60.736	Evidence for Emission
37	940526	2994	73205.789	8.2082e-05	48.576	Evidence for Emission
38	920525	1625	12421.74	8.0769e-05	16.128	Evidence for Emission
39	920406	1541	9853.55	8.0073e-05	NA	Corrupt or Empty Spectra
40	940921	3178	18493.105	7.6679e-05	44.096	Evidence for Emission
41	940301	2855	72637.078	7.5706e-05	42.496	Evidence for Emission
42	000302	8008	10225.0814	7.5650e-05	22.656	Evidence for Emission
43	970315	6124	56454.2175	7.3508e-05	NA	Evidence for Emission
44	920902	1886	1736.32	7.3169e-05	275.712	Evidence for Emission
45	980124	6576	23673.0575	7.3060e-05	45.056	Evidence for Emission
46	000429	8087	36442.8734	7.2102e-05	164.352	Evidence for Emission
47	990728	7678	39824.8894	7.0963e-05	42.752	Evidence for Emission
48	931008	2571	40150.68	6.9599e-05	NA	Corrupt or Empty Spectra
49	951219	4039	60679.73	6.8930e-05	58.816	Evidence for Emission
50	960114	4368	44104.777	6.8864e-05	36.48	Corrupt or Empty Spectra
51	920210	1385	35623.789	6.8733e-05	51.776	Corrupt or Empty Spectra

Continued on Next Page...

Table 3.1 – Continued

Rank	GRB Designation	BATSE Trigger Number	BATSE Trigger Time (UT s)	BATSE >300 keV Fluence (ergs cm^{-2})	BATSE T90 Duration	Notes
52	940414	2929	60385.559	6.1785e-05	NA	Evidence for Emission
53	940817	3128	31215.789	6.1389e-05	NA	Evidence for Emission
54	950208	3408	7824.049	5.9284e-05	58.56	Evidence for Emission
55	980810	6985	66929.3774	5.9186e-05	NA	Evidence for Emission
56	931026	2606	41757.34	5.7686e-05	134.688	Corrupt or Empty Spectra
57	980306	6629	34382.5615	5.7438e-05	239.552	Corrupt or Empty Spectra
58	970223	6100	30377.6735	5.7286e-05	16.256	Evidence for Emission
59	990802	7688	3883.5134	5.6545e-05	154.432	Corrupt or Empty Spectra
60	940526	2993	39326.809	5.6211e-05	44.8	Evidence for Emission
61	921015	1989	5792.39	5.6057e-05	272.448	Corrupt or Empty Spectra
62	970306	6115	10059.4655	5.4732e-05	122.496	Corrupt or Empty Spectra
63	941008	3227	48772.785	5.4334e-05	115.328	Corrupt or Empty Spectra
64	930131	2151	68231.680	5.3832e-05	19.2	Evidence for Emission
65	951011	3860	77679.281	5.3697e-05	31.488	Corrupt or Empty Spectra
66	950403	3492	84826.547	5.3073e-05	NA	Corrupt or Empty Spectra
67	960605	5486	29392.137	5.2081e-05	86.72	Evidence for Emission
68	960831	5591	37710.5376	5.0826e-05	135.488	Corrupt or Empty Spectra
69	970420	6198	72842.1855	4.9944e-05	10.496	Evidence for Emission
70	980225	6615	30564.0566	4.9904e-05	127.744	Corrupt or Empty Spectra

Continued on Next Page...

Table 3.1 – Continued

Rank	GRB Designation	BATSE Trigger Number	BATSE Trigger Time (UT s)	BATSE >300 keV Fluence (ergs cm^{-2})	BATSE T90 Duration	Notes
71	950301	3448	75761.328	4.9475e-05	NA	Corrupt or Empty Spectra
72	940119	2770	9730.71	4.9217e-05	181.088	Evidence for Emission
73	970816	6336	8264.4175	4.8072e-05	6.528	Evidence for Emission
74	940708	3067	74526.188	4.7132e-05	66.976	Evidence for Emission
75	980706	6904	57587.0414	4.6847e-05	25.856	Evidence for Emission
76	980329	6665	13478.4974	4.5303e-05	18.56	Evidence for Emission
77	970827	6349	35750.6255	4.4195e-05	82.688	Corrupt or Empty Spectra
78	971113	6476	58130.8495	4.4070e-05	NA	Corrupt or Empty Spectra
79	990712	7647	27919.4174	4.3174e-05	NA	Corrupt or Empty Spectra
80	960322	5304	19641.418	4.1926e-05	22.784	Corrupt or Empty Spectra
81	000511	8101	4319.9934	4.1854e-05	115.008	Corrupt or Empty Spectra
82	940529	3003	76736.148	4.0923e-05	37.632	Evidence for Emission
83	940319	2889	86240.922	4.0823e-05	NA	Corrupt or Empty Spectra
84	970704	6293	4096.8015	4.0018e-05	0.192	Corrupt or Empty Spectra
85	911202	1141	73729.711	3.9671e-05	NA	Corrupt or Empty Spectra
86	980703	6891	15765.2174	3.9160e-05	411.648	Evidence for Emission
87	921207	2083	57647.941	3.9117e-05	15.168	Corrupt or Empty Spectra
88	971220	6539	14793.7615	3.8762e-05	13.632	Evidence for Emission
89	971029	6454	22428.8975	3.8587e-05	616.256	Corrupt or Empty Spectra

Continued on Next Page...

Table 3.1 – Continued

Rank	GRB Designation	BATSE Trigger Number	BATSE Trigger Time (UT s)	BATSE >300 keV Fluence (ergs cm^{-2})	BATSE T90 Duration	Notes
90	940516	2890	29533.85	3.8145e-05	51.584	Corrupt or Empty Spectra
91	940623	3042	67583.641	3.5991e-05	181.952	Corrupt or Empty Spectra
92	950325	3481	63391.922	3.5822e-05	40.768	Evidence for Emission
93	911126	1121	46127.719	3.5797e-05	NA	Evidence for Emission
94	961102	5654	41903.8175	3.5463e-05	71.36	Corrupt or Empty Spectra
95	910619	394	51272.809	3.4792e-05	106.112	Evidence for Emission
96	941228	3330	27581.234	3.4649e-05	61.952	Corrupt or Empty Spectra
97	960623	5512	4728.521	3.4646e-05	90.336	Evidence for Emission
98	950522	3593	85283.188	3.4375e-05	59.072	Evidence for Emission
99	990311	7464	79905.5294	3.4331e-05	41.088	Corrupt or Empty Spectra
100	990108	7310	30066.4254	3.4082e-05	NA	Corrupt or Empty Spectra

3.2.5 Verification by Independent Visual Scan

Though the automated peak finding method was tested and proven successful at detecting rises in count rates, another method of search verification was also desired. A qualitative, but useful, method was to plot the count rates vs. time, and visually scan them for rises. This was done in a spreadsheet program that allowed a fit of 5th or 6th degree polynomials to intervals of time. The background rates would rise near the SAA and then slowly drop only to rise again as EGRET neared that region again. This caused the light curves to have a parabolic appearance, but with bumps and variation. The degree of polynomial was chosen to smoothly fit the large-scale fluctuations in background, and its justification was empirical, the choice of fit varying from interval to interval. The fits to these regions were only used as a reference for the eye, and not for any quantitative purpose.

When any points were encountered at which the rate appeared to be significantly above background (a qualitative judgment), the time was noted so it could be studied later. After finishing the visual scans of each burst, the time periods that were noted as possible peaks were looked up in the output of the automated peak finding program. The peak finding program output the strength of each accumulation interval in units of standard deviations above local background, so it was a simple matter to find out if the visually detected peak was above the confidence threshold. Any obvious discrepancies, such as a large peak found visually that did not correspond to a significant rise according to the peak finding program, would indicate a problem with the peak finding program. The visual scan was thus a

diagnostic tool. More detailed results are described in a following section (and in Tables 3.2 and following), but here it is noted that the visual scan did not detect any inefficiencies or problems with the peak finding program, though the program sometimes detected false peaks due to local decreases in the spectral rate.

Analyzing Peaks

For all time periods corresponding to a peak in rates, the local light curves were examined for any visible fluctuations in the local background that might have caused a false peak (see Figures 3.3 and 3.4 for examples). If there was no sign of a false peak due to background fluctuations, it was important to determine whether the peak could be associated with a gamma-ray burst, because there existed other possible reasons for a peak. It was possible that a rise in rates was caused by a statistical fluctuation in background, a solar flare, or even prompt emission from an untriggered burst. The first would be evident in the plot of the corresponding spectrum and the quality of its fit (discussed below), the second might be visible in space weather data, and the last might have been listed in any of two catalogs of untriggered gamma-ray bursts that searched through BATSE data (Kommers et al., 2001; Stern and Tikhomirova, 2002), or in a the detections of the Interplanetary Network (IPN) (Hurley et al., 2005). (The IPN used detections from a number of space missions of different types to localize possible bursts.) To look for evidence of a solar flare, GOES X-ray data were checked in the 1-8$\mathring{A}$ and 0.5-3$\mathring{A}$ bands and in the electron flux >2 MeV, the proton flux >1 MeV, and the α particles flux >150 MeV (National Geophysics Data Center web page, 2005). EGRET spark chamber

data were also searched for photons from the burst direction during the time period for the spectrum's accumulation interval. Given that the spark chamber had a much smaller field of view than the TASC, and that the spark chamber was sometimes powered down when the TASC was taking data, even if the TASC did detect burst emission, it was not certain that the spark chamber would record gammas also. However, the detection of spark chamber photons or a direction provided by the IPN or untriggered burst catalogs were the only methods of determining from what direction TASC-detected emission came.

If any peak was not eliminated because it was obviously and falsely caused by local fluctuations in the background, plots of the spectra using the standard background selection were created, examined and fitted to a single power-law over 1-10 MeV. Regardless if when the spectrum was accumulated (before, during, or after the prompt burst emission), a response matrix corresponding to the BATSE-reported burst direction was used. If the spectral rates showed that the standard background selection was not ideal, more appropriate background selections were attempted. If the spectrum showed evidence of energy in a greater or lesser energy range, a power-law fit was attempted over a more appropriate range also.

It was usually possible to have confidence in a quantitative judgement of a spectrum after a look at its plot. Figure 3.1 is an example of a reliable fit to a GRB 920902 spectrum that has good background subtraction and a well measured detection in the lower-energy range. Contrast this to Figure 3.2, which shows a spectrum whose spectral features may be artifacts of the background subtraction.

Instrumental effects were sometimes responsible for unreliable spectra. For examples of some well-defined spectra, refer to Figures 3.8 and 3.9, also discussed later in the chapter.

All of the spectral plots were first evaluated visually, and then all the fit parameters (spectral index and normalization constant) without regard to the numerical fit parameters. The fit parameters were then listed for those spectra, and it was found that the visual evaluation was a good predictor of the quality of fit as judged by the magnitude of the fit errors. When the error of a fit is expressed in terms of a percentage of the fit parameter, it was found that no spectrum was judged by the qualitative method to have good background subtraction and power-law consistent emission if its spectral index was unknown by more than 12%, or if its normalization constant unknown by more than 36%, or if the sum of those errors was more than 48%. Beyond that point in the list of spectra, the error in spectral fit jumped from 11.8% to 16.5%, the summed error was above 50% for all but one, and 14 of 27 spectra had a summed error greater than 100% (there was no upper limit on the percent error). The qualitative visual judgment was therefore consistent with a decrease in the quality of fit as given by quantitative parameters.

Comments on the Peak Analysis

The process of evaluating peaks and their associated spectra was intended to exclude from consideration any peaks that were obviously caused by false rises in rates, and any spectra that were not clearly consistent with characteristics reported for previously measured spectra in the same energy range. Both the visual evaluation

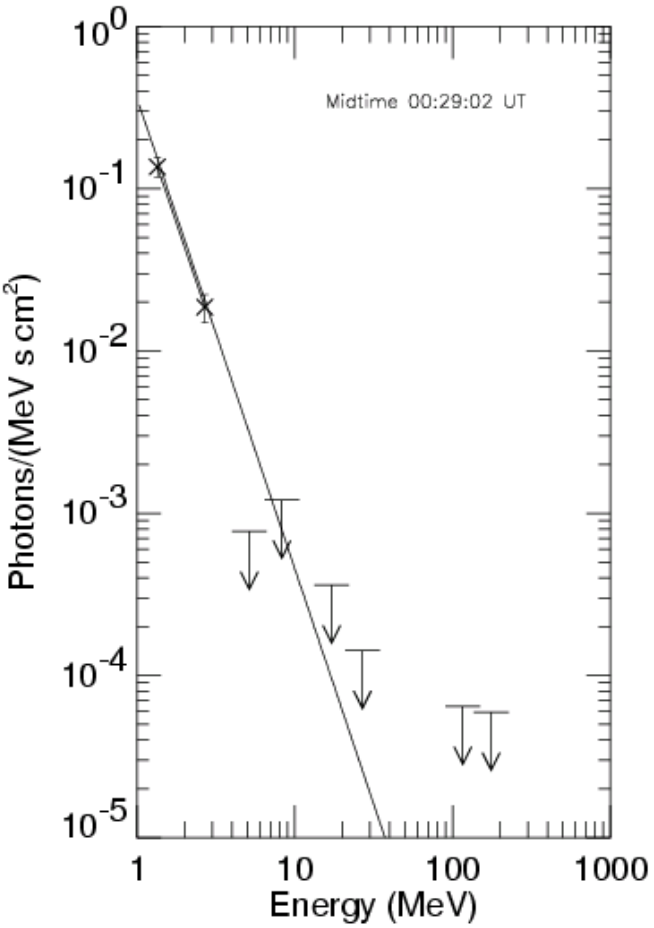

Figure 3.1: A spectrum from GRB 920902 that shows good background subtraction for a weak gamma-ray burst. The straight line is a power-law fit over 1-5 MeV. The two points shown are for binned data, but the fit was done to the unbinned energy spectra, which had a finer energy resolution. Upper limits are 1σ. The spectral index was measured to be 3.16 ± 0.31, while the normalization constant was $0.35 \pm 0.06\, photons/(MeV\, s\, cm^2)$. This is an example of a weak burst with good background subtraction and an acceptable power-law fit.

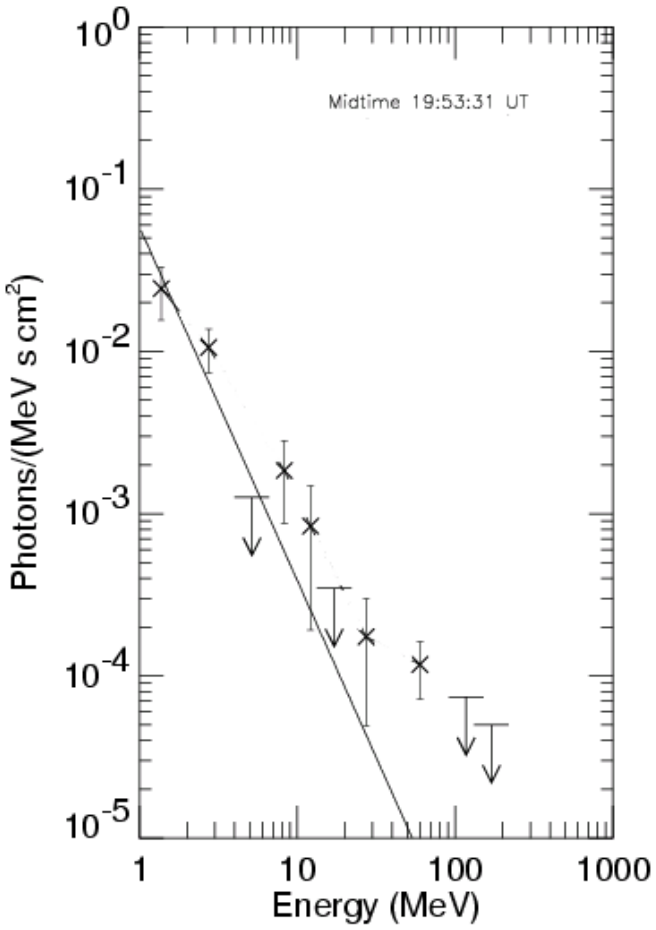

Figure 3.2: A spectrum that shows features that may be artifacts of the background subtraction. Fluctuations in the background spectra, sometimes due to instrumental effects, can cause both excess and insufficient background subtraction at different energies, rendering spectra unreliable. The straight line is an attempted fit over 1-10 MeV. Upper limits are 1σ.

and the power-law fit were important for the spectral evaluation.

A single power-law fit was attempted because the synchrotron and IC mechanisms believed to be responsible for burst emission, both prompt and delayed, produce emission that is consistent with a power-law. Furthermore, the well measured E_p, or break energy, is sharply peaked near 250 keV (Preece et al., 2000), and breaks in possible IC emission, prompt or delayed, are expected in the GeV range. There have been some observations of a break closer to 2 MeV (Schaefer

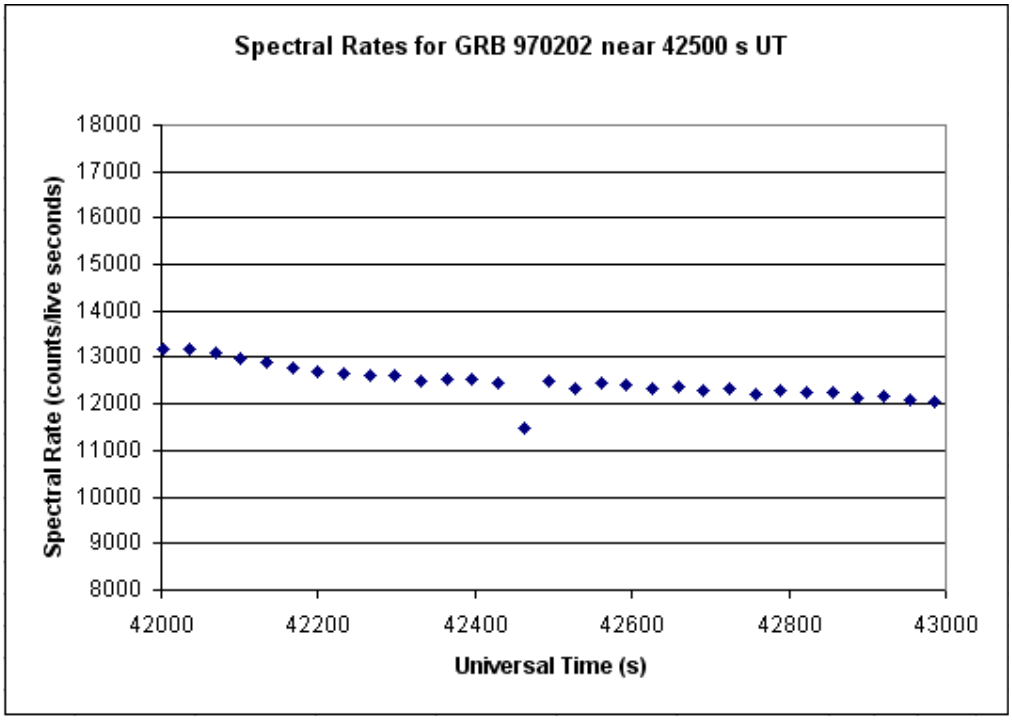

Figure 3.3: Spectral rates light curve for GRB 970202 showing a dip in rates. This kind of local decrease in rates could lead the automated peak finding program to indicate a nearby rise in rates that was, in fact, false.

et al., 1998), but these are consistent with the high-energy tail of the narrow E_p distribution, and there exist no published TASC observations of a break at the high end of the distribution. The latter fact does not indicate that breaks near 2 MeV cannot be found in TASC data, but it does confirm that breaks at that energy are relatively rare. Because the TASC is most sensitive in the ∼1-250 MeV range, most detections can be expected to follow a single power-law. This is confirmed by reported TASC observations.

Therefore, one quantitative means of determining whether possible emission in the TASC might be due to a GRB, is whether a power-law could be fitted to the background-subtracted data. Because of this assumption, the search is somewhat

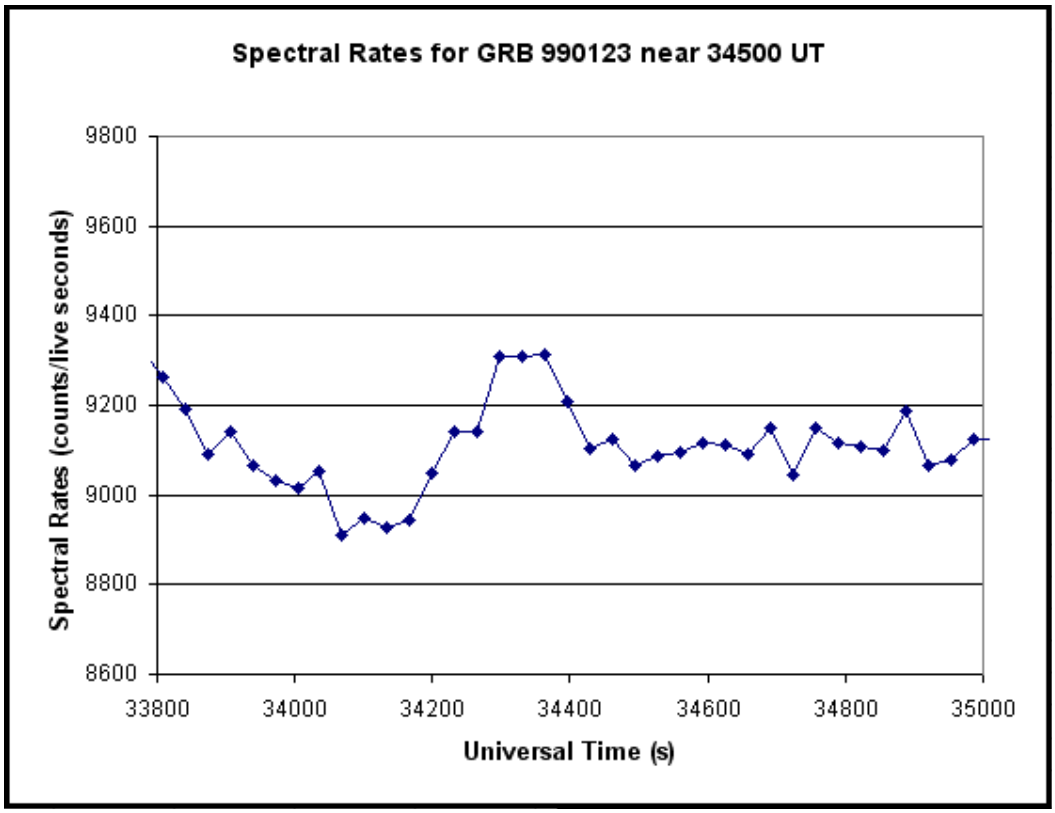

Figure 3.4: Spectral rates light curve for GRB 990123 showing rapid variation in rates. Local fluctuations of this type can make background subtraction difficult, and would sometimes lead the automated peak finding program to indicate local nearby peaks that were false. The lines connecting the data points were added for visual emphasis.

biased against emission that cannot be well fitted by a single power-law, and spectral breaks in the TASC-sensitive range might go undetected. However, breaks in the TASC range are infrequently detected, and it was necessary to make decisions regarding the type of emission for which the search would be sensitive. Consistently fitting over a smaller range, say 3-10 MeV, might better avoid the possibility of a poor fit due to a break below 2 MeV, but the narrow width of the E_p distribution mitigates this concern, as does the visual inspection. Furthermore, for the majority of bursts – those that peak near 250 keV – the fit is likely to be better if it includes the low energy end of the TASC data and does not unnecessarily exclude part of the

measurement. The power-law criterion is also theoretically and empirically justified, and it can be used to help evaluate spectra whose origin may otherwise be difficult to determine. In addition, the goal of this search is not to find every possible instance of delayed high-energy emission, but just some cases in which we can have reasonable confidence of the origin.

There was one very important exception to the spectral evaluation procedure as described above. If spark chamber photons were detected from the burst direction during any peak, the peak and its associated spectrum was considered to be possibly related to the original burst regardless of the spectrum's shape and fit. One such case was found, and it is described in Appendix A.

3.3 Results of the Search, and the Discovery of High-Energy, Post-Quiescent Emission

When spectral rate light curves of the 32 bursts were searched for rates over the 95% confidence threshold, all were found to have peaks over threshold before, during, or after BATSE emission (see Table 3.2). The average amount of time that it was actually possible to search surrounding each burst was 3.65 hrs out of 7, because of gaps in the telemetry due to passage through the SAA or for other spacecraft related reasons. Eighteen bursts had peaks over threshold that coincided with BATSE-detected emission, 9 bursts had peaks before the BATSE trigger, and 31 bursts had peaks after BATSE emission ended. Scanning the same light curves visually also found what looked like peaks, but these had either already been detected by the

automated scan, or the peaks were found to be below the confidence threshold. After creating and examining spectra, it was apparent that only 16 of the 32 bursts had evidence of TASC-detected power-law emission that was coincident with BATSE-detected emission. Seven of those bursts had TASC-detected emission that was previously published, but the other nine were not. One of the nine, described later, had very strong evidence of post-quiescent emission possibly up to 100 MeV (Wren et al., 2002). There were only two bursts that had spectra showing possible signs of delayed, high-energy emission. The remaining bursts had intervals with pre or post-burst peaks over threshold that were due to local fluctuations in background, or due to a recurring problem with the TASC analog digital converter in count bin 33. Others could not be associated with the burst using spark chamber photons, or by using the catalogs previously mentioned. The corresponding spectra did not show signs of high-energy emission upon close examination, and were most consistent with background fluctuations (see Appendix A).

3.3.1 Common Reasons for Disregarding Peaks and Spectra

The majority of peaks were eliminated as possibilities because of obvious local fluctuations in the background as evident in the spectral rates. Figures 3.3 and 3.4 are examples of this type of problem. The second most common reason for eliminating a peak was the discovery that some of the strongest peaks were caused by an artifact in the data. When the spectral data corresponding to several peaks were examined, there was an excess of counts in channel number 33 of the spectrum. This excess did not appear in the background intervals preceding or following the peak,

and it was consistently in channel 33 regardless of the energy to which the channel corresponded. This excess of counts caused the deadtime of the interval to increase dramatically, and thus its livetime to decrease. This decreased livetime relative to the surrounding intervals, in addition to the excess counts, led to a sudden rise in the spectral rate for that interval. The reason for a large excess of counts in the same ADC channel suggests that there was something wrong with the electronics, but it is beyond the scope of this thesis to initiate an investigation of the problem. Each peak interval was checked for spark chamber photons, but none were found for any of the peaks that were eliminated from consideration due to one of the reasons listed in the previous section.

Table 3.2: Summary of the search through 32 GRBs for high-energy emission. For each burst, the BATSE trigger time is listed along with the start and stop times of each $\sim$ 7 hour search. If peaks above threshold were found before, during, or after the BATSE T_{90} period, this is noted. When high-energy emission was detected during the T_{90} period, it is noted as "burst-time emission."

GRB Designation	BATSE Trigger Number	BATSE Trigger Time (UT s)	Search Start Time (UT s)	Search End Time (UT s)	Live Search Time (s)	Results
940217	2831	82962.07	79185.5	18606.7	10616.9	peaks pre, during, and post; burst-time emission
990104	7301	57753.7214	53915.4	79769.3	14123.2	peaks during and post; burst-time emission
990123	7343	35216.1214	30923.5	56974.0	15368.4	peaks during and post; burst-time emission
950425	3523	919.218	83396.2	22784.7	13533.1	peaks during; burst-time emission
980923	7113	72647.5214	68269.7	7789.23	13336.7	peaks pre, during, and post; burst-time emission
910814	678	69273.000	65416.7	4772.42	12648.5	peaks during and post; burst-time emission
990518b	7575	62325.4974	58197.7	84346.6	14155.9	peaks post
971110	6472	68006.8815	64180.9	85644.0	13041.7	peaks post
941017	3245	37173.938	32961.2	59994.7	16482.4	peaks during and post;

Continued on Next Page...

Table 3.2 – Continued

GRB Designation	BATSE Trigger Number	BATSE Trigger Time (UT s)	Search Start Time (UT s)	Search End Time (UT s)	Live Search Time (s)	Results
						burst-time emission
981203	7247	3552.9934	85790.4	25178.8	11763.7	peaks during and post; burst-time emission
991216	7906	58021.3694	55170.8	80074.5	11993.1	peaks pre and during; burst-time emission
990915	7766	83722.5534	79783.6	21269.2	11141.0	peaks during and post;
970411	6168	35545.8015	31783.6	57572.0	14909.5	peaks pre, during, and post; burst-time emission
990506	7549	41010.9374	37181.1	62969.5	12550.2	peaks post
980203	6587	82028.2575	81598.1	17382.0	12845.1	peaks post
960529	5477	43665.098	39577.2	58189.5	11239.4	peaks during and post; burst-time emission
990803	7695	23375.9294	16341.7	43768.5	15597.6	peaks post
910601	249	69734.508	65130.0	5370.42	16613.2	peaks during and post; burst-time emission
000101	7929	4799.2254	595.67	28481.2	16449.5	peaks pre and post
940526	2994	73205.789	69580.4	8968.8	13631.5	peaks during and post
940301	2855	72637.078	68974.2	7772.8	12812.1	peaks pre, during, and post; burst-time emission
000302	8008	10225.0814	6597.36	30911.2	11337.6	peaks post
970315	6124	56454.2175	51850.9	77999.8	12419.0	peaks pre and post
920902	1886	1736.32	83997.3	23156.3	12058.9	peaks pre, during, and post;

Continued on Next Page. . .

Table 3.2 – Continued

GRB Designation	BATSE Trigger Number	BATSE Trigger Time (UT s)	Search Start Time (UT s)	Search End Time (UT s)	Live Search Time (s)	Results
						burst-time emission
980124	6576	23673.0575	19771.0	45592.2	13762.6	peaks pre, during, and post; burst-time emission
000429	8087	36442.8734	32690.9	58249.9	15827.1	peaks post
990728	7678	39824.8894	35554.0	61768.4	15007.9	peaks during and post; burst-time emission
951219	4039	60679.73	56992.4	82780.8	13729.8	peaks post
920210	1385	35623.789	31784.5	57572.9	16710.8	peaks post
940414	2929	60385.559	55103.1	82169.5	10748.1	peaks post
940817	3128	31215.789	26992.3	53436.0	13303.8	peaks pre and post

3.3.2 Discovery of High-Energy, Post-Quiescent Emission from a Gamma-Ray Burst

Results

Two cases of possible delayed burst emission have been discussed in Appendix A, but neither of them can be conclusively associated with the bursts that precede them. However, the following detection shows strong evidence of being associated with the lower-energy, prompt-phase burst emission. This burst, GRB 990104, did not have emission preceding or following the prompt phase, but instead showed high-energy emission from a post-quiescent burst episode. This emission was not delayed, in that what was found was still coincident with BATSE-detected emission. However, the burst falls into the category of quiescent bursts, and emission in the TASC energy range had never been detected from the post-quiescent episode from such a burst. A description of this burst was published in 2002 (Wren et al., 2002).

GRB 990104 was the second of two bursts detected on January 4, 1999. It was very intense and it was the third on the original list of 100 used for this chapter. Its >300 keV fluence was $(4.12 \pm 0.21) \times 10^{-4}\, ergs\, cm^{-2}$. It is categorized as a burst with a quiescent period because there was an initial 52 s rise in the light curve, then a quiet period in light curves covering 25 keV to 20 MeV for 100 s. After that, there was a second burst period that was even more intense than the first. This second emission episode lasted approximately 100 s in the BATSE energy range before receding to background levels, though most of the emission occurred within a space of about 50 s. The total length of the burst was about 250 s, and its BATSE

T_{90} time was greater than that of 96% of BATSE bursts for which T_{90} is reported.

When GRB 990104 was detected, the EGRET spark chamber was occulted by Earth. The chamber was powered off, so only the TASC and the A-dome were taking data. Both the TASC and the A-dome are omnidirectional, which made it possible for the detection of a burst that was outside the spark chamber field of view (regardless of whether the spark chamber was powered on). Without spark chamber photons, the only way to determine the direction of the burst was with BATSE, which was able to localize it to $l = 224^o.93$, and $b = 24^o.51$. In spacecraft coordinates, the burst was 155^o from normal, placing it "underneath" the instrument.

Figures 3.5 and 3.6 show the rise in spectral rates before and after background subtraction. These peaks were 3.8σ and 17.7σ above background; the latter is the strongest peak detected during the search through the spectral rate light curves for any burst examined for this thesis. The TASC had rate counters with energy thresholds at 1, 2.5, 7, and 20 MeV, so after discovering strong power-law emission in the spectra for those time periods, EGRET ACD rates and TASC rates were also examined. A lossy compression was applied to the TASC rates before transmission to the ground, so they information they provide is somewhat crude. Figure 3.7 is a plot of the BATSE 25-60 keV light curve along with that of the ACD at >100 keV, and the TASC rates at >1 MeV, >2.5 MeV, >7 MeV, and >20 MeV. Emission in all the light curves is coincident, and there is evidence in the TASC rates for emission at least as great in energy as 7 MeV. There is a hint in the TASC counters that there is emission 84 s after the BATSE trigger, but the rise in rates is not confirmed in

the BATSE light curve, and no emission could be detected in TASC spectra for that time period. The spectra in Figures 3.8 and 3.9 show that emission was even greater than 7 MeV during the first detectable rise in spectral rates, which began 152 s after the BATSE burst trigger. This first spectrum had an index of 2.66 ± 0.17 and a normalization constant of 0.64 ± 0.12 photons cm^{-2} s^{-1} MeV^{-1} when fit over a 1-20 MeV range. The second has an index of 2.52 ± 0.03 and a normalization constant of 2.68 ± 0.12 photons cm^{-2} s^{-1} MeV^{-1} when fit over a 1-100 MeV range. The former spectrum showed clear evidence of emission through 10 MeV, with weaker evidence of emission to 20 MeV. Fitting it over 10 or 20 MeV did not yield different results. The second spectrum showed clear evidence of emission past 50 MeV, with weaker evidence that emission was detected out to 100 MeV. Fits over 1-20 MeV and 1-100 MeV yielded consistent results.

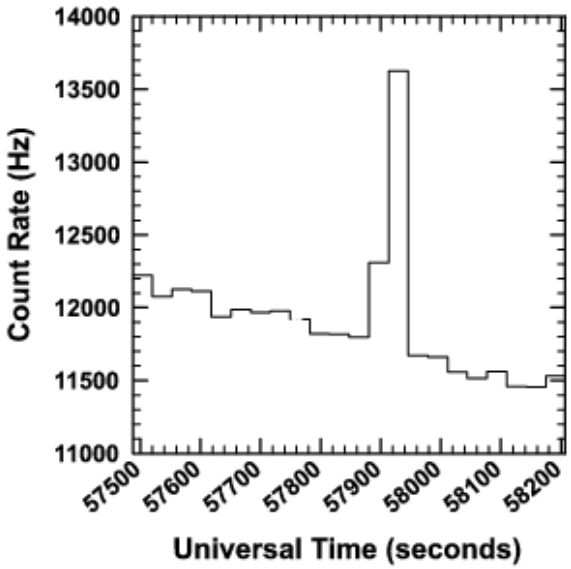

Figure 3.5: Spectral rates light curve for GRB 990104. The gap in rates is where the TASC was taking burst mode spectra and 32.768 s spectra were not being accumulated. From Wren et al. (2002).

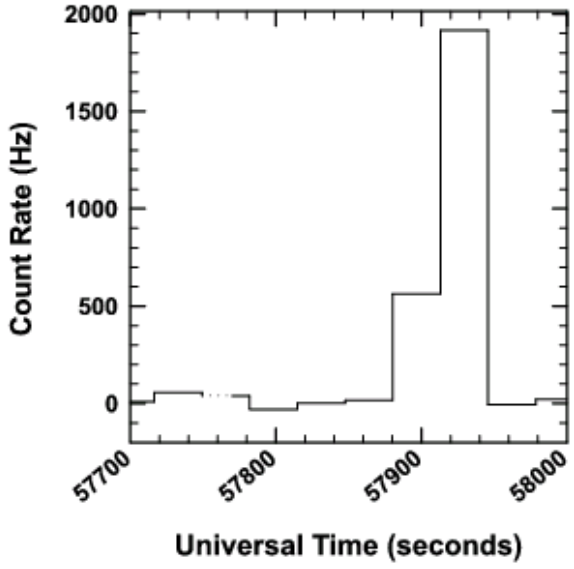

Figure 3.6: Residual spectral rates for GRB 990104. Background has been subtracted. From Wren et al. (2002).

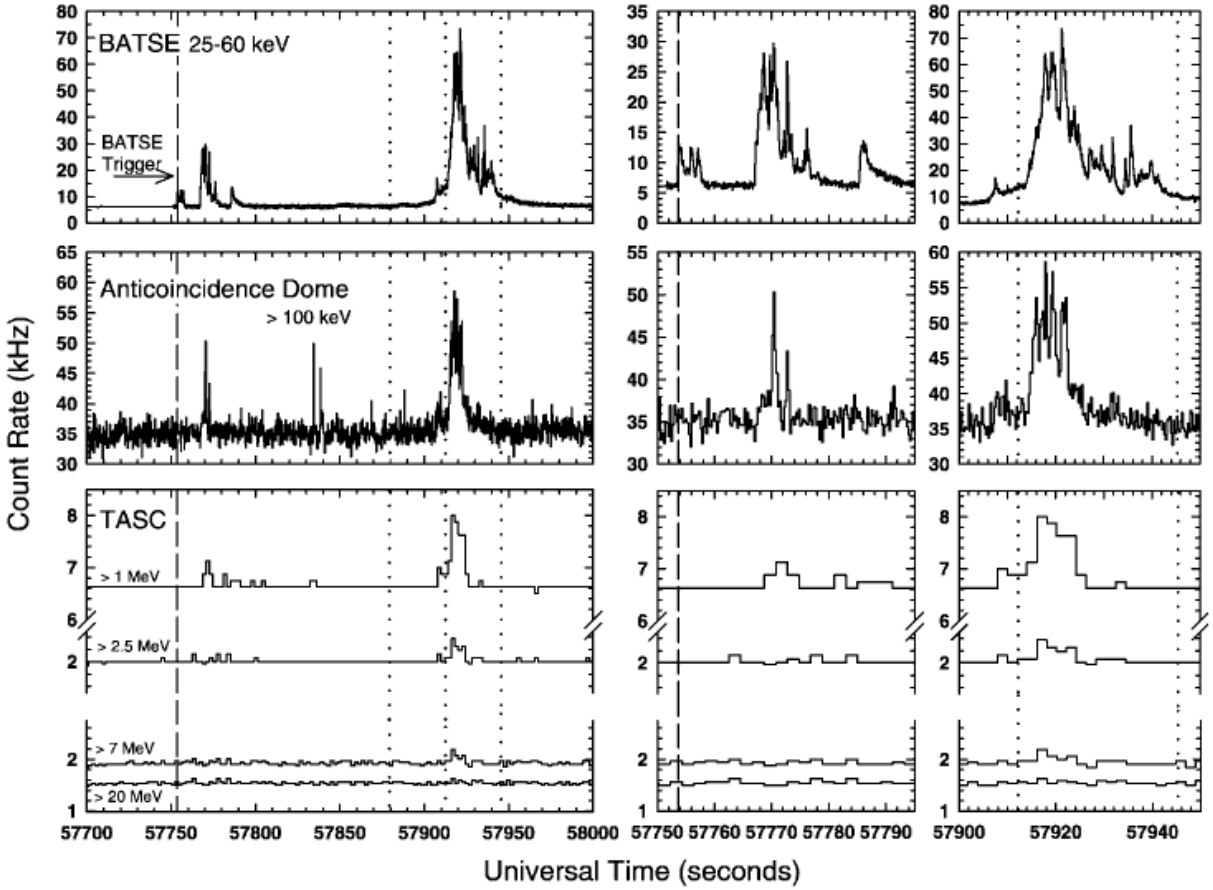

Figure 3.7: BATSE discriminator rates, EGRET ACD rates, and TASC housekeeping rates for GRB 990104. The dashed vertical line is at the time of the BATSE trigger. The dotted vertical lines mark the starting and stopping times of the TASC 32.768 s accumulation intervals. The spectra in Figures 3.8 and 3.9 correspond to those intervals. A quiescent period of 100 s is visible between the emission episodes.From Wren et al. (2002).

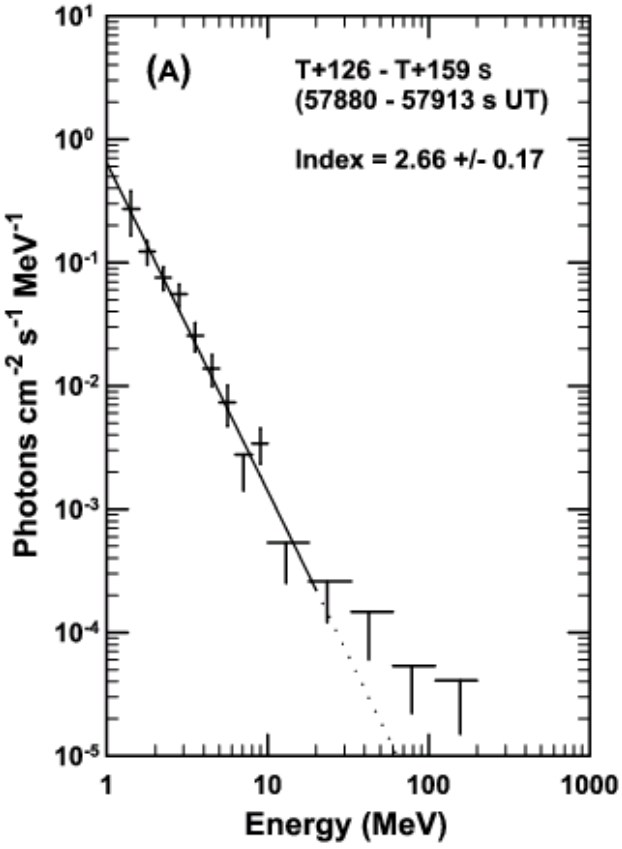

Figure 3.8: First of the two spectra covering the post-quiescent burst emission episode. Evidence of emission extends past 10 MeV, and the data could be fit up to 20 MeV with a result consistent with a 1-10 MeV fit. This spectrum was accumulated over the period from 57880–57913 s UT, which began 126 s after the BATSE trigger. From Wren et al. (2002).

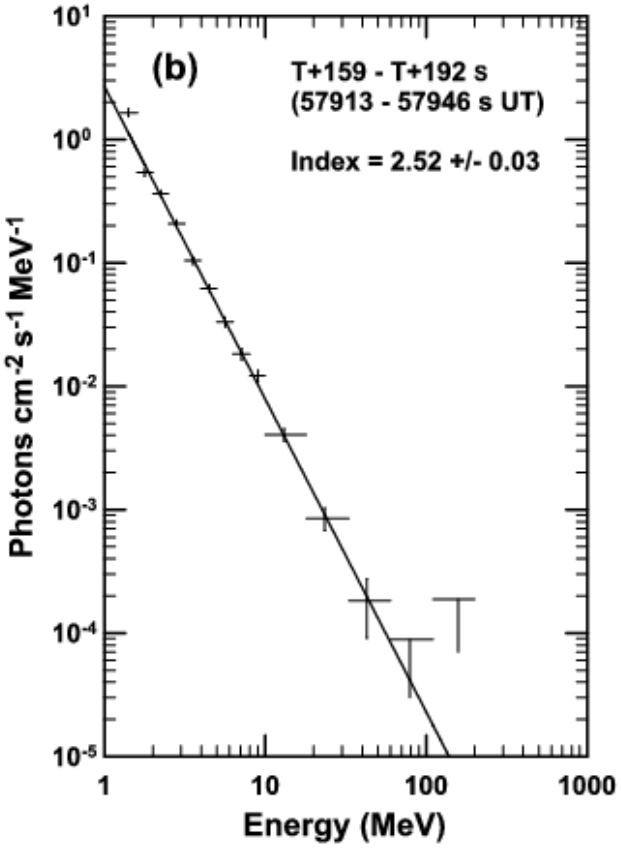

Figure 3.9: Second of the two spectra covering the post-quiescent burst emission episode. Evidence of emission extends past 50 MeV, and the data was fit up to 100 MeV with a result consistent with a 1-20 MeV fit. This spectrum was accumulated over the period from 57913–57946 s UT, which began 159 s after the BATSE trigger. From Wren et al. (2002).

The Significance of GRB 990104

This burst is significant for more than one reason. It is one of the longest, most fluent BATSE-detected bursts, and has a light curve with a long quiescent period. It is also the first detection of high-energy emission from a post-quiescent burst emission episode, and had one of the highest energy TASC-measured spectra yet reported. The high-energy spectra were accumulated for periods that coincided with lower energy (keV) emission that was approximately the same length as the quiescent period that preceded it. The first of the two spectra began accumulating during the BATSE quiescent period, and continued to accumulate as the BATSE light curve rose. The second spectrum began and ended during the most intense of the keV emission. No high-energy spectrum corresponded to the final tail of the BATSE emission, but the BATSE emission was also very weak during that period. It is apparent from the TASC count rates that the length of high-energy post-quiescent emission greater than 1 MeV lasted at least 24 s, and the lossy compression of TASC rates may have masked signs of more emission. It is clear from rates and spectra that high-energy emission did coincide with low-energy emission, and at a minimum, was detectable for $\sim 1/4$ the time that BATSE recorded low-energy emission.

The length of the emission period is relevant because of an observed one-to-one correlation between the length of the quiescent period and the post-quiescent emission (Ramirez-Ruiz and Merloni, 2001). It was argued that this relationship is only possible in the internal shock scenario (Fenimore and Ramirez-Ruiz, 2000), either due to an internal engine that goes dormant for a period or time, or because

of shocks of the same or decreasing Lorentz factor (Ramirez-Ruiz et al., 2001). For GRB 990104, the length of the low-energy post-quiescent emission is about the same length of the quiescent period that preceded it. The intensity of the high-energy emission clearly changes over time very similarly to the low-energy emission. The high-energy emission is consistent with a one-to-one correspondence between its length and that of the quiescent period the precedes it, though the emission falls below the TASC count rate sensitivity during the tails of the lower energy emission. The similar low- and high-energy light curves indicate that the low- and high-energy emission were likely caused by the same shock mechanism, whether it was internal or external. Since the low and high-energy emission do appear to be caused by shocks in the same location (internal or external), it is likely that the mechanism responsible for the quiescent period in the low-energy emission is also responsible for the quiescent period in the high-energy emission. In order to determine what the mechanism is, prompt X-ray observations may be necessary, because a quiescent period in the X-ray light curve may indicate dormant central engine (Ramirez-Ruiz et al., 2001).

Although it was among the very brightest of the BATSE bursts, GRB 990104 was overlooked by other researchers probably because its initial burst period was not strong, and previous searches through TASC emission were based on an assumption that high-energy emission would only be found during a low-energy prompt emission period. It is true that the 990104 high-energy emission happened to be coincident with low-energy emission, but the existence of the second emission episode was not

known in advance. Rather, it was discovered because of the time-extended search performed for this thesis.

Discovering this emission validates the basic premises upon which this search is based. Firstly, ordering by fluence in the BATSE highest-energy channel was a reasonable indicator of which bursts were likely to have stronger high-energy emission. Secondly, developing and using the TASC spectral rates for a significant rise is a valid approach for detecting high-energy emission candidates. Thirdly, the combined approach of visual inspection and power-law fitting of a candidate spectrum worked. Finally, it was worthwhile to search for extended periods of time after a burst trigger. Without the latter assumption, especially, this burst would not have been discovered. Furthermore, the discovery of this emission suggests that GLAST is likely to detect high-energy emission from gamma-ray bursts minutes or more after a burst trigger, and time-extended observations may yield other unexpected high-energy phenomena.

3.3.3 Searching for High-Energy Emission from Other Quiescent Bursts

After finding high-energy, post-quiescent emission from GRB 990104, several additional bursts that were known to have extended quiescent periods in the BATSE energy range were examined. These bursts are an additional set not originally found in the list of 100; they are listed in Table 3.4. A focus was placed on the few bursts that had quiescent periods lasting tens of seconds, because the possibility existed that the high-energy emission would last longer following a long quiescent period.

Also, the longer the post-quiescent emission, the more likely the TASC signal, integrated over 33 s, would be high enough above background for detection. Though there were several hundred bursts in the BATSE catalog with periods that met some definition of quiescence, those with long quiescent periods were infrequent, so the list was limited to only 8 bursts. One of these had incomplete data during the burst, so it could not be studied. The resulting list of 7 bursts were searched for evidence of high-energy emission. No additional evidence of high-energy emission was found, but this is not surprising given the relatively low > 300 keV fluence from each of these bursts. High-energy emission may have been present from the post-quiescent emission episodes, but if so, it was too weak to detect.

3.4 Summary and Conclusion

A method of performing an efficient, uniform search through EGRET TASC spectra for signs of high-energy emission preceding or following bright gamma-ray bursts was developed and implemented. The search was designed to be sensitive to emission that was detected over 32.768 s periods of time, and that fell within a ∼1-250 MeV energy range. The method was successful at detecting burst emission, and it uncovered one instance of very fluent post-quiescent emission that had been overlooked by previous searches. This was the first discovery of significant post-quiescent, high-energy burst emission that was coincident with lower-energy BATSE emission. This method also turned up the possibility of delayed emission in two cases that could not be ruled out, but also could not be definitively associated with gamma-ray bursts. However, because no conclusive evidence of delayed emission was found, an attempt was made to estimate the sensitivity of the search for the purpose of calculating an upper limit on how much pre or post-burst emission may have been present. That study is reported in Appendix A. Appendix B contains an assessment of the search procedure sensitivity.

GRB Designation	BATSE Trigger	Midtime (UT s)	BATSE T_{90} (s)	Approximate Quiescent Time (s)	BATSE $>$ 300 keV fluence (ergs cm^{-2})	Result
950608	3634	81272.5	142.048	50	2.6485e-05±2.1684e-06	no evidence
950711	3663	13789.1	204.416	90	1.7971e-05±1.6349e-06	no evidence
911005	869	27464.8	110.464	60	1.0594e-05±1.1039e-06	incomplete data
970815	6335	43624.4	149.184	60	5.0671e-06±1.6612e-06	no evidence
911016	907	39694.2	158.080	50	1.9172e-06±6.1636e-06	no evidence
960530	5478	62299.1	296.960	230	2.3373e-06±1.4856e-06	no evidence
911227	1235	3953.3	189.952	110	9.3166e-06±5.8794e-07	no evidence

Table 3.3: Long bursts with quiescent periods that we searched for high-energy emission after discovering high-energy, post-quiescent emission from GRB 990104. The BATSE T_{90} times are given, as are the approximate lengths of quiescent periods at BATSE energies. No evidence for high-energy emission was found, but this is not surprising considering the relatively low fluence for these bursts.

Chapter 4

GLAST Trigger Studies

4.1 Introduction

Chapter 2 described LAT detector systems, including the triggering and DAQ, which take the data and process it to some extent. After processing the data, the LAT transmits its data to relay satellites, and they transmit the data to the ground. There are limits on the amount of data that can be transmitted to the relay satellites in a given amount of time; although the data link is at 40 mbps, the LAT will not be in constant communication with relay satellites, so the allocation will be 1.2 mbps averaged over time. The LAT cannot transmit more data than the downlink allows, so it is important to have an accurate estimate of how much data the satellite will generate. Given that the average event is expected to be 3000 bits in size after packaging, GLAST can tolerate up to 400 triggers per second (the trigger rate).

Regardless of whether the event that causes the LAT to trigger is a cosmic ray or a gamma ray, it produces data that must be processed. Given the downlink restrictions, the processing involves determining whether the event is more likely a gamma or a background event. The goal is to reduce the background rate (which

dominates the trigger rate) to the level that the downlink can tolerate, while keeping as many gamma rays as possible. This filtering of events is discussed in detail in Chapter 5, but here the prerequisite issue of determining the trigger rate is considered. If the trigger rate is not known, it is not possible to determine what fraction of events need to be rejected in the filter.

The types of triggers considered are the primary types mentioned in Chapter 2. The tracker 3-in-a-row trigger is the most common, followed by the CAL LO and the CAL HI. Because this thesis is concerned with the detection of gamma-ray bursts, not heavy ions, and because the heavy-ion (CNO) trigger rate is expected to be low, it is not focused on in these studies. The relevant triggers are those from the tracker and CAL.

4.2 Limiting the Trigger Rate

The LAT will employ two methods of rate reduction onboard the instrument, each at a different location along the signal path. One of the methods, described in detail later in this chapter, is that of a *hardware trigger veto (HTV)*. This is a method of reducing the trigger rate by looking for patterns in the trigger primitives that suggest that the signals are caused by a cosmic ray. Hardware trigger vetoing approaches will be most useful during periods of high background. Although hardware trigger vetoing approaches must be relatively simple, because they rely on trigger primitives, they are advantageous in that they occur at the trigger level, so they are able to prevent the instrument from triggering and reading out the instrument data.

Hardware trigger vetoing methods work to screen out background while reducing instrument dead time.

The second method of rate reduction, event filtering, is done after triggering. Onboard filtering will occur after the instrument as triggered and data have been read out. Once the data have been sent to the EPUs, they are sent through the Onboard Filtering algorithms that are discussed in the next chapter. These algorithms determine whether the event was more likely background or a gamma ray. If the former, the event is eliminated from the data stream and not telemetered to the ground. If the event is judged to have been a gamma-ray candidate, the data are compressed and telemetered to the relay satellites for transmission to the ground. Once on the ground, data are sent through more sophisticated processing before being made available for science analysis. Ground processing makes use of the computing resources not available in space, and it is able to remove most of any remaining background events that were not previously eliminated from the data stream.

4.3 Using GlastSim to Characterize LAT Performance

It is true that the LAT trigger rate will only be known with certainty once the satellite is in orbit and taking real data, but it is possible to use GlastSim to get a good estimate of likely trigger rates. A primary goal of studying the trigger rates is to determine the input to the Onboard Filtering software, which then allows one to determine performance requirements for the Onboard Filter. In order to do this, it

is necessary to simulate an environment that the LAT will encounter when it is in orbit.

4.3.1 Functional Components of GlastSim

Simulating the LAT, its environment, and its response involves several components. A detailed description of the LAT geometry is encoded in XML, with technical drawings as the basis. The materials from which each physical component are made are contained in the description. Simulated particle fluxes are generated using the flux descriptions and the Monte Carlo portion of GlastSim code. Characteristics – energy, direction, flux ID, etc. – of each generated event (particle) are stored in ntuple format. When simulated particles intersect the satellite, the physical interaction between the particle and the satellite material is modeled by the widely used GEANT4 (GEANT4 web page, 2005) detector response modeling software developed at CERN. Interactions of different particle types with different materials are described by high energy physics theory, models, and parameterizations, the later of which are based on experiment.

As the instrument responds physically to the incident particle, the simulated detector systems also respond as they will when the LAT is operational. Silicon strips and ACD tiles are hit, and showers develop in the CAL. The instrument response is digitized, triggers are initiated, and events are packaged in a way that models what will happen when a particle interacts with the physical LAT. The packaged event is even passed through some of the same event processing code that will be used onboard the satellite. Finally, event reconstruction, or recon, algorithms

are applied to the digitized data. Particle tracks are found and the event energy is more precisely determined. This models the first steps of the process that will occur when the data are downloaded to the ground for analysis.

GlastSim was verified by the SLAC beam tests, which will be repeated in 2006. Details of the LAT's construction are continuously monitored and updated so that the simulation's instrument description corresponds to the LAT design. The input fluxes also accurately represent the space environment. The next sections include descriptions of these fluxes, how they were developed, and how they were used to study the LAT's performance.

4.3.2 Simulated Fluxes

For the purpose of studying the background rate, one can calculate an average orbital flux of cosmic rays, and then also simulate what happens during orbital variations. For this purpose, the collaboration created a library of fluxes, in addition to a facility that allow users to create their own simple sources by describing them in a few lines of XML. The collaboration's general approach for developing background fluxes was two pronged. One track was to review and compare results reported in cosmic-ray literature, and then to develop analytic functions that can accurately reproduce those results. Another approach was to incorporate existing programs that were developed by others who specialize in near-Earth radiation. The GlastSim flux package can either use the analytic functions to guide the Monte Carlo simulation in the creation of background fluxes that conform to empirical results, or draw on the external packages to generate background events.

The composite source used for most of the background studies is aptly named "backgndavgpdr," meaning that it models the set of average background fluxes that the LAT will encounter in orbit. The suffix, "pdr," is historic; it stands for "Preliminary Design Review," because the fluxes were originally created for early LAT design studies. The backgndavgpdr flux is actually a combination of five different fluxes, some of which are in turn composed of different fluxes themselves. Each of the five main component fluxes are models of background sources that are well known in the near-Earth space environment. The orbital environment for a satellite like GLAST is populated with many types of particles over a wide energy range, and each of these must be accounted for. The types of cosmic rays range from nuclei of low Z to high Z, to albedo photons from Earth, to electrons and positrons both from galactic sources and Earth albedo (Tylka et al., 1997). The composition of fluxes varies with orbital altitude and inclination, and with solar activity.

The average background flux is used to study the LAT response during the most common orbital conditions. Its use provides a measure of the average trigger rate, which allows us to determine the necessary degree of event filtering. It is not as useful for testing the LAT electronics and onboard software, however. For that purpose, a source that simulates the maximum background conditions and thereby puts a more strenuous load on the data systems and onboard software is desirable. The backgndmaxpdr serves this purpose, and it is described shortly.

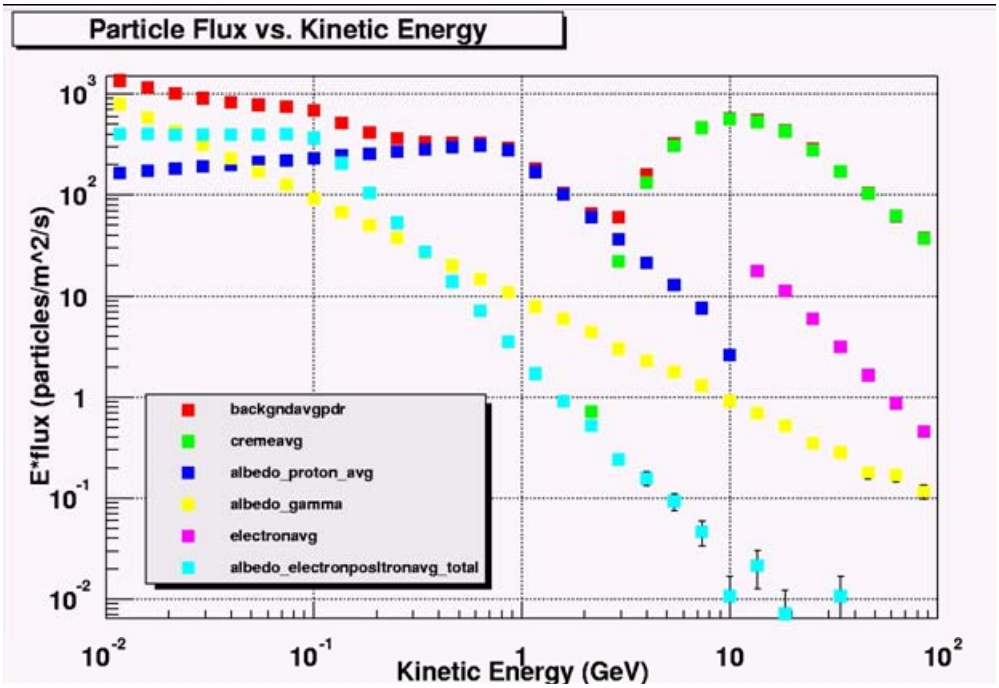

Figure 4.1: Average background fluxes used in GlastSim. The red "backgndavgpdr" is the sum of its component fluxes, also shown. These components (explained in the text) include cosmic protons and electrons, albedo protons and electrons, and albedo gamma rays.

Background Average Fluxes

GlastSim's backgndavgpdr flux us composed of composite fluxes that model galactic nucleons, galactic electrons, albedo protons, albedo electron-positrons, and albedo gamma rays. Figure 4.1 shows a plot of these fluxes as simulated in GlastSim. Each of these will be described in turn, beginning with the galactic nuclei.

The code describing nuclei is among the most complex, and was first developed by a team of people at the Naval Research Lab (led by Dr. Jim Adams). The package was dubbed the "Cosmic Ray Effects on Micro-Electronics," or the CREME suite of programs, and it was updated in 1996. It is CREME96 that was adapted for use within GlastSim. CREME96 is actually several programs that can be used to

create numerical models of the near-Earth cosmic-ray background, and it is publicly available on the internet (Tylka et al., 1997; CREME96 web page, 2005). With these programs, it is possible to model galactic cosmic rays from Z=1 to Z=92 under normal and solar-flaring conditions for a user configurable satellite orbit. The code is empirically based, using space weather models and data from a variety of cosmic-ray experiments (see references within (Tylka et al., 1997)). It is an industry standard, and is widely used by NASA, commercial satellite programs, and the Department of Defense.

CREME96 allows the user to specify the orbital inclination and altitude, and rely on the software to modulate the known cosmic-ray spectrum with the solar wind, filter it through the Earth's magnetosphere, and give the appropriate average orbital rate (Grove, 1997). Comparisons of the CREME96 model's prediction and measured data for galactic nucleons are found in Figures 4.2 and 4.3.

The CREME flux does not contribute much to the total until the energy is at about 2 GeV due to the geomagnetic cutoff. The cutoff describes the inability of charged particles to penetrate the Earth's magnetic field beyond a certain point (Lemaitre and Vallarta, 1933). That point is determined by the particle's magnetic rigidity, which is defined as its momentum per unit charge. Particles of low magnetic rigidity will be deflected before particles of higher rigidity, so those with greater rigidity will penetrate more of the magnetosphere. Each point in the magnetosphere has a threshold below which particles of a certain rigidity and incoming direction cannot arrive; this is the geomagnetic cutoff for that point.

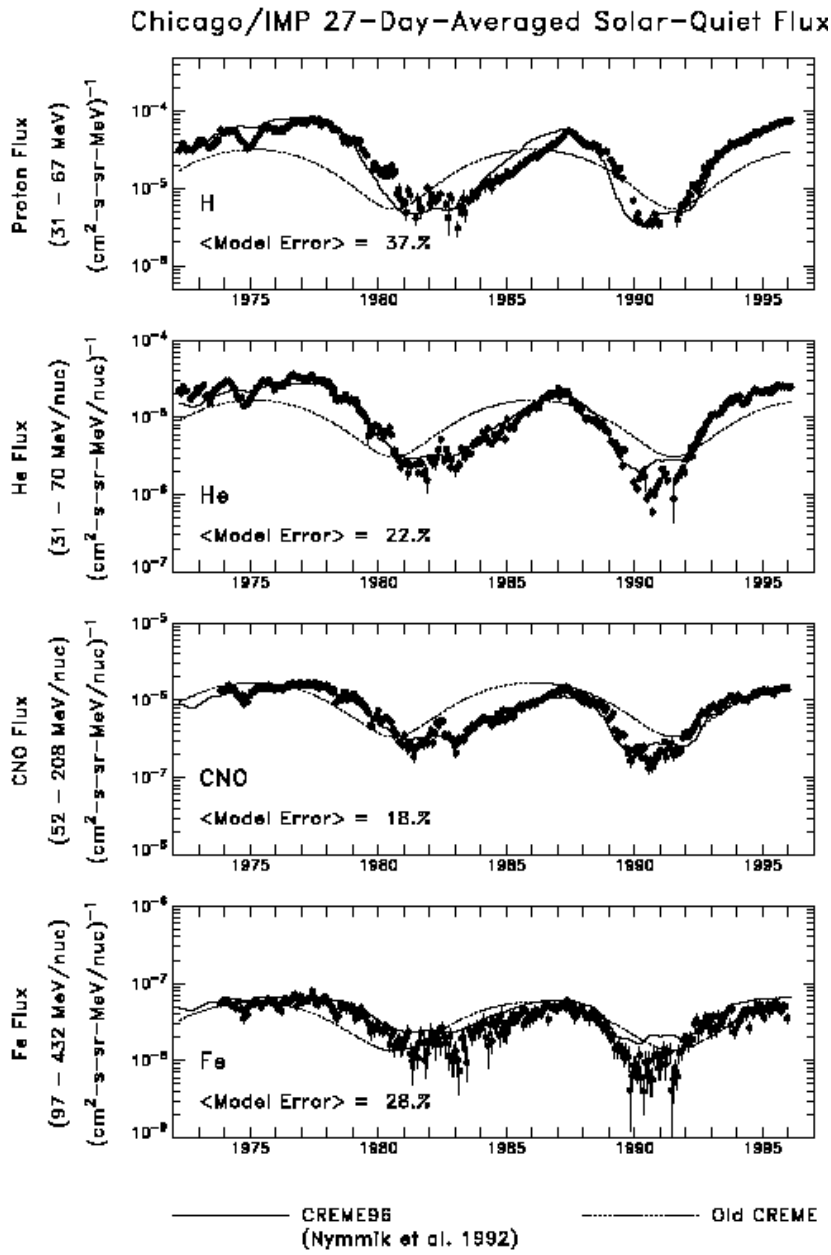

Figure 4.2: CREME96 model predictions for solar-cycle variations (solid curve) compared to galactic cosmic-ray data from the Chicago IMP-8/CRT experiment (Watts, 1971). The dashed line that does not agree as well with the data is from an older version of the CREME code. From (Tylka et al., 1997).

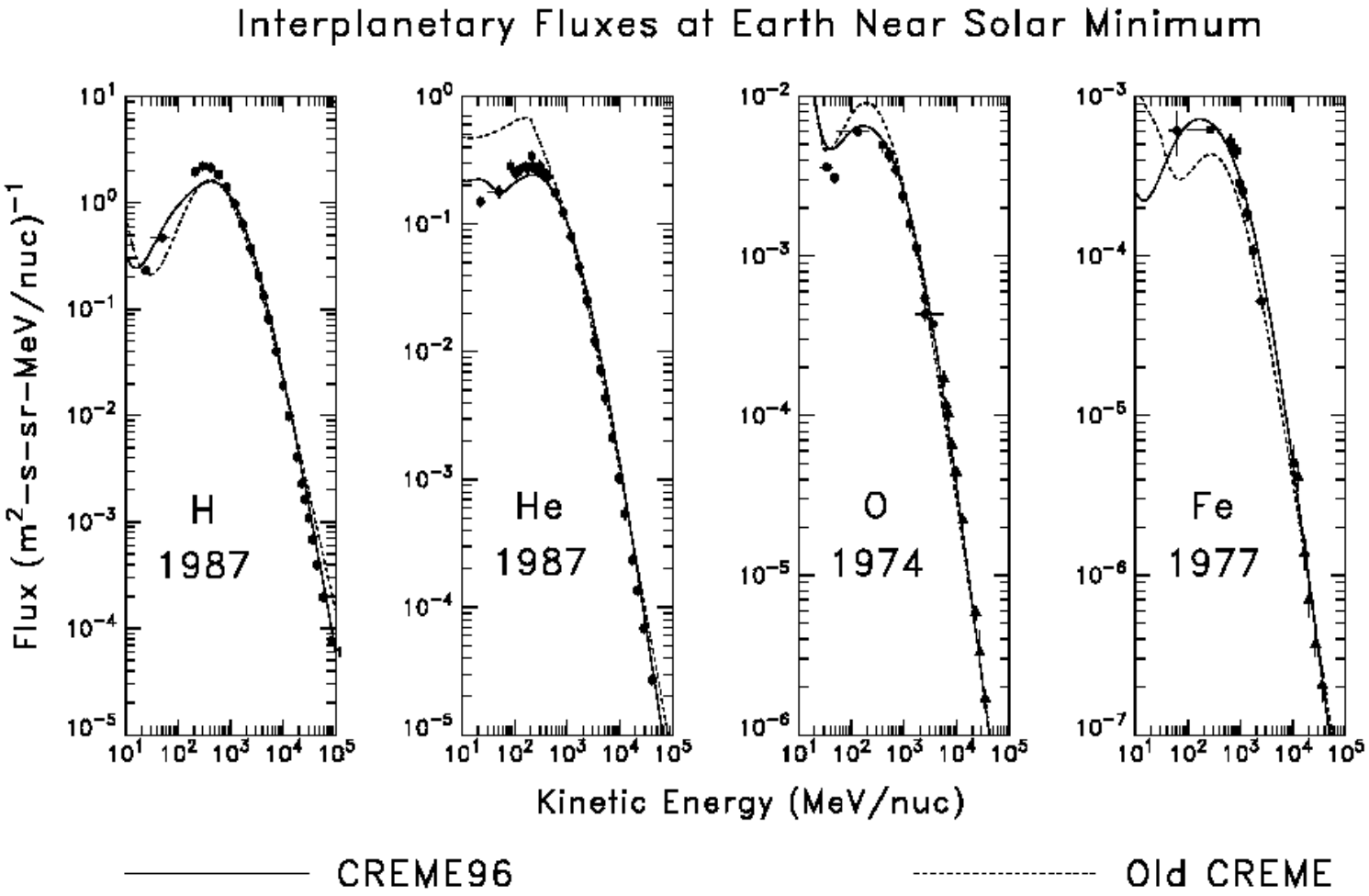

Figure 4.3: CREME96 model predictions for solar minimum spectra (solid curve) compared to galactic cosmic-ray data from the Chicago IMP-8/CRT experiment. The dashed line that does not fit the data as well is from an older version of the CREME code. From (Tylka et al., 1997).

Also exclusively at high energy (above 10 GeV), is a source named "electron-avg." This flux represents the galactic electrons mentioned earlier. In GlastSim, the galactic electron description is based on a differential photon spectrum power law cited in a paper, in which the authors describe observations of cosmic-ray electrons and positrons detected by the High-Energy Antimatter Telescope (HEAT) (Barwick, 1998). The HEAT results provide the most up-to-date data on this flux.

In Figure 4.1, the reader will note that there are several fluxes that heavily contribute at the lower energy range. Each of these is a different type of albedo source, which means they are no longer directly attributable to galactic radiation, but instead are due to cosmic-ray interactions in the Earth's atmosphere. Weakest at 10 MeV, but dominant above 200 MeV, is the average albedo due to protons. An important distinction made in the cosmic-ray literature is between splash albedo and reentrant albedo (Treiman, 1953). Splash albedo is very much what it sounds like: upward moving protons caused by energetic nuclei impinging on the Earth's atmosphere and causing particle showers. Splash albedo particles get trapped in the Earth magnetic field and travel to the opposite hemisphere where they reenter the atmosphere at the same geomagnetic latitude. Albedo protons can be distinguished from galactic protons because the former have a lower rigidity than the geomagnetic cutoff, so they could not have arrived from outside the magnetosphere.

There have been several experiments that measured the albedo proton flux at different locations; the most recent of these are BESS (Sanuki et al., 2000) and AMS (Alcaraz et al., 2000a,b). The two experiments were flown about the same time, but

measured the flux at different locations (BESS near the geographic north pole, and AMS at several positions in low-Earth orbit). However, their results agree very well. This is fortunate, because the GlastSim flux programmers decided to use AMS as the primary guide, partially due to the fact that AMS had data that showed the flux dependence on geomagnetic cutoff. Of course, the data were not comprehensive enough to provide information that would allow precise modeling at every possible orbital position of the LAT, so an average flux was created, with the understanding that there would be some uncertainty in the resulting rate. However, whenever an uncertainty was unavoidable, the decision was to err on the high side, making sure that if rates would be overestimated rather than underestimated. In fact, an internal LAT study concluded that the GlastSim albedo proton flux overestimates empirical data in certain latitude bins (Tylka, 2000). Even so, as is discussed in the next Chapter, when analyzing the software that filters events, it is understood that the wise course of action is to set a performance goal, but also allow for a healthy margin.

Two fluxes remain, and they are both classified as albedo. Figure 4.1 shows an albedo source that is particularly strong in the 10-100 MeV range and then drops off sharply, making it the weakest flux above a few hundred MeV. This source is composed of albedo electrons and positrons, and it is based on AMS data. The general form is of a broken power law with a differential photon spectral index of -1.0 up to 100 MeV, and an index of -3.2 above that energy.

The remaining flux is that of albedo gamma-rays, which is broken up into

two component fluxes in the GlastSim XML source files. Like each of the fluxes previously described, this is also based on experimental data, this time from the SAS-2 mission (Thompson et al., 1981). Most of the albedo gammas come from the limb of the Earth, which is seen as a ring at 113^o from zenith, and is seen as an oblate shape when the LAT is rocked away from zenith. In the simulation, the ring is defined to be between 105^o and 125^o from zenith, and its profile is that of a power law with a differential photon spectral index of -2.4 between 10 MeV and 10 GeV. In GlastSim, this albedo source had its own designation. The emission is normalized to agree with SAS-2 data, and one simplification is made. In reality, the Earth's magnetic field deflects primary cosmic rays (primarily protons) such that there is an East-West anisotropy that is dependent on the position on Earth and the charge and momentum of the primary particle (Johnson, 1933; Alvarez and Compton, 1933). Because of the polarity of the magnetic field, positively charged particles appear to arrive more intensely from a Westerly direction. Because interactions of primary cosmic rays in the atmosphere are what create albedo gamma-rays, the East-West effect is observed with that source also. In GlastSim, the East-West effect is accounted for by calculating an average value for all 360 degrees in azimuth, a sufficient approach for purposes of estimating background.

For the purposes of this dissertation, it is important to distinguish between the albedo gamma source that describes the limb, and the second component of the albedo gammas, called "albedo upwards." From orbit, albedo photons appear to arrive most intensely from the limb of the atmosphere, because the thickness of

the atmosphere is greatest along that line of sight. In contrast, the atmosphere is thinner long lines of sight going from the satellite to the atmospheric surface below. The initial model of albedo gammas only simulated the brighter limb flux. Later, the albedo_upwards flux was created, and its addition required some adjustments to Onboard Filtering tactics (which are described in the next chapter). Again, the data that the source is based on are published (Thompson et al., 1981), and they are represented in the XML by three angular bins from 115^o-132^o, 132^o-157^o, and 157^o-180^o from zenith. From an onboard filtering standpoint, these albedo are a challenge to remove, but it is possible to reduce their corresponding trigger rate substantially.

Background Maximum Fluxes

Many of the same fluxes that go into the average background are also found in GlastSim's simulation of the maximum background that the LAT will encounter in orbit. However, these same sources must be simulated at their extreme, rather than their average or "normal" intensities. For this purpose, a composite flux known as "backgndmaxpdr" is found in the GlastSim source description, and it is described here.

There is actually one flux that remains completely unchanged when considering the maximum case, and that is the albedo gamma source. The flux from these gammas is not expected to vary significantly, so their intensity is not scaled. The rest of the albedo sources, consisting of protons and electrons (along with their positron counterparts), are known to vary in intensity with orbital position. Passing through

areas of dense magnetic field lines is predictable, and this effect is measured and incorporated into the simulation by hard coding values that will be present when the LAT is at an orbital position that gives it the worst possible background due to its position. All of these values were extrapolated from the same AMS data mentioned above.

What is less predictable are the effects of solar modulation (flares and the 11 year solar cycle), but these things can also be estimated. To perform the estimation of the impact of solar modulation, GLAST scientists used the CRRES/SPACERAD Heavy Ion Model of the Environment (CHIME) software, which is a modern suite of code that reproduces effects of solar modulation especially well in the near-Earth environment (Chenette et al., 1994). It is based on data taken by the Combined Release and Radiation Effects Satellite (CRRES), and corrects some deficiencies in CREME programs. The GlastSim flux team used CHIME to simulate what would happen during a solar minimum, when trapped ions are at their highest. CHIME can be used to simulate galactic electrons, in addition to the cosmic-ray proton rate, over the course of the solar cycle. However, the effect of solar flares is not accounted for in the GlastSim simulation, because their occurrence is relatively infrequent.

4.3.3 GlastSim Ntuple Output and ROOT Analysis

For any LAT analysis, such as the tower crossing problem, for example, it is necessary to understand how the instrument responds to input. The LAT collaboration has approached this issue in a manner common to particle physics experiments on the ground. That is, to generate a set of quantities for each event in an ntuple

format, such that each event can be examined individually or in aggregate (often by histogramming various ntuple entries). This statistical approach to analysis requires the user to generate large samples of data with the Monte Carlo simulation, and the facility for doing that is very flexible.

The GlastSim ntuple, often referred to as the "MeritTuple," has quantities derived from every aspect of the simulation. There exist quantities that describe the Monte Carlo event (energy, direction, etc.), there exist quantities that describe the instrument response (where it was hit, how much energy was detected), there are entries that describe the orbit and telescope orientation, and there are entries that describe reconstruction efforts that will be performed on the ground (tracking, energy corrections, etc.). This makes for a very large set of data for each event, and it can all be analyzed with a high energy physics analysis package known as ROOT (ROOT web page, 2005).

ROOT is an object-oriented framework for doing physics data analysis, so it contains facilities for histogramming, curve fitting, graphics, and interactive data manipulation, among other things. It also contains a C++ command line interpreter that allows one to write macros in C++ and run them in real time without having to compile the code first. Because it is written in C++, ROOT can be integrated into C++ code, as it is in GlastSim. The bulk of the following analysis work was performed with ROOT, and most of the plots that follow were also generated with ROOT.

4.4 Background Trigger Rate Studies

Each of the simulated background fluxes were described earlier in this chapter, and here the trigger rates due to these fluxes are examined. Again, there were several reasons for wanting to understand the trigger rates in orbit. It is necessary to know if the LAT hardware and electronics can respond fast enough to take data resulting from these fluxes, and if not, the impact must be understood. In addition the onboard event filtering software has to be able to process the incoming data efficiently and effectively. It must filter events quickly and it must do it correctly, meaning that gamma rays must get through the filtering process. The first step towards refining the filtering process is characterizing the background. Both the average and maximum background were studied, and some work was done to help the flux group verify that their transition from older code to a rewrite was done correctly.

4.4.1 Results of Trigger Studies

The Trigger Rates

The first version of GlastSim (pdrApp) underwent major upgrades, including the move to GEANT4 from a different particle-matter interaction model (Gismo (Breakstone, 1994)). After the upgrade it was necessary to verify the simulation output, so that task was undertaken. Analytically calculated integrated fluxes for the backgnd-maxpdr source showed excellent agreement, indicating the GlastSim flux description was correct. However, it was found that the trigger rates were lower than pdrApp's

for most of the component fluxes (see Table 4.1), which suggested an implementation problem. Some programming errors were fixed by the responsible collaboration members, and the results were examined again. The discrepancy had been reduced (see Table 4.2), but not eliminated. The overall drop in the maximum background trigger rate when moving from pdrApp to GlastSim was 4.9±0.8%, and was 11.7±0.7 for the average background (Table 4.3).

Possible reasons for the rate decrease were investigated, beginning with a study of GlastSim's implementation of the tracker digitization[1]. The tracker noise occupancy (the amount of noise in the tracker) was varied first, and the number of hits in each layer of the tracker was looked at to see how that metric increased or decreased (see Table 4.4). The behavior was as expected: increased noise yielded more hits per layer. The trigger rate was then looked at to determine the effect of more hits per layer, and it was found that the different noise occupancy between pdrApp and GlastSim could not account for the change in trigger rate[2]. Neither was there any significant change in the mean number of tracker strip hits for each event, so it was concluded that the digitization was not a problem.

When moving from Gismo to GEANT4, the value of one of their common parameters was changed, so whether this could have been the reason for the trigger rate drop was studied. In each of the particle-matter interaction packages, the user must specify a range cutoff, which is a length (in mm) beyond which the production

[1]Digitization is the process of converting the analog signals from the instrument readout electronics to digital values that can be interpreted by the event processing units.

[2]The difference between the GlastSim and pdrApp trigger rate was 281 Hz, but changing the noise occupancy only changed the rate by 32 Hz.

Table 4.1: Initial comparison of pdrApp and GlastSim for the backgndmaxpdr source. The integrated fluxes and trigger rate are shown for the backgndmaxpdr source and its components. The trigger rate in GlastSim was significantly lower in GlastSim than pdrApp, even though the integrated input fluxes were almost identical. This seemed to indicate a problem either with GlastSim or pdrApp. Errors in trigger rates are statistical. No errors are reported for the integrated fluxes because those are analytical calculations based on the input flux formulae.

	backgndmaxpdr	chimemax	albedo proton max	albedo gammas	cosmic electrons	albedo electrons positrons
GlastSim						
Flux (kHz/m^2)	9.9	4.2	2.6	0.92	NA	2.2
All Triggers Rate (Hz)	5070 ± 42	46 ± 3	3014 ± 19	215 ± 4	NA	1795 ± 11
Tracker Triggers (Hz)	4813 ± 40	44 ± 3	2790 ± 18	196 ± 4	NA	1782 ± 11
CAL LO Triggers (Hz)	492 ± 13	22 ± 2	434 ± 13	26 ± 1	NA	9.7 ± 0.8
CAL LO & not Tracker (Hz)	257 ± 9	3.0 ± 1.0	223 ± 5	18 ± 1	NA	14 ± 0.9
CAL HI Triggers (Hz)	3.0 ± 1.0	3.0 ± 1.0	0	0	NA	0

Continued on next page...

	backgndmaxpdr	chimemax	albedo proton max	albedo gammas	cosmic electrons	albedo electrons positrons
CAL HI & not Tracker (Hz)	0	0	0	0	NA	0
pdrApp						
Flux (kHz/m^2)	9.9	4.2	2.6	0.92	0.043	2.2
All Triggers Rate (Hz)	12393 ± 61	7133 ± 46	3147 ± 46	221 ± 8	93 ± 5	1798 ± 23
Tracker Triggers (Hz)	11171 ± 58	6311 ± 43	2785 ± 29	206 ± 8	79 ± 5	1789 ± 23
CAL LO Triggers (Hz)	4001 ± 35	3221 ± 31	697 ± 14	19 ± 2	50 ± 4	14 ± 2
CAL LO & not Tracker (Hz)	1222 ± 19	821 ± 16	363 ± 10	15 ± 2	14 ± 2	9 ± 2
CAL HI Triggers (Hz)	18 ± 2	14 ± 2	0	0	4 ± 1	0.3 ± 0.3
CAL HI & not Tracker (Hz)	0.3 ± 0.3	0	0	0	0.3 ± 0.3	0

Continued from previous page.

Table 4.2: Final comparison of pdrApp and GlastSim trigger rates for backgndmaxpdr source. After problems with the GlastSim implementation of the maximum background fluxes were repaired, the agreement was better between GlastSim and pdrApp, though not identical. The 4.9% difference was assumed to be due to changes and improvements to other components of GlastSim code. Errors in trigger rates are statistical. No errors are reported for the integrated fluxes because those are analytical calculations based on the input flux formulae.

	backgndmaxpdr	chimemax	albedo proton max	albedo gammas	cosmic electrons	albedo electrons positrons
GlastSim						
Flux (kHz/m^2)	9.9	4.2	2.6	0.92	0.043	2.2
All Triggers Rate (Hz)	11783 ± 84	7029 ± 65	2911 ± 42	194 ± 11	86 ± 7	1561 ± 31
Tracker Triggers (Hz)	10795 ± 80	6364 ± 62	2643 ± 40	173 ± 10	73 ± 7	1544 ± 30
CAL LO Triggers (Hz)	3057 ± 43	2535 ± 39	431 ± 16	23 ± 4	49 ± 5	19 ± 3
CAL LO & not Tracker (Hz)	987 ± 24	666 ± 20	269 ± 13	21 ± 4	14 ± 3	17 ± 3
CAL HI Triggers (Hz)	139 ± 9	118 ± 8	0	0.6 ± 0.6	20 ± 3	0

Continued on next page...

	backgndmaxpdr	chimemax	albedo proton max	albedo gammas	cosmic electrons	albedo electrons positrons
CAL HI & not Tracker (Hz)	36 ± 5	29 ± 4	0	0	7 ± 2	0
pdrApp						
Flux (kHz/m^2)	9.9	4.2	2.6	0.92	0.043	2.2
All Triggers Rate (Hz)	12393 ± 61	7133 ± 46	3147 ± 46	221 ± 8	93 ± 5	1798 ± 23
Tracker Triggers (Hz)	11171 ± 58	6311 ± 43	2785 ± 29	206 ± 8	79 ± 5	1789 ± 23
CAL LO Triggers (Hz)	4001 ± 35	3221 ± 31	697 ± 14	19 ± 2	50 ± 4	14 ± 2
CAL LO & not Tracker (Hz)	1222 ± 19	821 ± 16	363 ± 10	15 ± 2	14 ± 2	9 ± 2
CAL HI Triggers (Hz)	18 ± 2	14 ± 2	0	0	4 ± 1	0.3 ± 0.3
CAL HI & not Tracker (Hz)	0.3 ± 0.3	0	0	0	0.3 ± 0.3	0

Continued from previous page.

of secondary particles is not computed. Changing the range cutoff back to its original value did not yield any statistically significant change in trigger rate (see table 4.5). After these studies that discovered no problems, the collaboration concluded that the change in trigger rate was likely due to the many code and flux upgrades, but not necessarily because of any problems with those upgrades. Because the discrepancy was never completely understood, when interpreting background rates, one allows for the possibility that there is some uncertainty built into the simulation. However, this uncertainty is not large enough to prevent us from using the background fluxes as a tool for understanding the instrument performance, or for developing methods to reject the background itself.

4.5 Reducing the Trigger Rate

With an average background rate around 3.6 kHz, and the average event size at 3 kbits even after compression, 11 megabits per second would be required to downlink the data. The LAT will have 1.2 megabits per second available, so it is clear the rate must be reduced to a maximum of 400 Hz, or by a factor of 9. There is also some uncertainty in the fluxes that the LAT will encounter, so 400 Hz is considered to be an absolute maximum. It is desirable to get the average background rate significantly below 400 Hz. The maximum estimated background rate approaches 12 KHz, which is even more of a problem; it will require a reduction of at least a factor of 30. The impact that hardware trigger vetoes can have on reducing the trigger rate was studied.

GlastSim	backgndavgpdr	cremeavg	albedo proton avg	albedo gammas	cosmic electrons	albedo e^+e^- average
Flux (kHz/m^2)	4.2	0.94	1.2	0.92	0.01	1.1
All Triggers Rate (Hz)	3626 ± 30	1597 ± 20	1009 ± 16	202 ± 7	10 ± 2	808 ± 14
Tracker Triggers (Hz)	3373 ± 29	1454 ± 19	952 ± 15	179 ± 7	8 ± 1	804 ± 14
CAL LO Triggers (Hz)	794 ± 14	624 ± 13	130 ± 6	28 ± 3	7 ± 1	6 ± 1
CAL LO & not Tracker (Hz)	253 ± 8	142 ± 6	82 ± 5	23 ± 2	2 ± 1	4 ± 1
CAL HI Triggers (Hz)	74 ± 4	67 ± 4	0.3 ± 0.3	0.8 ± 0.4	7 ± 1	0
CAL HI & not Tracker (Hz)	11 ± 2	10 ± 2	0.3 ± 0.3	0.3 ± 0.3	1.3 ± 0.6	0
pdrApp						
Flux (kHz/m^2)	4.2	0.94	1.2	0.92	0.01	1.1
All Triggers	4107	1660	1250	262	25	910
Percent Difference: (pdrApp-GlastSim)/pdrApp*100						
	11.7 ± 0.7	3.8 ± 1.2	19 ± 1	23 ± 3	60 ± 8	11 ± 2

Table 4.3: Comparison of pdrApp and GlastSim for the backgndavgpdr source. After the GlastSim flux implementation was fixed, the GlastSim average background trigger rate was about 12% lower than that of pdrApp. This lower rate was considered to be more accurate than the pdrApp rate. Errors in GlastSim rates are statistical. No errors are reported for pdrApp rates because the original data was not available and they could not be computed. Errors in the percent differences are derived from the GlastSim rate uncertainty alone.

Number of Hits in Layer	chimemax	albedo proton max	albedo gammas	cosmic electrons	albedo electrons positrons
GlastSim Layer 0	4.33±2.87	3.76±3.15	3.69±2.67	5.56±2.18	3.70±3.13
pdrApp Layer 0	4.29±2.83	3.80±3.17	3.78±1.08	7.84±12.44	3.85±3.13
GlastSim Layer 9	5.31±1.76	3.82±3.22	3.71±2.50	7.80±4.96	3.52±2.73
pdrApp Layer 9	5.26±0.90	3.92±3.22	4.05±2.32	11.85±12.97	3.73±2.83

Table 4.4: Hits per layer with the backgndmaxpdr source for GlastSim and pdrApp tracker triggered events. These are the mean number of silicon strip hits in layers 0 and 9 in the old pdrApp simulation and the newer GlasSim when simulated noise in the tracker is the same. The statistically equivalent values indicate that there are no problems with GlastSim digitization algorithms.

Tracker Trigger Rate (Hz) for Backgndmaxpdr Source					
backgndavgpdr	cremeavg	albedo proton avg	albedo gammas	cosmic electrons	albedo e^+e^- average
Original Rate	6430 ± 80	2674 ± 52	162 ± 13	70 ± 8	1571 ± 40
With Changed Cutoff	6336 ± 79	2645 ± 51	155 ± 12	72 ± 9	1586 ± 40

Table 4.5: Changing the Geant4 range cutof: backgndmaxpdr source, tracker triggered events. The GlastSim original range cutoff was not the same as that in pdrApp. When reduced to the pdrApp value no statistically significant change in the trigger rate for any of the component fluxes is seen.

4.5.1 Hardware Trigger Vetoes

Two primary types of hardware trigger vetoes are under consideration for the LAT. Also looked at were some variations of those hardware trigger vetoes and an additional method of rate reduction that could be used as a third hardware trigger veto if necessary. In this context, the term "hardware trigger veto" is used to indicate a method of reducing, at the trigger level, the number of events that enter the data stream. This is accomplished by rejecting events that have certain characteristics that are more commonly associated with background event than gamma-ray events.

Only primitive information regarding tile hits and types of triggers is necessary to enact any of the hardware trigger veto variations discussed below.

Types of Hardware Trigger Vetoes

The 16 towers of the LAT are covered by an ACD that is segmented into 89 separate tiles. The top (or front) of the ACD is a 5x5 grid of tiles, arranged such that there are 16 intersections where the corners of 4 tiles meet. Each of these intersections is above one of the 16 towers, so that each tower is shadowed on the top by some portion of 4 ACD tiles. This arrangement is such that most of the top face ACD tiles shadow more than one tower (the only exceptions are the corner tiles). Each tower is also shadowed by ACD tiles on the side faces, which each consist of 4 rows of ACD tiles. The top 3 rows, numbered from 0 to 2 starting at the top, each have 5 tiles. The bottom row (number 3) is one long tile, which brings the total on each face to 16. $16 \times 4 + 5 \times 5 = 89$ tiles. Each corner tower is shadowed on the side by 14 different ACD tiles, 7 on an X oriented face, and 7 on a Y oriented face. Towers on the edge of the LAT, but not in a corner, are shadowed on the side by 7 tiles on one face, and the 4 towers in the core of the LAT are not shadowed by any side tiles.

The first hardware trigger veto (HTV1) uses the shadowing of towers by tiles to quickly reject events that are likely to be background. If a cosmic-ray passes through the LAT, it will first be detected in the ACD in the tile it passes through. It is then likely to create a track as it passes through one or more tracker towers. Finally, it may or may not deposit energy in the CAL, depending on its trajectory.

Conversely, most gamma rays will not cause an ACD tile to register enough energy to put it over its veto threshold. This basic difference in behavior can still be used to quickly eliminate background events.

HTV1 works by looking for triggered towers that are shadowed on the front or the side by an ACD tile that is over veto threshold. This is best achieved by considering hits in the entire front of the ACD and only top two rows on the side faces. The bottom two rows are more likely than the rest to go over threshold because of backsplash created when an energetic particle hits the CAL, so hits in the bottom rows are always ignored for this hardware trigger veto. Furthermore, if a CAL HI trigger is present, the probability of backsplash causing hits even in the upper tiles increases. For this reason, HTV1 is only enacted if there is *not* a CAL HI trigger, and a tower triggers that is also shadowed by a tile in the top or upper two side rows. The presence of a CAL HI trigger disengages the hardware trigger veto – switches it off – so it is referred to as a CAL HI switch.

The second type of hardware trigger veto (HTV2) is less complicated, but it is based on the same principle. The design is to activate HTV2 when any ACD tile in the front face or the upper two rows is over its veto threshold, and when there is not a CAL LO trigger. CAL LO triggers are more common than CAL HI triggers, so a CAL LO switch will disengage a hardware trigger veto more often than a CAL HI. For HTV2, with its less stringent geometrical requirements (enacting when any ACD tile is hit, rather than requiring a tower-shadow tile match), it was believed necessary to have a means of disengaging it more often in order to balance its

behavior.

Because it is possible, using GlastSim, to test different variations of instrument configurations, the above hardware trigger vetoes without CAL switches, and with alternate CAL switches (CAL LO instead of CAL HI, and vice versa) were also studied in order to verify that the best possible configurations were chosen.

Implementing the Hardware Trigger Vetoes in GlastSim

Nether of the two hardware trigger vetoes were hard coded into GlastSim before the study began, but only HTV1 had to be added in the form of an addition to GlastSim source code. Examining HTV2 was possible through the use of the ROOT analysis environment and the GlastSim ntuple, which contains variables that keep track of whether the top of the ACD or specific side rows were hit. The ntuple also contains information on whether an event caused a CAL HI, CAL LO, or tracker trigger.

GlastSim does not, however, output information on whether a triggered tower was shadowed by a hit ACD tile. In order to generate this information, an addition to the simulation that made this determination for each event was written. After this information was made available, it was possible to study each configuration of hardware trigger vetoes and CAL switches.

Results of Hardware Trigger Veto Studies

When dealing with the background rates in any way, the essential issues remain the same. The primary goal is to eliminate enough background to meet the down-link requirement, while rejecting as few gamma rays as possible. As stated earlier,

hardware trigger vetoing methods are only the first possible step in background elimination; the next chapter describes more sophisticated Onboard Filtering methods that will also be used. To evaluate the hardware trigger vetoing methods, their impact on background events and gamma rays is examined, and the best performance balance is found.

Results for the maximum background, the average background, and the upwards going albedo fluxes follow. The most important findings are: a CAL switch is necessary or too many gamma rays are rejected; there are two hardware trigger veto configurations that perform similarly both with respect to gamma rays and background; it is verified that using a hardware trigger veto will not get the background rate low enough to meet bandwidth limits on its own, so additional filtering will be necessary; and finally, one hardware trigger veto rejects gamma rays that are later rejected by the software Onboard Filtering anyway.

The first task in this analysis was to assess the performance of the hardware trigger vetoes when the incoming source is gamma rays. The fewer the gammas rejected by a hardware trigger veto, the better. GlastSim was programmed to generate 4 sets of gamma-ray events at the following energies: 100 MeV, 1 GeV, 10 GeV, and 100 GeV. Gammas in all 4 runs were generated uniformly from incoming angles ranging from LAT zenith to 90^o from zenith, so no incoming angle was preferentially selected. HTV1 and HTV2 were then tested on different cuts of gammas: tracker triggered events only, tracker triggered and greater than 5 MeV in the CAL, and events that passed an initial version of the LAT ground based background rejection

analysis. The last of these is useful because gammas inadvertently rejected by a hardware trigger vetoing method are less of a concern if those same gammas would later be inadvertently rejected by the ground based background rejection anyway. (This is *not* the same as the Onboard Filtering that has been mentioned.) This is discussed more in Chapter 5. Here, just note that the collaboration describes events that pass the ground based background rejection as "goodEvents," or those that pass the "goodEvent" cuts. These cuts are undergoing refinement as the mission progresses, so they are not relied upon for any final analysis, but they are a useful performance benchmark nonetheless.

Table 4.6 shows the results for HTVs 1 and 2 as applied to gamma rays selected with different cuts. HTV1 performs better, eliminating fewer gammas, for tracker triggered events except at the highest energies. Conversely, HTV2 eliminates fewer gammas that trigger the tracker and deposit 5 MeV in the CAL except at the lowest energy range, though the statistical uncertainties are large enough to overwhelm any difference in performance. For gamma events that are not eliminated by the ground based background rejection, neither hardware trigger veto does much elimination, though the sample size is so low (due to the numerous background cuts) that it is not possible to detect a performance difference.

With regard to background rejection, good performance is defined by which hardware trigger veto eliminates the most background, getting us closer to the 400 Hz limit. Once the hardware trigger veto with the best background elimination is determined, the goal is to pick a hardware trigger veto that balances background

	Tracker Triggers		Tracker & 5 MeV		goodEvents	
Energy (GeV)	HTV1	HTV2	HTV1	HTV2	HTV1	HTV2
0.100	12.8 ± 0.3	16.6 ± 0.2	4.8 ± 0.0	6.6 ± 0.2	0	0
1	18.9 ± 0.5	28.6 ± 0.4	10.7 ± 0.3	9.5 ± 0.3	3.5 ± 0.3	2.6 ± 0.1
10	22.5 ± 0.5	30.9 ± 0.4	12.2 ± 0.2	9.4 ± 0.3	2.0 ± 0.2	0
100	18.0 ± 0.5	17.3 ± 0.5	10.3 ± 0.1	8.1 ± 0.2	0.1 ± 0.1	0

Table 4.6: Percentage of gammas eliminated by HTVs 1 and 2. Results for three different cuts are shown: tracker triggered events, tracker triggered events with 5 MeV in the CAL, and events that pass the ground based background rejection.

and gamma performance. The only relevant selection is that of all triggered events, so that is all that were examined for both the maximum and average background sources. In addition to these, the rejection of upward going albedo was looked at, because that source was not included in backgndmaxpdr or backgndavgpdr. Table 4.7 has the results for hardware trigger veto background rejection for all-triggered events. HTV1 eliminates more backgndmaxpdr and backgndavgpdr, but slightly less of the separate albedo source than HTV2. When backgndmaxpdr and the upwards albedo rates are summed, HTV1 eliminates more than HTV2. For backgndavgpdr with upwards albedo, the statistical uncertainty masks any difference between HTV1 and HTV2. Still, it appears that HTV1 does a better job at eliminating the most troublesome maximum background.

Flux	Trigger Rate (Hz)	Rate after HTV1 (Hz)	% Reduced by HTV1	Rate after HTV2 (Hz)	% Reduced by HTV2
backgndmaxpdr	11823 ± 119	3281 ± 63	72.2 ± 1.6	3610 ± 52	69.5 ± 1.2
backgndavgpdr	3632 ± 43	1046 ± 23	71.2 ± 1.8	1087 ± 23	70.1 ± 1.7
upwards albedo	267 ± 5	185 ± 5	30.7 ± 1.0	172 ± 4	35.6 ± 1.1
backgndmax + albedo	12090 ± 124	3466 ± 68	71.3 ± 1.6	3782 ± 56	68.7 ± 1.2
backgndavg + albedo	3899 ± 48	1231 ± 28	68.4 ± 1.8	1259 ± 27	67.7 ± 1.7

Table 4.7: Percentage of background fluxes eliminated by HTVs 1 and 2. The event selection was all-triggered events. Residual rates and the percentage reduced are shown after applying both hardware trigger vetoes.

The above results do not complete our study, as it was also necessary to verify that the default hardware trigger vetoes are indeed the best performers of all possible CAL switch variations. These variations are: HTVs 1 and 2 without any CAL disengagement switch, HTV1 with a CAL LO switch, and HTV2 with a CAL HI switch. Any hardware trigger veto is only the first step towards reducing the event rate, and onboard event filtering will proceed later. Ultimately, the most important metric is the event rate after a hardware trigger veto and an Onboard Filter have been applied. Therefore, the performance of the HTVs in conjunction with the Onboard Filter (described in the next chapter[3]) was also studied.

Tables 4.8 through 4.13 have the results of hardware trigger veto impact on gamma rays for different event selections and hardware trigger veto variations. One thing that is visible in each of the tables is that both hardware trigger vetoes perform better (eliminate fewer gammas) when they are disengaged with any CAL switch. The effect is significant enough that a hardware trigger veto without a CAL disengagement switch should not be used. The other pattern is that when taken in conjunction with Onboard Filter, HTV1 eliminates fewer gamma rays than HTV2. In other words, HTV1 incrementally removes fewer than HTV2 when they are applied along with Onboard Filter. The hardware trigger veto variation that removes the smallest fraction of gamma rays is HTV1 with a CAL LO switch instead of a CAL HI.

When one looks at the background sources with different hardware trigger

[3]Chapter 5 describes how we improved the performance of the Onboard Filtering algorithms from their initial state. The version of Onboard Filter that we use in this Chapter 4 study is the final, improved version of the Filter described in Chapter 5.

veto variations, Tables 4.14 through 4.16, it is apparent that the hardware trigger veto variations that remove the most background are those that do not have a CAL switch. They also work best when combined with the Onboard Filter. However, it was just stated that using a hardware trigger veto with no CAL disengagement switch is not advisable. When one looks at hardware trigger veto variations that do have a CAL switch, the best performing tactic is to use the Onboard Filter in conjunction with HTV1.

HTV1 with Onboard Filter is the most desirable choice for background rejection. This combination performs well, but not better than all other hardware trigger veto variations when applied to gamma rays. However, the performance difference between the best performing hardware trigger veto variation for gammas applied with the Onboard Filter[4], and the original HTV1 with Onboard Filter, is not significant enough to override the very good background rejection of the original-HTV1-with-Filter combination. So far, it appears that the best choice of a hardware trigger veto is HTV1, provided that Onboard Filtering occurs later in the data stream. Even this combination of HTV and Filter does not reduce the event rate to a level that meets the downlink requirement during periods of maximum background. However, short-term spikes in the background rate are acceptable as long as the orbit average is limited to 400 Hz.

Though HTV1 appears to be a good choice, there is one remaining method to consider, and that is the crude hardware trigger vetoing method of eliminating any event that deposits less than 5 MeV in the CAL. Table 4.17 shows what happens

[4]HTV1 with a CAL LO switch instead of CAL HI.

when this cut is employed by itself and with the Onboard Filter. Looking at the background rates first, notice that it works very well against upwards albedo, but not against other background. It is necessary to use the Onboard Filter in conjunction with this method; the combination does reduce the rates to levels consistent with the other hardware trigger vetoes. However, if one looks at the gamma performance, it is apparent that the amount of elimination this method does to low energy gammas is significantly more than other hardware trigger vetoing methods. For this reason, it is not recommended that this crude method be used, so it is better to fall back on HTV1 with its CAL HI disengagement switch.

If HTV1 with its CAL HI switch is used, the albedo upwards rate is 123 ± 4 Hz, and the average background rate is 267 ± 5 Hz, for a total of 390 ± 6 Hz, which is close to the mission cap of 400 Hz. However, these figures are already derived from the application of the Onboard Filtering software, so some additional work beyond Onboard Filtering and hardware trigger vetoing is required. A place to start may be with additional cuts designed to remove albedo gammas specifically, because the existing methods do not perform well against them. Both the backgndavgpdr and backgndmaxpdr source fluxes contain a source that produces albedo gammas from the Earth's limb, so an attempt at reducing albedo gamma in general would also reduce the backgndavgpdr and backgndmaxpdr rates.

Energy (GeV)	HTV1 without switch	HTV1 with CAL LO switch instead	HTV2 without switch	HTV2	Onboard Filter Alone	HTV1 w/o switch ORed w/ Filter	Incremental Rate Reduction (IR)
0.100	12.8 ± 0.3	12.8 ± 0.3	16.6 ± 0.4	16.6 ± 0.4	28.5 ± 0.5	29.3 ± 0.5	0.8 ± 0.9
1	18.9 ± 0.3	18.0 ± 0.4	28.6 ± 0.6	22.4 ± 0.4	36.3 ± 0.6	39.6 ± 0.7	3.3 ± 1.1
10	37.7 ± 0.5	19.8 ± 0.4	51.8 ± 0.7	30.9 ± 0.5	36.9 ± 0.6	51.2 ± 0.7	14.3 ± 1.2
100	67.9 ± 0.5	16.6 ± 0.4	79.3 ± 1.1	17.3 ± 0.4	29.5 ± 0.7	77.6 ± 1.1	48.1 ± 1.6

Energy (GeV)	Filter ORed w/ HTV1 w/ LO switch	IR	HTV2 w/o switch ORed w/ Filter	IR	Filter ORed w/ HTV2	IR
0.100	29.3 ± 0.5	0.8 ± 1.0	30.2 ± 0.5	1.7 ± 0.9	30.2 ± 0.5	1.7 ± 1.0
1	37.6 ± 0.6	1.3 ± 1.2	43.4 ± 0.7	7.1 ± 1.2	38.3 ± 0.6	2.0 ± 1.2
10	37.4 ± 0.6	0.5 ± 1.2	63.6 ± 0.8	26.7 ± 1.3	37.7 ± 0.6	0.8 ± 1.2
100	30.0 ± 0.5	0.5 ± 1.2	88.0 ± 1.2	58.5 ± 1.7	30.2 ± 0.5	0.7 ± 1.2

Table 4.8: Percentage of tracker triggered gammas eliminated by hardware trigger vetoes and Onboard Filtering – HTV1 with CAL LO switch. If HTV1 is changed to use a CAL LO disengagement switch, it does little additional damage to gammas relative to that done by Onboard Filter.

Energy (GeV)	HTV1 without switch	HTV1	HTV2 without switch	HTV2 with CAL HI switch instead	Onboard Filter Alone	HTV1 w/o switch ORed w/ Filter	Incremental Rate Reduction (IR)
0.100	12.8 ± 0.3	12.8 ± 0.3	16.6 ± 0.4	16.6 ± 0.4	28.5 ± 0.5	29.3 ± 0.5	0.8 ± 1.0
1	18.9 ± 0.3	18.9 ± 0.5	28.6 ± 0.6	28.6 ± 0.6	36.3 ± 0.6	39.6 ± 0.7	3.3 ± 1.3
10	37.7 ± 0.5	22.5 ± 0.5	51.8 ± 0.7	25.0 ± 0.7	36.9 ± 0.6	51.2 ± 0.7	14.3 ± 1.3
100	67.9 ± 0.5	18.0 ± 0.5	79.3 ± 1.1	19.7 ± 1.1	29.5 ± 0.7	77.6 ± 1.1	48.1 ± 1.8

Energy (GeV)	Filter ORed w/ HTV1	IR	HTV2 w/o switch ORed w/ Filter	IR	Filter ORed w/ HTV2 w/ HI switch	IR
0.100	29.3 ± 0.5	0.8 ± 1.0	30.2 ± 0.5	1.7 ± 1.0	30.2 ± 0.5	1.7 ± 1.0
1	39.6 ± 0.7	3.3 ± 1.3	43.4 ± 0.7	7.1 ± 1.3	43.4 ± 0.7	7.1 ± 1.3
10	38.9 ± 0.6	2.0 ± 1.2	63.6 ± 0.8	26.7 ± 1.4	40.3 ± 0.6	3.4 ± 1.2
100	30.3 ± 0.7	0.8 ± 1.4	88.0 ± 1.2	58.5 ± 1.9	30.6 ± 0.7	1.1 ± 1.4

Table 4.9: Percentage of tracker triggered gammas eliminated by hardware trigger vetoes and Onboard Filtering – HTV2 with CAL HI switch. HTV1 does the best job of not eliminating gammas, but it does not do as good a job as HTV1 with a CAL LO switch (previous table).

Energy (GeV)	HTV1 without switch	HTV1 with CAL LO switch instead	HTV2 without switch	HTV2	Onboard Filter Alone	HTV1 w/o switch ORed w/ Filter	Incremental Rate Reduction (IR)
0.100	4.8 ± 0.2	4.8 ± 0.2	6.6 ± 0.2	6.6 ± 0.2	6.2 ± 0.2	6.9 ± 0.2	0.7 ± 0.4
1	10.7 ± 0.4	6.3 ± 0.2	18.2 ± 0.4	9.5 ± 0.3	11.4 ± 0.3	16.1 ± 0.4	4.7 ± 0.7
10	32.2 ± 0.6	8.6 ± 0.3	50.0 ± 0.8	9.4 ± 0.3	17.6 ± 0.4	36.6 ± 0.7	19.0 ± 1.1
100	70.6 ± 1.2	7.6 ± 0.3	84.3 ± 1.2	8.1 ± 0.3	13.7 ± 0.4	72.8 ± 1.1	59.1 ± 1.5

Energy (GeV)	Filter ORed w/ HTV1 w/ LO switch	IR	HTV2 w/o switch ORed w/ Filter	IR	Filter ORed w/ HTV2	IR
0.100	6.9 ± 0.2	0.7 ± 0.4	7.7 ± 0.2	1.5 ± 0.4	7.7 ± 0.3	1.5 ± 0.5
1	13.0 ± 0.3	1.6 ± 0.6	21.4 ± 0.5	10.0 ± 0.8	14.2 ± 0.4	2.8 ± 0.7
10	18.4 ± 0.4	0.8 ± 0.8	52.7 ± 0.9	35.1 ± 1.3	18.6 ± 0.4	1.0 ± 0.8
100	14.3 ± 0.4	0.6 ± 0.8	85.6 ± 1.3	71.9 ± 1.7	14.5 ± 0.4	0.8 ± 0.8

Table 4.10: Percentage of tracker triggered gammas, with greater than 5 MeV in the CAL, eliminated by hardware trigger vetoes and Onboard Filtering – HTV1 with CAL LO switch. HTV1 performs better than HTV2 again.

Energy (GeV)	HTV1 without switch	HTV1	HTV2 without switch	HTV2 with CAL HI switch instead	Onboard Filter Alone	HTV1 w/o switch ORed w/ Filter	Incremental Rate Reduction (IR)
0.100	4.8 ± 0.2	4.8 ± 0.2	6.6 ± 0.3	6.6 ± 0.3	6.2 ± 0.3	6.9 ± 0.3	0.7 ± 0.6
1	10.7 ± 0.4	10.7 ± 0.4	18.2 ± 0.5	18.2 ± 0.5	11.4 ± 0.4	16.1 ± 0.5	4.7 ± 0.9
10	32.2 ± 0.6	12.2 ± 0.4	50 ± 0.8	14.7 ± 0.4	17.6 ± 0.5	36.6 ± 0.7	19 ± 1.2
100	70.6 ± 1.2	10.3 ± 0.5	84.3 ± 1.3	11 ± 0.5	13.7 ± 0.5	72.8 ± 1.2	59.1 ± 1.7

Energy (GeV)	Filter ORed w/ HTV1	IR	HTV2 w/o switch ORed w/ Filter	IR	Filter ORed w/ HTV2 w/ HI switch	IR
0.100	6.9 ± 0.3	0.7 ± 0.6	7.7 ± 0.3	1.5 ± 0.6	7.7 ± 0.3	1.5 ± 0.6
1	16.1 ± 0.5	4.7 ± 0.9	21.4 ± 0.6	10 ± 1.0	21.4 ± 0.6	10.0 ± 1.0
10	20.2 ± 0.5	2.6 ± 1.0	52.7 ± 0.8	35.1 ± 1.3	30.7 ± 0.6	13.1 ± 1.1
100	14.7 ± 0.5	1.0 ± 1.0	85.6 ± 1.3	71.9 ± 1.8	15.0 ± 0.6	1.3 ± 1.1

Table 4.11: Percentage of tracker triggered gammas, with greater than 5 MeV in the CAL, eliminated by hardware trigger vetoes and Onboard Filtering – HTV2 with CAL HI switch. HTV1 performs better than HTV2, but comparison with the previous table shows that using the CAL LO switch rejects fewer gammas.

Energy (GeV)	HTV1 without switch	HTV1 with CAL LO switch instead	HTV2 without switch	HTV2	Onboard Filter Alone	HTV1 w/o switch ORed w/ Filter	Incremental Rate Reduction (IR)
0.100	0	0	0	0	0	0	0
1	3.5 ± 0.2	0.9 ± 0.1	10.0 ± 0.3	2.6 ± 0.1	4.4 ± 0.2	7.3 ± 0.3	2.9 ± 0.5
10	19.2 ± 0.5	0	42.2 ± 0.9	0	4.0 ± 0.2	22.0 ± 0.5	18.0 ± 0.7
100	65.0 ± 1.3	0	88.3 ± 1.7	0	1.0 ± 0.1	65.5 ± 1.3	64.5 ± 1.4

Energy (GeV)	Filter ORed w/ HTV1 w/ LO switch	IR	HTV2 w/o switch ORed w/ Filter	IR	Filter ORed w/ HTV2	IR
0.100	0	0	0	0	0	0
1	4.9 ± 0.2	0.5 ± 0.4	12.7 ± 0.4	8.3 ± 0.4	5.8 ± 0.2	1.4 ± 0.4
10	4.0 ± 0.2	0	43.7 ± 0.9	39.7 ± 1.1	4.0 ± 0.2	0
100	1.0 ± 0.1	0	88.3 ± 1.7	87.3 ± 1.8	1.0 ± 0.1	0

Table 4.12: Percentage of "Good Events" (gammas) eliminated by hardware trigger vetoes and Onboard Filtering – HTV1 with CAL LO switch. HTV1 still incrementally rejects fewer gammas than HTV2 (with respect to the Onboard Filter).

Energy (GeV)	HTV1 without switch	HTV1	HTV2 without switch	HTV2 with CAL HI switch instead	Onboard Filter Alone	HTV1 w/o switch ORed w/ Filter	Incremental Rate Reduction (IR)
0.100	0 ± 0.0	0 ± 0.0	0 ± 0.0	0 ± 0.0	0 ± 0.0	0.0 ± 0.0	0 ± 0.0
1	3.5 ± 0.3	3.5 ± 0.3	10.0 ± 0.5	10.0 ± 0.5	4.4 ± 0.3	7.3 ± 0.4	2.9 ± 0.4
10	19.2 ± 0.7	2 ± 0.2	42.2 ± 1.0	3.9 ± 0.3	4 ± 0.3	22.0 ± 0.8	18 ± 0.8
100	65.0 ± 2.0	0.1 ± 0.1	88.3 ± 2.3	0 ± 0.0	1 ± 0.2	65.5 ± 2.0	64.5 ± 2.0

Energy (GeV)	Filter ORed w/ HTV1	IR	HTV2 w/o switch ORed w/ Filter	IR	Filter ORed w/ HTV2 w/ HI switch	IR
0.100	0 ± 0.0	0 ± 0.0	0 ± 0.0	0 ± 0.0	0 ± 0.0	0 ± 0.0
1	7.3 ± 0.4	2.9 ± 0.7	12.7 ± 0.6	8.4 ± 0.9	12.7 ± 0.6	8.4 ± 0.9
10	5.7 ± 0.4	1.7 ± 0.7	43.7 ± 1.1	39.7 ± 1.4	7.5 ± 0.4	3.5 ± 0.7
100	1 ± 0.2	0 ± 0.4	88.3 ± 2.3	87.3 ± 2.5	1 ± 0.2	0 ± 0.4

Table 4.13: Percentage of "Good Events" eliminated by hardware trigger vetoes and Onboard Filtering – HTV2 with CAL HI switch. HTV1 incrementally rejects fewer gammas than HTV2 (with respect to the Onboard Filter), but HTV1 with a CAL LO switch performs better than HTV1 with its CAL HI switch.

Backgndmaxpdr Trigger Rate (all triggers): $11,823 \pm 119$ Hz		
All With CAL LO Switch		
HTV and Filter variation	% Reduced	Remaining Rate (Hz)
Onboard Filter	91.1 ± 3.2	1053 ± 34
HTV1 with CAL LO instead	59.2 ± 1.1	4824 ± 53
HTV1 w/o switch	73.1 ± 1.6	3181 ± 51
Filter ORed w/ HTV1 w/ CAL LO instead	91.4 ± 3.3	1023 ± 33
Filter ORed w/ HTV1 w/o switch	94.7 ± 4.2	631 ± 27
HTV2	69.5 ± 1.4	3610 ± 52
HTV2 w/o switch	87.0 ± 2.6	1529 ± 40
Filter ORed w/ HTV2	91.4 ± 3.3	1014 ± 33
Filter ORed w/ HTV2 w/o switch	95.7 ± 4.8	504 ± 24
All With CAL HI Switch		
HTV and Filter variation	% Reduced	Remaining Rate (Hz)
Onboard Filter	91.1 ± 3.2	1053 ± 36
HTV1	72.2 ± 1.6	3281 ± 63
HTV1 w/o switch	73.1 ± 1.6	3181 ± 62
Filter ORed w/ HTV1	94.3 ± 4.1	674 ± 28
Filter ORed w/ HTV1 w/o switch	94.7 ± 4.2	674 ± 28
HTV2 with CAL HI instead	86.0 ± 2.5	1650 ± 45
HTV2 w/o switch	87.0 ± 2.6	1529 ± 43
Filter ORed w/ HTV2 w/ CAL HI instead	95.3 ± 4.5	553 ± 26
Filter ORed w/ HTV2 w/o switch	95.7 ± 4.8	504 ± 25

Table 4.14: Maximum background rate after different hardware trigger veto and filtering configurations. Even though HTV2 with no switch eliminates the most background, and HTV1 with its CAL HI switch is also a good performer, the best balance between background rejection and gamma-ray efficiency is found in HTV1 with a CAL HI switch or HTV2 with a CAL LO switch.

Backgndavgpdr Trigger Rate (all triggers): $3,632 \pm 43$ Hz		
All With CAL LO Switch		
HTV and Filter variation	% Reduced	Remaining Rate (Hz)
Onboard Filter	90.8 ± 3.7	336 ± 13
HTV1 with CAL LO instead	60.0 ± 1.3	1451 ± 27
HTV1 w/o switch	72.8 ± 1.9	986 ± 22
Filter ORed w/ HTV1 w/ CAL LO instead	91.1 ± 3.8	323 ± 13
Filter ORed w/ HTV1 w/o switch	94.2 ± 4.7	211 ± 10
HTV2	70.1 ± 1.7	1087 ± 23
HTV2 w/o switch	86.1 ± 2.9	505 ± 16
Filter ORed w/ HTV2	91.3 ± 3.8	318 ± 13
Filter ORed w/ HTV2 w/o switch	95.2 ± 5.2	175 ± 9
All With CAL HI Switch		
HTV and Filter variation	% Reduced	Remaining Rate (Hz)
Onboard Filter	90.8 ± 3.6	336 ± 13
HTV1	71.2 ± 1.7	1046 ± 23
HTV1 w/o switch	72.8 ± 1.8	986 ± 22
Filter ORed w/ HTV1	93.3 ± 4.3	245 ± 11
Filter ORed w/ HTV1 w/o switch	94.2 ± 4.7	211 ± 10
HTV2 with CAL HI instead	84.0 ± 2.6	579 ± 17
HTV2 w/o switch	86.1 ± 2.9	505 ± 16
Filter ORed w/ HTV2 w/ CAL HI instead	94.1 ± 4.7	214 ± 10
Filter ORed w/ HTV2 w/o switch	95.2 ± 5.2	175 ± 9

Table 4.15: Average background rate after different hardware trigger veto and filtering configurations. The same result holds for average background as did for maximum background. The best balance between gamma and background performance is found in either HTV1 with a CAL HI switch or HTV2 with a CAL LO switch.

Albedo Upwards Trigger Rate (all triggers): 267 ± 5 Hz		
All With CAL LO Switch		
HTV and Filter variation	% Reduced	Remaining Rate (Hz)
Onboard Filter	51.8 ± 1.9	128 ± 4
HTV1 with CAL LO	29.2 ± 0.9	189 ± 5
HTV1 w/o switch	30.6 ± 1.0	185 ± 5
Filter ORed w/ HTV1 w/ CAL LO instead	53.4 ± 1.9	124 ± 4
Filter ORed w/ HTV1 w/o switch	53.9 ± 2.0	123 ± 4
HTV2 with CAL LO instead	35.5 ± 1.2	172 ± 4
HTV2 w/o switch	37.8 ± 1.2	166 ± 4
Filter ORed w/ HTV2	54.7 ± 2.0	121 ± 4
Filter ORed w/ HTV2 w/o switch	55.2 ± 2.0	119 ± 4
All With CAL HI Switch		
HTV and Filter variation	% Reduced	Remaining Rate (Hz)
Onboard Filter	51.8 ± 1.6	128 ± 4
HTV1	30.6 ± 0.8	185 ± 5
HTV1 w/o switch	30.6 ± 0.8	185 ± 5
Filter ORed w/ HTV1	53.9 ± 1.7	123 ± 4
Filter ORed w/ HTV1 w/o switch	53.9 ± 1.7	123 ± 4
HTV2 with CAL HI instead	37.7 ± 1.0	166 ± 4
HTV2 w/o switch	37.8 ± 1.0	166 ± 4
Filter ORed w/ HTV2 w/ CAL HI instead	55.2 ± 1.8	119 ± 4
Filter ORed w/ HTV2 w/o switch	55.2 ± 1.8	119 ± 4

Table 4.16: Upwards going albedo rate after different hardware trigger veto and filtering configurations. Albedo gammas from the surface of Earth's atmosphere (rather than the limb), look very similar to low energy (<1 GeV) celestial gammas in the tracker. No hardware trigger vetoing methods are very successful at eliminating the albedo, but their rate is relatively low to begin with.

Impact on Gammas				
The 5 MeV Cut			5 MeV Cut or Onboard Filter	
Energy	% Reduced by 5 MeV Cut		% Reduced by 5 MeV Cut or Onboard Filter	
100 MeV	40.8 ± 0.9		44.7 ± 1.0	
1 GeV	28.7 ± 0.7		36.9 ± 0.8	
10 GeV	24.0 ± 0.9		37.9 ± 1.2	
100 GeV	20.2 ± 1.2		31.3 ± 1.6	
Flux	% Reduced	Rate (Hz)	% Reduced	Rate (Hz)
backgndmaxpdr	42.3 ± 0.8	6819 ± 196	92.0 ± 1.3	944 ± 233
backgndavgpdr	49.5 ± 1.0	1834 ± 73	93.2 ± 1.6	245 ± 84
albedo	87.9 ± 3.7	15.9 ± 7.4	94.2 ± 3.9	7.7 ± 7.5

Table 4.17: Gamma ray and background elimination by the 5 MeV energy cut for gammas and background sources. The top half of the table shows the percentage of gamma-rays rejected by a 5 MeV energy cut (events with <5 MeV in the CAL are rejected) and by a 5 MeV cut in conjunction with the Onboard Filter. The lower half of the table shows the same thing, along with the remaining background rate, for different background sources. Here, "albedo" refers to the albedo from Earth's atmosphere's surface. Note that the energy cut in conjunction with Onboard Filter is highly effective at eliminating background, but low energy gamma rays are rejected at a high rate also.

4.6 Summary and Conclusions

The LAT trigger rates for different background sources have been studied, and it was found that without onboard event rate reduction, the amount of data will overwhelm the downlink limitations by about a factor of 9. In order to meet the downlink requirement, it is necessary to use a combination of a hardware trigger veto and a software filter. It was found that there is a particular hardware trigger veto that eliminates a high fraction of background while not rejecting many gamma rays that would not later be rejected by the Onboard Filter. Having a hardware trigger veto and Onboard Filter reject an overlapping sample of gamma rays, rather than different sets of events, is highly desirable, because it minimizes the overall rejection of these events.

In addition to the trigger rate and rate reduction analyses, a study of how the collaboration might use muons to understand the tracker tower alignment before launch was performed. It was found that it was necessary to tilt the LAT to its side to take data, but it was only necessary to do this for two adjacent sides, not all four. Also studied was the impact of possible hardware failures that might occur in space. It was concluded that a loss of one layer in a tower or even an entire tower will not jeopardize the mission.

Chapter 5

The Onboard Event Filter

5.1 The Need for an Onboard Filter

As mentioned in the previous chapter, the use of a hardware trigger veto alone will not reduce the background rate enough to meet GLAST mission requirements for downlink. Additional event filtering methods must be used, and a software Onboard Filter was included in the design for this purpose. This chapter describes the Onboard Filter, its performance, improvements made to its algorithms, and the development of new filtering algorithms that enhance onboard background rejection.

5.2 Description of the Filtering Problem

The purpose of filtering is to reduce the data rate, which is mainly due to background, so that it meets the downlink requirement[1]. This is not, however, the same as a background rejection analysis in which one tries to reduce the background contamination of a gamma-ray source in order to get a pure signal; on the contrary,

[1] As stated in Chapter 4, the time-averaged downlink will be about 1.2 Mbps

the data transmitted to the ground will have the minimal onboard filtering possible while still meeting the downlink requirement. The remaining background will be removed later by ground-based methods that select gamma-ray candidate events in the data while removing probable background events. The task in onboard filtering is to reduce the data rate to the level necessary for downlink while keeping as many gamma rays in the sample as possible.

This task is very challenging because of the large phase space that describes gamma-rays incident upon the LAT. Gammas are detected from the wide LAT field of view over 6 decades in energy, can convert at different depths in the LAT, and can create multiple secondary particles that also interact with the detector. Gammas differ from background in that it is desired to detect and retain the signal from gammas that just come from within the LAT field of view, while the simultaneous attempt is made to reject background events that come from all directions. Though a large phase space describes the incident particles and their interactions within the LAT, the success of onboard filtering can be gauged by looking primarily at two things. The first is whether the background rate has been reduced enough to meet the downlink requirement. The second is the fraction of gamma-ray events that the Onboard Filter removes from the data stream; it is desirable to keep the fraction of rejected gammas to a minimum.

5.3 Onboard Filter Logic

Methods of background rejection were studied during the early development of the LAT, and prototype cuts suitable for an online filter were devised as a proof of concept. These initial algorithms were implemented only in the offline reconstruction using ntuple quantities, and their use showed that it would be possible to reduce the background to an acceptable level. It was then necessary to implement the studied cuts as onboard flight software algorithms (the Onboard Filter) that could be used to benchmark CPU use and other resources.

The Onboard Filter based on early background rejection studies was designed and implemented in the C programming language by James J. Russell of the LAT Flight Software Group at SLAC, and it was designed to run with efficiency on the PowerPC Event Processing Units. This early version of the Onboard Filter could then be evaluated on high-fidelity, full-scale electronics test beds, and with data that was formatted as it will be onboard the LAT. A next step undertaken for this thesis was to then embed the early version of Onboard Filter into the GlastSim environment for further testing with simulated source and background fluxes. This is described in more detail in section 5.4. The results of the work done for this chapter were then given to the Flight Software Group as feedback for the ongoing refinement of the Onboard Filter.

The event filtering code consisted of 16 different cuts, or reasons to veto an event. Vetoes that used a minimum of processing power and were also likely to occur at a high rate were placed before those that were predicted to be less frequent. This

strategy would allow the filter to reject as many events as possible with a minimal drain on computing resources.

When Onboard Filter determines whether an event should be vetoed, it notes the reason for the veto in a 32 bit summary word. The first 15 bits (numbered 0 to 14) are status bits that can be used for debugging, and the next 16 bits are used to describe which vetoes are active for that event. The remaining summary bit is set if the event is vetoed for any reason. Because of the bit placement, the vetoes are numbered from 15 to 30, and because of the order in which the vetoes occur within the code, the first veto encountered in the algorithm is veto 30 and the last one is veto 15. The only two deviations from the veto ordering scheme are when vetoes 21 and 17 appear before they would otherwise be expected. For consistency with the code, its veto labeling method is used throughout this dissertation.

Onboard Filter was designed to be flexible, in that it will be possible to upload changes to the code once GLAST is in orbit. This will allow for vetoes to be turned on or off, and for the values of different parameters to be changed. In flight, Onboard Filter will usually stop processing an event if the event does not pass one of the veto cuts. This ensures that CPU cycles are not wasted. However, a *pass-through* mode will allow some events, at a prescaled rate, to pass through the rest of the Filter in order to allow other vetoes to activate for the same event. This will be used as a diagnostic check for monitoring on the ground. In order to evaluate the Filter's performance before flight, it was necessary to embed it into GlastSim. When run as part of GlastSim, the Filter was run in pass-through mode so the workings of each

veto could be examined in detail.

In the early implementation of Onboard Filter, events were rejected for many different reasons, all of which were based on what kind of signature a background event was likely to create, and what kind of gamma-ray event might be less scientifically useful. Although the primary goal is always to eliminate background while keeping gamma rays, any event filtering is imperfect and will reject some gamma rays no matter its level of sophistication. The key is to try to limit the reduction of gamma rays to those that are less likely to have scientific value. Some of the original vetoes were more successful than others at rejecting background while not eliminating gammas, while others had to be abandoned or altered in order to meet this goal. It was also necessary to devise some new algorithms in order to deal with the problem of albedo gamma rays from Earth's atmosphere. Figures 5.1 through 5.3 show the early logic of Onboard Filter in flow chart form. The Filter performance is described later, and is best summarized by Figures 5.4 through 5.10.

5.3.1 Description of Each Veto

What follows is a description of each of the Onboard Filter vetoes in its initial implementation[2]. Later in this chapter, changes to this logic are described (see Figures 5.19-5.21).

[2]Another description of Onboard Filter is found in Wren (2004a).

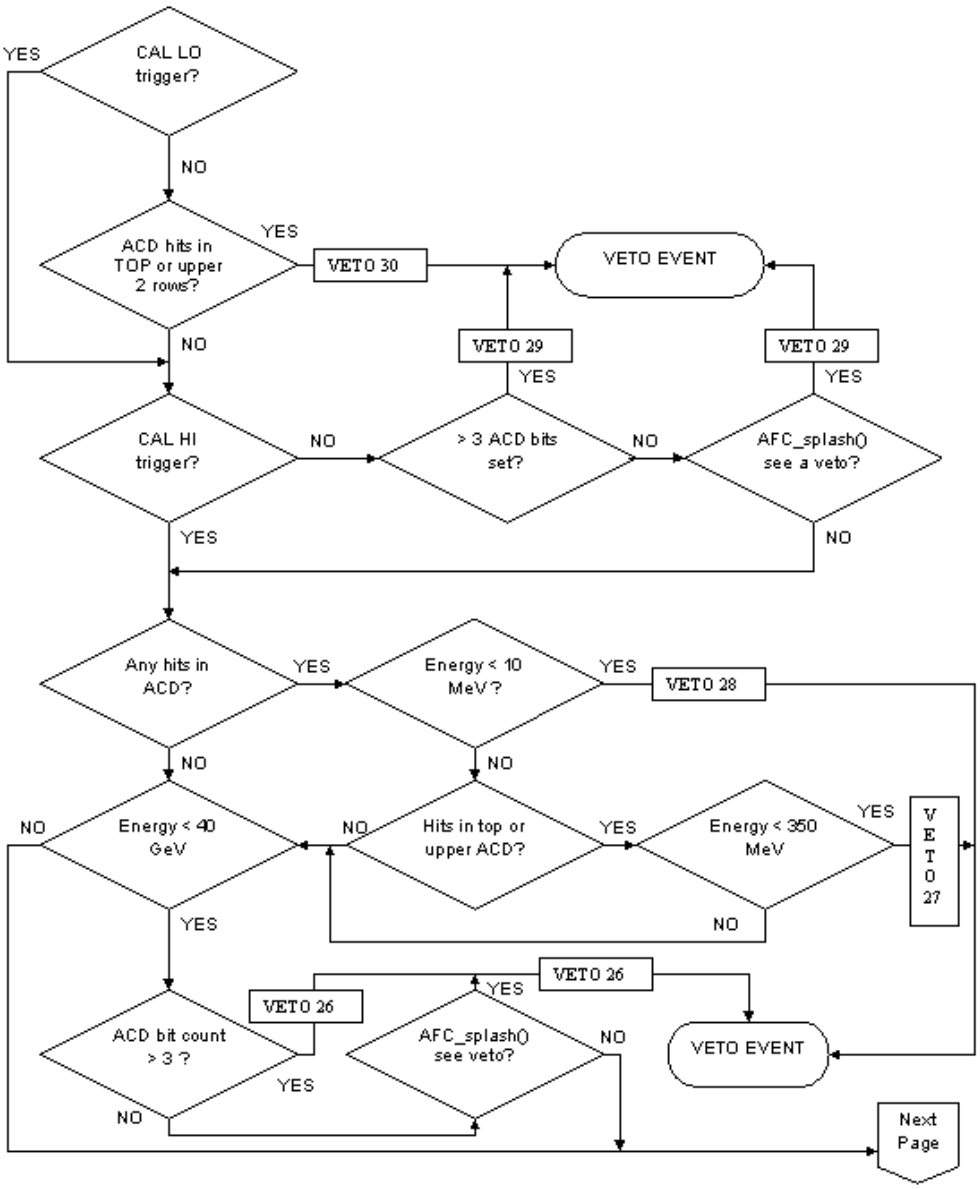

Figure 5.1: Initial Onboard Filter Logic - Page 1. The flow of the initial implementation of the Onboard Filter logic and vetoes. See the text for an explanation of each veto cut. This logic was revised in a later version in order to improve the performance (see Figures 5.19-5.21 for comparison).

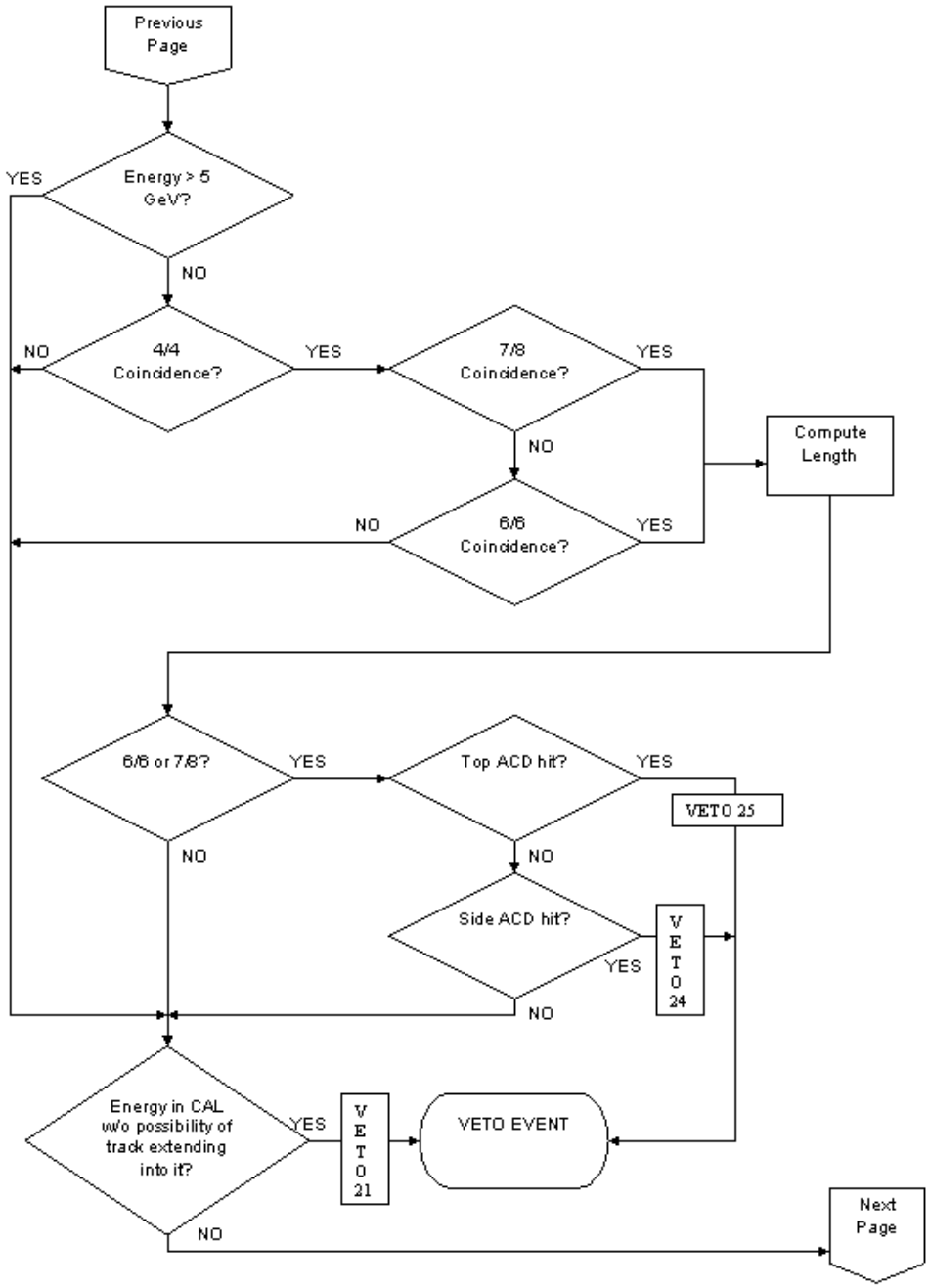

Figure 5.2: Initial Onboard Filter Logic - Page 2

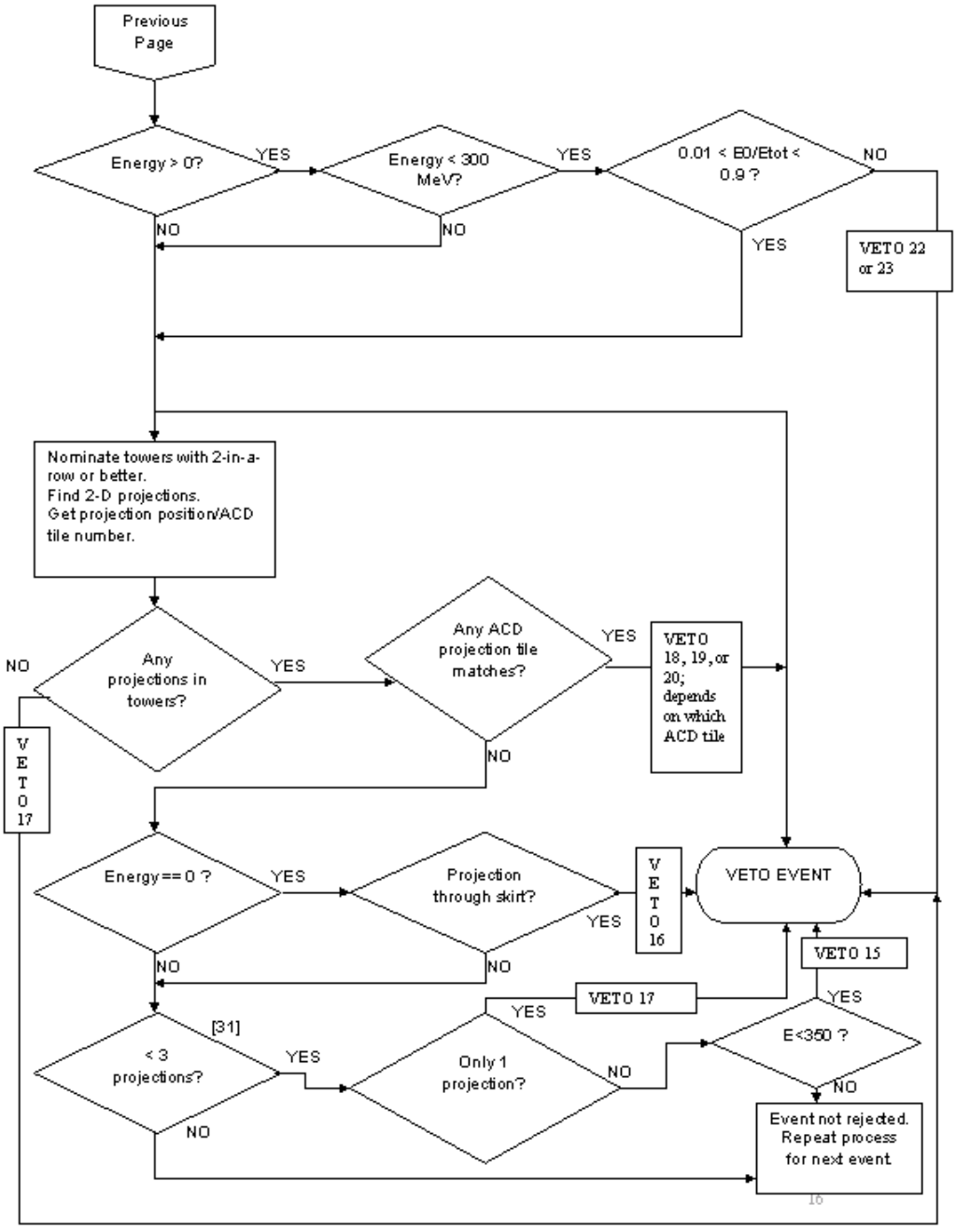

Figure 5.3: Initial Onboard Filter Logic - Page 3

Veto 30

Veto 30, the first one that processes an event, was designed to distinguish between background events that cause an ACD tile hit, and gamma rays that would otherwise self-veto. A gamma ray that does not deposit enough energy to cause a CAL LO trigger may generate conversion products that one or more secondaries will cause a lower ACD tile to go over threshold. However, for a low energy event, it is not as likely that backsplash from the CAL will cause a secondary to travel all the way up to one of the ACD tiles in the front face or the upper two rows of a side face and cause a hit[3]. Veto 30 is based around this assumption, so it looks to see if there are any events without a CAL LO trigger that have one or more hit ACD filter tiles. If this is the case, the likely reason is not backsplash from a gamma-ray event. Rather, the cause was probably the passage of a low-energy charged particle through an upper ACD tile. When veto 30 finds these conditions, it eliminates the event.

Veto 29

Veto 29 is slightly more complex. Unlike veto 30, it concerns events that do cause backsplash. Veto 29 eliminates events that have a CAL LO trigger, but not a CAL HI, and still show evidence of backsplash. The backsplash evidence is either 4 or more ACD tiles over threshold (any tiles), or any three hit ACD tiles distributed such that one of the tiles is not touching one of the other two on the side or a corner (it is separated from the others). In Figure 5.1, this no-clustering condition

[3]Collectively, these tiles are known as *filter tiles*.

is labeled according to its function call in the code: "AFC_splash()."

The AFC_splash() condition is present because it might be possible for a gamma to convert to an e^+e^- pair that could then pass out the side of the LAT (depending on the trajectory). The pair, and any other secondaries, could cause ACD tiles to go over veto threshold. One would expect that the particles would follow trajectories that were similar to the original gamma, and any hit tiles would be tightly clustered. This is an effect that one would not expect on average from CAL backsplash. The AFC_splash() condition is looking for evidence of backsplash, so it looks for tiles that are *not* clustered.

In general, the higher the energy of a gamma-ray event, the greater the probability that backsplash will cause ACD hits. Veto 29 only eliminates lower-energy events (those without a CAL HI), because eliminating higher-energy events with filter tile hits introduces the danger of gamma-ray rejection. If the gamma ray is not energetic enough to cause a CAL HI trigger, it is still possible for it to cause enough backsplash to put a few filter tiles over threshold. However, if more than 3 tiles, any tiles, go over threshold for an event that is not energetic enough to cause a CAL HI trigger, the event was more likely caused by charged particle background, because they cause larger showers at a given energy. Sideways-going cosmic-rays are a common cause of multiple tile hits.

Vetoes 28 and 27

The next veto, number 28, is similar to veto 30 in that it compares the level of activity in the ACD to that in the CAL. Specifically, it looks to see if there is less

than 10 MeV of uncorrected energy in the CAL[4] and requires that the ACD be completely quiet, or the event will be vetoed. This requirement is more stringent than that in veto 30.

If the ACD has any hits at all, and there is less than 10 MeV in the CAL, it is most likely that the reason for the hit was a cosmic ray. However, if the energy is more than 10 MeV, but less than 350 MeV, the Onboard Filter allows the bottom two rows of the ACD to have tile hits, but the upper ACD filter tiles must have no hits. This is possible for the reason explained above: a gamma ray with little energy might generate enough conversion products to create ACD hits in the lower rows, but not the upper rows or front. If there is a low-energy event that coincides with ACD hits in the filter tiles, it is most likely because of a cosmic ray. This condition will cause veto number 27 to be set. Note that the only difference between veto 27 and veto 30 is that veto 27 is activated when the energy is between 10 and 350 MeV, but veto 30 is activated when there is a CAL LO trigger. It is possible to have 10 to 350 MeV in the CAL without causing a CAL LO trigger, but it is not possible to have a CAL LO without a minimum of 100 MeV. Because veto 30 has the broader energy condition and comes first, it will eliminate many of the events that would also get rejected by veto 27.

Veto 26

Like veto 29, veto 26 uses two types of backsplash detection. First, if the energy in the CAL is less than 40 GeV, and there are more than 4 tiles hit, the event is

[4]Recall that when transmitted to the ground, the CAL energy deposit is corrected for leakage and other effects, including dead material, gaps, and energy losses in the tracker.

judged to be a background event. It was believed that a gamma ray with less than 40 GeV would not cause a large enough backsplash from the CAL to cause 4 tiles to go over threshold.

Now if the energy in the CAL is less than 40 GeV, but exactly 3 tiles are hit, veto 26 also checks the pattern of hits in the ACD. As with previous vetoes, the premise is that the conversion of a gamma could produce secondaries that pass out the side of the ACD, causing tile hits. Veto 26 checks for tile clustering; if clustering is not found, the event is rejected as background.

Veto 21

At this point in the Onboard Filter algorithm, the event processing has gone through five veto cuts, and they all have to do only with the ACD and the CAL. With many of the remaining vetoes, Onboard Filter examines tracker activity. The first of these, number 21, evaluates what is called a *Z-bottom* veto. The Z-bottom veto rejects an event if the event has at least 10 MeV in the CAL, but does not show evidence that a particle track is pointing at the CAL. The necessary track evidence is defined as strip hits in any of the 4 of 6 planes of silicon adjacent to the CAL. If 4 planes are hit, and there is greater than 10 MeV, the event is not vetoed.

This veto was designed to remove the events caused by upward-going cosmic rays that interact in the CAL and create upward-going gammas. These gammas might pass into the tracker and convert a few layers up from the CAL, producing tracks that are separated from the CAL by a few layers.

Vetoes 25 and 24

Continuing through the algorithm, vetoes 24 and 25 deal with a combination of ACD and tracker information. Recall, the modular design of the LAT allows each tower to self-trigger when there is a 3-in-a-row. This means that when 6 consecutive planes of silicon, or 3 X-Y pairs have hits, a tracker trigger is initiated. However, vetoes 24 and 25 are not restricted to dealing with towers that have tracker triggers. They also consider towers that *almost* have a tracker trigger, because the Filter allows for the possibility that the tracker trigger condition is more restrictive than necessary for these vetoes. The Filter recognizes that some events might have tracks that do not cause a hit in one of a series of silicon planes. The algorithm first builds a list of those towers that have a minimum of 4 hit planes out of 4 consecutive planes of silicon (a 4/4 coincidence). The list of 4/4s is just the starting point. Once those towers are identified, vetoes 24 and 25 look within them for either 7 hit planes out of 8 consecutive planes (7/8) or 6 hit planes out of 6 consecutive planes of silicon (6/6). Searching for 7/8s is more computationally intensive than searching for a simple 4/4 or 6/6, and each 7/8 coincidence contains a 4/4, so searching for 4/4s is a method of quickly identifying possible 7/8s.

Once towers with 6/6 and 7/8 coincidences are identified, the algorithm looks for hit ACD tiles that are adjacent to those towers. This task is split between the two vetoes. Veto 25 looks above a "triggered" tower to see if any of the 4 tiles above that tower (that shadow it) are over veto threshold. If so, and if the 6/6 or 7/8 began in the top three layers (top 6 planes), the veto is activated. The layer

condition is present to help ensure a link between the tower trigger and the ACD hit – a signature of a cosmic ray. Veto 24 looks to the side of an edge or corner tower to see if one of the ACD tiles in the upper two rows of the adjacent side face (or faces) is hit. If so, and if the beginning of the 6/6 or 7/8 is at the same height or below the tile, the veto is activated. This layer-height condition is present to guard against the rejection of a gamma ray whose products exit out the side of the LAT as they travel downwards. Such an event would have a track starting in a layer that might be higher or at the same height as a hit ACD tile.

If a tower is shadowed by both a side tile and a front face tile, only veto 25 is set for the top face veto, because this cut comes first in the code, and it is not necessary to look at veto 24 also. These vetoes are present because a triggered tower that is adjacent to a hit ACD tile may be a sign of a cosmic ray that passed through the tile and triggered the tower.

Vetoes 23 and 22

The next two vetoes, numbers 23 and 22, deal entirely with energy distributions in the CAL when the event deposits less than 300 MeV. Veto 23 requires that the energy in the layer next to the tracker be 1% to 90% of the total energy deposit in the CAL, because downward-going low-energy gammas should deposit a large fraction of their energy in the top layer. If the energy in this layer is less than 1% of the total, veto number 23 is set. If the energy in the layer is greater than 90% of the total energy, veto number 22 is set. These simple ratio checks are designed to ensure that the particle responsible for the energy deposit enters into the CAL

from the tracker and moves downward. This requires that at least 1% of the total energy be deposited in the layer next to the tracker, and that the shower develop as it moves away from the tracker such that not greater than 90% of the energy is not deposited in the first layer the particle encounters. Cosmic rays, or even gammas, that do not pass through the tracker first may have energy distributions in the CAL that are inconsistent with these ratio checks, and they will be vetoed.

Veto 17

The next veto, number 17, which is present in more than one location in the Filter, asks if there is any possibility of reconstructing a track. It asks if there are any locations in a tower where there are at least 4 planes of silicon hit in a row. If so, Onboard Filter decides that processing may continue, because this is some indication that the more sophisticated ground reconstruction might be able to find a track. However, if the 4 planes condition is not met, the event is rejected, because a gamma ray without a track has limited scientific use, and many events with few plane hits are low energy background events, especially gamma-ray albedo.

Vetoes 20, 19, 18, and a Description of the Track Finding Method

The next three vetoes are related, and they are among the most complicated of the 16. Each of them requires that Onboard Filter do fast track reconstruction and then project the tracks back to the ACD to see if they intersect an ACD tile that is hit. This is similar to vetoes 24 and 25, which looked for a match between a triggered tower and a shadowing ACD tile, but the track-tile matching done here is more

complicated and more accurate. If an ACD tile is hit, and there is a track pointing to it, the reason was very likely a cosmic ray. Veto number 20 checks to see if a track points to a tile in the front of the ACD, while veto 19 checks the upper two rows of the side faces, and veto 18 checks the lower two rows of the side faces.

Onboard Filter's track finding method is tower based, so the track finding algorithm loops over towers that have what the Filter code defines as the potential to have a track. This potential requires strip hits in at least 4 planes of silicon in a row – a less stringent requirement than the 6/6 or 7/8 required for vetoes 24 and 25. The track finding algorithm does not actually look for three-dimensional tracks, but instead forms two-dimensional *projections* that are formed by strips that are oriented in either the X or Y direction. X strips are those that can be used to measure distance along the X-axis; regardless of their position in the tracker, they are each parallel to the Y-axis. Conversely, the Y strips are parallel to the X-axis, but measure distance in the Y direction. As the algorithm searches for projections, it first begins with the X strips. On a given plane within a tower, these strips are organized into 4 ladders of 384 strips each, spaced 0.228 mm apart (the *strip pitch*). Between each ladder is a gap of approximately 9.5 strips. The strips are numbered from 0 to 1535 within each tower, beginning at the -X (or -Y) end.

Before examining each strip for a hit, the code looks only in the X orientation for every occurrence of three X-planes in a row that have strips. The hit strips are allowed to occur anywhere on the planes within a single tower. If there are more than 3 planes in a row with strip-hits, each occurrence of a 3-planes-in-a-row is

noted. For example, 5 planes in a row would be counted as three occurrences of a 3-planes-in-a-row. After making a list of the locations of each 3-planes-in-a-row, the algorithm begins at the uppermost plane at the first strip-hit it encounters on that plane (going from lesser numbered to greater numbered strips). The strip-hit temporarily anchors the top of the projection as the algorithm begins to look down into the tower. With the top of the projection anchored, the algorithm goes down two X planes to the last layer of the 3-planes-in-a-row to fine the lesser numbered strip-hit. The algorithm then draws an imaginary line between the top and bottom hits, and determines where the line crosses the plane in the middle.

The middle plane does contain at least one strip-hit somewhere among the 4 ladders, but it could be anywhere on the plane within that tower. Drawing a line between strip-hits on the top and bottom planes of a 3-planes-in-a-row gives the algorithm a starting point from which to look for the middle hit. A hard-coded tolerance of 32 strips (which can be updated from the ground if necessary) is the distance the algorithm will look for a strip-hit to either side of intersection of the middle layer and the imaginary line. If there are multiple strips that lie in the range defined by the tolerance, the closest strip to the imaginary line is chosen. Once the middle strip-hit is settled upon, a projection is defined by connecting a line between that strip and the layer above. Even though three planes are used to find a projection, only the top two hits define the projection. Still, all three hits belong to the projection, which is then extended down more planes beyond the original 3-planes-in-a-row. The algorithm looks for any strip hits that lie close to the extended

projection (allowing the tolerance to increase as the projection extends), and adds those hits to the projection. It also extends the projection upwards in case hits were for some reason missed. Any hit can be assigned to only one projection, so once it is assigned, it is removed from a list of hits that can be used for any remaining projection finding in the tower.

If the strips on the middle plane lie outside the range defined by the tolerance, no projection is defined, but the anchor in the top plane remains fixed. The bottom anchor is allowed to move, though. If there exist any other hits on the third layer down, the bottom of the imaginary line is anchored to the next hit on that layer. This defines a new intersection with the middle layer, and the algorithm applies the tolerance as it searches for hits within that range on the middle layer. If this process continues until a line has been drawn from the top hit to each bottom hit, and still no hits are found, that top hit will no longer serve as the anchor. If there are other hits in the top layer, they will be used in turn as top anchor, and the looping over hits will continue until all hits are assigned to projections, or all possible projections have been found. When that happens, if there are any remaining 3-planes-in-a-row, the algorithm will go to the top plane of that set of three, and the process will start again. In short, every possible combination of hits is explored until all hits that can be assigned to a projection are assigned to a projection.

This projection finding process is repeated for the Y strip orientation before the algorithm moves on to the next tower. Once all towers are examined and the routine exits, a projections has been compiled. These are the projections used for

all the track related vetoes.

Because the projections are defined only by two parallel strips on different planes, they are 2 dimensional; projections define a plane, not a line in space. This plane is projected to a face of the ACD, and the algorithm determines which tiles it intersects. If the plane intersects the top face, the number of tiles intersected is always a row or column of 5. If two planes intersect the top face, one in the X-direction, and one in the Y-direction, a row of tiles and a column of tiles will intersect in one common ACD tile, which is then checked for a hit. Because the intersection of planes defines a 3-D line that defines a particle track, any ACD tile over threshold that is in turn intersected by two planes suggests that a single cosmic ray was responsible for both the hit tile and the track. Veto 20 is enacted if this is the case.

When the Filter searches for track-tile matches for side ACD tiles, it projects only one plane to a side face. The plane that is used is the one that will intersect an entire row of tiles on one or two ACD faces that are parallel to the strips that define the plane. Whether one or two faces are intersected depends on the slope of the plane and how it is positioned within the tracker. The other projection plane is not used, because for the ACD faces perpendicular to the strips that define that plane, the plane always intersects as a diagonal or vertical line. No single row of ACD tiles is intersected by that plane unless the slope happens to be very shallow. Rather than deal with the complicated geometry of determining which tiles the diagonal intersects, Onboard Filter ignores the side faces that are perpendicular to the strips,

and only focuses on the horizontal rows of tiles intersected on the other two faces. If any tile in one of these horizontal rows is over threshold, and the row of tiles is at or above the height of the tracker hit responsible for the projection, the algorithm recognizes that there is a possibility that the hit coincided with a tracker track, and the event is vetoed. If a hit tile is below the highest tracker hit, the event is not eliminated, because the tile hit could have been caused by a gamma converting in the tracker and its secondaries passing out the side as they travel downward. Veto 19 is activated if the ACD tile is in the top two rows, and veto 18 is activated if the tile is in the next two rows down.

Vetoes 16 and 15

There remain only two veto conditions for an event to filter through. The first of these, veto number 16, asks whether the projections found earlier pass through the gap between the ACD and the top of the CAL. This region is known as the *skirt*. Events that do this, if gammas, are less useful scientifically because they leave no energy deposit in the CAL. The events may also be background that came up from below. If an event makes it through the skirt cut, Onboard Filter moves on to the final vetoes.

First, the number of projections found earlier is checked. If there was only one projection, veto 17 would be set (this is its second opportunity to get set). If only two projections were found, and the CAL energy is less than 350 MeV, veto 15 is activated. This is because lower energy gamma rays are expected to produce two resolvable tracks, because the separation angle between the resulting electron-

positron pair is large. At least three projections are necessary in order to create two 3-D tracks, so the absence if this signature indicates that the event may have been background. At this point, the onboard filtering is complete.

5.4 Onboard Filter Performance

Before any Onboard Filter code can be allowed to run in flight, it must be extensively tested. Some of the testing is centered around how much processing time is necessary, and some is concerned with the effectiveness of the algorithm when attempting to discriminate between gammas and background. The former type of testing is performed by members of the collaboration who use high-fidelity, full-scale electronics test beds. The latter type of testing was performed for this thesis, and is described below. It showed that as implemented initially, the Onboard Filter eliminated too many gamma rays. A solution to that problem was developed and implemented for this thesis. It was also found that the Onboard Filter did not eliminate a high enough fraction of albedo gamma-rays. Several possible solutions to that problem were developed and tested also. An updated configuration of Onboard Filter is presented, along with its performance, later in this chapter.

5.4.1 Testing Onboard Filter

Chapter 2 explained that the Onboard Filter was embedded in GlastSim, and that it could take as input different fluxes that were generated by the simulation. In order to test the Onboard Filter performance, only a few fluxes are necessary. There are the usual background fluxes, backgndavgpdr and backgndmaxpdr, and there is the

albedo_upwards source that was described in Chapter 4. To test gammas, one can select photons of any energy and incident angle, but exploring the huge phase space of incident angles, energy, and conversion region calls for the use of a broader source. The most useful source for this purpose is called *all_gamma*. It consists of gamma rays thrown at the simulated LAT from LAT zenith to 90^o from zenith, and from energies ranging from 18 MeV to 180 GeV with a differential photon spectrum that follows an E^{-1} power-law. This energy range was chosen because it provides data over a full six decades that fall within the LAT energy sensitivity[5].

The differential photon spectral index of -1 was chosen to provide equal numbers of events in each logarithmic energy bin. This helps ensure good statistics at all energies. At the same time, processing higher energy events in GlastSim uses more computing time, so the use of a power-law achieves a balance between statistics and effective area[6]. Finally, the events are thrown at the LAT from the entire upper hemisphere, which gives good statistics from all angles. If enough gamma rays are simulated with this artificial flux, the user can select from the output files which incoming angles and which energies to study. This is usually more economical and practical than generating many different sets of data for a variety of angles and

[5]When appropriate, gammas were sometimes only generated up to 18 GeV with this source, because the highest energy events create many secondaries, and consume a lot of processing time. This makes them time consuming to create.

[6]The Monte Carlo calculation of effective area as follows. In GlastSim, the LAT is embedded in a sphere with a projected area of 60,000 cm^2. A selection of events is then defined – tracker triggers, for example – and for bins of each incident direction, we divide the number of events passing the trigger and selection criteria by the number of events thrown randomly and uniformly at the cross sectional area. This gives, for each direction, the fraction of events from that direction that meet the selection criteria. Finally, this fraction is multiplied by the area of the cross section that events are allowed to pass through. This translates the fraction at each direction into an effective area with units in cm^2.

energies.

The first Onboard Filter performance evaluation involved looking at the percentage of events vetoed for different fluxes and different selections of those fluxes. When looking at the Filter performance with respect to gamma rays, a focus was usually on those events that were more likely to be scientifically useful. A very modest requirement for this is that they cause a reconstructible track in the tracker, something that is almost always associated with a tracker trigger. For this reason, the most generous selection criterion used here for the gamma-ray performance evaluation is that they cause a tracker trigger. For the purpose of computing the remaining background rate after filtering, all the main triggers (tracker, CAL LO, and CAL HI) were considered.

Another event selection used in this chapter is the set of *goodEvent* cuts first mentioned in Chapter 4. This is a set of cuts currently under development for the ground-based background rejection. After event data is transmitted to the ground for processing, a series of cuts will be applied to remove as much background from the sample as possible. The remaining events will have a high probability of being scientifically useful gamma rays, denoted here as *goodEvents*. The definition of the goodEvent cuts used for the work in this chapter included a set of cuts to determine whether the energy of the event was well measured, a set of cuts to determine whether the direction of the event was well measured, a set of cuts to determine whether the event had a well reconstructed track, and a some other cuts that are associated with a high probability that the event was a gamma ray. All of these

cuts were developed by the collaboration with a Bayesian analysis of millions of background and gamma-ray events, and the development of the cuts is ongoing.

By looking at the Onboard Filter's impact on goodEvents, one gets the best measure of the Filter's performance, because the goodEvents are those that will be available for ground-based analysis. However, it is equally important to evaluate the Filter's performance with regard to triggered events, so as not to bias the Filter and weight one set of cuts over another. Basing Onboard Filter cuts entirely upon their impact on goodEvents is unwise, because the goodEvent cuts may conceivably change in the future. Ideally, an analysis done with the Filter "turned on" and with the Filter "turned off" would have very similar results.

Before beginning the analysis, it was deemed important to determine whether the vetoes were implemented properly and working as intended. Testing this involved a detailed event-by-event comparison of the Onboard Filter results with the GlastSim graphical event display. Events were examined, and then compared with the output of Onboard Filter. A simple, but significant bug was found and corrected before continuing. This was not unexpected, as the Onboard Filter code was early in its development cycle.

5.4.2 Initial Onboard Filter Performance Results

Runs of the maximum background source showed that Onboard Filter was rejecting $94.6 \pm 1.0\%$ of all-triggered background events, leaving 639 ± 196 Hz remaining[7]. The

[7]These errors are statistical, and are based on the number of events generated in the GlastSim run.

average background source showed that Onboard Filter was rejecting 95.1±1.2% of that source for all triggers, bringing the remaining rate to 166±41 Hz. This is lower than the requirement of a 400 Hz average imposed by the downlink limitation, so the filter performed well for background rejection. The frequency of individual vetoes for all-triggered average background is plotted in Figure 5.4. Two types of frequencies are represented in the plot. In grey are the *inclusive* frequencies, which means the frequency of the veto regardless of whether other vetoes were activated in pass-through mode. The much smaller brown bars represent the *exclusive* frequencies, which are only incremented when the veto is the only one responsible for rejecting an event. In the figure, exclusive vetoes are quite rare in comparison to inclusives, which means that most background events would be removed for more than one reason if the Filter were operated in pass-through mode. This suggests that if veto cuts were altered or removed completely from the Filter logic, most background events would still be eliminated. This possibility was studied, and the results will be presented shortly.

Much of GLAST science will rely upon gamma rays around 1 GeV, so for some initial insight into which vetoes were most active, the frequency of individual vetoes were plotted for these 1 GeV tracker triggered events. Figure 5.5 shows the frequency of vetoes when the filter is run in pass-through mode. To determine the number of events that would have survived processing if an individual veto cut were not active, one should look at the distribution of exclusive vetoes. The very low frequency of exclusive vs. inclusive vetoes shows that most events can be eliminated

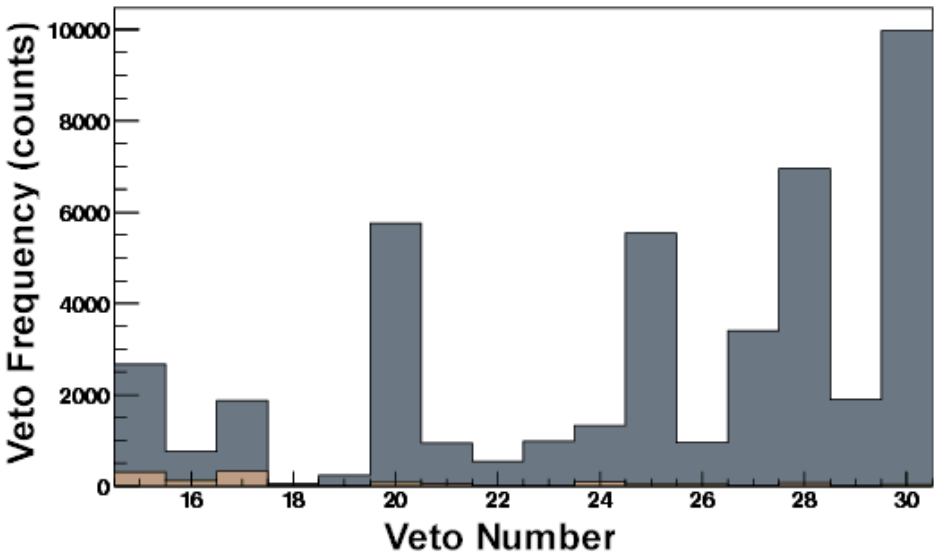

Figure 5.4: Veto frequency for all-triggered average background after code correction. Gray represents the relative frequency of inclusive vetoes; brown represents the relative frequency of exclusive vetoes.

for more than one reason. However, the ratio of exclusive to inclusive vetoes is higher than for background, which suggests that there may be a significant number of gamma rays eliminated for only one reason, and altering that veto reason would allow those gammas to pass through the Filter as is desired. This process will be described shortly. Figure 5.5 has limited use, because its single energy does not provide information on where vetoes are active in the large phase space in which gammas can be described. For that type of information, Figures 5.6 and 5.7 are more useful. Each sub-plot within those figures shows the number of events with a tracker trigger (black histogram), and those that were exclusively vetoed (blue histogram) for each individual veto as a function of the incident energy.

It is clear from Figures 5.6 and 5.7 that each veto is particularly active in a

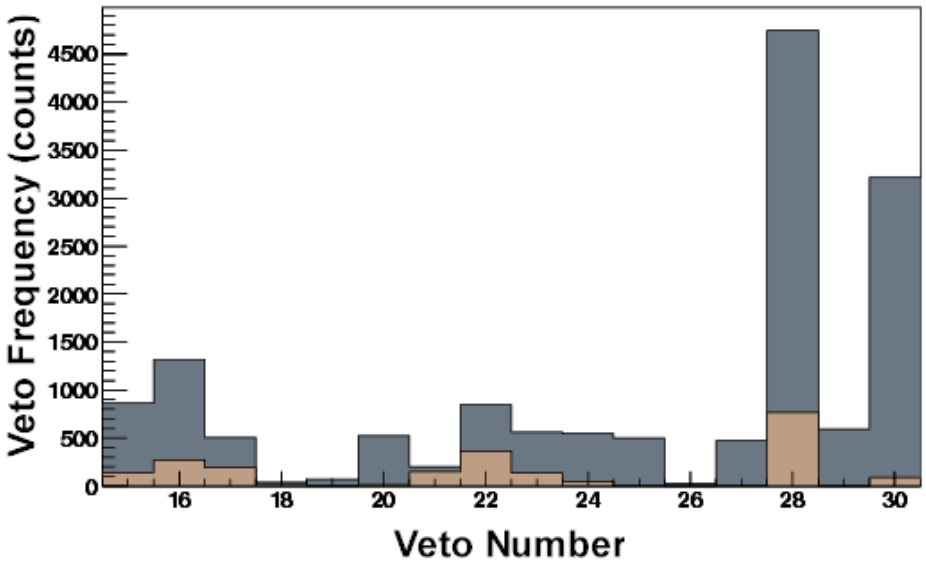

Figure 5.5: Veto frequency for tracker triggered 1 GeV gammas for the initial Onboard Filter implementation.

different energy range. Some, such as number 15, are very active at lower energies, while others, such as number 26, limit their elimination of gammas to the higher end of the energy range. When these 16 vetoes are combined, they eliminate at least 40% of tracker-triggered gamma rays at all energies, as seen in Figure 5.8. At lower energies, the fraction vetoed is above 80%. The rate of rejection increases as the incident angle from LAT zenith increases, as shown in Figure 5.9. The normally incident gammas tend to produce tracks that are easier for Onboard Filter to detect and reconstruct. At shallow angles, gammas tend to cross towers - making onboard projection reconstruction difficult - and the gammas have a tendency to cause more splash, especially at higher energies. These factors are responsible for the rising rejection rate as the angle deviates from LAT zenith.

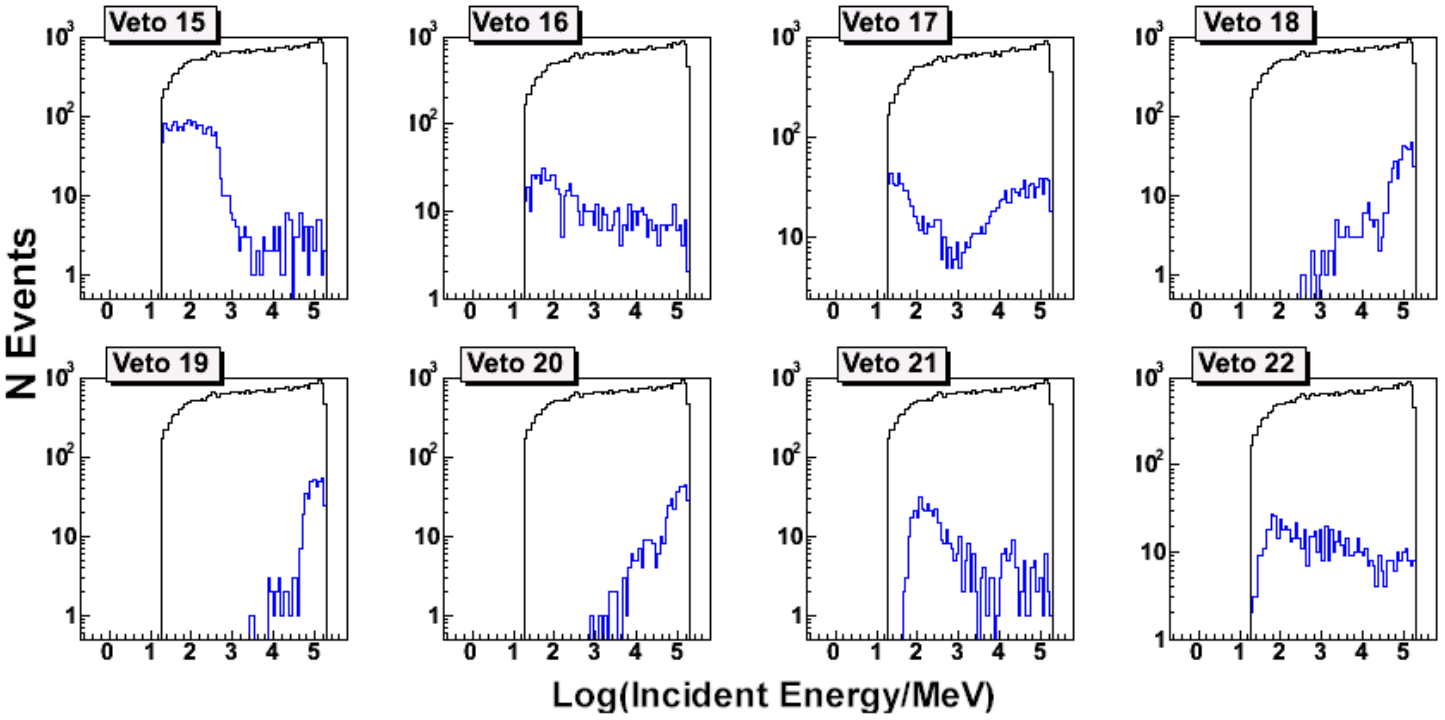

Figure 5.6: Veto vs. log of incident energy for tracker-triggered gammas for the initial Onboard Filter implementation. The black line shows the distribution of tracker-triggered events, while the blue histogram shows the distribution of exclusive vetoes for each veto. Vetoes 15 through 22 are shown.

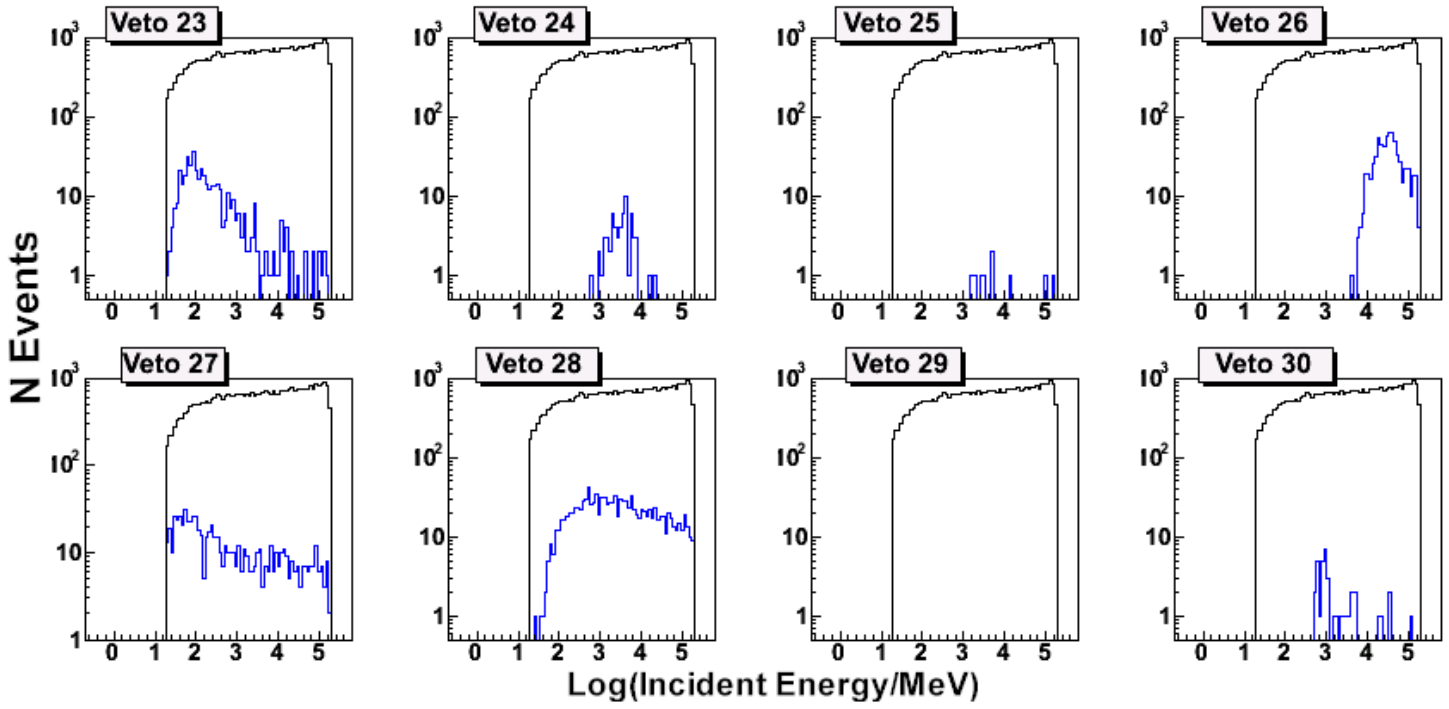

Figure 5.7: Veto vs. log of incident energy for tracker-triggered gammas for the initial Onboard Filter implementation. The black line shows the distribution of tracker-triggered events, while the blue histogram shows the distribution of exclusive vetoes for each veto. Vetoes 23 through 30 are shown.

A quantitative measure of the Filter's performance can be obtained by calculating the effective area at normal incidence in different energy bins. See Tables 5.1 and 5.2 for the initial Onboard Filter performance as measured in effective area and field of view[8] for both tracker-triggered gammas, and for the goodEvent gammas. For both tracker-triggered and goodEvent selections, the effective area at normal incidence is less at lower energies, but this is before any onboard filtering. After the Onboard Filter is applied, the effective area is also decreased most substantially at lower energies, which is what one would expect after viewing Figure 5.8. The third column, labeled *% Remaining After Filter Applied*, is the percentage of the post-Filter effective area at normal incidence relative to the pre-Filter effective area at normal incidence for that energy bin. For tracker-triggered gammas, the application of the Onboard Filter reduces the effective area at normal incidence to 18% of its pre-Filter value. This rises to greater than 80% at higher energies. The pattern is similar for the goodEvent selection, where the fraction vetoed is very high below 200 MeV. This is also evident in Figure 5.10, which is a plot of the fraction of goodEvents vetoed by the initial Onboard Filter as a function of incident energy.

The mission requirement is that the LAT have an effective area at normal incidence of at least 8000 cm^2 for gamma rays with incident energy of 1-10 GeV. The selection of events used for this requirement will be the events remaining after ground-based background rejection – the goodEvents. It is apparent that the requirement is marginally satisfied, but it is also clear that the LAT performance

[8]The LAT convention is to define field of view as the effective area integrated over all angles (from zenith), normalized by dividing by the effective area at normal incidence, and then multiplying by 2π to account for all azimuthal angles and to convert the result into a solid angle.

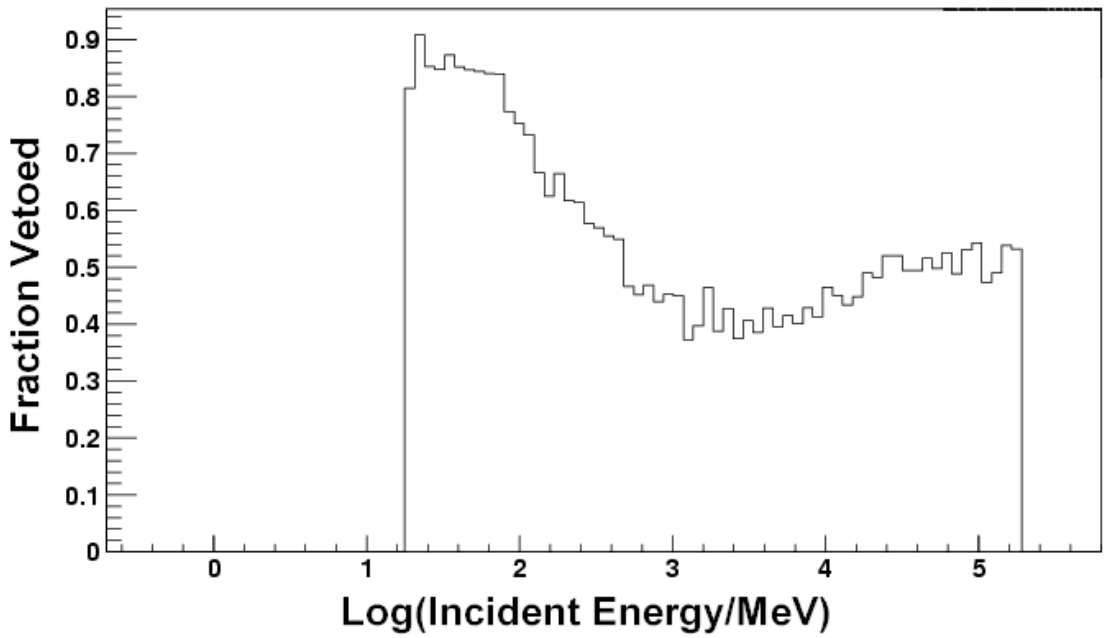

Figure 5.8: Fraction of 18 MeV - 180 GeV tracker-triggered gammas vetoed vs. log of incident energy for the original Onboard Filter. Lower-energy events were rejected at a particularly high rate. See Figure 5.10 for a similar plot for goodEvents, which is a better representation of the Onboard Filter's impact on gammas used for analysis.

would benefit from an improved Filter in other energy bins. Not all of the burden for improvement falls upon the Onboard Filter, as the goodEvent cut alone reduces the effective area substantially, but the goodEvent cut is still under development at the time of writing. Later it will be shown that even as the work for this thesis was being done, the collaboration's efforts to improve the goodEvent cuts did increase the effective area. In addition, work for this thesis reduced the Filter's negative impact on goodEvents substantially.

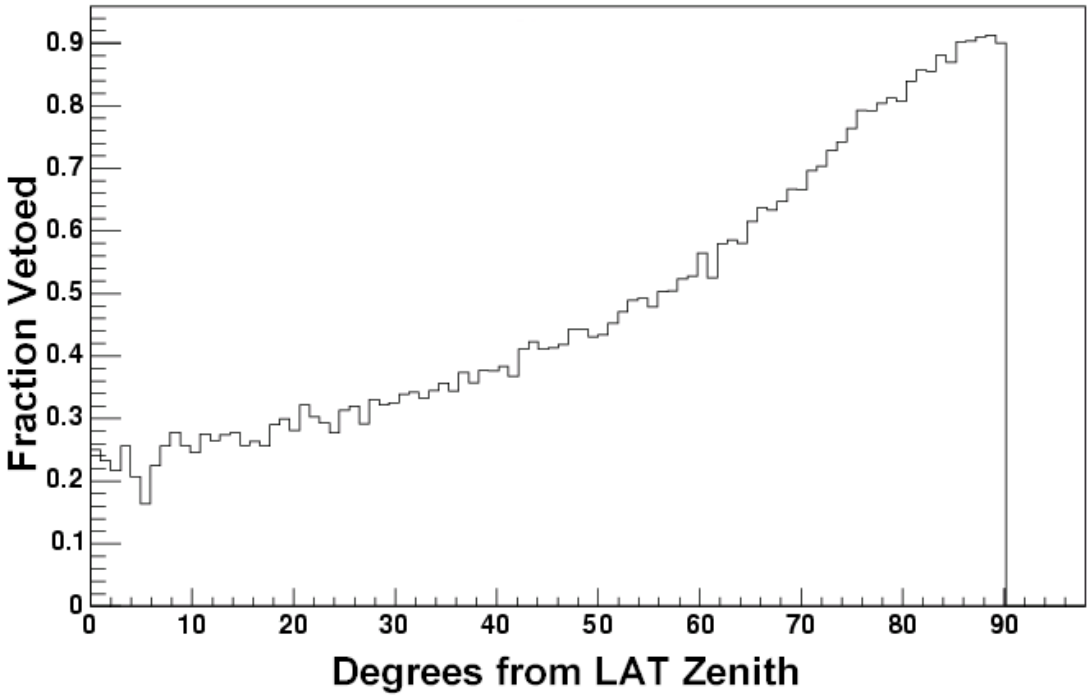

Figure 5.9: Fraction of 18 MeV - 180 GeV tracker-triggered gammas vetoed vs. angle from LAT zenith for the original Onboard Filter. The fraction of events rejected rises as the incident angle deviates from normal, because conversion products become more common, and tracks are more difficult to reconstruct.

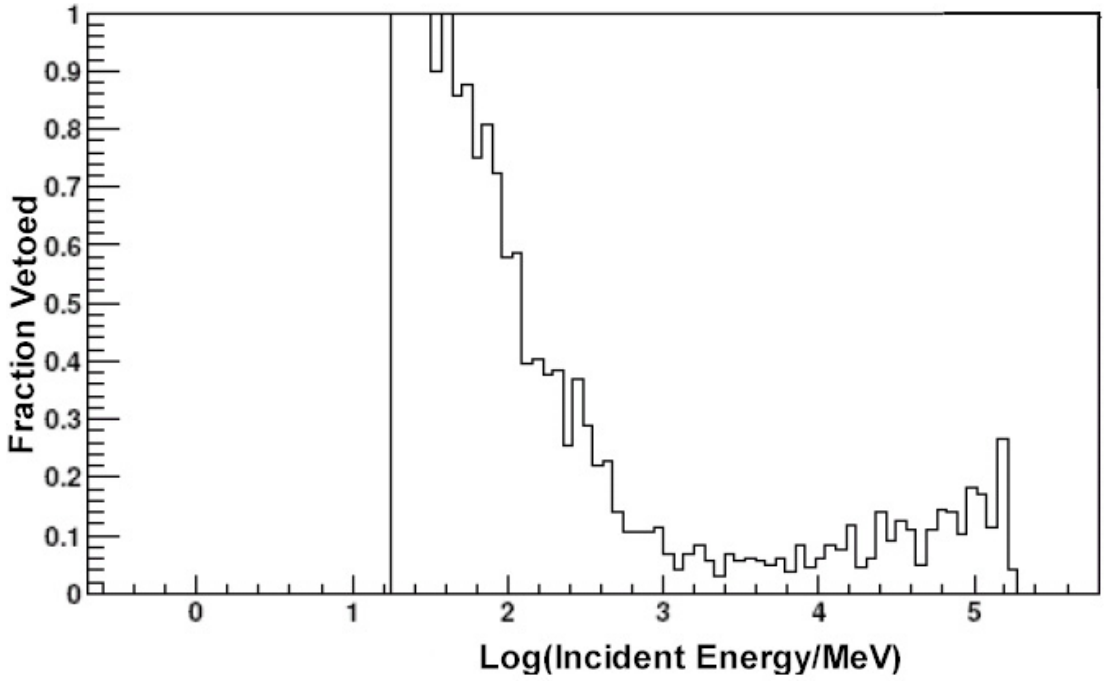

Figure 5.10: Fraction of goodEvent 18 MeV - 180 GeV gammas vetoed vs. log of incident energy for the original Onboard Filter. This plot is a good representation of what the Onboard Filter's impact would be to gammas used for ground-based analysis. The high fraction vetoed at lower energies shows that improvement is desirable.

Effective Area and Field of View for Tracker Triggered Gammas

Energy (MeV) and Cut(s)		Aeff at Normal Incidence (cm^2)	% Remaining After Filter Applied	Field of View (sr)
18-50	Tkr Trig	7794 ± 401		3.42 ± 0.18
	Filter Applied	1423 ± 171	18 ± 2	2.59 ± 0.33
50-100	Tkr Trig	10122 ± 557		4.36 ± 0.25
	Filter Applied	2607 ± 282	26 ± 3	3.13 ± 0.35
100-200	Tkr Trig	12059 ± 629		4.54 ± 0.24
	Filter Applied	5767 ± 435	48 ± 4	2.83 ± 0.22
200-300	Tkr Trig	13091 ± 845		4.42 ± 0.29
	Filter Applied	8073 ± 664	62 ± 6	2.90 ± 0.24
300-1000	Tkr Trig	12766 ± 471		4.75 ± 0.18
	Filter Applied	9684 ± 410	76 ± 5	3.15 ± 0.14
1000-10K	Tkr Trig	13391 ± 355		4.98 ± 0.14
	Filter Applied	11224 ± 325	84 ± 3	3.44 ± 0.11
10K-30K	Tkr Trig	13604 ± 515		5.28 ± 0.21
	Filter Applied	11438 ± 472	84 ± 5	3.28 ± 0.14
30K-180K	Tkr Trig	14910 ± 431		5.53 ± 0.17
	Filter Applied	12132 ± 389	81 ± 4	3.36 ± 0.12

Table 5.1: Initial effective area at normal incidence and field of view for tracker triggered gammas, before and after Onboard Filtering. Before Onboard Filter is labeled as "Tkr Trig," and after Onboard Filter is labeled "Filter Applied." These values were valid before the Onboard Filter had been updated as described in this chapter. All errors are statistical.

Effective Area and Field of View for goodEvent gammas

Energy (MeV) and Cut(s)		Aeff at Normal Incidence (cm^2)	% Remaining After Filter Applied	Field of View (sr)
18-50	goodEvents	124 ± 51		0.93 ± 0.44
	Filter Applied	62 ± 36	50 ± 36	0.70 ± 0.48
50-100	goodEvents	828 ± 159		1.63 ± 0.33
	Filter Applied	337 ± 102	41 ± 15	1.46 ± 0.47
100-200	goodEvents	2294 ± 274		2.11 ± 0.26
	Filter Applied	1770 ± 241	77 ± 14	1.99 ± 0.28
200-300	goodEvents	3545 ± 440		2.30 ± 0.29
	Filter Applied	3218 ± 419	91 ± 16	2.20 ± 0.29
300-1000	goodEvents	6340 ± 332		2.32 ± 0.13
	Filter Applied	5922 ± 321	93 ± 7	2.30 ± 0.13
1000-10K	goodEvents	8321 ± 280		2.67 ± 0.10
	Filter Applied	8076 ± 276	97 ± 5	2.63 ± 0.10
10K-30K	goodEvents	7280 ± 377		2.87 ± 0.16
	Filter Applied	7183 ± 374	99 ± 7	2.68 ± 0.15
30K-180K	goodEvents	5892 ± 271		2.97 ± 0.15
	Filter Applied	5630 ± 265	96 ± 6	2.65 ± 0.14

Table 5.2: Initial effective area at normal incidence and field of view for goodEvent gammas, before and after Onboard Filtering. These values were valid before the Onboard Filter had been updated as described in this chapter. All errors are statistical.

5.5 Improving the Onboard Filter

Several approaches were used for improving the performance of the Onboard Filter. The first was to make sure that the Filter worked as intended. If the logic was incorrectly implemented, or there were bugs in the code, it was thought that fixing those errors might improve the performance. Because it is difficult to find programming errors by simply reading through the code line by line, another method of code verification was desired. It was decided that writing a logical equivalent of Onboard Filter and then comparing its output with Onboard Filter was one such method. A side benefit of writing an emulation of Onboard Filter was that because it did not have to be optimized for speed, it could be written in an easier to read format. This would allow other members of the LAT collaboration, who are not experts in the difficult Onboard Filter code, to understand the logic and make changes to it if they wanted to develop and test a new algorithm.

Another approach to improvement is to study changes to the logic itself. Even if the implementation of the original Filter logic was correct, the first set of algorithms could possibly be improved upon. However, the Filter's success at eliminating background, and its relative success at keeping gamma rays, suggested that parts of the Filter were working well. Rather than design a completely new set of algorithms, it was thought possible to modify the existing Onboard Filter logic in such a way to eliminate fewer gammas, yet continue to eliminate enough background to meet the 400 Hz requirement. A component of the Filter logic that required special attention was the onboard projection finding, because a look at Figures 5.6 and 5.7

show that some projection related vetoes (numbers 15, 16, 17, 18, 19, and 20) occur with relatively high frequency. As explained in the next chapter, onboard tracks (built from projection pairs) may also be useful for onboard science, so the good projection finding is important.

The remainder of this chapter describes the examination of projection finding, studies of changes to the Filter logic, the writing of an emulation that led to the discovery of problems with Onboard Filter, and the reevaluation of an improved Onboard Filter's performance. After that work was completed, a new albedo gamma-ray flux was made available by the collaboration and integrated into GlastSim. We will see that this new background source presented a problem, and it required the development of targeted filtering methods that were devoted to removing that source. After all this work was completed, the gamma-ray performance had improved, and the background rejection requirement was met. Even so, relatively high rejection of very low-energy gamma rays continues to be an area for improvement.

5.5.1 Evaluating the Projection Finding Method

As just stated, the projection finding method was a identified as a possible area of improvement, because several of the projection related vetoes were relatively active. Earlier in the chapter, the description of projection finding mentioned the hard-coded tolerance that is used by the algorithm to find middle plane hits. If no middle plane hits can be assigned to a projection, a projection is not found, so the choice of a correct tolerance is important. The default value of 32 strips is equal to 7.296 mm, and the average distance between two X layers of silicon is 4.44

times that. For a vertical track, this allows for multiple scattering of up to 12.7^o to either side, which is generous enough to account for all but the extreme tails of the scattering distributions for the lower energy events. Onboard Filter does not change the tolerance as the angle deviates from vertical by increasing the number of strips on one side of the virtual projection, and decreasing it on the other. This is something that could possibly be implemented in a look-up table, but it is also desirable to minimize the amount of computation involved, and the original code designer considered a fixed 32 strip tolerance to be an adequate compromise between speed and accuracy.

However, it is possible that the 32 strip tolerance is not adequate and is the reason for some of the activation of vetoes 15 and 17. Studying this possibility involved changing the hard-coded tolerance and running different sets of gammas and background to see what happened to the veto frequency.

The all_gamma source was used to generate gamma rays from the LAT upper hemisphere between 18 MeV and 18 GeV. These runs were done with the tolerance set at the original 32 strips, and then 64, 96, 192, and 384 strips. The last value causes the projection finding method to look a full ladder-width in either direction. Figure 5.11 shows what happened to the percentage of all-triggered gammas vetoed as the strip tolerance was increased. The error bars are statistical (based on the number of events generated). Two things are evident in the plot. One is that the change in events vetoed is statistically insignificant. The second is that although there is no significant decrease overall, when going from 64 to 96 strips there is a

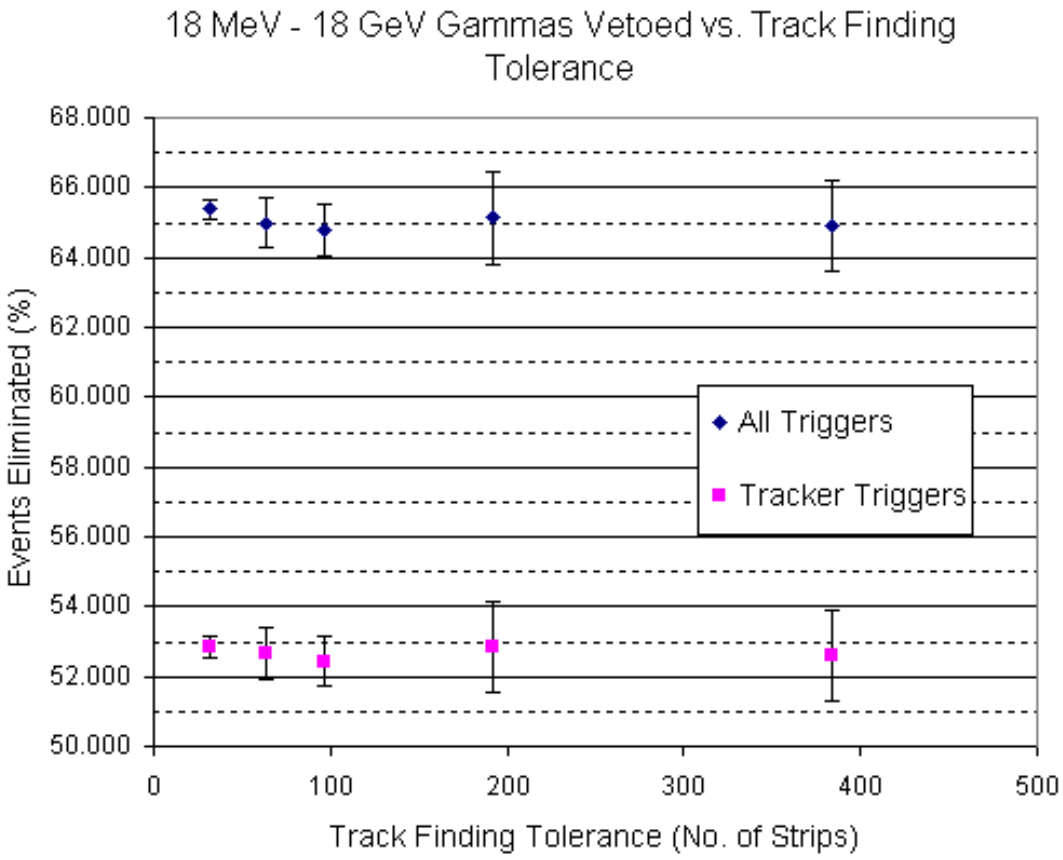

Figure 5.11: Percentage of all-triggered and tracker-triggered 18 MeV - 18 GeV gammas vetoed as a function of the track finding tolerance. As the track finding tolerance is increased, there is no statistical change in the number of gammas vetoed. Errors are statistical. The 64 and 96 runs used identical events. The 192 and 384 runs used a different set of identical events.

decrease (0.21%). The decrease is real because the exact same events were run as input to Onboard Filter for these runs. Another identical set of events was used for the 192 and 384 strip runs, and when going from 192 to 384, there is a real decrease of 0.24%. Even though this might suggest a pattern, 0.21% and 0.24% are still small compared to the 0.72% and 1.31% statistical uncertainties in veto rate for those sets of runs.

An event-by-event analysis in the GlastSim event display was also performed, and a method of reconstructing and displaying all possible 3-D tracks from the 2-D

projections was developed. These could then be compared visually with the hits visible in the event display. Events from the tolerance=32 run were selected if they had an active veto 17 and the ground based reconstruction was able to find a track. It was apparent that many of the events were rejected because the particle track crossed tower boundaries, and the projection finding routine was not able to find hits on three planes of silicon because the third hit was often in the next tower. This is a fundamental problem with tower based projection finding (used only onboard) that is addressed in Chapter 6. It was clear that even increasing the tolerance to the full width of a tower would still allow tower-crossing event vetoes. In order to eliminate these from the study of events that might have the potential for recovery with a tolerance increase, the next set of events examined were restricted to those that had an incident direction that was within 30 degrees of vertical. These events were then examined according to their energy: 18-500 MeV, 0.5-1 GeV, 1-10 GeV, and >10 GeV.

Increasing the tolerance to 64 strips was enough to recover more than half of the lowest energy events, but it required an increase to 192 strips to recover 90%. The recovered projections tended to have very inaccurate directions when compared to the Monte Carlo. It was best that Onboard Filter rejected their associated events in the first place.

For events in the next energy bins, 500 MeV – >10 GeV, the problem was distinctly different. Events were rejected not because there were not straight particle tracks, but because there would be a hit on one plane, then the next plane would

not have a hit, and then the next two planes would have hits. Without 3 planes in a row, projections were not found. Other variations on the theme of missing planes were also evident. Sometimes this was because the particle would hit a strip on the edge of one ladder, then pass between ladders – not registering a hit – when it went down a plane, and would then enter into another ladder. Nothing can be done about the uninstrumented regions between the ladders, since this is built into the design. Furthermore, increasing the tolerance will not recover events that do not deposit a necessary hit, because there is no hit to look for. In order to recover events that miss a plane for any reason, it would be necessary to rewrite the projection finding code such that it does not require three planes of silicon and so that it can handle a gap between layers. The issues raised by the individual event analysis suggest that simply increasing the tolerance will not improve projection finding and projection related veto performance.

A look at Figure 5.12 confirms the conclusions of the individual event analysis, and shows why the veto rate did not drop after increasing the tolerance. The plot shows the exclusive veto frequency of each veto bit for all 5 runs. The 1σ error bars are statistical. Note that veto 17 did decrease as the tolerance increased, but veto 15 increased. Given the structure of the Onboard Filter code, this is not a surprise. Veto 17 is activated if there are less than two projections. If projections are recovered by increasing the tolerance, veto 17 will not activate, and the event processing will continue with vetoes 16 and 15. If the event makes it to veto 15, which asks for at least 3 projections at low energy, it is still likely that it will

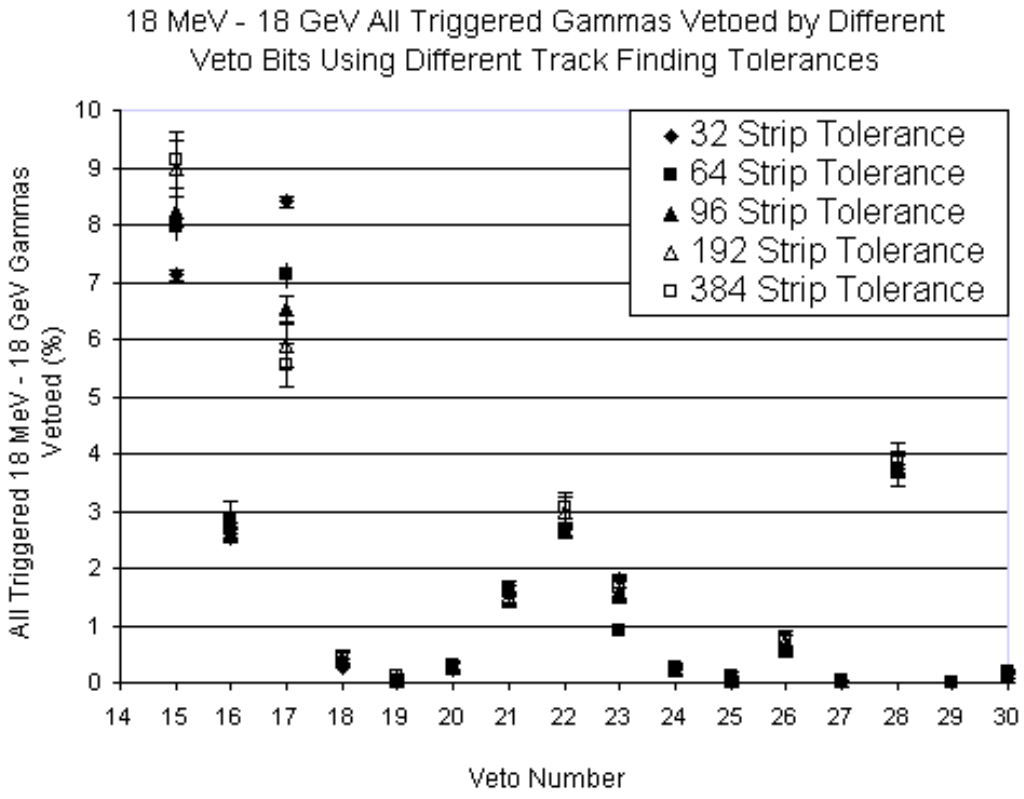

Figure 5.12: Exclusive veto percentages of each bit for all-triggered 18 MeV - 18 GeV gammas as tracker tolerance is varied. Five tolerances were tested, and the exclusive veto frequency for each bit is shown. As the tolerance is changed, the frequency of some vetoes decrease while others increase. Errors are statistical.

eliminate most of the events that were recovered by veto 17. This is because it is not as likely that increasing the tolerance will recover two or three projections as it is that the increase will recover one. And it is even less likely for the low-energy events that veto 15 applies to, because those events tend to have a scarcity of hits. So even though increasing the tolerance succeeds in reducing veto 17, this method will not solve the overall veto rate problem as long as veto 15 is relevant.

Even if increasing the tolerance did significantly lower the gamma-ray veto rate, the problems with tower crossings and the inability to deal with missing planes would remain. Figure 5.13 shows that the background rejection rate does not im-

prove (rise) with a tolerance increase, so we see no benefit with that flux either. Besides it being undesirable to increase the tolerance beyond what is physically reasonable, it is potentially dangerous, because it is possible that newly available, fake, unphysical projections might point back to a hit ACD tile and cause a veto. If the event were originally vetoed by number 17 (no tracks), this would not be an issue, because the end result is the same. But what of events that have a good track and are not vetoed? If the projection finding were to find additional projections that intersect a hit ACD tile, it is possible that a good gamma would be lost. Figure 5.14 magnifies a section of Figure 5.12 to reveal that this phenomenon does occur. Vetoes 18, 19, and 20 are those that match a track to a hit tile. Notice that as the tolerance increases, these vetoes increase in frequency. One may object that so do numbers 25 and 26, which are not track related. This reminds us that some statistical increases in exclusive veto frequency in a plot like this can be because events that had been rejected for two reasons (say veto 17 and 26) and did not contribute to the plot, now are rejected for only one reason (say veto 26), and now have an effect in the plot. In this case, the magnitude of the increase after changing the tolerance is actually an indication of how often the veto occurred in combination with veto 17. It is possible that this is what is happening with vetoes 18 and 19, because it is not impossible for them to occur at the same time as veto 17. They only require one projection, which is not enough to prevent veto 17 from happening. However, veto 20 does require two projections (an intersection of a row and column of ACD tiles in the front face), so it is incompatible with veto 17, and the rise in frequency is real

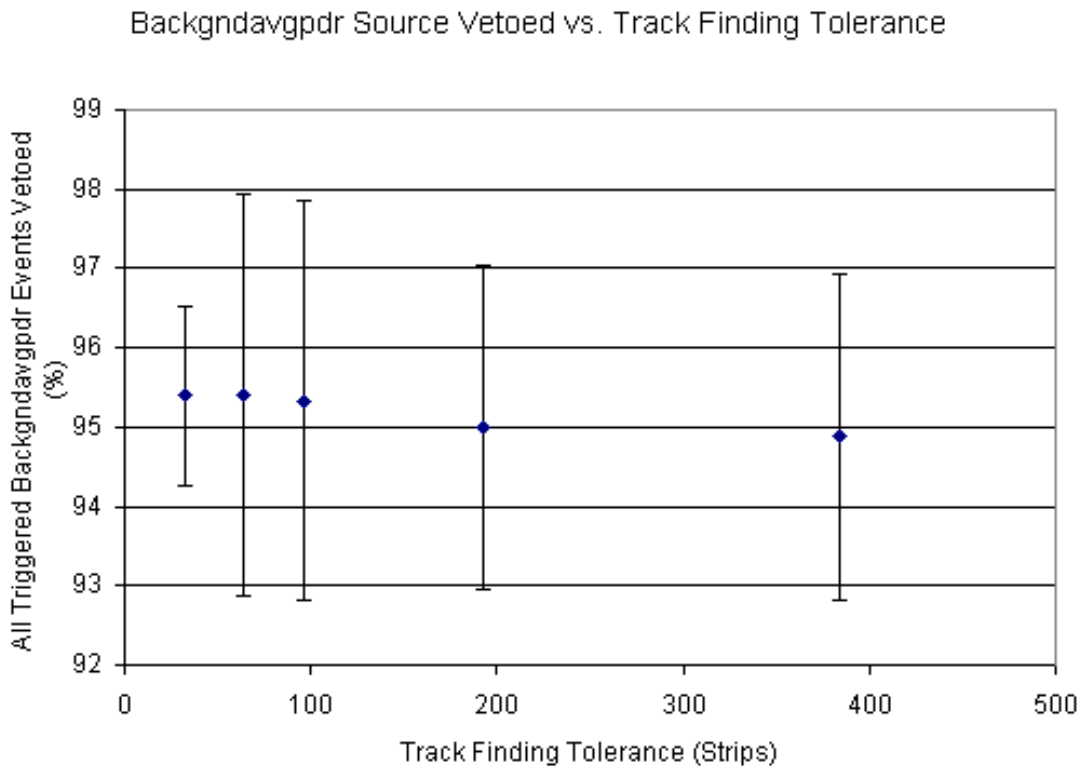

Figure 5.13: Veto percentage of all-triggered average background as a function of track finding tolerance. As the track finding tolerance is increased, there is no statistically significant change in the fraction of background events rejected. Errors are statistical.

(though we concede that the error bars weaken this conclusion). So, we see that the danger of false vetoes is still valid. When this concern is combined with previously mentioned reservations about a tolerance increase, this discussion compels one to reject a greater track finding tolerance as a solution to the high gamma-ray veto rate.

5.5.2 Studying Changes to the Onboard Filter Logic

Because increasing the projection finding tolerance is not an answer to the high gamma veto rate, changes to the Filter logic were considered. Referring to Figures

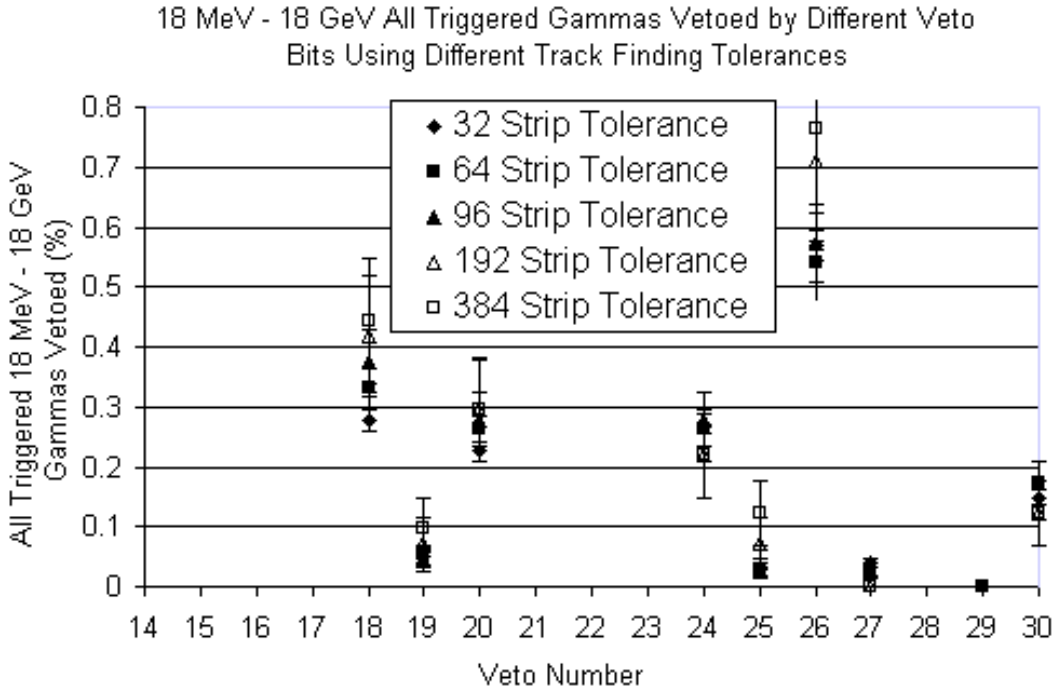

Figure 5.14: Close-Up view of figure 5.22. Note the rise in vetoes 18, 19, and 20 as the tolerance increases. This may suggest that increasing the track finding tolerance leads to false tracks that cause gammas to be vetoed. Errors are statistical.

5.4 through 5.7 again, recall that most background events are rejected for more than one reason, while many gamma-ray events are eliminated for only one reason. This is a good thing, because it suggests that altering the Filter logic or eliminating a particular veto would not necessarily allow background events to then pass through the Filter. Conversely, the relatively large fraction of gamma rays that are rejected by a single veto would be recovered if the offending veto were removed or altered. The strategy adopted here is to carefully adjust the Onboard Filter logic to allow more gamma rays through while maintaining high background rejection.

In Figures 5.6 and 5.7 the veto dependence on energy is apparent, and it suggests that one computationally simple method of altering the Onboard Filter would be to impose energy cuts on existing vetoes. However, Onboard Filter will have no knowledge of the incident energy of an event. Rather, it will know the energy as measured in the CAL. This is a simple sum of the energy deposit in the calorimeter logs, and onboard, it is not compared to shower profiles and corrected for leakage. In order to place energy cuts on existing vetoes, it is necessary to understand the veto activity as a function of raw CAL energy. Figures 5.15 and 5.16 show this for tracker-triggered gamma rays. Some vetoes, such as numbers 16, and 27, appear to be inactive, but upon closer examination, one will note that many events with zero energy deposit in the CAL are rejected.

Though the goal is to reduce the fraction of gamma rays vetoed, the background rate must also be kept below a 400 Hz ceiling, so energy cuts can not be imposed without regard to their impact on background rejection. If the average

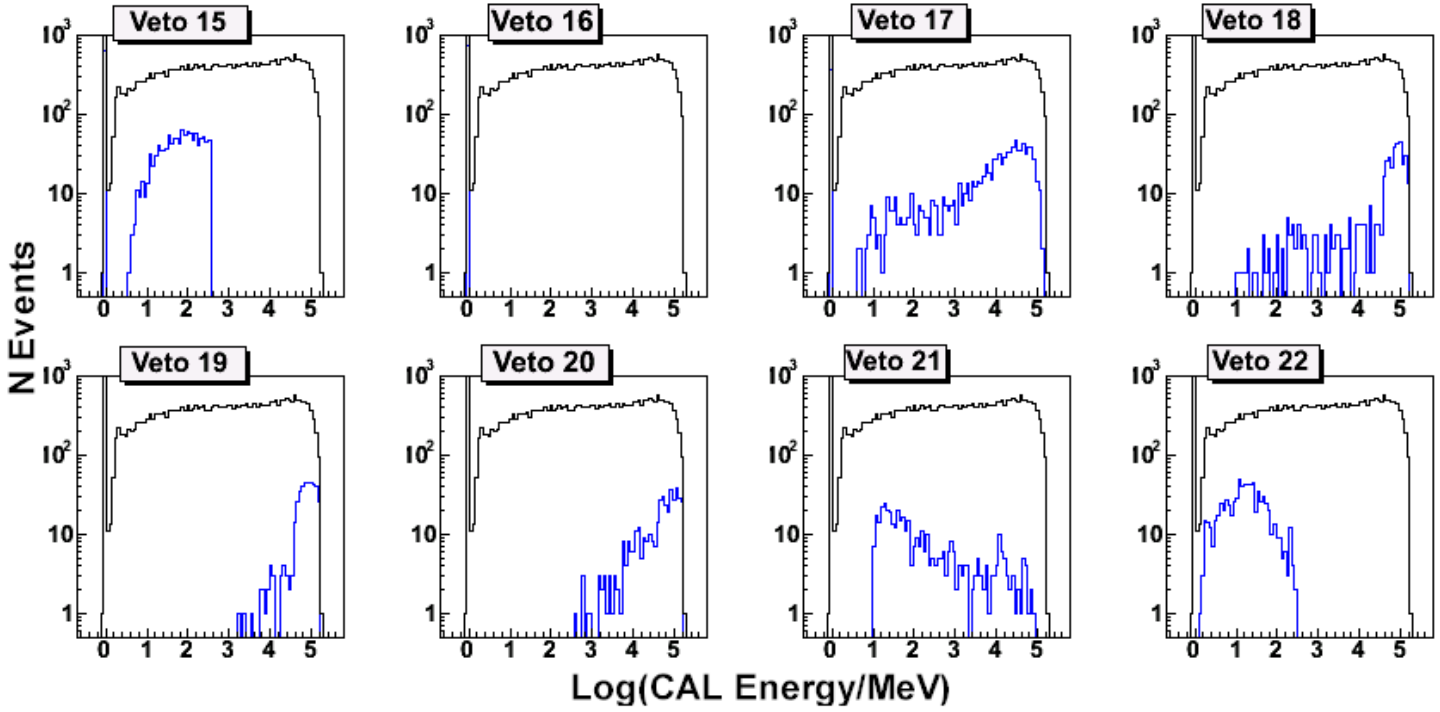

Figure 5.15: Veto vs. log of raw CAL energy for tracker-triggered gammas for the original Onboard Filter. The black distribution shows the raw CAL energy of tracker-triggered gamma rays, while the blue distributions show the number of gamma-rays vetoed by different Filter vetoes. Each blue histogram in each subplot only shows those events eliminated by the single veto corresponding for that plot. If an event is eliminated by more than one Filter veto, that event does not appear in any of the subplots. By definition, veto 16 is only active for events with zero CAL energy deposit. The sharp cutoff for veto 15 is also evident.

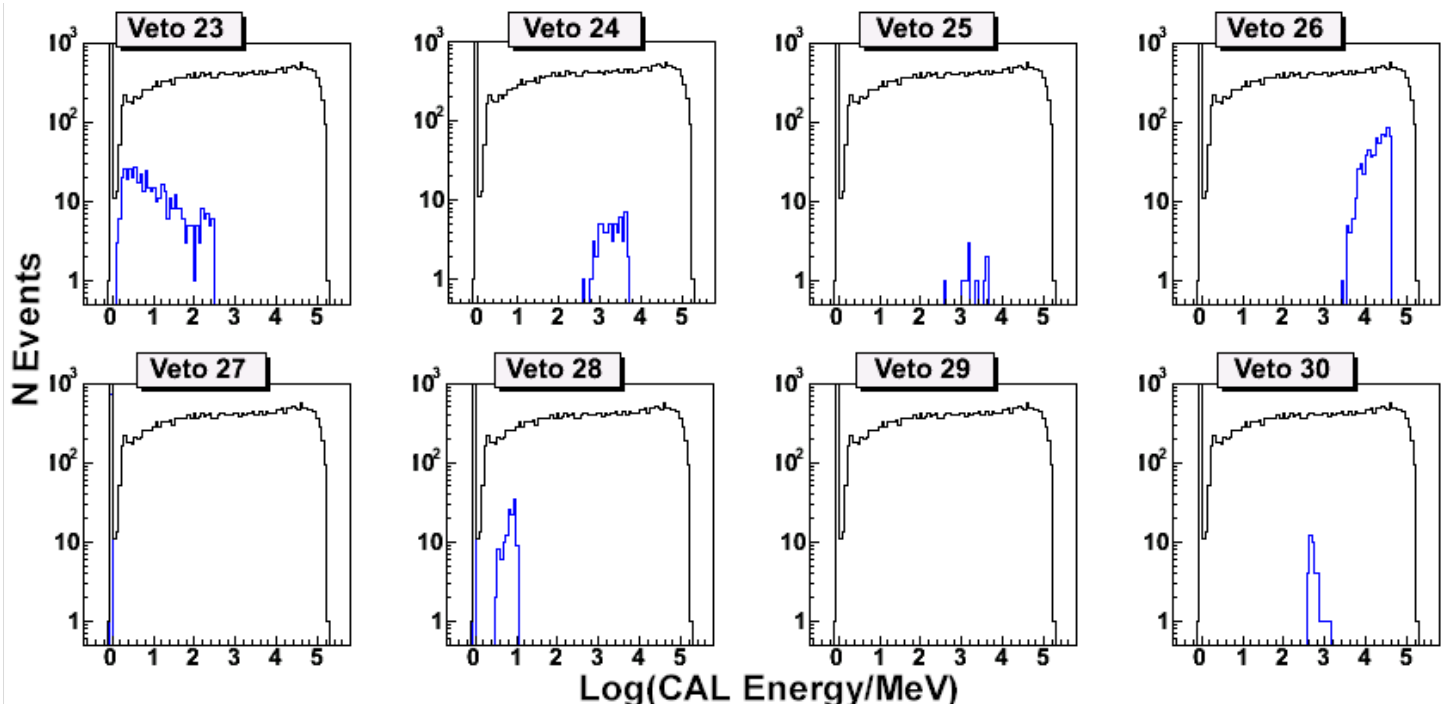

Figure 5.16: Veto vs. log of raw CAL energy for tracker-triggered gammas for the original Onboard Filter. The black distribution shows the raw CAL energy of tracker-triggered gamma rays, while the blue distributions show the number of gamma-rays vetoed by different Filter vetoes. Each blue histogram in each subplot only shows those events eliminated by the single veto corresponding for that plot. If an event is eliminated by more than one Filter veto, that event does not appear in any of the subplots. Veto 27 is only active for events with no or little CAL energy measurement. Veto 29 is not active on its own.

background trigger rate is assumed to be at or near 3600 Hz (see Chapter 4), a 89% average background veto rate is necessary at a minimum. To have a more comfortable margin, a minimal rejection rate of 90% would be more desirable. In order to gauge the possible impact on background, the veto frequency vs. CAL energy distributions are also plotted in Figures 5.17 and 5.18. Judging whether an energy cut will be effective at reducing gamma-ray rejection while still allowing for background reduction involves examining each veto vs. energy distribution for both gammas and background, and looking for an acceptable cut location. This is described in more detail shortly.

Energy cuts are not the only type of change considered for Onboard Filter. It may also be possible to remove certain vetoes completely, and later it will be shown that adding additional cuts may be necessary. It is important to note that alterations to Onboard Filter cannot be applied without consideration of their impact on the processing time. Because Onboard Filter is written such that earlier vetoes (higher numbers) are more simple and generally use fewer clock cycles, if an early veto is removed, the processing time for that event may increase. CPU cycles are a finite resource in the LAT, and they must be conserved. So as a general rule, the attempts to alter the filter started with lower numbered vetoes, which occur late in the event processing, because most events (overwhelmingly background) are rejected before getting that far in the processing.

Figures 5.8 and 5.10 showed that the rejection rate for lower energy gammas is especially high. Likewise, there is a rise in veto rate at the upper end of the energy

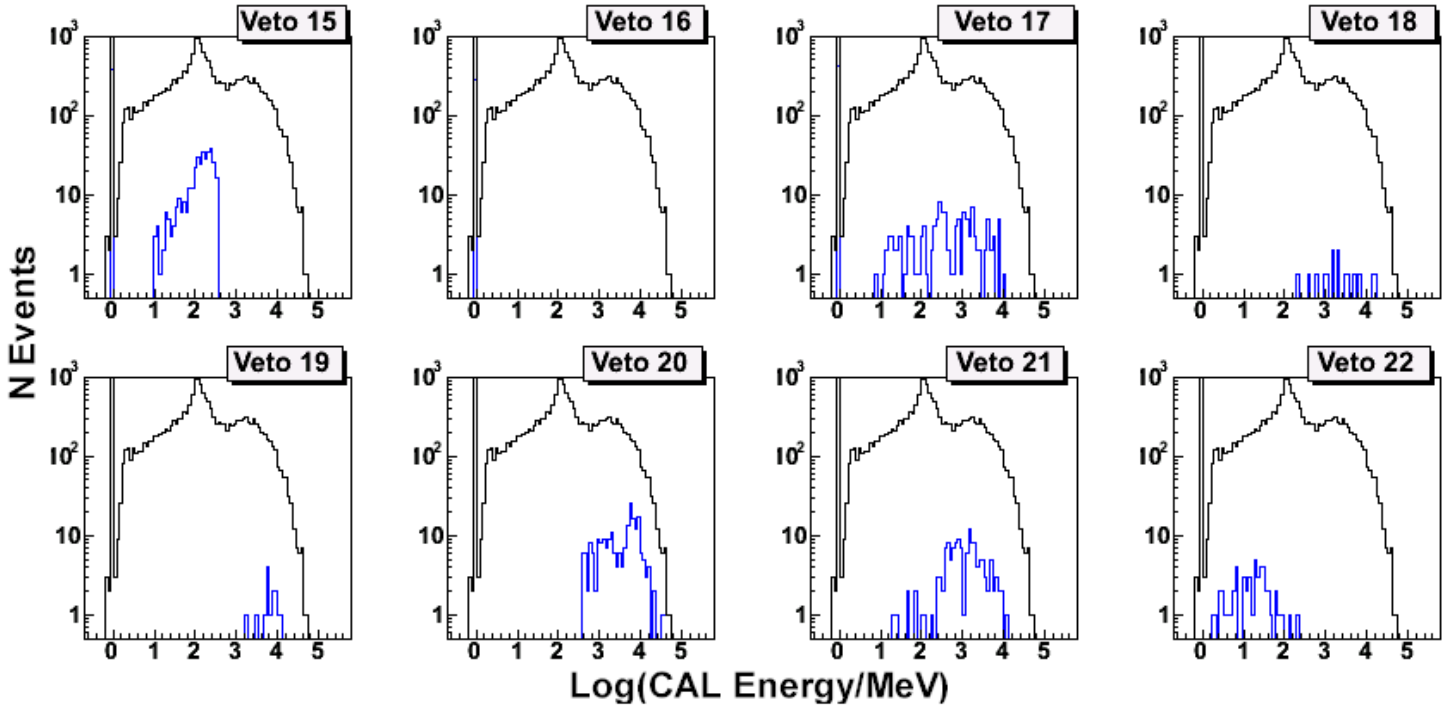

Figure 5.17: Veto vs. log of raw CAL energy for all-triggered average background after the Filter code correction described in the text. The black distribution shows the raw CAL energy of all-triggered gamma rays, while the blue distributions show the number of gamma-rays vetoed by different Filter vetoes. Each blue histogram in each subplot only shows those events eliminated by the single veto corresponding for that plot. If an event is eliminated by more than one Filter veto, that event does not appear in any of the subplots.

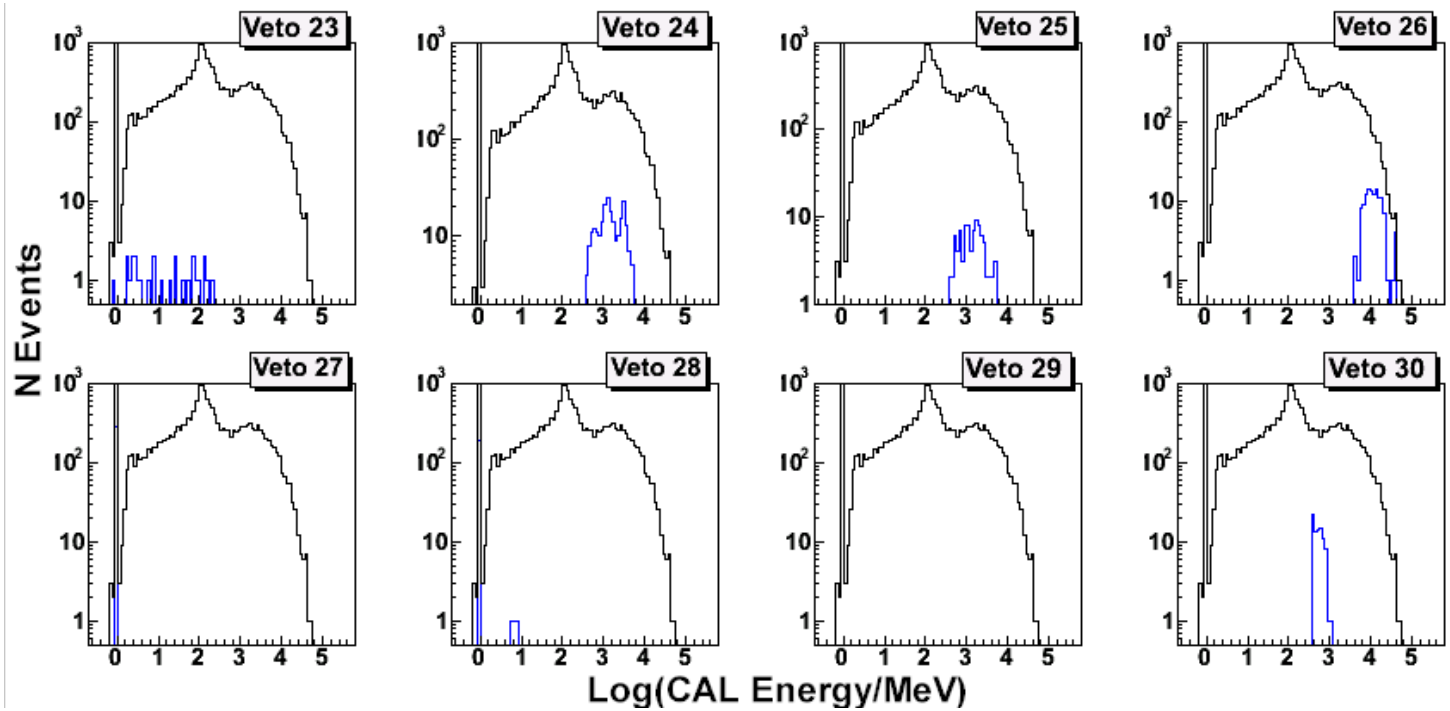

Figure 5.18: Veto vs. log of raw CAL energy for all-triggered average background after the Filter code correction described in the text. The black distribution shows the raw CAL energy of all-triggered gamma rays, while the blue distributions show the number of gamma-rays vetoed by different Filter vetoes. Each blue histogram in each subplot only shows those events eliminated by the single veto corresponding for that plot. If an event is eliminated by more than one Filter veto, that event does not appear in any of the subplots.

scale. Therefore, efforts to reduce the veto rate began with a focus on the ends of the energy scale. A look at Figure 5.6 shows that lower-energy gammas are especially removed by vetoes 15 and 17, and vetoes 18, 19, and 20 increase the high-energy gamma veto rates. Other vetoes are also active, but for the first attempt at altering the filter, these five vetoes were the focus.

Referring back to Figure 5.15, note the sharp cutoff of veto 15 at 350 MeV, a cutoff specified in the original Filter code. Below this cutoff, the veto is very active. In *Trial 1*, veto 15 was removed completely, because its reduction of gamma rays was greater than the reduction it did to background (see Figure 5.17). Veto 17 shows exhibits interesting behavior, with a significant reduction of gammas across a wide energy range, especially regarding those that deposit less than a few hundred MeV. Its impact increases below a 1 GeV CAL deposit, and is especially strong below 100 MeV. Conversely, Figure 5.17 shows that it only eliminates background above about 250 MeV. Because of its broad reduction of gammas, it might be advantageous to remove the veto entirely, but restraint must be shown because it still eliminates a substantial fraction of background. However, veto 17 should not be implemented unless the CAL energy deposit is greater than 250 MeV. In *Trial 1*, an energy cut was placed such that veto 17 that would only be enabled if the raw CAL energy was greater than 250 MeV. This would protect many of the lower energy gamma rays while still allowing veto 17 to remove background.

Turning our attention to the higher energy range, Fig. 5.15 shows that veto 18 eliminates gammas above 10 MeV, but especially reduces them when the energy gets

higher (these are log-log plots). Its impact on background is relatively small, but not ignorable, and it is best to be as conservative as possible when making changes. The veto can be kept, but restricted so that it does not activate above a 30 GeV deposit, which is approximately where it starts to reject a significant fraction of gammas. This also preserves much of its contribution to background rejection.

Veto 19 exhibits a similar problem, except that its impact is limited to a narrower energy range. Restricting its activity to events that deposit less than 10 GeV limits its reduction of gammas, while allowing it to continue to have most of the same impact that it had on background. With veto 20, the pattern continues, and it is not difficult to determine where the cut should go. Note that it is relatively active when background is the source, but the bulk of the background reduction is below 30 GeV, which is where we happen to see a sharp rise in the number of gammas rejected. This is where the cut is placed.

At this point, veto 15 has been removed completely, and cuts have been placed on vetoes 17, 18, 19, and 20. After running new samples of gamma rays and average background, the impact can be evaluated. The background rejection dropped to 92.4±1.1% for all-triggered events, but the energy-averaged gamma-ray veto rate went down to 58.3±1.5%, which is a drop of 6.8%. If only tracker triggered gammas are considered, the rejection rate went down from 52.8±0.5% to 44.7±1.5%, an 8.1% decline. These alterations to Onboard Filter appear to be successful, but with a background at 92.4%, there is still room for improvement.

Proceeding with a focus on the gamma-ray energy range with the greatest

reduction, the low-energy events, it is clear that vetoes 22 and 23 are particularly active. The exclusive frequencies of these cuts are not very active for background, however, so they were removed and the impact calculated. The all-triggered background rate drops to 91.3±1.6%, but the all-triggered gamma veto rate rises to 53.9±1.2%. This is a statistical effect, but there is clearly no drop. However, the veto rate of tracker triggered gamma events does go down to 38.2±1.1%. This was *Trial 2*.

There was still room to go with background, so a restriction was placed on veto 21, which strongly vetoes low-energy gammas. It rejects background primarily above 100 MeV, so it is now only allowed to activate if there is at least 100 MeV in the CAL. This causes the all-triggered background veto rate to drop slightly to 90.9±1.6%, and the all-triggered gamma veto rate to go to 52.6±1.1%, which is still statistically equivalent to the *Trial 1* result. The tracker-triggered veto rate does drop slightly, though, to 36.5±1.0%. This was *Trial 3*.

With about 30-40 Hz margin to work with, there is still room to increase the gamma acceptance, so the fourth Trial removes another relatively active veto, number 26. This veto is responsible for rejecting much of the background that deposits in the higher-energy range. However, there is comparatively little background in that energy range anyway. When the effect is examined, we see that the all-triggered background veto rate drops less than half a percent to 90.5±1.1%, for a remaining rate of about 340 Hz. The all-triggered gamma veto rate went to 51.2±0.8%, and the tracker triggered gamma rate goes down two percent to 34.5±0.8%. Any addi-

tional changes beyond this point bring the background rate very close to the 400 Hz limit, so care is necessary. Figures 5.19, 5.20, and 5.21 show the logic of this *Trial 4*, where the grey boxes are those logic elements that were removed. The new energy cuts are also noted in the figures.

Several additional variations were tested, but they caused the background rate to go too high, so they were not implemented. For example, *Trial 5* removes veto number 28 and causes the background veto rate to drop down to 88.2±0.9%, for a remaining trigger rate of about 425 Hz. A safer alternative is *Trial 6*, which removes veto 16, which by definition only rejects events that do not deposit anything in the CAL, and may therefore have less scientific use. The background rate for *Trial 6* drops down to the limit, at 90.0±1.5%. The all-triggered gamma veto rate goes to 47.6±1.0%, with a 30.5±0.9% rejection of tracker triggered events. Going this close to the 400 Hz limit does not leave margin for error, so it is safer to use the less aggressive *Trial 4*. The *Trial 4* version of Onboard Filter is summarized in Table 5.3.

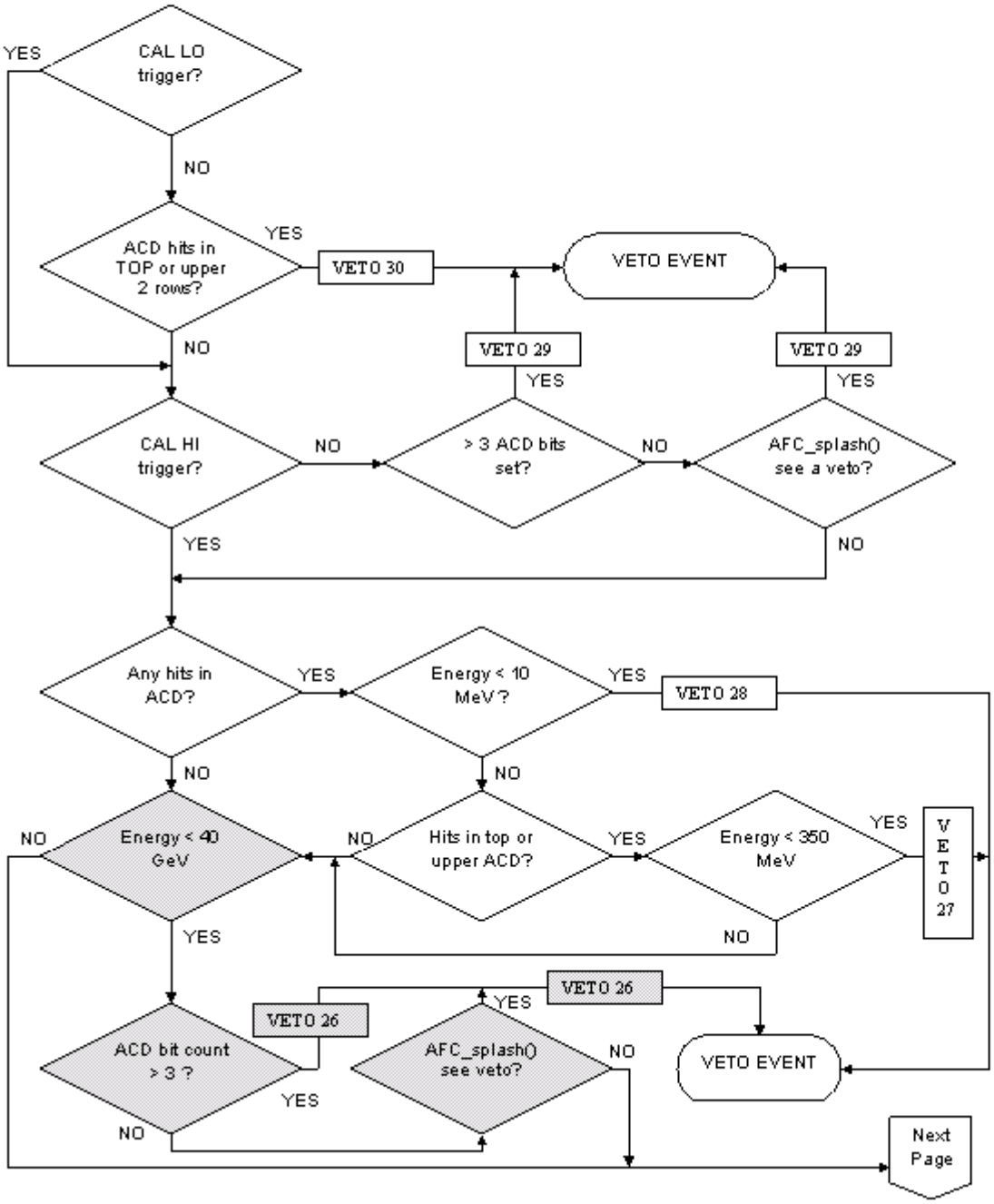

Figure 5.19: Revised Onboard Filter Logic - Page 1. Grey boxes correspond to vetoes that were removed from the algorithm. Compare to Figure 5.1.

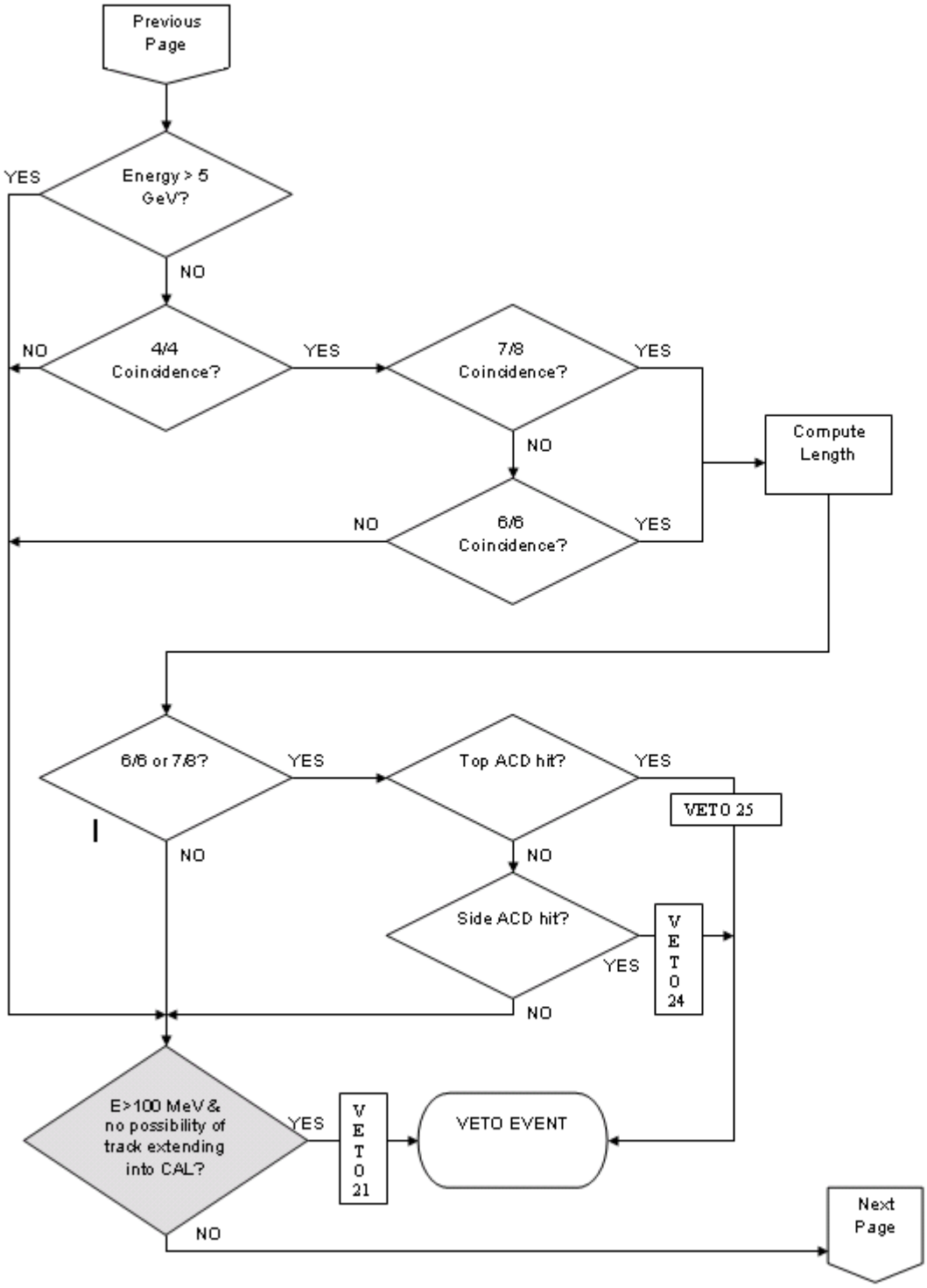

Figure 5.20: Revised Onboard Filter Logic - Page 2. The grey box indicates that a change was made to the veto logic. In this case, the CAL was required to have at least 100 MeV in order for veto 21 to be active. Compare to Figure 5.2.

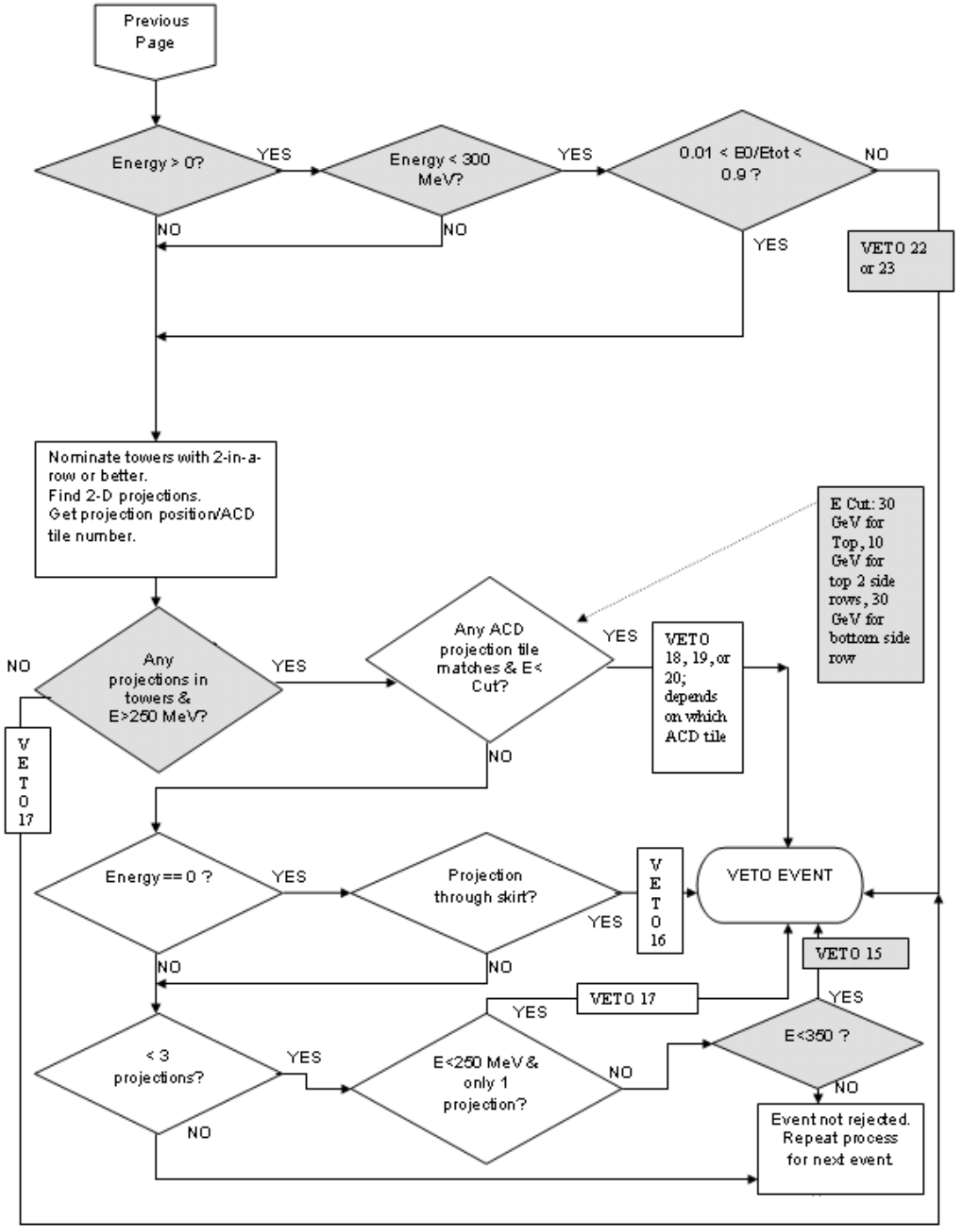

Figure 5.21: Revised Onboard Filter Logic - Page 3. Grey boxes indicate logic that was changed or removed. Vetoes 15, 22, and 23 were removed. Veto 17 was only allowed to activate when there was at least 250 MeV in the CAL. Vetoes 18, 19, and 20 have energy requirements as indicated in the text box. Compare to Figure 5.3.

Veto Number	Veto Description Before Changes	Changes Made for *Trial 4*
30	ACD upper tile hit, but no CAL LO trigger	none
29	Splash: CAL LO, but no CAL HI trigger, and any 4 tiles hit OR 3 tiles in splash pattern	none
28	No energy in CAL, but ACD tile is hit	none
27	E<350 MeV, and ACD filter tile hit	none
26	Splash: >4 tiles hit for E<40 GeV, OR 3 this in splash pattern	DISENGAGED
25	ACD tile hit in top face shadows a tower with a tracker trigger	none
24	ACD tile hit in upper 2 rows of a side face is adjacent to tower with tracker trigger	none
23	Ratio of E in top layer of CAL to total CAL E is <0.01	DISENGAGED
22	Ratio of E in top layer of CAL to total CAL E is >0.90	DISENGAGED
21	CAL E>10 MeV, and no evidence of track into CAL	Changed to E>100 MeV
20	One X and one Y track projection intersect a hit ACD tile	Require E<30 GeV
19	One track projection intersects one of two upper rows of side ACD tiles, in which there is a hit	Require E<10 GeV
18	One track projection intersects one of two lower rows of side ACD tiles, in which there is a hit	Require E<30 GeV
17	No evidence of at least one 3-D track (2 projections)	Require E>250 MeV
16	Projection may have passed through the gap between the CAL and the ACD	none
15	CAL E<350 MeV, and no evidence of 2 or more tracks (3 projections)	DISENGAGED

Table 5.3: Summary of Onboard Filter veto cuts before and after *Trial 4* revisions. The left column is the veto number designation, the middle column is a brief description of what conditions cause the veto to activate, and the right column has changes made to that veto for the *Trial 4* revisions. Four vetoes were disengaged completely, and five others have new or changed energy cuts. In this table, all mentions of energy refer to the raw calorimeter energy.

Before assessing the gamma-ray performance of the revised Onboard Filter and comparing it to the original, it is necessary to pause for a description of an effort to emulate the Onboard Filter logic. Writing the emulation allowed for the discovery of bugs in the Onboard Filter code, and fortunately, the background rejection rate increased when they were repaired. At the same time, a new background flux was introduced to GlastSim. It represented the albedo gamma-ray flux coming from the surface of the Earth's atmosphere (as opposed to just from the limb), and it increased the overall background rate. The net result was that the remaining background rate for the revised Onboard Filter rose from 340 Hz to about 380 Hz, and it was decided that additional filters were necessary in order to target the albedo gammas specifically. The next sections describe the Onboard Filter emulation, the revised Filter's performance with regard to gamma rays, and the development of new albedo cuts.

5.5.3 Emulating the Onboard Filter

The Onboard Filter emulation is referred to as *FilterAlg*, and it was written to be a logically equivalent but more compact, easier to understand version that was easily integrated into GlastSim. The output of FilterAlg is in the same format as Onboard Filter's summary word, so the two can be directly compared for each event. By running events through Onboard Filter and FilterAlg, and then investigating events that did not have identical output, both Onboard Filter and FilterAlg were debugged.

One Onboard Filter error was an omission of a call to the routine that generates

a list of towers that may have the possibility of a track. This was easily fixed. Another involved the two vetoes (24 and 25) that looked for triggered towers that were shadowed on the side or the top by one or more hit ACD tiles. This logic error had no impact on the final result, at least to the extent that it was possible to generate test events on one personal computer (several hundred thousand events).

After these errors were fixed, FilterAlg's and Onboard Filter's output matched. Around the same time, collaboration members discovered that the geometry of the ACD tile arrangement had changed slightly, and the version of Onboard Filter that had been tested should be updated. After these fixes, FilterAlg was made available to the LAT collaboration, along with documentation on its functions (Wren, 2004b). Because FilterAlg did not operate under the same CPU constraints as Onboard Filter, it was easier to read, and thus easier to alter. LAT scientists were free to try their own algorithms by making changes to FilterAlg, and examples of this were programmed into the code by the author.

5.5.4 Performance of the Revised Onboard Filter

After comparing FilterAlg and Onboard Filter output, it was easier to have confidence that the Filter worked as intended, and either one could be used as an analysis tool. At this point, the revised Onboard Filter's performance was reevaluated. The average background rejection rate went to 93.6±0.8% for all-triggered events, for a remaining background of about 229 Hz. This is a 3.1% rise in rejection rate, and a >110 Hz decrease in the rate remaining after filtering.

Gammas also showed a slight increase in their rejection rate. The veto rate

for tracker triggered gammas from 18 MeV to 180 GeV went from 34.5±0.8% to 36.7±0.4%, an absolute difference of over 2% (or a $\sim$ 6% increase relative to the initial number rejected). This is not unexpected, because a more successful background rejection will usually reject more gammas. However, the rejection of goodEvents is limited to 4.4±0.2% of the total number of goodEvents. The collaboration altered the details of the goodEvent cut while the Onboard Filter was undergoing revision, so the selection of events is not exactly the same. However, the improvement of Onboard Filter is real, and is not influenced by the event selection. The improvement is easily visible if one compares Figures 5.22 and 5.23, the fractions of tracker-triggered and goodEvent gammas rejected as a function of energy for the revised Onboard Filter, to Figures 5.8 and 5.10, which were generated with the original Onboard Filter. The fraction of gamma rays rejected is substantially reduced, especially at the energy extremes. The revised Onboard Filter has very little impact on goodEvents, which is especially important. Also compare Figures 5.24 and 5.25 to Figures 5.6 and 5.7. These are the familiar plots of exclusive veto frequency vs. incident energy for each individual veto. Some vetoes appear to be more damaging than they were in the original Filter, but this is an illusion. In reality they are no more active, but they are now the only veto responsible for a gamma's rejection, whereas they previously worked in concert with one or more vetoes. This causes them to show up in the exclusive distributions.

One can see how little impact Onboard Filter now has on tracker-triggered and goodEvents by looking at the effective area and field of view of the LAT. Table 5.4

has these values for the revised Onboard Filter. The values can be compared to those for the original Onboard Filter as found in Table 5.1. More relevant are the values for goodEvents reported in Table 5.5. The table shows that the effective area for goodEvents rose due to the changed goodEvent definition, and the updated Onboard Filter now has no discernible impact on low-energy goodEvents. Furthermore, the effective area after filtering is above the 8000 cm^2 requirement between 1-10 GeV. It is actually above that amount in every bin above 300 MeV, even though no official requirement is made outside the 1-10 GeV range. The field of view is also larger than the 2 sr requirement and the 2.4 sr goal. It is clear that the revised Onboard Filter allows the LAT to perform at a level that exceeds requirements. The effective area for goodEvents is limited by the definition of the goodEvent cut more than it is limited by Onboard Filter, and members of the LAT collaboration are working to further improve the goodEvent selection.

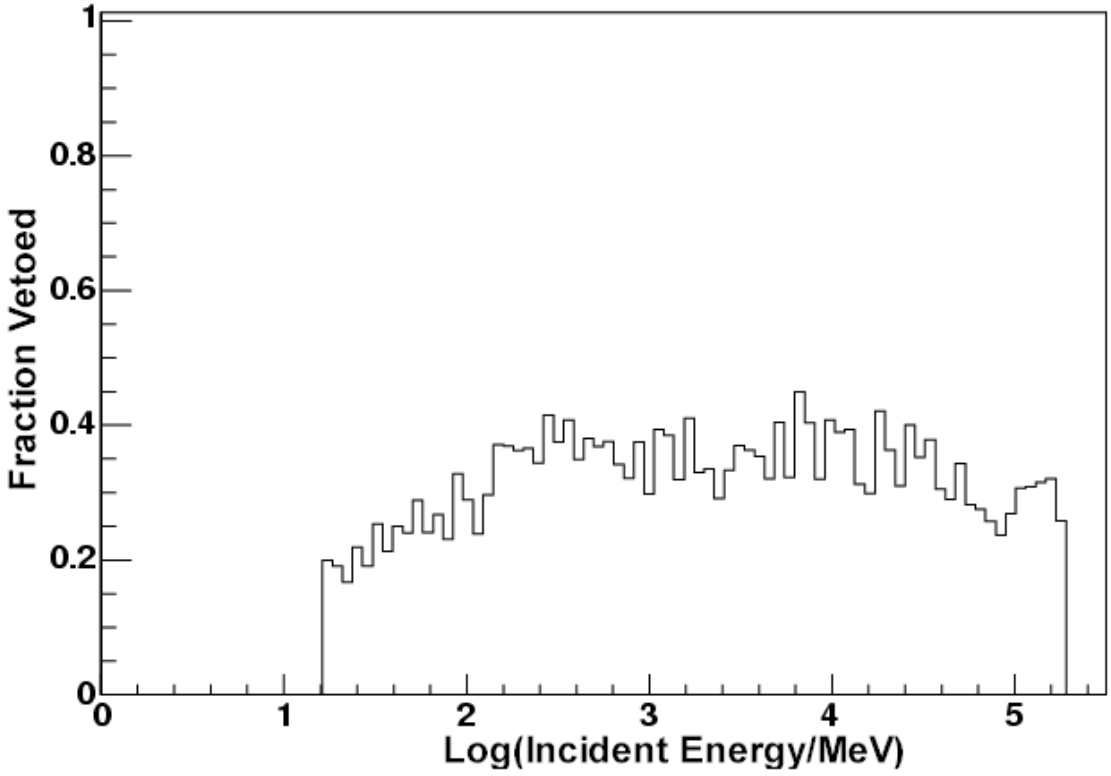

Figure 5.22: Fraction of tracker triggered 18 MeV - 180 GeV gammas vetoed vs. log of incident energy for the revised Onboard Filter. Compared to the result for the initial implementation of Onboard Filter, as shown in Figure 5.8, the improvement is substantial.

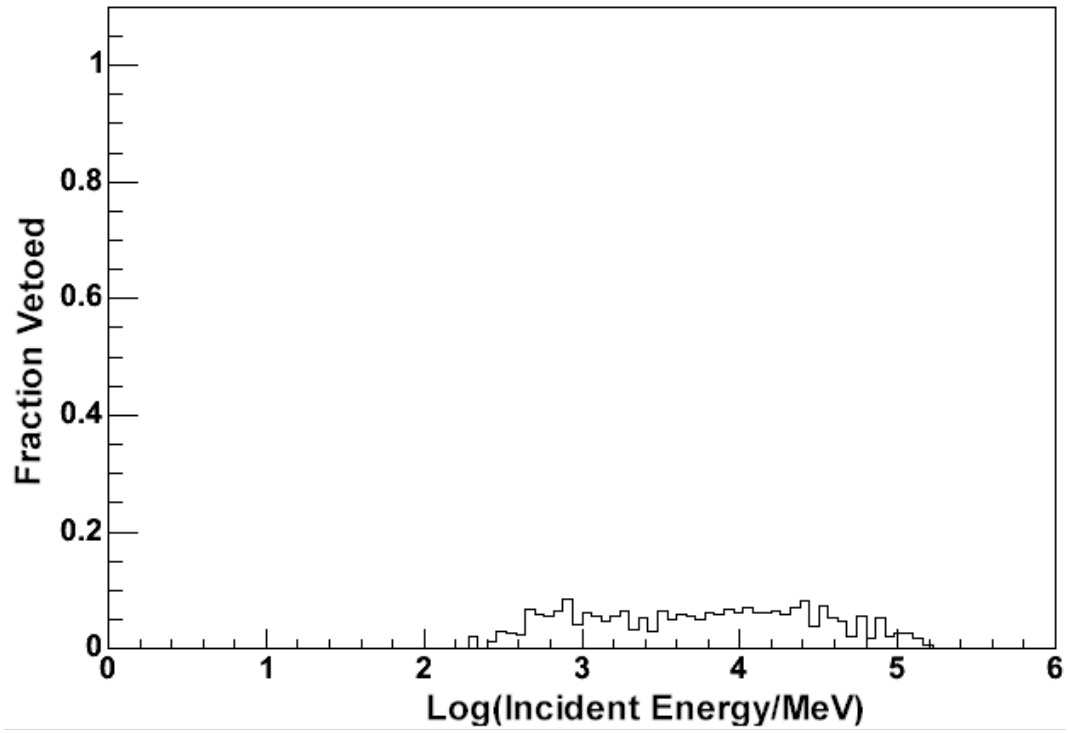

Figure 5.23: Fraction of goodEvent 18 MeV - 180 GeV gammas vetoed vs. log of incident energy for the revised Onboard Filter. Compared to the result for the initial implementation of Onboard Filter, as shown in Figure 5.10, the improvement is substantial. The fraction of goodEvents removed by Onboard Filter is the best measurement of the Filter's impact on gammas that are likely to be used for ground-based analysis.

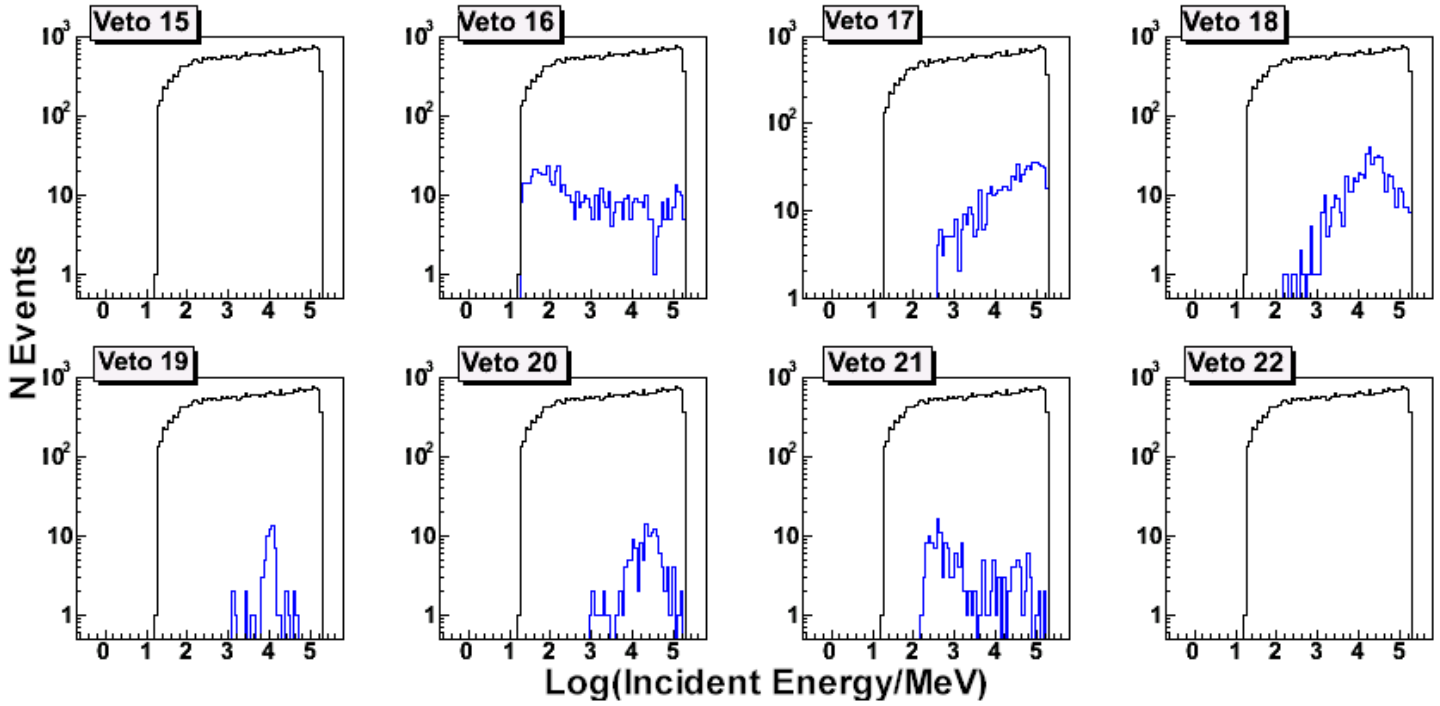

Figure 5.24: Exclusive veto frequency vs. log of incident energy for tracker triggered gammas. Compared to Figures 5.6 and 5.7, it appears in Figures 5.24 and 5.25 that some vetoes have become more active after revising Onboard Filter. However, this is deceptive, because these plots are for the exclusive veto frequency, which only shows the events that are removed by a single veto. Events that are shown to be removed here were also removed by the initial implementation of Onboard Filter, but they were likely also rejected by at least one other veto, which prevented them from showing up in Figures 5.6 and 5.7. Confirmation that the revised Onboard Filter performs better than the initial implementation is visible in Figures 5.22 and 5.23. Here, though, it is possible to see that certain vetoes are no longer active.

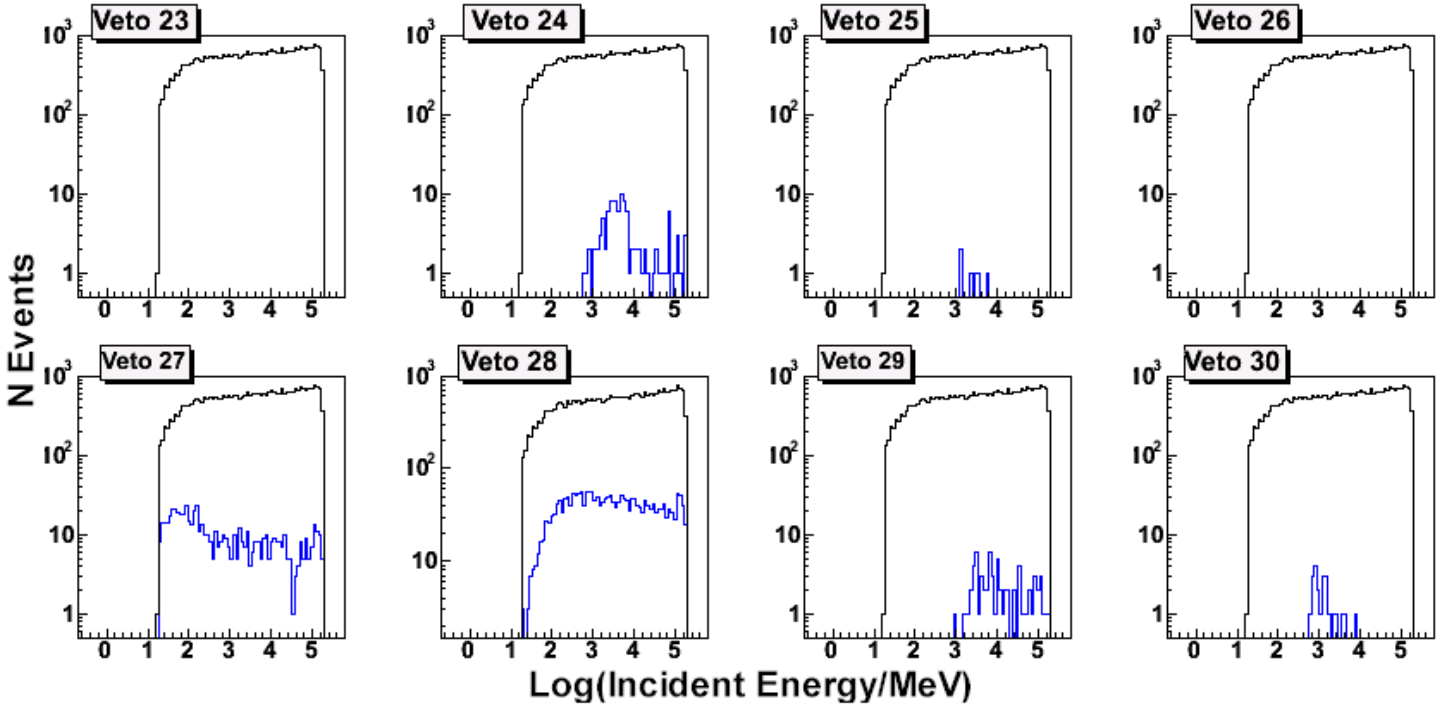

Figure 5.25: Exclusive veto frequency vs. log of incident energy for tracker triggered gammas. See the caption of Figure 5.24 for a description of Figures 5.24 and this Figure.

Effective Area and Field of View for Tracker Triggered Gammas

Energy (MeV) and Cut(s)		Aeff at Normal Incidence (cm^2)	% Remaining After Filter Applied	Field of View (sr)
18-50	Tkr Trig	7537 ± 529		3.70 ± 0.27
	Filter Applied	6274 ± 483	83 ± 9	3.46 ± 0.27
50-100	Tkr Trig	11068 ± 766		3.98 ± 0.28
	Filter Applied	9532 ± 710	86 ± 9	3.37 ± 0.26
100-200	Tkr Trig	12475 ± 821		4.39 ± 0.29
	Filter Applied	10531 ± 754	84 ± 9	3.54 ± 0.26
200-300	Tkr Trig	11682 ± 1045		5.14 ± 0.51
	Filter Applied	8252 ± 930	71 ± 11	4.12 ± 0.46
300-1000	Tkr Trig	13704 ± 645		4.38 ± 0.42
	Filter Applied	11945 ± 602	87 ± 7	3.29 ± 0.17
1000-10K	Tkr Trig	13753 ± 478		4.84 ± 0.17
	Filter Applied	12555 ± 457	91 ± 5	3.37 ± 0.13
10K-30K	Tkr Trig	13477 ± 685		5.44 ± 0.28
	Filter Applied	12084 ± 649	90 ± 7	3.76 ± 0.21
30K-180K	Tkr Trig	14968 ± 569		5.41 ± 0.21
	Filter Applied	13432 ± 539	90 ± 6	4.14 ± 0.17

Table 5.4: Initial effective area at normal incidence and field of view for tracker triggered gammas, before and after Onboard Filtering. Before Onboard Filter is labeled as "Tkr Trig," and after Onboard Filter is labeled "Filter Applied." These values were valid before the Onboard Filter had been altered as described in this chapter. All errors are statistical.

Effective Area and Field of View for goodEvent gammas

Energy (MeV)	and Cut(s)	Aeff at Normal Incidence (cm^2)	% Remaining After Filter Applied	Field of View (sr)
18-50	goodEvents	854 ± 178		1.97 ± 0.43
	Filter Applied	854 ± 178	100 ± 2	1.97 ± 0.43
50-100	goodEvents	3813 ± 449		2.12 ± 0.26
	Filter Applied	3813 ± 449	100 ± 17	2.12 ± 0.26
100-200	goodEvents	6157 ± 577		2.83 ± 0.27
	Filter Applied	6157 ± 577	100 ± 14	2.83 ± 0.27
200-300	goodEvents	6449 ± 776		3.13 ± 0.38
	Filter Applied	6449 ± 776	100 ± 18	3.08 ± 0.37
300-1000	goodEvents	9975 ± 550		2.48 ± 0.14
	Filter Applied	9550 ± 538	96 ± 8	2.47 ± 0.15
1000-10K	goodEvents	9745 ± 403		2.76 ± 0.12
	Filter Applied	9479 ± 397	97 ± 6	2.72 ± 0.12
10K-30K	goodEvents	8845 ± 555		2.87 ± 0.18
	Filter Applied	8601 ± 547	97 ± 9	2.68 ± 0.18
30K-180K	goodEvents	8327 ± 424		2.97 ± 0.14
	Filter Applied	8176 ± 421	98 ± 8	2.65 ± 0.14

Table 5.5: Initial effective area at normal incidence and field of view for goodEvent gammas, before and after Onboard Filtering. These values were valid before the Onboard Filter had been altered as described in this chapter. All errors are statistical.

5.6 Eliminating Albedo Gamma Rays

By the time FilterAlg had been finished, a new albedo gamma-ray flux was available in GlastSim. Previously, only albedo gammas from Earth's limb (by far the brightest region) had been simulated as a part of the backgndavgpdr and backgndmaxpdr sources. The newer albedo_upwards flux (also called *surface albedo*) simulates gammas coming from the surface of Earth's atmosphere, and the flux is a significant source of additional background.

When this flux was tested, the new version of Onboard Filter did not eliminate a large fraction of events. The all-triggered event rate for this source is 138±4 Hz, with a rejection rate of only 47.6±1.0%. When this is combined with the average background rate, the total goes to 380 ± 114 Hz, which is uncomfortably close to the 400 Hz limit. Rather than continue to alter the Onboard Filter code, which works well with regard to gamma rays in its revised form, the decision was made to develop one or more cuts that can reduce the trigger rate from the albedo flux specifically. In order to prevent any rejection of goodEvent gamma-rays, each albedo cut is restricted to acting on those events that deposit less than 5 MeV in the CAL. Each goodEvent is required to have at least a 5 MeV deposit.

Onboard Filter has trouble eliminating albedo gammas for many of the same reasons that it does not eliminate gammas that come from above (in LAT coordinates). Some of the changes made to Onboard Filter were designed specifically to prevent the veto of low-energy gammas, but over 90% of albedo that cause the LAT to trigger are lower-energy with less than 1 GeV of incident energy, which is why

their elimination rate is found to be only 47%. This makes it especially challenging to remove albedo without also lowering the low-energy gamma-ray acceptance rate. Depending on observatory orientation, there are differences in the way celestial and albedo gammas interact in the LAT, though, and some of these differences can be exploited for the purpose of creating cuts.

5.6.1 Development of new Albedo Cuts

When the LAT is zenith pointed, albedo gammas from the limb only deposit energy in the CAL for about 20% of triggered events, and albedo from the rest of the atmosphere only deposit energy for about 14% of those events. Looking at the fraction of events in different bins of incident energy, albedo from the surface with 18-30 MeV only deposit energy 5% of the time, 90 to 110 MeV only deposit energy 22% of the time, and from 490-510 MeV only 71% of the time. Contrast this to gammas coming from the upper hemisphere of LAT coordinates in the same energy bins. Those with 18-30 MeV deposit energy for 22% of triggers, 90-100 MeV gammas deposit energy for 65% of triggers, and 490-510 MeV gammas deposit energy 84% of the time. At every energy range, these downward moving gammas[9] deposit energy in the CAL more often than albedo gammas coming from the surface of Earth's atmosphere. This discrepancy can be used to eliminate albedo while not inflicting

[9]In LAT coordinates, they come from above and to the side. Albedo generally come from below, so they can be considered upward moving. If the LAT is rocked to the side (tilted from zenith), albedo may preferentially enter the LAT through the side rather than from below, and some celestial gammas will enter from below. However, on the whole, the terms "downward," "upward," "above," and "below" are useful descriptions for the average behavior of the source relative to the LAT. In the LAT's usual pointing mode, triggers on celestial gamma rays will primarily be those coming from above in LAT coordinates.

damage on most low-energy gammas from celestial sources. All of the albedo cuts described in this chapter are only enacted when the CAL registers no energy deposit. As noted above, this also prevents the rejection of any goodEvent gammas.

Another difference in the instrument response for albedo vs. downward moving gammas is that Onboard Filter's projection finding method has a more difficult time reconstructing tracks for albedo. In addition, albedo gammas come from Earth's atmosphere, while celestial gammas enter the LAT from every direction that is not occulted by Earth. Here, the possibility of exploiting the incident direction in order to develop a cut is explored.

Events with no CAL deposit are of limited scientific use, but when developing any cut, an attempt is made to reject as few gammas of any type anyway. If it is ever desired to make the albedo cuts more aggressive, they could be changed to operate on events that have a small amount of energy in the CAL, but more downward moving gammas would be endangered.

Method I

Because the LAT is most efficient at triggering on events that pass within about 70 degrees of LAT zenith, most of the celestial gamma-ray triggers are caused by events that come into the front or side of the instrument and cause a 3-in-a-row tracker trigger. Recall that this means that at least 6 consecutive planes of silicon are hit, and it is usually the case that the top two planes are part of the same sandwich that form one layer. That downward moving gammas usually create tracks that start in the same layer is an important point. When a track extends farther than 3

layers, as they often do, it is not unusual for Onboard Filter to reconstruct it as an X-projection that ends in one layer, and a Y-projection that ends in another. This is due to multiple Coulomb scattering and inefficiencies in the way that Onboard Filter assigns hits to a track.

If we imagine the process for albedo gammas that come from below and travel upwards, we can imagine the reverse of the downward going gamma triggering process. Instead of projections starting at the same top layer and possibly ending in different bottom layers, albedo gamma projections may start in the same bottom layer and end in different top layers. It is submitted here that it is reasonable to assume that any 3-dimensional track be composed of two 2-dimensional projections that *start in the same layer*. For downward moving gammas, the starting layer is closest to the top of the ACD. For albedo gammas, it is closest to the CAL. If only events with X and Y projections that do not start in the same top layer and do not have a corresponding energy deposit in the CAL are removed, they are likely be albedo gammas. A potential problem with this method is that if the Onboard Filter's projection finding method is improved, it is possible that it may be able to assign more hits to albedo projections, and the ending layers (the top layers) of X and Y projections may become the same for those events. Even so, the performance of this method is examined below because it is promising for the current version of the Onboard Filter code.

Method II

A second method is based entirely on the physics of multiple scattering. Because particles are scattered farther from their original direction as they lose momentum, they tend to be deflected more as they pass through material in the tracker. If a projection has at least 4 hits (4 planes of silicon), it is possible to measure two multiple scattering angles (see Figure 5.26). If the parent gamma came from above, the second angle should be greater than the first. In contrast, if the parent gamma came from below, the top angle should be greater than the bottom. By comparing these angles, it may be possible to determine whether the event came from above or below. The advantage of this method is that it is based on sound physics. The disadvantage is that it is only as good as the projection finding routine. If the performance of the projection finding improves with future upgrades to Onboard Filter, the performance of this cut could also improve, provided that there are at least four consecutive hits available in each orientation.

Method III

A third cut was developed, which eliminates events with an incident direction consistent with Earth's atmosphere. Effectively implementing this cut is not trivial because it uses Onboard Filter projections, and therefore ultimately relies on the Filter's projection finding technique. Since the projection finding assumes that events are downward moving, it begins its search at the top of a 3-in-a-row. Though it allows its strip tolerance to increase as it searches downward through the tracker,

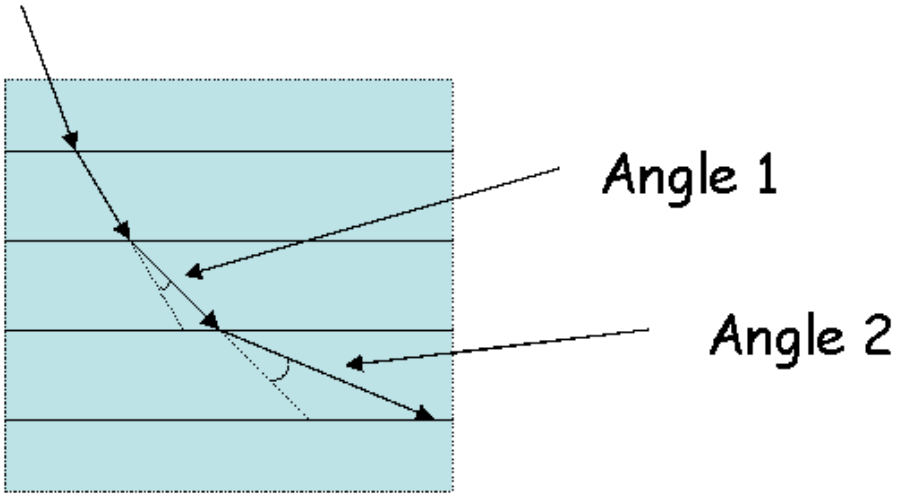

Figure 5.26: Diagram showing the increase of multiple scattering angles with loss of momentum. Momentum decreases as the particle moves through the tracker. This causes the multiple scattering angles to get larger.

it does not always find all the hits that are associated with a particle track either because the particle scatters out of range, or because the projection finding method is misled by hits that are not associated with the particle's path. Downward going events tend to produce an increasing number of hits in the tracker as they progress through more layers, so the process of finding hits and associating them with projections simply becomes less accurate as the projections get longer. The method tends to add hits to projections when those hits should not be included at all. For these reasons, only the uppermost hits of a projection can be reliably used for determining an event direction. In recognition of this, Onboard Filter only uses the first two hits of a projection in its veto algorithms.

The best conceivable direction based albedo cut would reconstruct a 3-D track and check whether the direction of the track is consistent with the Earth atmosphere. It was previously stated that a well defined track from a downward going event ought

to have projections that start in the same upper layer. Though this is a good way to ensure an accurate gamma-ray track reconstruction, it is ineffective for albedo because their projections tend not to share the same uppermost layer. Therefore, forming 3-D tracks from an upper layer is not a plausible option.

Upward going albedo might tend to have projections that start in the same bottommost layer, but using the bottommost hits for 3-D track reconstruction is also not a good option because the projection finding always starts at the top of the tracker and moves downward. Regardless of a particle's trajectory, the bottommost hits of a projection are less reliable. Since using 3-D tracks is not possible, and because it is best to require an albedo cut to only use the uppermost hits of a projection, a method was developed that uses only those hits. Though these hits are most reliable for determining the direction of celestial gammas, their degraded accuracy is only relevant for albedo, so using the upper hits only decreases the effectiveness of the cut for albedo. Conversely, downward moving celestial gammas are more protected from incidental removal.

This method, like the rest, only considers events that deposit no energy in the CAL. It also only looks at what happens in the outer towers of the LAT, because albedo enter in from the side. Finally, only projections that are formed by strips that run parallel to the tower face are used.

The planes formed by these projections will exit the side of the LAT such that they may intersect a row of ACD tiles, depending on the exit angle. The same plane may intersect another row of ACD tiles on the opposite side of the LAT

also. If projected out the other two sides that are perpendicular to the strips, the intersection of projection plane and ACD plane creates a diagonal line (see Figure 5.27). We are not concerned with these two sides, though. If the study is limited to those projections that can create horizontal lines when they intersect the ACD, it is apparent that when they are extended downward to the Earth's atmosphere, their planes will either intersect the Earth's atmosphere, just touch the surface as a tangent, or miss it completely. If there is an intersection or touch, it means that it is possible that the projection was caused by an albedo gamma.

Figure 5.27 helps to illustrate the alternate possibility that the projection came from below the LAT, but not from the atmosphere. It is even more likely that the event may have come from above or to the side. . The top half of the figure shows a plane exiting out the side of the LAT and intersecting the Earth's atmosphere. This projection plane represents all possible paths that a parent gamma (or cosmic ray) could have taken (or as best as the reconstruction can determine). We can now visualize how the event may have come from the atmosphere, but may also have come from above or the side. However, this is the best one can do without reconstructing a 3-D track using the other projection.

In order to calculate the angles from which events should be rejected, one must know where the Earth is in LAT coordinates. In Figure 5.28 we see a top down view of the LAT above Earth, and a box is drawn around the atmosphere. The LAT is rocked a few degrees towards the Y+ side. Each side of the box is parallel to an edge of the LAT, and will also be parallel to any intersection of a projection plane coming

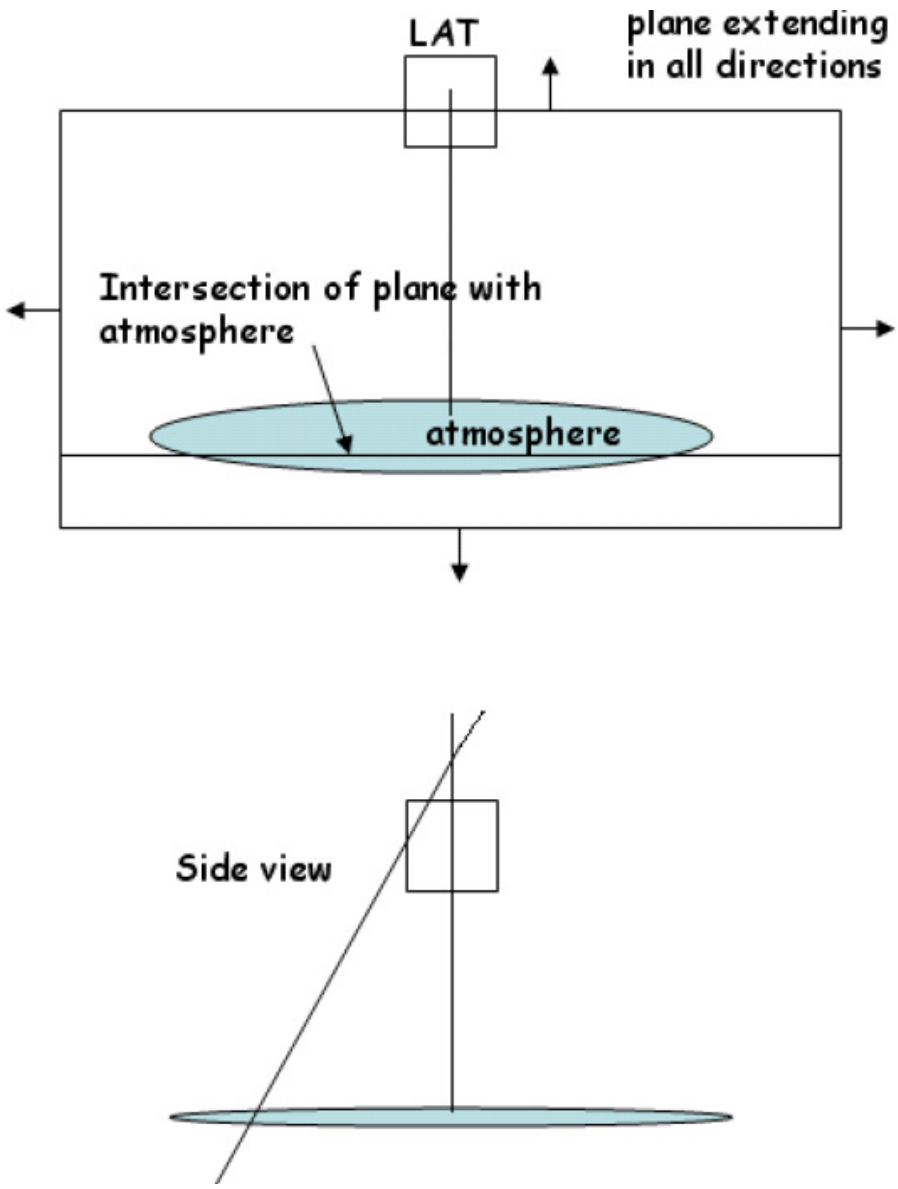

Figure 5.27: Upper figure: the LAT is above the Earth, whose limb is represented by the ellipse. An Onboard Filter projection plane extends in all directions and intersects the Earth's atmosphere. It can intersect the ACD as a horizontal line as it passes out the side, if the angle allows it. Lower Figure: a view from the side. When the plane is extended out the side, it intersects the ACD as a diagonal line.

out the corresponding side of the LAT. Figure 5.29 is another view that shows how the box around the atmosphere helps define a 4-sided pyramid. The dotted lines are not the edges, they are lines that lie in the plane of each pyramid face. This albedo cut is designed to reject, at a minimum, all events that fall within that pyramid. It also will reject events that come from the inverse of the pyramid as it projects upwards, and from the sideways projections of the pyramid into space. If only one projection is required to intersect the atmosphere, not both the X and the Y, the cut will remove more events at the expense of accuracy because the area of possible elimination is not limited to the pyramid[10].

This region is constantly shifting as the LAT rocks back and forth and orbits the Earth, so it is does not consistently encompass the same area on the celestial sphere. Its geometry is complicated and difficult to visualize, but the point is that the method will remove albedo while it also removes gammas from a portion of the sky. Because it is desired to begin aggressively by removing as many albedo as possible, this is how the cut is implemented it for this study.

Method IV

Because it is good to also have a fail-safe, last resort method in place in case the other three are unusable for some reason, a fourth albedo reduction method is presented. It simply rejects any event that has no energy deposit in the CAL. Overwhelmingly, gammas that do not deposit energy are albedo, so the cut is not unreasonable.

[10]The region from which events can be rejected can also be visualized by allowing one hourglass, "X" shape to cut through a sphere from one side to the other, from "East" to "West," or 0^o to 180^o, and then do the same from "North" to "South."

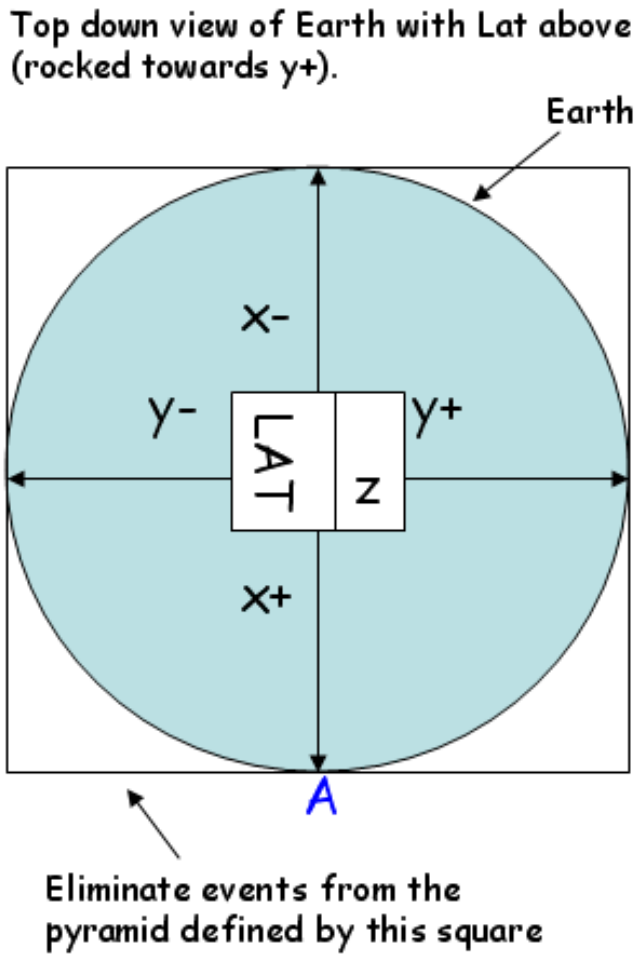

Figure 5.28: A top-down view of a the LAT rocked towards the Y+ side, with the Earth underneath. A box is drawn around the Earth such that its sides are parallel to the top-down view of the sides of the LAT. Events with a direction consistent with coming from inside the box are rejected because they may be albedo from the atmosphere.

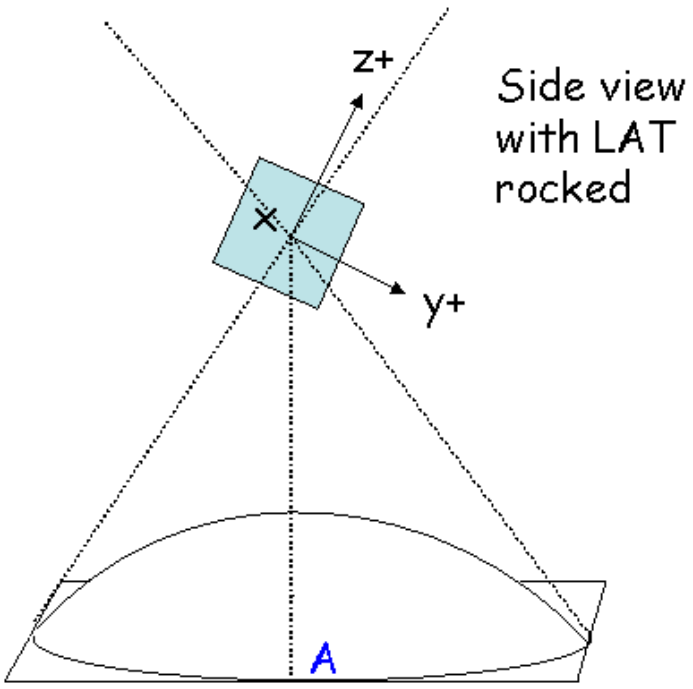

Figure 5.29: A side view of the LAT rocked towards the Y+ side. A four sided pyramid is formed by the box drawn around the Earth and the apex at the LAT. Events with a direction consistent with coming from inside the box are rejected as albedo.

5.6.2 Performance of Albedo Cuts

These methods were coded and then tested on the albedo upwards source and the average background source (which already includes albedo from the limb). Also evaluated was the impact on gamma rays over the 18 MeV - 180 GeV energy range. The orientation of the LAT is important for these studies, because the albedo source comes from a changing location relative to the LAT depending on where the LAT is pointing. It is shown in this section that both the first and third methods were quite successful at removing albedo, but they did also reject a substantial fraction of lower-energy downward moving gammas.

Performance when the LAT is Zenith Pointed

Table 5.6 shows the rates for all-triggered surface albedo and the standard average background source after applying the revised Onboard Filter or Onboard Filter plus one of the albedo cuts. For this study, the LAT was oriented such that it was pointing directly away from Earth. After applying the Onboard Filter, the average background plus surface albedo event rate was 380 ± 114 Hz[11] with $93.3 \pm 2.2\%$ of all-triggered events eliminated. 380 Hz is below the 400 Hz cap, but still quite close. Of these 380 Hz, 138 ± 5 Hz are due solely to the albedo from Earth's surface. This underscores the fact that albedo are indeed a very strong background source.

The four proposed albedo cuts have varying success at removing the new background mix. The first method reduces the all-triggered event rate from 380 ± 114

[11] All uncertainties are statistical and dependent on the size of the Monte Carlo run.

Hz with just Onboard Filter to 234 ± 115 Hz when the albedo cut is also used. The second method is not as effective, only reducing the rate to 343 ± 114 Hz. The third method performs similarly to the first, reducing the event rate to 253 ± 115 Hz. Finally, the fourth method reduces the rate to 163 ± 114 Hz. These cuts did not reject any events with an energy deposit in the CAL. All could be made even more effective if they rejected events with up to 5 MeV, which would still not impact the goodEvents.

These cuts do eliminate some all-triggered gamma-ray events. Table 5.5 shows the percentage of all-triggered downward going gammas eliminated in different incident energy bins up to 1 GeV, the energy at which the albedo source decreases substantially. The gamma source used here had the familiar E^{-1} power law spectrum, so that it is weighted towards producing more lower-energy events than higher. If we look at the gamma-ray events with incident energy above 1 GeV that do not deposit energy in the CAL and also survive Onboard Filter, we see that their total is less than 4% of all-triggered events. Only this small fraction of gammas above 1 GeV could potentially be harmed by an albedo cut that requires no energy deposit. This is easily verified by a look at Figure 5.30, which has plots showing the fraction of all-triggered gamma-rays eliminated by Onboard Filter (black line), and Onboard Filter working with the three primary albedo cuts (color lines). When the lines overlap, only the black line is visible. Note that for downward going gammas above 1 GeV, the fraction of events eliminated by the multiple scattering cut (red) and the projection-layer based cut (blue) is indiscernible. The direction based cut (green),

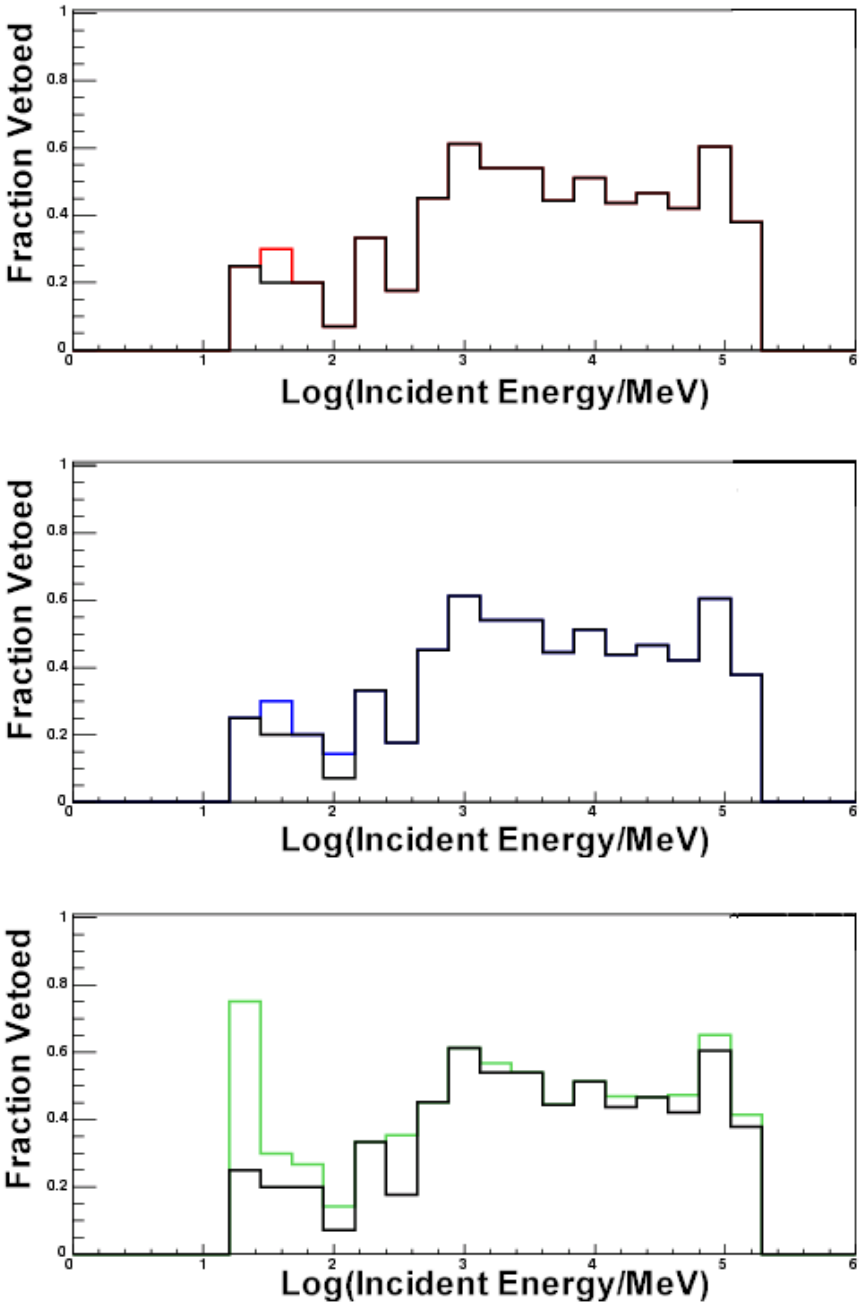

Figure 5.30: Fraction of all-triggered downward going gamma rays eliminated by Onboard Filter and Onboard Filter combined with different albedo cuts when the LAT is zenith pointed. The X-axis is the log_{10} of the incident energy in MeV. The Y-axis is the fraction of events eliminated. The black line indicates the fraction removed by Onboard Filter alone, while the color lines indicate the fraction removed by Onboard Filter ORed with albedo cuts. Where the color line and black line overlapped, only the black line is visible. Red indicates the multiple scattering cut, blue indicates the projection-layer cut. Green indicates the directional cut. All-triggered events were used for this evaluation, because the performance of all cuts appears to be the same for goodEvents. This is because none of the albedo cuts remove any goodEvents, which require a minimum 5 MeV CAL deposit, while the albedo cuts only remove events that have no CAL energy deposit.

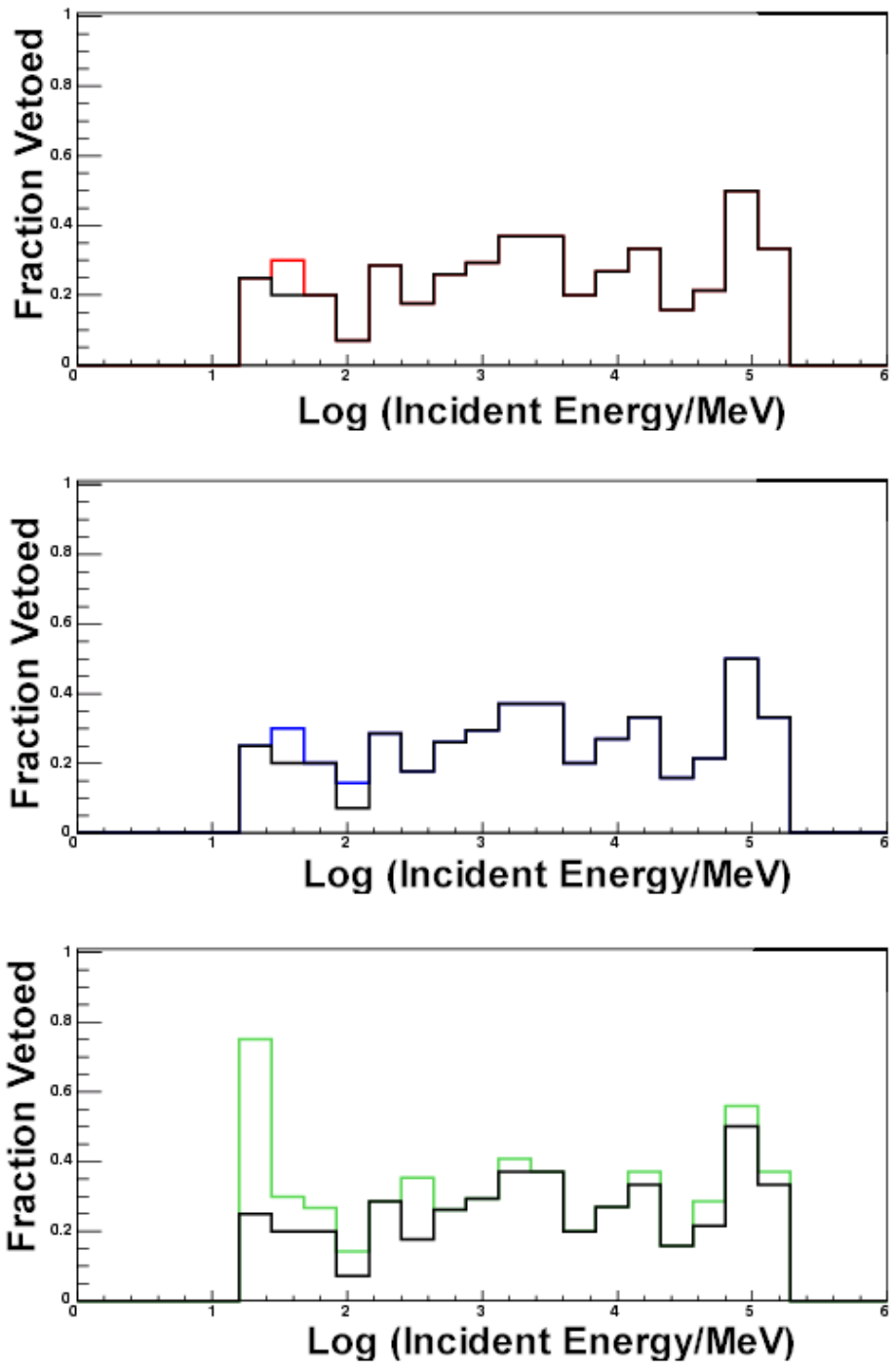

Figure 5.31: Fraction of tracker triggered downward going gamma rays eliminated by Onboard Filter and Onboard Filter combined with different albedo cuts when the LAT is zenith pointed. It is useful to use triggered events to compare albedo cuts, but these plots are not indicative of the impact on events used for ground-based analysis, because none of the albedo cuts remove any goodEvents whatsoever.

however, does eliminate a substantial fraction of low and high-energy downward going gammas. Figure 5.31 shows the same cuts but for tracker triggered events.

The multiple scattering cut eliminates the smallest fraction of gamma rays, but it is also relatively ineffective at removing albedo because of inefficiencies in the projection finding method. The fourth method that simply cuts on energy eliminates a very high fraction of gamma rays in addition to albedo, so it should be regarded as a last resort. The two middle performers are the directional cut and the projection-layer cut; their numbers are close for both gamma rays and albedo, though the projection-layer cut eliminates slightly more albedo and fewer gammas.

Either the first or third methods would get the total background rate into a desirable 250 Hz range. The projection-layer cut does not require knowledge of spacecraft orientation, which could make it easier and shorter to code, and thus faster to execute. However, if the projection finding methods are revised, it is possible that the frequency of the discrepancy between projection starting layers could decrease, and this is what the cut is based on. The directional cut, conversely, does require pointing knowledge, and also eliminates events from a large portion of the celestial sphere. However, it is only likely to improve in performance if the onboard projection finding is improved, and it could be made more restrictive by requiring both an X and a Y projection to intersect the atmosphere instead of just one. The directional cut is not favored, though, because it can never distinguish between upward going and downward going particles. This means it will always eliminate celestial gammas from a large portion of the field of view. The collaboration might

consider combining a projection-layer cut and a directional cut to further reduce the number of downward going gammas rejected (logically *AND* the cuts), but this still preferentially eliminates downward moving gammas from specific regions. An application of the projection-layer cut on its own does not specifically target any particular region, so even if it eliminates more downward moving gammas than it would ANDed with a direction cut, at least the elimination is not unnecessarily inconsistent over the field of view.

	Triggered	After Filter	After Filter OR Proj-Layer	After Filter OR Mult-Scat	After Filter OR Direction	After Filter OR No Energy
All Triggers, Zenith Pointed LAT						
Surface Albedo						
Rate (Hz)	264±3	138±5	63±6	128±5	59±6	19±5
% rejected		47.6±2.1%	76.2±1.8%	51.4±2.0%	77.6±1.8%	92.7±1.7%
Backgndavgpdr						
Rate (Hz)	3630±55	242±109	177±109	215±109	194±109	144±109
% rejected		93.3±2.2%	95.1±2.2%	94.1±2.2%	94.7±2.2%	96.0±2.2%
Total						
Rate (Hz)	3894±58	380±114	234±115	343±114	253±115	163±114
Tracker Triggers, Zenith Pointed LAT						
Surface Albedo						
Rate (Hz)	258±3	138±5	63±6	114±5.4	59±6	19±5
% rejected		45.9±2.2%	75.5±1.8%	55.9±2.0%	77±1.8%	92.6±1.7%
Backgndavgpdr						
Rate (Hz)	3381±53	234±105	174±105	not calculated	189±105	130±105
% rejected		93.1±2.3%	94.8±2.3%	not calculated	94.4±2.3%	96.1±2.3%
Total						
Rate (Hz)	3639±56	372±110	237±111	not calculated	248±111	149±110

Table 5.6: Event rates and rejection percentages for surface albedo and average background after the application of different filters. The LAT is zenith pointed.

Energy Range	% Removed by Filter	% Removed by Filter OR Proj-Layer Cut	% Removed by Filter OR Mult-Scat Cut	% Removed by Filter OR Directional Cut	% Removed by Filter OR No Energy Cut
All Triggers, Zenith Pointed LAT					
18-20 MeV	17.9±6.1	55.4±12.4	25.0±7.5	60.7±13.2	89.3±17.4
20-50 MeV	19.6±1.6	42.3±2.6	25.7±1.9	43.9±2.6	69.2±3.6
50-100 MeV	25.0±1.7	34.0±2.1	26.7±1.8	37.7±2.2	47.8±2.6
100-300 MeV	35.4±1.5	38.2±1.6	35.6±1.5	38.7±1.6	41.7±1.7
300-1K MeV	56.2±1.6	56.5±1.6	56.3±1.6	56.4±1.6	56.9±1.6
18-1K MeV	41.6±0.9	47.4±1.0	42.7±0.9	47.4±1.0	53.2±1.0
Tracker Triggers, Zenith Pointed LAT					
18-20 MeV	17.9±6.1	55.4±12.4	43.4±10.5	60.7±13.2	89.3±17.4
20-50 MeV	19.6±1.6	42.3±2.6	34.9±2.3	43.9±2.6	69.2±3.6
50-100 MeV	25.0±1.7	34.0±2.1	32.7±2.1	37.7±2.2	47.8±2.6
100-300 MeV	32.5±1.5	35.5±1.5	34.5±1.5	35.7±1.6	39.1±1.6
300-1K MeV	36.7±1.4	37.2±1.4	37.0±1.4	37.0±1.6	37.7±1.2
18-1K MeV	30.9±0.8	37.0±0.9	35.3±0.9	37.9±1.0	44.7±0.9

Table 5.7: Percent of Downward Going Gamma Rays Removed by Different Filters. The LAT is zenith pointed.

Performance when the LAT is rocked 35^o

When in orbit, the LAT will not usually be pointing directly away from Earth. In order to confirm that the directional cut and the projection-layer cut provide satisfactory performance with regard to the rate reduction of background sources, the LAT was rocked 35^o and 60^o to the side. Table 5.8 shows that as the LAT is tilted 35^o away from Earth zenith, the trigger rate for surface albedo drops slightly to 251 ± 3 Hz, and the rate after Onboard Filter increases slightly to 142 ± 6 Hz. The total rate of the background mix after only the Onboard Filter is 373 ± 88 Hz. However, both the directional method and the projection-layer method reduce the total background to 245 ± 91 to 252 ± 91 Hz, which is comparable to the rate when the LAT was zenith pointed. Likewise, these two methods have a very similar impact on lower-energy gamma rays, as shown in Table 5.9. The multiple scattering method and the simple energy cut method were not examined in detail for a tilted LAT, because their zenith-pointed performance was so distinctly unfavorable compared to the two methods that give balanced results, but Figures 5.32 and 5.33 do show the performance of the three cuts visually.

Performance when the LAT is rocked 60^o

When the LAT is tilted to 60^o from zenith, the overall trigger rate increases to 4067 ± 36 Hz, and is only reduced to 453 ± 66 Hz after Onboard Filter (see Table 5.10). The increase in background rate in comparison with that for the zenith pointed LAT all comes from the average background flux, which includes the albedo

from Earth's limb. When the LAT tilts this far, more of the tracker is exposed to the limb, and limb albedo can enter at an angle that even allows them to start towards the top of the tracker and go "down" towards the CAL. At this orientation, the LAT event data clearly require filtering beyond Onboard Filter. Again, both the directional cut and the projection-layer cut perform similarly, cutting the data rate down between 301 ± 67 and 315 ± 67 Hz. With regards to non-albedo gammas, the directional cut still does not perform quite as well (see Table 5.11). Figures 5.34 and 5.35 show the performance of these cuts for downward going gammas visually.

It is possible to reduce the average background rate to a safe, 234 ± 115 to 315 ± 67 Hz, depending on LAT orientation. This does require sacrificing some lower-energy gamma rays, but referring back to Figure 5.8 and comparing it to the tracker trigger data in Table 5.7, it is apparent that the albedo cuts in combination with the revised Onboard Filter eliminate significantly fewer gamma rays than the original version of Onboard Filter. Also, none of the tested albedo cuts target any events that have an energy deposit in the CAL, which means that goodEvents are preserved.

	Triggered	After Filter	After Filter OR Proj-Layer	After Filter OR Mult-Scat	After Filter OR Direction	After Filter OR No Energy
All Triggers, LAT Rocked 35 Degrees						
Surface Albedo						
Rate (Hz)	251±3	142±6	63±6	134±5	65±6	21±5
% rejected		43.5±1.9%	74.9±1.9%	46.6±2.2%	74.3±1.9%	91.8±1.8%
Backgndavgpdr						
Rate (Hz)	3679±43	239±85	182±85	not calculated	187±85	143±85
% rejected		93.5±1.7%	95.0±1.7%	not calculated	94.9±1.7%	96.1±1.7%
Total						
Rate (Hz)	3930±46	380±91	245±91	not calculated	252±91	164±90
Tracker Triggers, LAT Rocked 35 Degrees						
Surface Albedo						
Rate (Hz)	243±3	141±6	63±6	119±5	64±6	20±5
% rejected		41.8±1.9%	75.4±1.9%	51±2.1%	73.6±1.9%	93.8±1.8
Backgndavgpdr						
Rate (Hz)	3448±42	232±82	175±82	not calculated	180±82	136±82
% rejected		93.3±1.7%	94.9±1.7%	not calculated	94.8±1.7%	96.3±1.7%
Total						
Rate (Hz)	3691±45	373±88	238±88	not calculated	244±88	142±87

Table 5.8: Event rates and rejection percentages for surface albedo and average background after the application of different filters. The LAT is rocked 35 degrees.

Energy Range	% Removed by Filter	% Removed by Filter OR Proj-Layer Cut	% Removed by Filter OR Mult-Scat Cut	% Removed by Filter OR Directional Cut	% Removed by Filter OR No Energy Cut
All Triggers, LAT Rocked 35 Degrees					
18-20 MeV	14.9±5.0	58.2±11.7	not calculated	58.2±11.7	83.6±15.1
20-50 MeV	21.3±1.7	41.3±2.6	not calculated	47.9±2.9	68.9±3.7
50-100 MeV	25.4±1.8	34.6±2.1	not calculated	37.4±2.3	46.8±2.6
100-300 MeV	38.0±1.6	40.5±1.6	not calculated	41.3±1.6	43.4±1.7
300-1K MeV	60.4±1.7	60.6±1.7	not calculated	60.9±1.6	61.2±1.7
18-1K MeV	44.9±0.9	49.3±1.0	not calculated	50.7±1.0	55.3±1.1
Tracker Triggers, LAT Rocked 35 Degrees					
18-20 MeV	31.3±7.8	58.2±11.7	41.8±9.4	58.2±11.7	83.6±15.1
20-50 MeV	20.2±1.7	41.3±2.6	36.0±2.4	47.9±2.9	68.9±3.7
50-100 MeV	26.8±1.8	34.5±2.1	34.0±2.1	37.4±2.3	46.7±2.6
100-300 MeV	35.1±1.5	37.6±1.6	36.7±1.6	38.5±1.7	40.7±1.7
300-1K MeV	41.5±1.6	41.8±1.6	48.7±1.7	42.2±1.7	42.7±1.6
18-1K MeV	34.1±0.9	39.4±0.9	38.2±0.9	41.2±1.0	46.7±1.0

Table 5.9: Percent of celestial gamma Rays removed by different filters. The LAT is rocked 35 degrees.

	Triggered	After Filter	After Filter OR Proj-Layer	After Filter OR Mult-Scat	After Filter OR Direction	After Filter OR No Energy
All Triggers, LAT Rocked 60 Degrees						
Surface Albedo						
Rate (Hz)	264±5	179±5	86±6	171±5	91±6	34±5
% rejected		36.2±2.2%	69.6±1.8%	39.4±2.2%	67.7±1.8%	87.8±1.7%
Backgndavgpdr						
Rate (Hz)	3804±31	274±61	215±61	not calculated	224±61	171±61
% rejected		92.8±1.2%	94.3±1.2%	not calculated	94.1±1.2%	95.5±1.2%
Total						
Rate (Hz)	4067±36	453±66	301±67	not calculated	315±67	205±66
Tracker Triggers, LAT Rocked 60 Degrees						
Surface Albedo						
Rate (Hz)	274±5	179±5	85±6	154±5	90±6	34±5
% rejected		41.8±2.3%	75.4±1.8%	43.8±2.1%	66.9±1.8%	87.5±1.7
Backgndavgpdr						
Rate (Hz)	3597±30	264±59	206±59	not calculated	216±59	162±59
% rejected		92.6±1.2%	94.3±1.2%	not calculated	94.0±1.2%	95.9±1.2%
Total						
Rate (Hz)	3865±35	443±64	291±65	not calculated	307±65	171±64

Table 5.10: Event rates and rejection percentages for surface albedo and average background after the application of different filters. The LAT is rocked 60 degrees.

Energy Range	% Removed by Filter	% Removed by Filter OR Proj-Layer Cut	% Removed by Filter OR Mult-Scat Cut	% Removed by Filter OR Directional Cut	% Removed by Filter OR No Energy Cut
All Triggers, LAT Rocked 60 Degrees					
18-20 MeV	25.4±7.4	59.3±12.7	not calculated	69.5±14.1	91.5±17.2
20-50 MeV	23.7±2.0	45.1±3.0	not calculated	51.8±3.2	64.4±3.8
50-100 MeV	30.8±2.1	39.5±2.4	not calculated	43.1±2.6	56.4±3.1
100-300 MeV	39.9±1.9	46.3±2.0	not calculated	47.4±2.0	49.8±2.0
300-1K MeV	49.7±1.8	66.6±1.8	not calculated	67.0±1.8	67.3±1.8
18-1K MeV	40.0±1.0	55.2±1.1	not calculated	57.0±1.1	61.1±1.2
Tracker Triggers, LAT Rocked 60 Degrees					
18-20 MeV	25.4±7.3	59.3±12.7	35.6±9.0	69.5±14.1	95.1±17.7
20-50 MeV	23.7±2.0	45.1±3.0	38.8±2.7	51.8±3.2	70.5±4.0
50-100 MeV	30.8±2.1	39.5±2.4	38.3±2.4	43.2±2.6	51.6±2.9
100-300 MeV	39.9±1.8	43.0±1.9	41.7±1.8	44.2±1.9	46.7±2.0
300-1K MeV	49.7±1.8	50.1±1.8	50.0±1.8	50.7±1.8	51.3±1.8
18-1K MeV	40.0±1.0	45.7±1.1	44.0±1.0	47.8±1.1	52.8±1.2

Table 5.11: Percent of celestial gamma rays removed by different filters. The LAT is rocked 60 degrees.

5.7 Summary and Conclusions

This chapter began with a discussion of the need to reduce the amount of data that would be transmitted to the ground, because the amount of data resulting from the trigger rate investigated is nearly ten times higher than what the downlink will allow. In order to meet the downlink requirement, the data will be compressed and filtered, and the filtering needs to reduce the event rate to below 400 Hz. The filtering will be accomplished in flight by an Onboard Filter, which employs a set of algorithms that are designed to identify and reject background, but allow gamma rays into the data stream. It was shown that the Onboard Filter, in its original configuration, eliminated many gamma rays, especially at low energy, and this caused the effective area and field of view to drop lower than is desirable. Some programming errors were found and fixed, and the logic of the filter was altered in order to improve its performance. An emulation of Onboard Filter that assisted in finding problems with the filter was written, and it also allows other users to test prototype cuts.

The revised Onboard Filter's performance is significantly better than the original with regard to gamma-ray retention, and the effective area and field of view exceed mission requirements. The lowest energy bin that was examined, 0-50 MeV, is below 8000 cm^2, but this is not a violation of the mission requirement, which only states that the 8000 cm^2 value must be met between 1 and 10 GeV. When gamma-ray events that were not eliminated by the ground-based background rejection were examined, a similar trend was found in that the Onboard Filter did reject a small fraction of these gamma rays. However, in no energy bin was the Onboard Filter

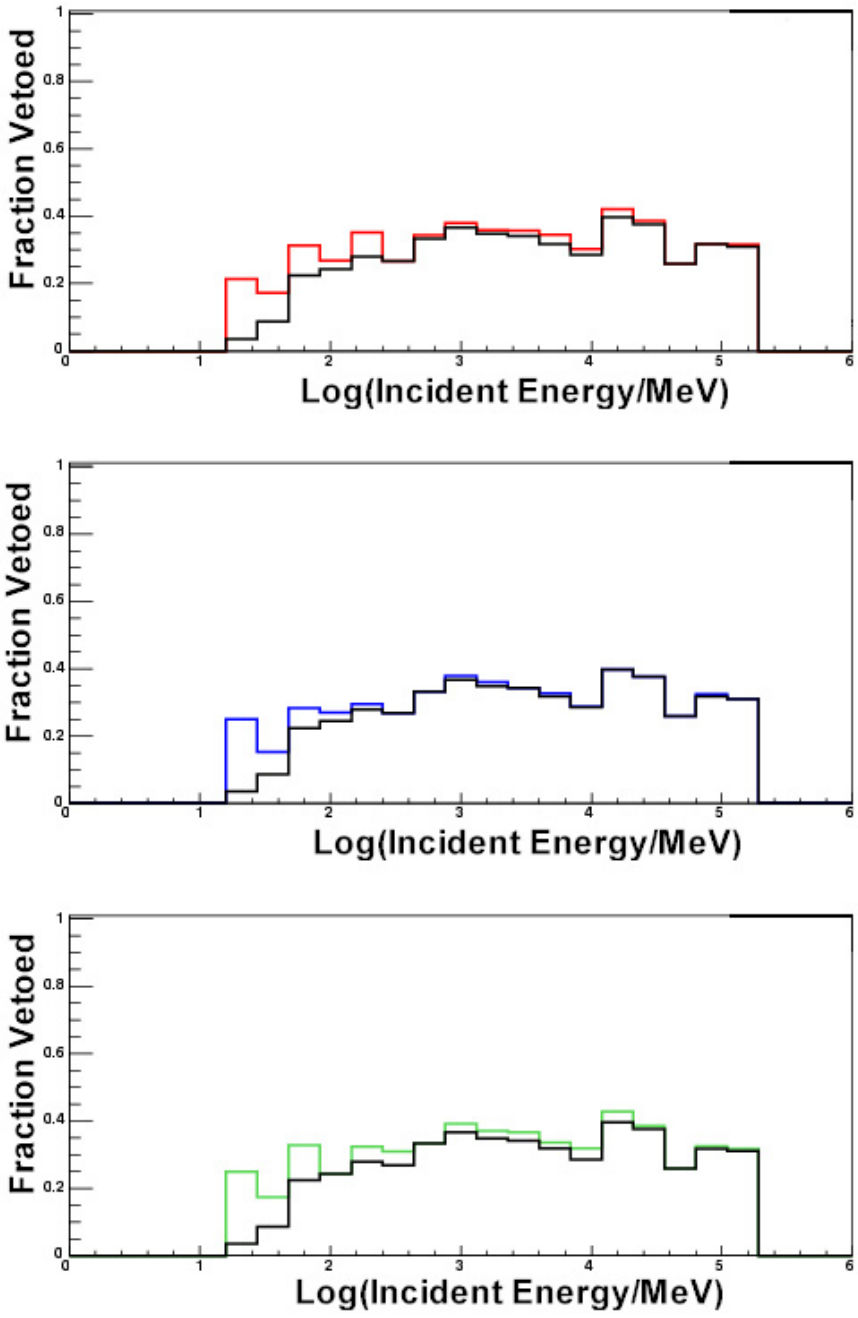

Figure 5.32: Fraction of all-triggered downward going gamma rays eliminated by Onboard Filter and Onboard Filter combined with different albedo cuts when the LAT is rocked 35 degrees from zenith. The conventions in this plot are the same as in Figure 5.30. Though the fraction of all-triggered gammas removed appears somewhat high, no goodEvents are removed by the albedo cuts, because the albedo cuts only reject events that have no energy deposit, and goodEvents have at least 5 MeV in the CAL. The albedo cuts are thus able to reduce the backround rate without impacting the ground-based analysis, as it is currently implemented.

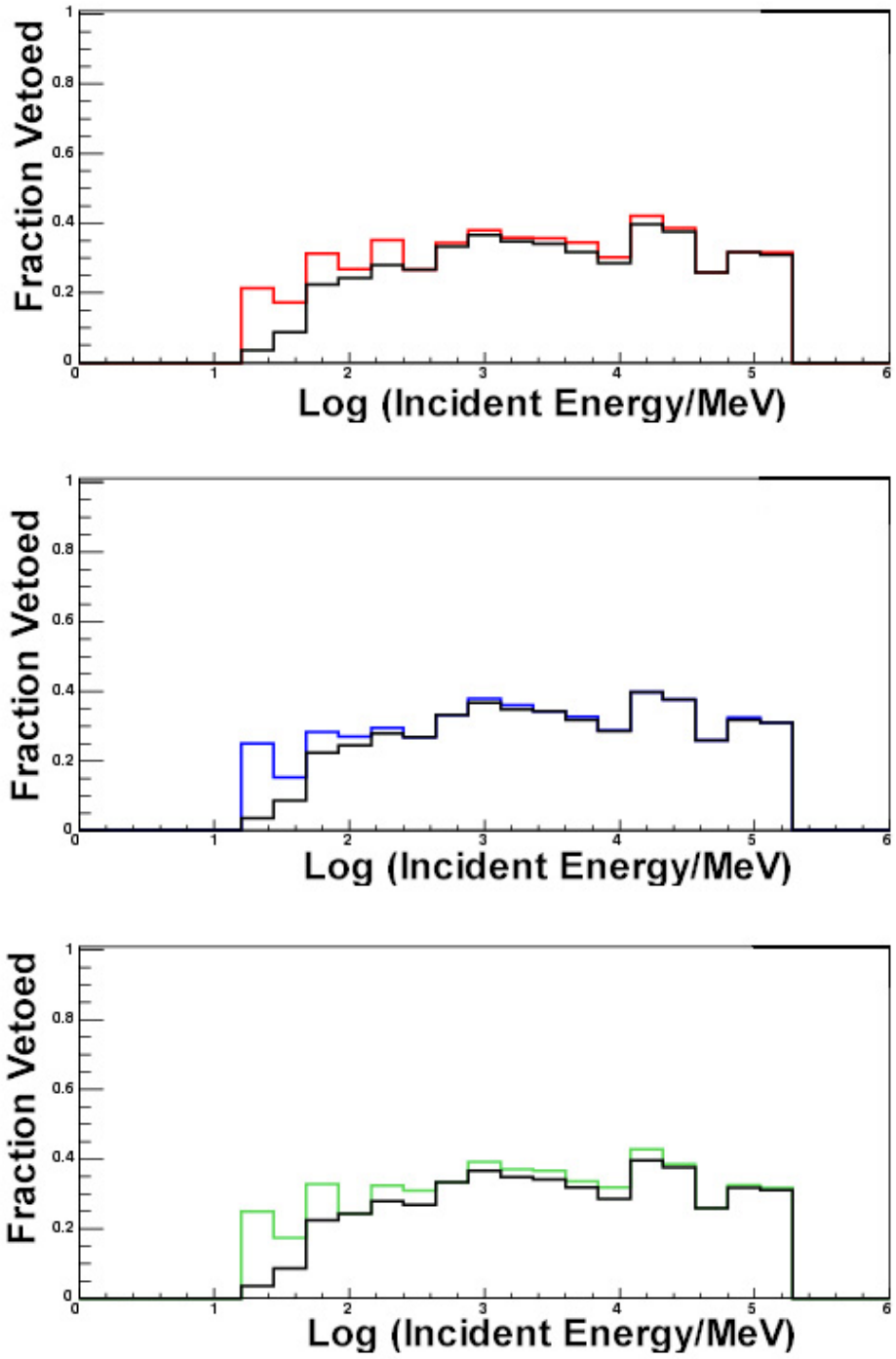

Figure 5.33: Fraction of tracker triggered downward going gamma rays eliminated by Onboard Filter and Onboard Filter combined with different albedo cuts when the LAT is rocked 35 degrees from zenith. The conventions in this plot are the same as in Figure 5.30. Though the fraction of tracker-triggered gammas removed appears somewhat high, no goodEvents are removed by the albedo cuts, because the albedo cuts only reject events that have no energy deposit, and goodEvents have at least 5 MeV in the CAL.

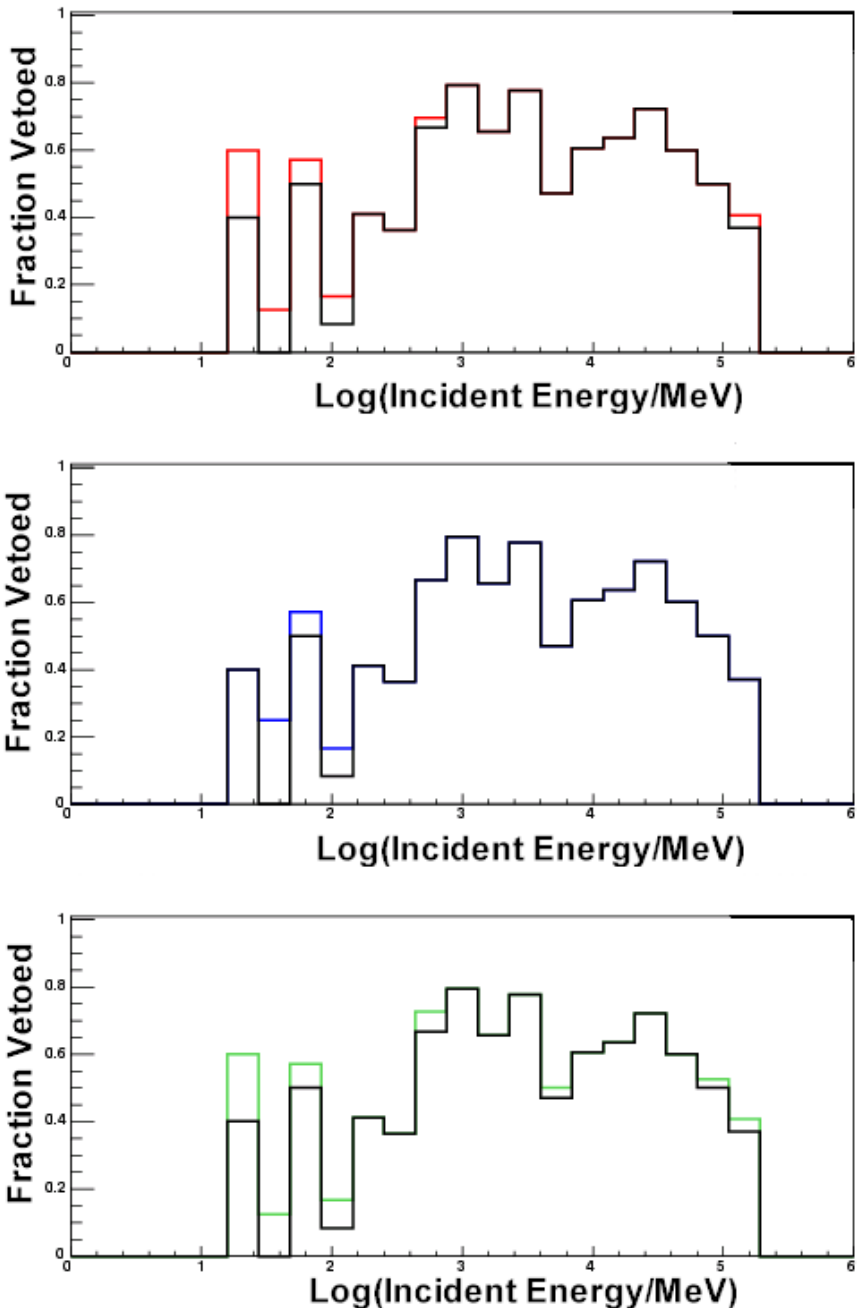

Figure 5.34: Fraction of all-triggered downward going gamma rays eliminated by Onboard Filter and Onboard Filter combined with different albedo cuts when the LAT is rocked 60 degrees from zenith. The conventions in this plot are the same as in Figure 5.30. Though the fraction of all-triggered gammas removed appears somewhat high, no goodEvents are removed by the albedo cuts, because the albedo cuts only reject events that have no energy deposit, and goodEvents have at least 5 MeV in the CAL.

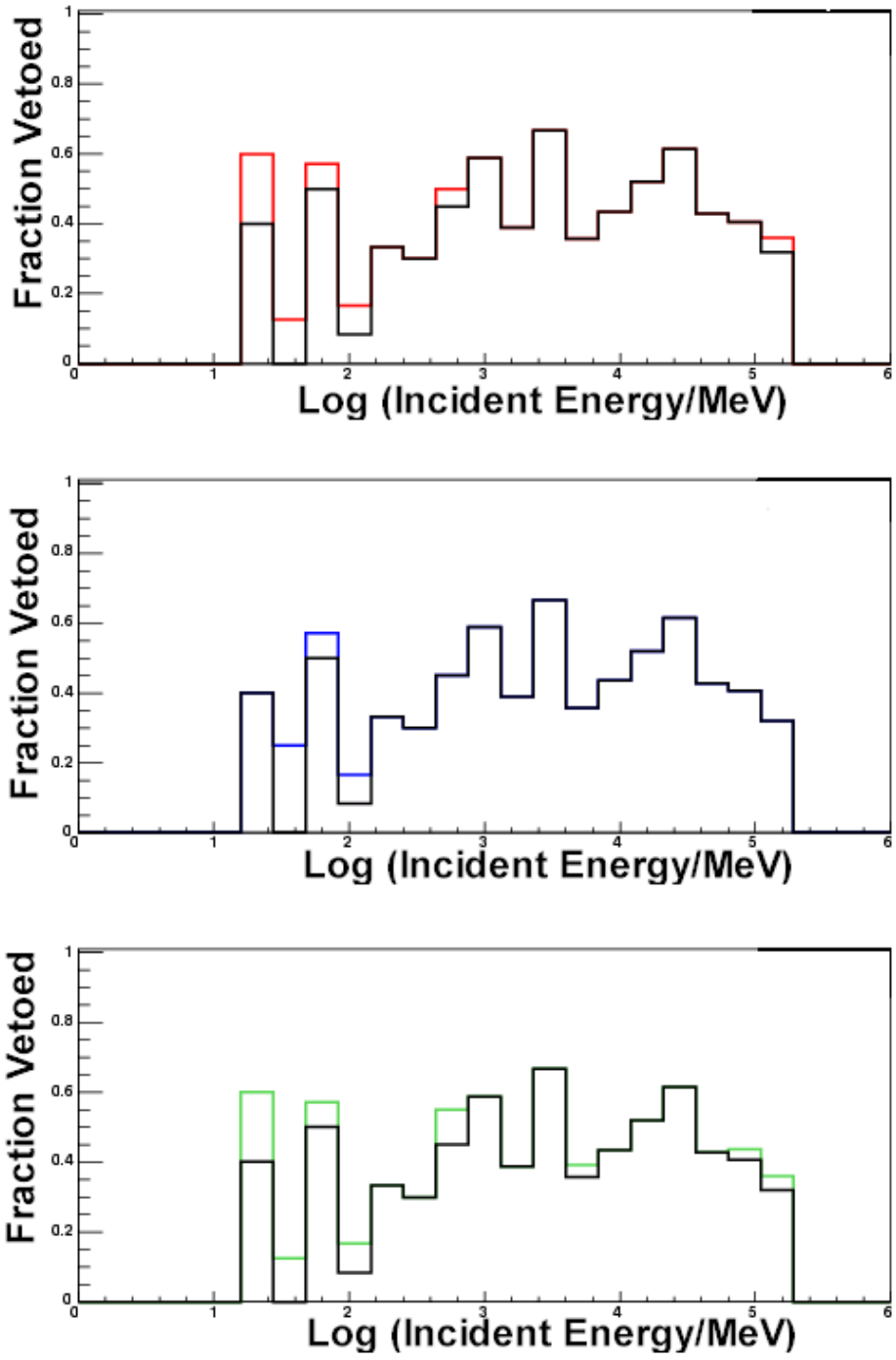

Figure 5.35: Fraction of tracker triggered downward going gamma rays eliminated by Onboard Filter and Onboard Filter combined with different albedo cuts when the LAT is rocked 60 degrees from zenith. The conventions in this plot are the same as in Figure 5.30. Though the fraction of tracker-triggered gammas removed appears somewhat high, no goodEvents are removed by the albedo cuts, because the albedo cuts only reject events that have no energy deposit, and goodEvents have at least 5 MeV in the CAL.

responsible for lowering the peak effective area below the mission requirement.

Also reported is the Filter's performance regarding albedo gammas. Because Onboard Filter is designed to allow gamma rays through, it was not successful at removing albedo, so cuts that were successful at identifying albedo gamma-ray candidates were developed and tested. Two of the cuts were especially successful at removing albedo while minimizing the rejection of downward going gamma rays. All cuts removed some downward going gammas with low incident energy, but events were only considered for removal if they deposited no energy in the CAL. Even though downward going gammas were rejected by the albedo cuts, the impact was still less than the initial implementation of Onboard Filter, so these prototype cuts can be regarded as a success.

One of the albedo cuts used Onboard Filter's two dimensional track projections to crudely determine the direction of an incoming event. In the next chapter, methods of extending the sophistication of onboard event direction finding are described. These methods work by reconstructing 3-D tracks from Onboard Filter projections. Also developed and studied was a method of track finding unrelated to Onboard Filter projections. The aim of the following work is to reconstruct tracks onboard for the purpose of detecting and localizing gamma-ray bursts in real-time with the LAT.

Chapter 6

Towards Real-Time Gamma-Ray Burst Detection in the LAT

Presented here is a description of an initial end-to-end study of whether it will be possible to meet the mission requirement for gamma-ray burst detection in the LAT, independent of external burst triggers. The study intended to explore whether GRB detection would be possible under reasonably realistic circumstances, to show what currently works well, and to show where and how improvements can be made before GLAST is launched. For this work, it was necessary to reduce the background rate to a level at which an onboard detection algorithm (developed by the LAT GRB science group) would trigger on simulated bursts. To this end, several possible filtering methods for additional background reduction have been developed and tested. Three methods of track reconstruction were also created, one of which uses a Hough Transform image recognition algorithm. The results of these studies are presented here. After simulated gamma-ray bursts were run through a well-performing set of filters, and the burst's event tracks reconstructed with a well-performing reconstruction method, they were processed with the burst detection algorithm. Those results

are interpreted and reported here, and recommendations are offered about how to proceed with studies of onboard burst detection as the GLAST mission continues.

6.1 Motivation for Real-Time GRB Detection in the LAT

Some of the most valuable information regarding gamma-ray bursts have come from fast observations of the afterglow, and this continues to be true. Detection of the high-energy prompt emission is also important. Because there exists a possibility of hard bursts with a lack of lower-energy emission upon which the GBM could trigger, it is important that the LAT be able to trigger on bursts independently. This would give the LAT the potential to quickly localize bursts and issue alerts to the burst community for rapid follow-up observations (Bonnell and Norris, 2004). Observations over a wide range of energies are extremely valuable for constraining properties of the GRB prompt emission and its transition to afterglow.

6.2 Simulating GRBs in GlastSim

In order to develop and test burst detection algorithms for the LAT, members of the collaboration developed two burst simulations. One is based on the relativistic fireball shock model (Omodei, 2002), and one is a phenomenological model extrapolated from BATSE energies (Norris, 2004). The relativistic shock model generates shells with different Lorentz factors that are randomly chosen, and the user is able to vary their parameters (thickness, initial separation, total energy budget, etc.). The shocks produced when shells collide are simulated, and the photon flux from

both synchrotron and inverse-Compton emission is calculated. From the computed flux, the program extracts individual photons to feed to GlastSim, and they are then processed in the same way that other GlastSim events are processed. This produces temporal and spectral features resembling real bursts.

The phenomenological model takes a different approach, in that it is based on BATSE data, and parameters such as peak fluxes, durations, pulse widths, and spectral power-laws are extrapolated to LAT energies. Refinements to this model may include pulse clustering, improved pulse-width energy dependence, spectral softening as the burst evolves, duration and peak energy dependencies on the peak flux, redshift-dependent attenuation by the infrared background, and possible effects of quantum gravity (Norris, 2004). For this chapter's work, a set of bursts were simulated with the relativistic shock-based burst generator, because the phenomenological model was undergoing upgrades. Of course, these represent only educated guesses about the largely unknown high-energy behavior of bursts that GLAST will uncover.

6.3 GRB Detection in the LAT

The primary method of onboard burst detection under development for the LAT uses temporal and spatial information in a maximum-likelihood method (described shortly). This is a well-established means of determining if a pattern of events on the sky have a high probability of being associated with a single source. The goal of the work described in this chapter was to develop the science selections producing

good input for the algorithm and an environment in which it can operate.

In this context, the term *environment* refers to the level of residual background with which the GRB algorithm contends, where a low rate of background events remaining after filtering constitutes a good working environment for the algorithm. *Good input* refers to both the number of gamma-rays from each burst that are made available to the algorithm, and the accuracy of the reconstructed tracks for those gamma-ray events. The more accurately the reconstruction determines the true direction of the incoming events, the more easily an algorithm will be able to trigger on a burst; and the greater the number of gamma-rays, the better the methods will be able to detect the GRBs to begin with. In flight, onboard GRB detection will be followed by burst localization, but this chapter's work focuses on showing that real-time detection is possible. This resulted in two promising sets of event filters and two track reconstruction methods that were tested for several simulated gamma-ray bursts, most of which were found by the GRB detection algorithm.

6.3.1 The Temporal-Spatial Likelihood Method of Burst Detection

A combined temporal-spatial likelihood method has been developed (Bonnell and Norris, 2004), which will have as input events that first pass the Onboard Filter cuts. The events will pass an additional background filter before serving as input to the burst detection algorithm. The additional filter is a set of cuts that will reduce the average event rate from 367 ± 7 Hz to a level at which the detection algorithm can successfully find and trigger on bursts. An initial study of the algorithm's

effectiveness by the GRB science team used a background rate of 12 Hz and tracks from the ground-based reconstruction (Bonnell and Norris, 2004). The team also did some testing with a background up to 64 Hz, and believed that the algorithm might still have success if the target residual background rate was relaxed from $\sim$ 12 Hz to 30-60 Hz. When beginning this the work for this chapter, the residual background rate target was thus 30-60 Hz.

The detection algorithm requires the relative arrival times of events, and the direction of the event in local coordinates. A future version may also make use of the event energy. A fixed number of events, N, are processed by the algorithm at any given time, regardless over how much time the events arrive. After examining N events, the sliding window moves forward in time by a fraction of N, allowing a few new events into the sample, and removing the same number of older events, keeping the total number the same. A larger window allows more gamma-ray burst photons to be present at any given time, but it also allows in more background. The background rate is determined using the number of events in the previous window divided by the time period that window covers.

To determine whether the spatial distribution of events within the current window is consistent with a GRB, the algorithm computes the angular distance between each pair of events. Each event is considered to be the potential center of a cluster, and any events within a given radius (currently $\rho = 17^o$) are temporarily associated with the possible cluster. The average distance between the chosen event and others in the potential cluster is computed and stored. This is repeated for

each of the N events, and the cluster with the smallest average distance is kept for additional processing.

The next step compares the spatial distribution of events in the cluster to a random distribution of events on the sky. Ideally, the probability of a distance, d_i, between events randomly distributed on the sky, versus the observed distances in the cluster, is given by:

$$P(d_i) = \frac{1 - cos(d_i)}{2} \tag{6.1}$$

where $0^o < d_i < 180^o$. The above equation is used by the detection algorithm, but a future version may be altered to correct for exposure effects, because the LAT effective area changes with the incident angle in instrument coordinates. The GRB detection algorithm uses the sum of the total *log* probability for the cluster, given by the sum over i of all $Log_{10}(P(d_i))$. When this method is implemented, it is necessary to set a probability threshold beyond which the likelihood of burst-type clustering is high enough for the algorithm to trigger. Some experimentation is necessary to find a good threshold; if it is too stringent, the algorithm will not trigger, but if it is too lenient, false triggers will be common. For the probability of events arriving with a given temporal separation, Δt_i, the algorithm computes the sum of $Log_{10}(1 - e^{-X})$, where $X = Rt_i$, the rate times the interval. Like the spatial trigger, a threshold must be chosen for this temporal likelihood also. Finally, a stronger case for triggering is made when both log-likelihoods above are added for a joint spatial-temporal log-likelihood.

As a final check, in place primarily as a fail-safe or diagnostic trigger for especially bright bursts, the detection algorithm also allows for a simple rate trigger. If the count rate exceeds the preceding background rate by a pre-determined significance, the algorithm will trigger. This is the least sophisticated of the methods, but is effective for bright bursts, and would provide a means of detecting problems with the likelihood methods if they did not trigger for the same bright bursts.

6.4 Reaching the Background Reduction Requirement

The success of the likelihood method depends heavily upon a low background rate and a good (small) point spread function (the calculation of which is explained below). A high background will dilute the signal from burst photons, making the detection of clustering in time and space more difficult to detect, and if the direction of a burst photon is not well determined, spatial clustering will be difficult to detect. The third factor that can improve the likelihood of localizing a burst is the field of view. The larger area visible to the LAT at any given time, the greater chance that a burst will trigger in the instrument.

6.4.1 Background Filters and Results

The approach towards reducing the background rate was first to make use of Onboard Filter cuts that had been disengaged (in Chapter 5) to increase the background rejection rate. The cuts to remove albedo events, described in the last chapter, were also used. By trying different combinations of Onboard Filter and albedo cuts, it would be possible to find methods of reducing the background rate to the desired

level while keeping the gamma-ray rejection fraction low. The background used for the performance evaluation was the combination of backgndavgpdr and the surface albedo source, a complete background flux.

The vast majority of GRB photons are at the lower energy end of the scale. The higher rate of lower energy photons makes them valuable especially to the temporal triggering part of the detection algorithm. Higher-energy photons are fewer, but they are more accurately reconstructed than lower energy photons from the same burst. Therefore it is desirable to eliminate as few gamma-rays as possible over a wide energy range.

Testing Filters

There were a total of 14 sets of cuts, or Filters (Table 6.1) to which the Chapter 5 albedo cuts were added in different combinations. When deciding upon the Filters, the intent was not to create and test every possible combination of Onboard Filter vetoes. Rather, an attempt was made to choose sensibly as the effects of each change on the background and downward going gamma rays were examined. Because many cuts tend to eliminate the same events, only a few of the Filters tested showed significant differences in the way they affected the test fluxes.

Table 6.2 shows the remaining background rates after each of the Filter and albedo cut combinations. There are several configurations that reduce the background rate to the 30-60 Hz target range, and the best performer with regards to celestial gammas must be chosen.

Label	Restored Vetoes
Filter 1	22, 23, 26
Filter 2	19, 20, 22, 23, 26
Filter 3	18, 19, 20, 22, 23, 26
Filter 4	18, 19, 20, 21, 22, 23, 26
Filter 5	17, 18, 19, 20, 21, 22, 23, 26
Filter 6	15, 17, 18, 19, 20, 21, 22, 23, 26
Filter 7	15, 17, 18, 19, 20, 22, 23, 26
Filter 8	15, 17, 19, 20, 21, 22, 23, 26
Filter 9	15, 17, 19, 20, 22, 23, 26
Filter 10	15, 19, 20, 22, 23, 26
Filter 11	15, 17, 22, 23, 26
Filter 12	15, 17, 19, 20, 26
Filter 13	15, 17, 26
Filter 14	15, 17

Table 6.1: List of veto cuts restored to Onboard Filter for the purpose of testing additional gamma-ray burst detection filters. Listed vetoes are those that were restored to their state before Onboard Filter was altered as described in Chapter 5.

Cut:	All triggered background rates after different cut combinations.					
	None	Filter Only	F OR LC	F OR DC	F OR (LC AND DC)	F OR LC OR DC
Filter 1	3907 ± 38	317 ± 11	148 ± 7	not calculated	–	–
Filter 2	3774 ± 117	289 ± 32	141 ± 23	152 ± 23	220 ± 28	72 ± 16
Filter 3	3852 ± 37	290 ± 10	149 ± 7	140 ± 7	214 ± 9	75 ± 5
Filter 4	3812 ± 37	303 ± 10	146 ± 7	137 ± 7	219 ± 9	64 ± 5
Filter 5	3812 ± 37	200 ± 9	146 ± 7	88 ± 6	169 ± 8	64 ± 5
Filter 6	3812 ± 37	96 ± 6	75 ± 5	44 ± 4	85 ± 6	34 ± 4
Filter 7	not tested	–	–	–	–	–
Filter 8	3812 ± 37	97 ± 6	76 ± 5	43 ± 4	85 ± 6	33 ± 4
Filter 9	3812 ± 37	97 ± 6	76 ± 5	43 ± 4	85 ± 6	33 ± 4
Filter 10	3812 ± 37	203 ± 9	76 ± 5	94 ± 6	136 ± 7	34 ± 4
Filter 11	3855 ± 39	101 ± 6	84 ± 6	49 ± 4	92 ± 6	41 ± 4
Filter 12	3812 ± 37	97 ± 6	76 ± 5	44 ± 4	85 ± 6	34 ± 4
Filter 13	3875 ± 59	107 ± 10	92 ± 9	55 ± 7	98 ± 9	48 ± 7
Filter 14	3857 ± 67	110 ± 11	88 ± 10	56 ± 8	100 ± 11	44 ± 7

Table 6.2: Background rejection performance of different filter versions and albedo cut combinations. The background source was the combined average background and the surface albedo source, and the rates are for all triggered events. *F* indicates *Filter*, *LC* indicates *projection-layer albedo cut*, DC indicates *directional albedo cut*. "OR" and "AND" are the boolean operators. All errors are statistical.

Recommendations

For each Filter and albedo cut combination, plots of the fraction of gamma rays eliminated between 18 MeV and 180 GeV were generated. The gammas were thrown

uniformly from all directions between the upper hemisphere of LAT coordinates. See Figure 6.1 for an example of the fraction of tracker triggered gammas eliminated by Filter 9 with both the directional and projection-layer albedo cuts (section 5.6). Tracker triggers were plotted because only events with a possibility of a track are useful for GRB detection in the LAT.

To reach a target background rate near 30 Hz, Filter 9 with the projection-layer and directional albedo cuts (see section 5.6.1) worked best, because that combination rejected the smallest fraction of gamma rays. The resulting rate, as shown in Table 6.2, was 33 Hz (also see Figure 6.1). It was also found that Filter 9 with only the projection-layer albedo cut reduced the background rate to 76 Hz while eliminating a slightly smaller fraction of low-energy gamma rays than Filter 9 with both albedo cuts (Figure 6.2). Though the residual background rate is higher than the 60 Hz upper-bound target rate, the performance advantage encouraged the testing of that Filter combination in addition to that which produced a 33 Hz background rate. A slightly higher number of gammas at low energy might help the temporal portion of the detection algorithm to trigger.

6.5 Onboard Track Reconstruction

After rate reduction, it is necessary to reconstruct 3-dimensional tracks that can be fed to the burst detection algorithm. The most obvious approach to track reconstruction is to use the 2-D projections already found in Onboard Filter. There is also the option of using strip hits (the same that are packaged and used for projec-

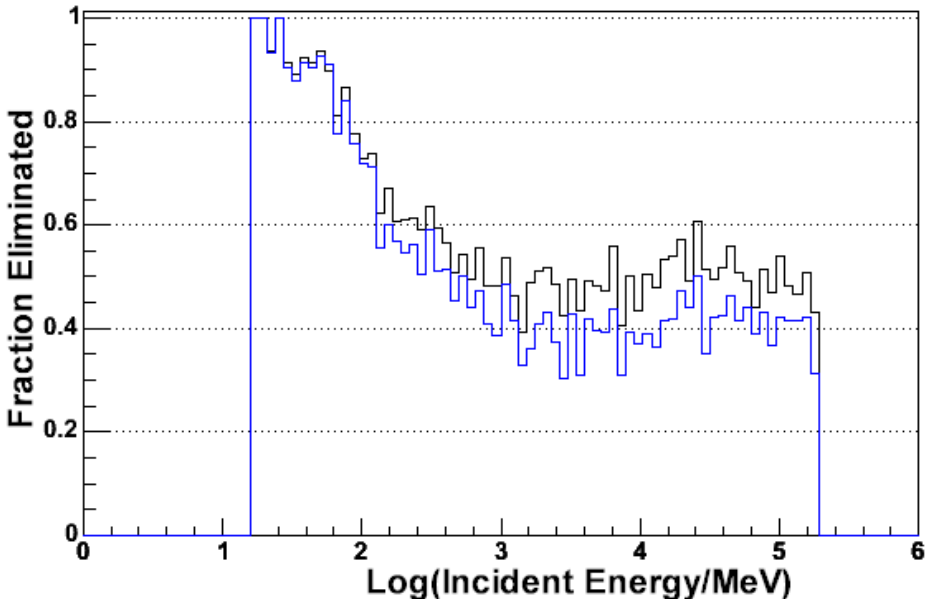

Figure 6.1: Fraction of gamma rays eliminated by Filter 9 with the projection-layer and directional albedo cuts. The event selection for the black histogram was tracker triggered events. The event selection for the blue histogram was for tracker triggered events for which the ground-based tracking method can successfully reconstruct a track within 10^o of incident energy, and for events that were incident within 75^o of normal. The blue histogram thus represents those events that have some hope of being reconstructible and useful on the ground. The residual background rate is 33 ± 4 Hz.

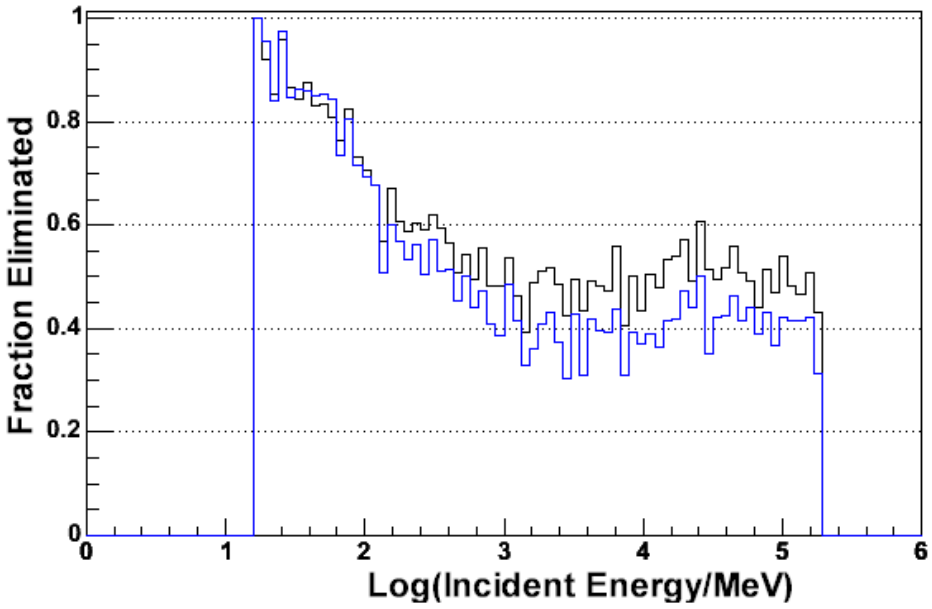

Figure 6.2: Fraction of gamma rays eliminated by Filter 9 with the projection-layer albedo cut. The event selection for the black histogram was tracker triggered events. The event selection for the blue histogram was for tracker triggered events for which the ground-based tracking method can successfully reconstruct a track within 10^o of incident energy, and for events that were incident within 75^o of normal. The blue histogram thus represents those events that have some hope of being reconstructible and useful on the ground. The background rate is reduced to 76 ± 5 Hz. Though the fraction eliminated is above 80% at low energies, a GRB with a power-law index of -2 will have 400 more photons at 50 MeV than at 1 GeV. The slightly smaller fraction of gammas eliminated below 100 MeV for this set of cuts as compared to that used for Figure 6.1 may give this set of cuts an advantage for the temporal portion of the burst triggering algorithm, because the overall number of events at low energy is relatively high.

tion finding in Onboard Filter) in any other method that developed independently of Onboard Filter's projection finding. In this section, both of these approaches are explored.

6.5.1 Creating 3D Tracks: Onboard Filter Based Methods

There is a compelling argument in favor of using Onboard Filter projections for onboard GRB science. It is only necessary to select and combine the X and Y projection vectors to calculate the orientation of a 3-D track within the LAT. This has the advantage that it is not necessary to perform any computationally intensive track or projection finding. However, this method uses projections that were never intended for the precise determination of incident direction.

Though tracks from Filter projections may not be ideal, it was necessary to have tracks to study the GRB detection algorithm. By using projection-constructed tracks, it was possible to start with what was available, and then determine whether improvements were necessary. The fundamental problem when using Onboard Filter projections is of projection or track selection, because the Onboard Filter makes no attempt to determine which of the projections it finds is the most reliable indicator of the incident particle or photon direction. Here, this is called the *track selection problem.*

Two solutions to the track selection problem were developed and tested. Both methods began by considering each tower in turn. Within each tower, a loop first selected an X projection (the first in Onboard Filter's unordered list), and then initiated another loop over the Y projections. If the X and Y projection began in

the same layer, they were paired, and the loop continued to look for more possible pairs. If none were found, the loop over Y projections continued until a common-layer pair was found or the Y projections were exhausted. All combinations of X and Y projections were tested by this common-layer condition. Upon completion of the Y loop, control returned to the X loop, which went to the next X projection and repeated the process. Three-dimensional tracks were reconstructed from all pairs that passed that common-layer condition.

Method I: Number of Associated Hits

At this point, the track selection methods diverged. For each 3-D track, two measures of length were computed, with the intention of selecting the longest track as the one to send to the GRB algorithm. Both of these used the criteria that the start point of the track was the midpoint of the common layer[1], and the endpoint was the midpoint between the last layer for which both projections had hits. If one projection extended to more layers than the other, the extra extension was not used to compute the 3-D track's length.

The two lengths computed were the number of layers hit by the 3-D track, and the length of the 3-D track as measured in arbitrary units. Early testing showed that the two measures of length were highly correlated, so the number of layers hit was used as the primary selector. It is faster because it does not require the computation

[1]The X and Y planes are separated by a small amount. When combining the projections, it is necessary to shift the X and Y vectors so that their start points are at the same vertical position in order to compute the resulting 3-D vector. This does not affect the orientation of the 3-D track at all, it merely shifts it up or down within the LAT by a small amount. The track points back to the same point on the celestial sphere regardless of its vertical position within the LAT.

of a real length, and it is a better metric in the sense that if the longest track is desired, it is not biased towards particles that enter the LAT at shallow angles (those would tend to create longer tracks for a given number of layers hit).

Here the problem of multiple tracks is encountered, so tie-breaking methods are enacted. If more than one track has the same number of associated hits, and the tracks are found in different towers, the track which lies in the tower containing the most projections is selected. If that does not break the tie, the track that begins at the highest point within the tower is selected. In the case that the tie is still not broken, the first track in the list is chosen. If a projection-based method is used when GLAST is in flight, further refinements may be necessary. For the limited purpose of an initial test of onboard burst detection, however, the tie breakers used were sufficient.

Method II: Highest Starting Point

The second method is very similar to the first, except that instead of first selecting the longest track (as measured in layers hit), the track that begins in the highest layer is chosen. The tie-breakers are then the tower with the greatest number of projections, and then the track with the greatest number of hits. This method is based on the assumption that it is not necessarily the longest track that best represents the trajectory of the incident gamma, but that the uppermost strip hit in the tracker is the first interaction of the gamma (or particle) with the tracker. The first strip hits are the least deflected by multiple scattering, so they ought to be the most accurate hits associated with the track. A problem with this method

is that the wrong track could be selected if backsplash goes higher into the tracker than the original track.

6.5.2 An Alternate Method: The Global Hough Transform

Both of the methods above have one limitation that may be important for GRB finding: the Onboard Filter projection finding stops at the boundary of a tower. This is only a feature of Onboard Filter projection finding, and a similar limitation does not apply to the ground-based reconstruction. In Onboard Filter, if a track crosses from one tower to the next, that track may not be found, or if it is found because there are enough hits in one or both towers, the correct length or starting layer will not be computed. As shown shortly, tower-crossing thus degrades the performance of any projection-based track reconstruction method for events that enter the LAT a few tens of degrees from LAT zenith. Because GRBs can occur at any time anywhere on the celestial sphere, the LAT would be better equipped to detect GRBs if the LAT had as large a field of view and as high an effective area as possible. For this reason, a method of track finding and reconstruction that does not depend on the tower-based Onboard Filter projections was developed.

This method makes use of an established image recognition technique known as a *Hough Transform* (Hough, 1959). The technique is well suited for finding regular patterns (such as straight lines) in a noisy field of discrete points. In the context of LAT track finding, the points are the clustered strip hits that Onboard Filter uses for track reconstruction, and the noise is composed of strip hits unrelated to the primary track; the fields are the X and Y views of the tracker, but not bounded by

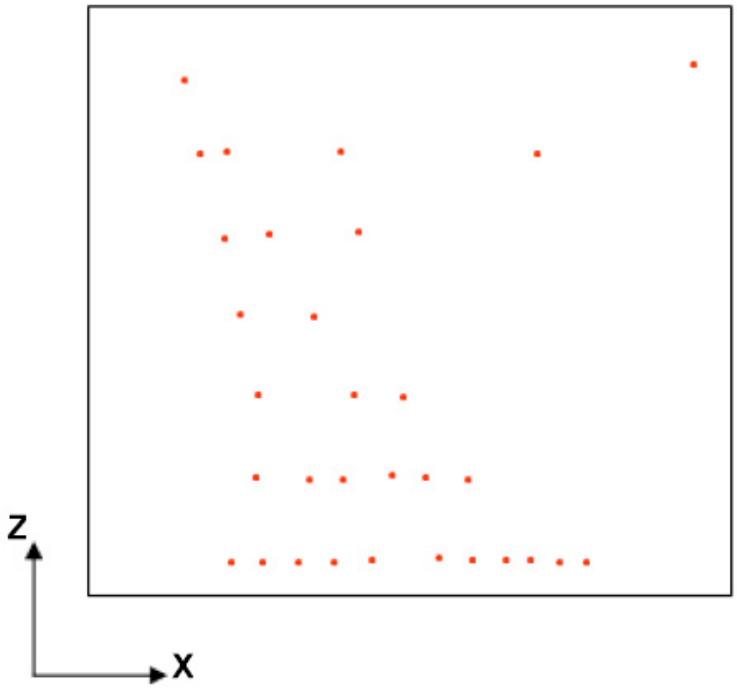

Figure 6.3: Diagram of a side view of the LAT. In this kind of view, we can impose a new Cartesian coordinate system on a side face. This set of coordinates is only used for the Hough Transform. Each strip hit, regardless of "depth" in the LAT, is represented as a red dot to which we assign a coordinate pair. The origin of the coordinate system can be placed anywhere.

tower boundaries; and the patterns are the tracks left by particle traversal.

When applying the transform, the X and Y orientations of the LAT are considered independently. It does not matter which orientation is considered first – they are equivalent in this method – so the Y orientation can be used as an example. By viewing the LAT face-on from the Y direction, it looks like the X-Z coordinate plane, where Z measures vertical distance (see Figure 6.3). Any hits on an X-oriented strip can be represented in the plane by an (X,Z) coordinate pair.

The coordinate pairs are all the information that the Hough Transform requires. It attempts to find colinear points by transforming each point in Cartesian space into a separate curve in (ρ, θ) parameter space. See Figure 6.4, in which three

colinear points (strips hits) lie in the Cartesian coordinate plane. If a line is drawn perpendicularly from the line common to the hits to the origin of the Cartesian coordinate system, it can be described in terms of a length, ρ, and an angular measure from the X axis, θ. Through each point (hit) in Cartesian space, one can draw an infinite number of lines by varying the angle of the line with respect to the X axis. If the (ρ, θ) pair associated with each line in parameter space is plotted, a sinusoidal curve is generated. Every hit in the plane thus has an associated curve in parameter space, and these curves will intersect at a common (ρ, θ) if their corresponding Cartesian points lie on the same line. If a single ρ, θ coordinate pair that describes the Cartesian space line can be found, a potential 2-D track is found. When this is done for both the X and Y LAT orientations, there exist two projections from which a 3-D track can be reconstructed. This is very similar to what was done when using Onboard Filter projections, except that the 2-D Hough tracks extend across tower boundaries and use every hit in the tracker.

In practice, this method works best by quantizing the (ρ, θ) parameter space so that it is represented by a two-dimensional histogram. Each (ρ, θ) bin is incremented as the path of the (ρ, θ) curve dictates, and the intersection of curves will be represented by the bin with the most counts. If the binning is chosen to be too coarse, the determination of the (ρ, θ) pair will be imprecise because parallel portions of nearby curves will fall in the same bin. Conversely, if the binning is chosen to be too fine, there is a risk that the curves will not all intersect in the same bin, which leads to ambiguities as to which (ρ, θ) bin is best. A little bit of trial and

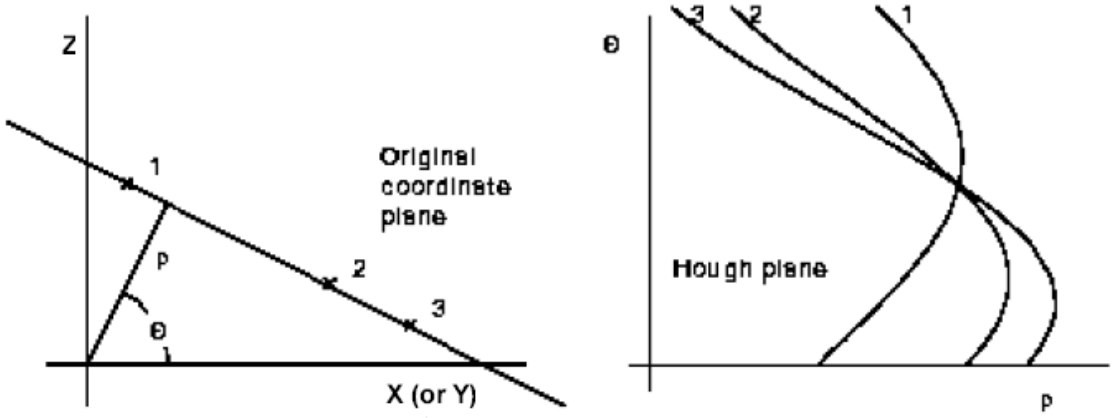

Figure 6.4: The Hough Transform. Three points in the Cartesian plane (left) are colinear. A perpendicular line is drawn from the origin to the line passing through the points. This perpendicular has a length, ρ, and is θ degrees from the X axis. An infinite number of lines can be drawn through each point in Cartesian space, and each line has an associated (ρ, θ) that can be plotted in (ρ, θ) parameter space as a sinusoidal curve. When this is done for multiple points that lie in Cartesian space, multiple (ρ, θ) curves are generated in parameter space. Where these curves cross, at a single value of (ρ, θ), is the description of the line that is common to all of them in the Cartesian plane.

error leads to a satisfactory bin selection. It was found that a 180x180 (ρ, θ) grid worked well.

In addition to its disregard for tower boundaries, the Hough Transform has the advantage that it is algorithmically simple and easy to implement. One need only to loop over all hits in each LAT orientation, incrementing θ in small steps and calculating ρ according to $\rho = (X or Y)cos(\theta) + Zsin(\theta)$, where $X(or Y)$ and Z are the Cartesian coordinates of the hit. After looping over all the hits in an orientation, one need only find the histogram bin with the most counts. The corresponding (ρ, θ) value gives the position of the 2-D track for that strip orientation. Note that the term "track" is used, rather than "tracks." The Hough Transform may find several track candidates, which will be detectable as peaks in the (ρ, θ) histogram, but the track corresponding to the highest peak is chosen. This corresponds to the

straightest track.

Finding the (ρ, θ) pair is not the end of the process, because the bin width introduces an ambiguity into the track position. This can be visualized as a *blurry track* when translated back into Cartesian coordinates. This is not necessarily a bad thing, and it is easily overcome. It is possible to proceed by calculating the coordinates of the blurry track's intersection with the different layers of the tracker. For each orientation, the algorithm looks for strip hits that fall within the boundaries defined by the blurry track. The two uppermost hits found in each orientation are used to determine the direction of the 2-D tracks that are combined to get a final, precise 3-D track. The possibility that more than one hit might fall within the blurry track boundaries is not accounted for, because the binning is tight enough that this is not a big concern, and because the upper layers of the tracker are usually sparsely populated. One could average the positions of more than one hit if desired, but for the purposes of this study, fine tuning on that scale was not a concern.

An important caution is that when applying this method to the LAT, care must be taken to find not only the right binning, but also to avoid false tracks. Because strips in the LAT lie in planes, and because the number of secondary particles generated in an event increases as the event progresses through the tracker, many planes will have multiple hits. The Hough Transform is an excellent detector of colinear points, and would be highly biased towards finding the perfectly colinear hits on an individual plane. For this reason, when filling the phase space, the algorithm excludes the region within 15^o of LAT horizontal. Tracks entering the LAT from

this region are weakly triggering anyway, and those that do trigger are rejected by filtering methods at a high rate also, so this constraint does not significantly restrict the field of view on its own.

At lower energies, Hough method may be disadvantages, because multiple scattering, especially at lower energies, can create tracks that are not straight. In the next section, we will see that the Hough method does perform better at higher energies, and it may be best utilized if only enacted when multiple scattering is less important.

6.5.3 Results of Track Reconstruction Methods

Point Spread Function for Onboard Reconstruction

To determine the performance of the track reconstruction methods, the angular separation between known event directions and their reconstructed directions are first measured. The accuracy of the track reconstruction can be described in terms of the separation that is at least as large as that for 68% or 95% of reconstructed events. These values are known as the 68% and 95% containment radii of the point spread function (PSF).

GlastSim was used to generate gamma rays at energies of 100 MeV, 1 GeV, 10 GeV and 100 GeV from the upper hemisphere of LAT coordinates. The events were passed through the Onboard Filter from Chapter 5, and reconstructed using the three track reconstruction methods. The 68% confidence containment radii for those events that passed the Filter cuts and had a ground-based reconstructible track were

plotted (see Figures 6.5 and 6.6, and Table 6.3). Of the two Filter projection-based methods, the second method outperformed the first, so the first method was removed from further consideration. Then, both for the Onboard Filter developed in Chapter 5, and for the Filter 9 cuts described above, more events were generated at the same four energies. The second Onboard Filter based track reconstruction method, the Hough Transform method, and the ground-based track reconstruction method were used to calculate the 68% confidence and 95% confidence containment radii for all triggered events that passed the Chapter 5 Onboard Filter, all triggered events that passed Filter 9 and the projection-layer albedo cut, and all triggered events that passed Filter 9, the projection-layer albedo cut and the directional albedo cut. The results are tabulated in Tables D.1 through D.12 in Appendix D.

Regardless of the event selection (the choice of filter and albedo cuts), or the track reconstruction method, the PSF improves as the energy increases. As expected, for each individual energy and for each event selection, the sophisticated ground-based track reconstruction outperforms both onboard methods. When comparing reconstruction methods, it is important to note that even for the same energy and the same top level event selection, the PSF is not always calculated for the same set of events, because each event reconstruction uses different input and therefore is able to reconstruct different events. Specifically, Method II uses Onboard Filter projections that start in the same tower and same layer, while the Hough Transform uses its own "projection" finding and is not restricted to a single tower. However, the overlap between methods is substantial. Judging the success of the methods

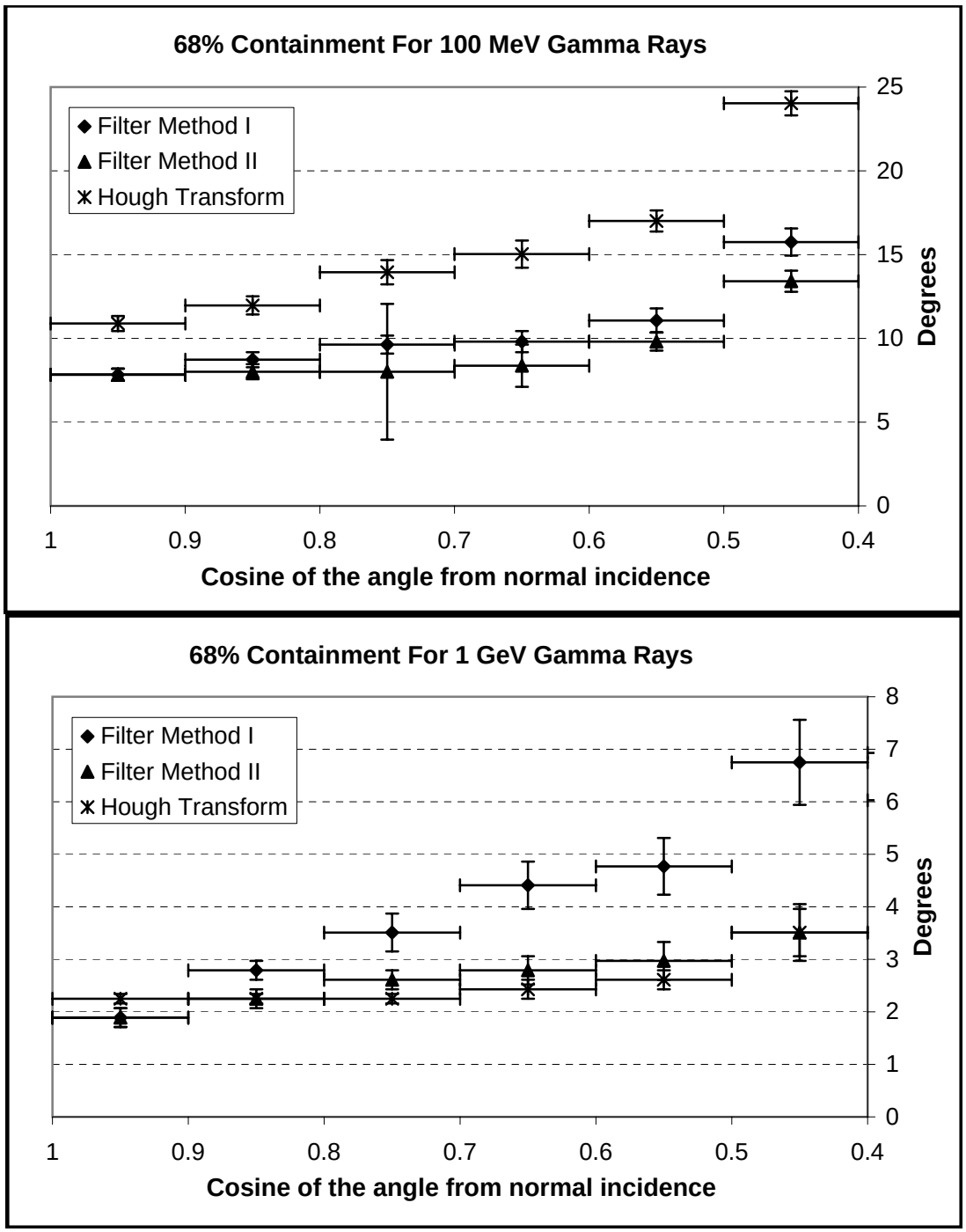

Figure 6.5: The 68% confidence containment radii for 100 MeV and 1 GeV gamma rays reconstructed by three methods. The events were those that triggered, passed through the Chapter 5 Onboard Filter, and for which the ground-based reconstruction could reconstruct a track. The uncertainties reflect the precision with which the values could be determined given the number of events generated, and the binning of the PSF histograms. For all tested energies, Method II outperforms Method I in most angular bins, reported in terms of the cosine of the angle as measured from normal incidence. The Hough Transform performs better than MI or MII as the deviation from zenith increases. The corresponding values are in Table 6.3.

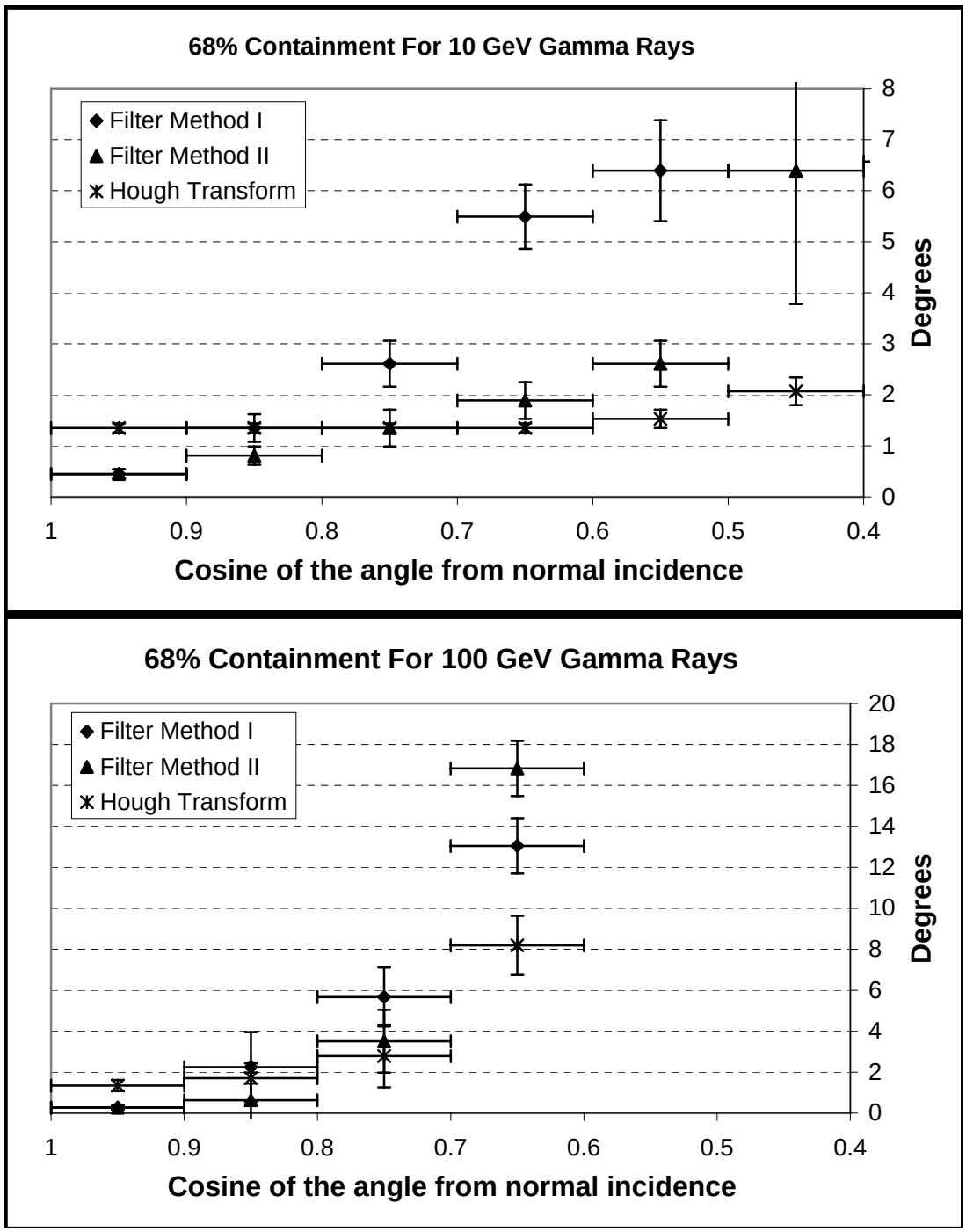

Figure 6.6: The 68% confidence containment radii for 10 GeV and 100 GeV gamma rays reconstructed by three methods. The events were those that triggered, passed through the Chapter 5 Onboard Filter, and for which the ground-based reconstruction could reconstruct a track. The uncertainties reflect the precision with which the values could be determined given the number of events generated, and the binning of the PSF histograms. For all tested energies, Method II outperforms Method I in most angular bins, reported in terms of the cosine of the angle as measured from normal incidence. The corresponding values are in Table 6.3.

must take into account the efficiency of reconstruction in addition to the PSF. The Hough method is found to consistently reconstruct 2-12% more tracks than the Filter based Method II, and for gamma energies of 1, 10 and 100 GeV, reconstructs more tracks than the ground based benchmark. The only way to determine whether the few percent difference is important would be through extensive testing using a large number of simulated gamma-ray bursts. This is commented on shortly.

Looking at the tables, beginning with 100 MeV gammas (Tables D.1–D.3), one sees that the 68% containment radius is better for Method II than the Hough Transform for any selection of gammas. Increasing the energy to 1 GeV (Tables D.4–D.6), for the most relevant events – those that pass Filter 9 and some combination of albedo cuts – the Hough method outperforms Onboard Filter Method II except for events close to normal incidence. This is due to the ability of the Hough transform to reconstruct tracks without regard to tower boundaries. All the way out to about 66^o ($cos(\theta) = 0.4$, where θ is the angle from normal incidence), the Hough value for the containment radius is relatively flat. Similar behavior is seen at 10 GeV, except that the Hough does not outperform Method II until the incident angle is 53^o from normal incidence. However, the difference between the Hough and Method II is small for angles between zenith and 53^o. Between 53^o and 73^o, the Hough performance is comparatively impressive. At 100 GeV, the pattern does not repeat, and the Hough method only outperforms Method II in the narrow 60^o to 73^o range, and even at that point the reconstruction is so poor as to not be at all useful. Gamma rays of such high energy create such a large number of secondary particles

that it is difficult for the two methods to find the initial track.

At present, neither of the methods outperforms the other in every energy range. At low energies, Method II has an advantage, but in the intermediate range, the Hough transform is the better choice. For very high energy photons, neither method performs well beyond 45^o from normal incidence, but Method II is better until that point is reached. Because very high energy photons are rare, the performance of either method in the 100 GeV range can be considered to be of less importance than at lower energies.

6.6 Results of an Onboard GRB Detection Study

The goal this chapter's work was to develop and evaluate methods of reducing background to the point at which the prototype gamma-ray burst detection algorithm would work, and then to provide feasible track reconstruction methods that could be used as a realistic input to the algorithm. Next, it is demonstrated that even with prototype filters, track reconstruction methods, and burst detection algorithm, it is possible to meet the LAT science requirement goal of detecting gamma-ray bursts in real-time if the LAT triggers on at least 100 gammas of incident energy greater than 1 GeV within a 20 second period.

6.6.1 Generating and Processing Simulated Bursts

To test these filters and track reconstruction methods, the GlastSim burst generator based on the relativistic fireball shock model was used to produce five bursts of varying strength. This model was not designed to allow the user to input desired

observable characteristics, such as length of time, spectral index, peak energy, and total fluence. Rather, one has to input the number of shocks, the total energy, the range of Lorentz factors, and the fraction of inverse-Comption vs. synchrotron emission. To verify that the simulated spectra and flux were realistic, bursts were generated, and their incident count spectra were converted into differential photon spectra to which a power-law was fit. In this way, it was possible to compare the spectral indices to those of known EGRET TASC bursts, and determine that the resulting spectra were realistic. The time profiles of the bursts were also viewed to see if they looked reasonable, though this is a subjective judgment, and any student of bursts is aware of the adage:"every gamma-ray burst is different."

As a final check, the power-law fits were extrapolated back to the TASC energy range and an estimate of burst fluence was calculated. The obvious assumption is that the power-law is valid when extrapolated back a decade in energy, but it is acceptable for this simple check. (See Figure 6.7 for an example of a fit.) The burst chosen was GRB 990104, described in Chapter 3. The fit properties for the more intense of the spectral periods for that burst were used, as were the fits for the simulated bursts, to calculate an estimated fluence over 1-200 MeV. The results along with some basic characteristics of each of the simulated bursts are contained in Table 6.4. Each of the estimated fluences is close to or below the $(2.5 \pm 0.2) \times 10^{-4}\, ergs/(MeV\, s\, cm^2)$ obtained by integrating the most intense GRB 990104 spectrum over the same energy range. The total number of triggered gamma rays above 1 GeV is below the LAT requirement for the last three bursts,

but stronger bursts were tested also. As will be shown, the burst finding algorithm only required a small fraction of the available photons for very prompt (usually $< 1\ s$) detection even for the weakest bursts in the sample.

The burst generator did produce bursts with reasonable time profiles (see Figure 6.8 for an example), and the spectral indices were all near an acceptable $\beta = -2$. The number of times the LAT triggered on photons above 1 GeV within 20 seconds was counted, and the resulting number was used as a benchmark. The number of photons for which the ground based track finding was able to reconstruct a direction was also noted, because those are the only photons one could reconstruct onboard in a best-case scenario. Each burst was then processed with Filter 9 with the layer cut, and Filter 9 with the layer and direction cuts, because it was desirable to test the performance of the GRB detection algorithm for bursts processed by a filter that corresponded to a 76 Hz background, and a filter that corresponded to a 33 Hz background. Each burst was also processed with the Method II and the Hough track reconstructions so those could be compared. After processing the bursts, a fraction of the original triggered photons remained. The output files only contained the time of the photon trigger, the energy of the photon, and its LAT coordinates in θ from nadir, and ϕ measured from the X-axis.

Bursts were generated at a constant ϕ angle of 30^o, and at 7.5^o, 37.5^o, and 70^o from LAT zenith. The azimuthal angle was chosen so the bursts were not arriving from a direction directly orthogonal or parallel to any set of tracker strips, yet were also not arriving from the same angle to both X and Y strips, as they would be if

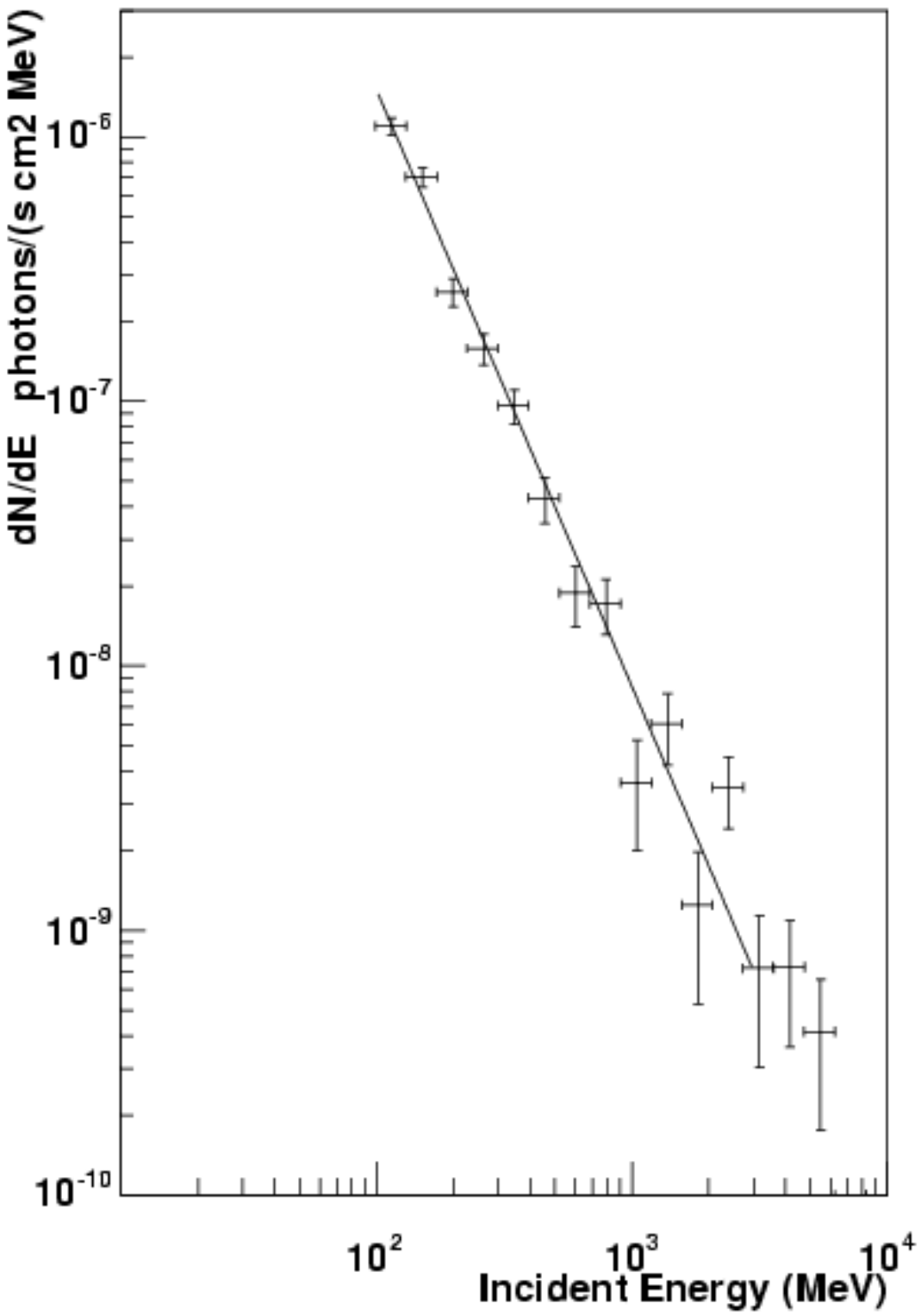

Figure 6.7: Differential photon spectrum with power-law fit to burst E. The spectral index is -2.25 ± 0.14 and the normalization constant is $(4.2 \pm 2.2) \times 10^{-4}\, photons/(MeV\, s\, cm^2)$ for a fit over 100-3000 MeV.

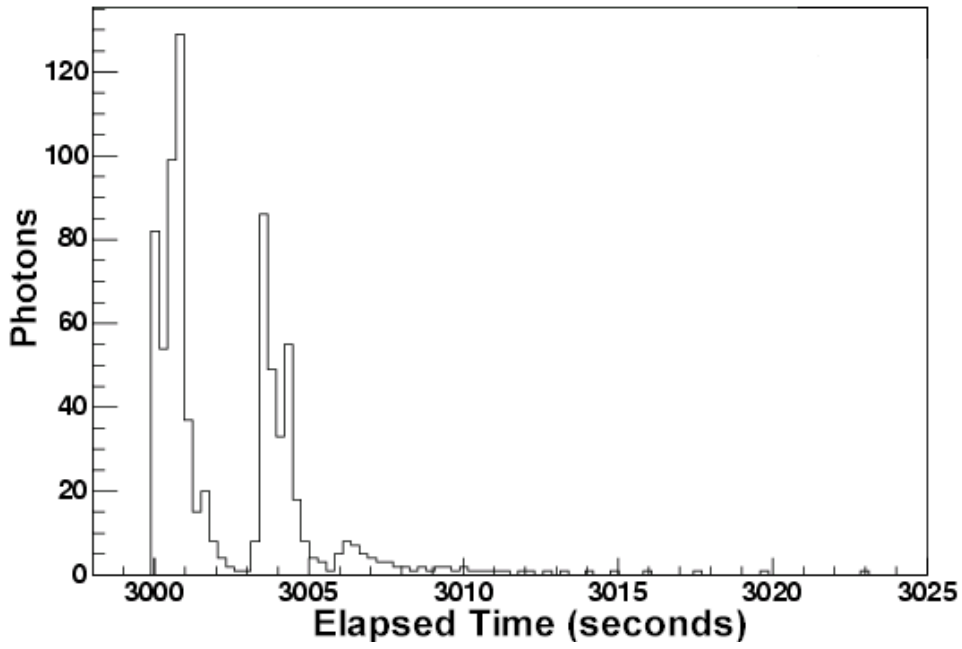

Figure 6.8: Light curve of burst *E*. The start time of the burst is arbitrarily set at t=3000 s.

$\phi = 45^o$ had been chosen. The altitude angles were chosen to place the burst close to zenith, where photons would most easily trigger, at a point at the very edge of the field of view, and at a point in-between. Bursts of different strengths as measured in terms of the photon metrics just discussed were generated.

At this point, the LAT GRB analysis software was used to merge the burst photons with a background uniformly but randomly dispersed from LAT zenith down to 80^o from zenith for all azimuthal angles. The background was not generated from a flux previously described, but was simply drawn from a list of thousands of random coordinates. This was adequate for these purposes, because the only data required by the burst detection algorithm was an event time and a coordinate pair. Every burst generated was between 7.5 and 70 degrees from LAT zenith, so this background insured that the reconstructed burst photons were surrounded by

randomized background noise. When the burst photons were merged into this background, their relative trigger times were preserved. Arrival times for the background events were randomized, but averaged to about 30 Hz and 75 Hz (these are not exactly 33 Hz and 76 Hz, but are well within the uncertainties reported in Table 6.2, and they were already available from existing background files).

With each burst embedded in a randomized background, their events were fed individually to the GRB detection algorithm. Because it is desirable to have the algorithm trigger as soon as possible after the beginning of a burst, an event window of $N = 20$ was chosen. This was also a window size successfully tested in an earlier study by the GRB science team (Bonnell and Norris, 2004). The events in the window were incremented in steps of 4 events when the algorithm was done processing a set of 20. A small window helps with the prompt detection of a burst, yet at the same time, it is progressively more difficult to detect a burst as the number of available events decreases. For a 75 Hz background, 20 events corresponds to 0.27 s. A limited attempt was made to explore the large parameter space of this algorithm, but only for the purpose of determining whether altering the default parameters would enable better detection performance than expected. For the 30 Hz background, parameters of $N = 10$ events and a 2 event increment were started with.

6.6.2 Results with Different Track Reconstruction Methods and Background Filters

Each of the five simulated bursts were placed at three angles in instrument coordinates, and they were each processed through two background filters, and with two track reconstruction algorithms. If the detection algorithm did not trigger, the event window was increased, and the algorithm was run again, so there were a total of 45 detection attempts for the 30 Hz background, and a total of 34 attempts for the 75 Hz background.

The results of the studies are contained in Appendix D in Table D.13. There are three ways that a burst can trigger the detection algorithm: on the temporal distribution, on the spatial distribution, and on the event rate. The likelihood thresholds were left at the GRB science team's current defaults[2], which were chosen to avoid false triggers. The values will be revised after further study by other investigators.

Table D.13 reports the time at which the algorithm triggered for the temporal probability, the spatial probability, the combined probability of those distributions, and the rate above background. Also listed is the burst position and the number of burst photons passing the 33 Hz background cuts. Table D.14 has the same information, but for the filter that yields a 76 Hz background.

The GRB detection generally worked better with the 76 Hz background filter and the Hough transform track reconstruction. Evidence for this is first seen for

[2] $Log(p) = -10$ for the temporal statistic, $Log(p) = -20$ for the spatial statistic, and $Log(p) = -30$ for the combined statistic.

burst C at 70^o from zenith. It was not detected when the background was 30 Hz and there were 35 available photons. However, when the same burst was run through the less aggressive background filter, it was detected 0.145 s after the first photon with the Hough transform method. The Onboard Filter MII reconstruction did not lead to a spatial trigger, but the GRB detection algorithm did generate a temporal trigger 0.125 s after the first photon arrived. Burst D was also not detected at 70^o when embedded in either background, and at 37.5^o, the burst was only detected with the Hough transform when the background rate was 30 Hz. At 75 Hz, the same burst was more easily found by MII, but this is because the GRB algorithm encountered a false trigger before the burst – something that has nothing to do with the track reconstruction method[3]. Burst E was detected using both track reconstruction methods for a 30 Hz background out to 37.5^o, but not found for either method at 70^o. Even when the background was allowed to rise to 75 Hz, neither reconstruction method led to detection that far off axis.

It was necessary to adjust parameters in the GRB detection algorithm in order to detect some bursts, and for those bursts not detected, more than one set of parameters were attempted without success. It is not suggested that the parameters used are optimal, and no claim is made that a different choice would have led to burst detection for those bursts not triggered. However, what is clear is that the burst detection algorithm requires tuning.

The GRB algorithm was able to detect bursts with as few as 41 available

[3]Reducing the false trigger rate was not a subject explored for the work presented here. It involves adjusting the algorithm parameters to maximize burst detection while minimizing the false trigger rate.

photons (those that passed through the filter cuts and had reconstructible tracks) out to 37.5^o from LAT zenith, and out to 70^o, on the very edge of the field of view, when only 51 photons were available. If one looks at how soon after the initial photon bursts were actually detected, it is clear that only a fraction of these totals were necessary for burst detection. For example, the burst with 41 photons was detected only 0.719 s after the initial photon arrived. An examination of the event list shows that only 14 photons fell within that period.

The filter that yields a 76 Hz background allowed for easier burst detection, and the Hough transform track reconstruction method worked better in this burst sample. The Hough transform's better off-axis performance, especially in the 1-10 GeV range, gave it an advantage for off-axis bursts. All of the detected bursts were bright, but had reasonable time profiles, fluences, and spectra. Even with the prototype background filters, track reconstructions, and burst detection algorithm, the LAT science requirement for burst detection will likely be exceeded.

6.7 Next Steps

Only a small portion of the possible burst detection parameter space has been explored, but it has been shown that LAT burst detection is possible with more than one filter configuration, more than one background rate, and more than one track reconstruction method. The goal was not to explore all available background filters or the large parameter space offered by the GRB detection algorithm. Still, some suggestions are offered here on how to explore that space, along with some

next steps for improving onboard burst detection.

6.7.1 Background Rejection

We saw that the choice of event filters is very important for real-time burst detection. There are many possible ways to achieve any target background rate, and each choice has a different effect on gamma rays. Burst detection was tested with two background rates corresponding to two sets of background filters, and it was found that bursts were more easily detected with the higher rate than the lower. This was not a surprise because the less aggressive filter allowed more low-energy gamma rays to survive the cuts, and it shows that filters that allow for better gamma-ray retention are important even if the difference between the fraction of gammas eliminated appears to be small. For this reason, it is suggested that a next step for improving burst detection is a series of trials with the different background filters presented in Table 6.2. It would even be worth trying Onboard Filter (as developed in Chapter 5) without any additional background cuts.

6.7.2 Track Finding

Reconstructing tracks onboard the LAT is a potentially time consuming process, but two possible ways to do this were already found. MII is the fastest method because the 2-D projections are already created, and they need only be assembled into 3-D tracks. MII also performs better than the Hough transform on axis, and sometimes out to several tens of degrees depending on energy and event selection. However, there was evidence that the Hough transform performs better off-axis

in the important 1-10 GeV range (important because the containment radius is small, which leads to spatial triggers in the burst detection algorithm), and this led to better burst detection. Before spending time implementing a flight software algorithm, it was necessary to test the potential of a Hough transform method. Because the Hough transform did show promise, it is now important to write a flight software implementation of the technique.

For the Hough method to work efficiently, with a minimum detection of false tracks, it may be prudent to limit the Hough transform to considering hits only in the upper few layers of the tracker. Lower layers tend to have many more hits, especially for high energy events, and because of multiple scattering, even hits associated with lower energy events do not contain as high a quality of information as those in higher layers. It might also be possible to improve the Hough transform performance by implementing it only when there is an energy deposit in the CAL. This would ensure that it is used for the less frequent, higher energy events that deposit in the CAL. The Hough's use would thereby be more limited to the energy range in which it outperforms MII. It also might be possible to incorporate information about the energy centroid in the CAL into a track finding method. This could guide in track selection if there were multiple tracks, or it could act as an anchor – a point through which each track must pass. As things currently stand, this may not be necessary, because spatial triggers were possible with only a few photons.

Rather than immediately try to alter the current track finding methods, it may be best to leave them as they are while testing filter variations. If refinement of

track reconstruction methods is still desired, it can most likely be pursued without repeating any filter trials. This is most likely the best course of action at the time of writing because the Onboard Filter projection finding is currently being studied and updated by Onboard Filter's original author. An MII based on an updated projection finding method will thus have to be tested in the future, though a significant improvement is not expected off-axis, because the projections will still not cross tower boundaries. If an Onboard Filter projection-based method is decided upon, the only suggested attempt at additional improvement is an enhancement of the track selection by considering a straightness parameter, possibly in the form of a linear fit to the component projections – its quality measured by a χ^2 parameter. Something similar is done in the ground-based track reconstruction, and it might yield some benefit onboard also.

6.7.3 GRB Detection Algorithm

An obvious suggestion for onboard burst detection improvement is to improve the burst detection algorithm. However, no evidence exists that the current algorithm is not adequate, and it were not written by the author of this thesis to begin with. The final judgment of whether the onboard detection software is in a good working state is not made here. The LAT mission requirement states that if 100 or more photons with energy greater than 1 GeV are detected within 20 seconds from a gamma-ray burst, the burst detection algorithm must trigger on the burst. As tested, the algorithm exceeded the detection requirement by detecting simulated bursts with as few as 13 photons with greater than 1 GeV. Therefore, the detection

algorithm, when operating in a 75 Hz background environment and supplied with tracks reconstructed with methods developed for this thesis, performed well enough in its present configuration to exceed the LAT mission requirement. The goal for this study was satisfied.

6.7.4 GRB Localization

Now that it has been determined that the real-time detection of bursts in the LAT is possible, GRB localization studies can also progress. The LAT GRB science team had developed a localization method that first tries to determine when the detected burst started and stopped by looking for the times at which the joint probability first goes over threshold, and then for the last time at which the probability was over threshold. These endpoints define the length of the burst and its position in time. Then all those events falling within the start and stop time have their positions averaged to get an approximate center of the aggregate cluster. Then only the photons falling within 7^o of the center are sent to the localization algorithm.

This algorithm can use an energy dependent PSF to weight each event. Such a feature would cause the localization to favor events with greater energy, because their directions are generally better determined. Regardless of whether energy weighting is used, the spatial centroid is calculated, and then the process is iterated twice, each time using only those events that are within 7^o of the new centroid. After the third iteration, the position of the burst is determined. This localization method should be tested with the background filters and track reconstructions described in this chapter.

6.8 Conclusion

Though this chapter's work was successful, it was necessary to adjust some of the GRB detection algorithm parameters in order to find the simulated bursts. Many trials will be necessary to find a good region in the phase space – a region where the detection efficiency is high, yet false triggers are rare. Testing the many background filters for two track reconstruction methods, along with exploration of the large parameter space provided by the GRB detection algorithm, will be a substantial project. However, the initial studies described in this chapter show that such an undertaking is likely to be fruitful.

Burst Label	Total Elapsed Time (s)	Triggered Photons	Triggered w/ $E > 1GeV$	Triggered w/ $E > 1GeV$ & Gnd Recon	Spectral Index from Fit	Normalization From Fit (ergs/(cm^2 s MeV))	Estimated 1-200 MeV Fluence (ergs/(cm^2 s MeV))
A	23.0	2163	175	115	-2.20 ± 0.09	1.45 ± 0.41	$(1.7 \pm 0.6) \times 10^{-4}$
B	7.2	1033	112	77	-2.04 ± 0.09	1.84 ± 0.54	$(1.0 \pm 0.4) \times 10^{-4}$
C	9.4	433	40	29	-2.17 ± 0.11	2.26 ± 0.79	$(1.2 \pm 0.5) \times 10^{-4}$
D	23.6	268	18	10	-2.35 ± 0.13	2.44 ± 0.95	$(2.2 \pm 1.0) \times 10^{-4}$
E	23.0	176	13	8	-2.25 ± 0.14	3.95 ± 1.74	$(4.2 \pm 2.2) \times 10^{-4}$

Table 6.3: Characteristics of simulated bursts used for testing the GRB detection algorithm, background filters, and track finding methods. Each burst is labeled A–E, and for this table, was positioned at an incident angle of 7.5^o from normal (LAT zenith), and 30^o from the X-axis. Its total elapsed time is reported in seconds, along with the number of photons that triggered the LAT, the number of photons of greater than 1 GeV (incident energy) that triggered, and the number of $E > 1$ GeV that triggered and could be reconstructed on the ground. The spectral index and normalization constants are for a power-law fit to the data over 100-3000 MeV, a region that had enough counts for a good fit. The fluence was estimated by extrapolating the fit back to the 1-200 MeV range.

68% containment radius for gamma rays (degrees)						
	100 MeV			1 GeV		
Range $cos(\theta)$	Filt MI	Filt MII	Hough	Filt MI	Filt MII	Hough
1.0 - 0.9	7.83 ± 0.36	7.83 ± 0.36	10.89 ± 0.45	1.89 ± 0.18	1.89 ± 0.18	2.25 ± 0.09
0.9 - 0.8	8.73 ± 0.45	8.01 ± 0.45	11.97 ± 0.54	2.79 ± 0.18	2.25 ± 0.18	2.25 ± 0.09
0.8 - 0.7	9.63 ± 0.54	8.01 ± 4.05	13.95 ± 0.72	3.51 ± 0.36	2.61 ± 0.18	2.25 ± 0.09
0.7 - 0.6	9.81 ± 0.63	8.37 ± 1.26	15.03 ± 0.81	4.41 ± 0.45	2.79 ± 0.27	2.43 ± 0.18
0.6 - 0.5	11.07 ± 0.72	9.81 ± 0.54	17.01 ± 0.63	4.77 ± 0.54	2.97 ± 0.36	2.61 ± 0.18
0.5 - 0.4	15.75 ± 0.81	13.41 ± 0.63	24.03 ± 0.72	6.75 ± 0.81	3.51 ± 0.54	3.51 ± 0.45
0.4 - 0.3	28.71 ± 1.26	27.09 ± 0.63	40.41 ± 1.62	11.79 ± 1.35	6.93 ± 0.63	6.03 ± 0.36
0.3 - 0.2	45.81 ± 0.99	42.57 ± 1.98	59.13 ± 2.7	61.29 ± 2.16	58.41 ± 2.16	36.81 ± 2.25
0.2 - 0.1	90.27 ± 1.62	90.09 ± 0.9	83.43 ± 0.81	94.41 ± 1.53	96.39 ± 1.62	85.59 ± 0.9
0.1 - 0.0	100.35 ± 0.72	112.59 ± 1.44	98.73 ± 2.25	117.27 ± 1.35	117.09 ± 1.44	109.89 ± 1.44
	10 GeV			100 GeV		
Range $cos(\theta)$	Filt MI	Filt MII	Hough	Filt MI	Filt MII	Hough
1.0 - 0.9	0.45 ± 0.09	0.45 ± 0.09	1.35 ± 0.09	0.27 ± 0.09	0.27 ± 0.09	1.35 ± 0.27
0.9 - 0.8	1.35 ± 0.27	0.81 ± 0.18	1.35 ± 0.09	2.25 ± 1.71	0.63 ± 1.8	1.71 ± 0.27
0.8 - 0.7	2.61 ± 0.45	1.35 ± 0.36	1.35 ± 0.09	5.67 ± 1.44	3.51 ± 1.53	2.79 ± 1.53
0.7 - 0.6	5.49 ± 0.63	1.89 ± 0.36	1.35 ± 0.09	13.05 ± 1.35	16.83 ± 1.35	8.19 ± 1.44
0.6 - 0.5	6.39 ± 0.99	2.61 ± 0.45	1.53 ± 0.18	60.21 ± 1.26	55.89 ± 1.35	66.87 ± 2.61
0.5 - 0.4	16.47 ± 0.9	6.39 ± 2.61	2.07 ± 0.27	93.87 ± 1.17	79.65 ± 1.26	65.61 ± 1.35
0.4 - 0.3	52.11 ± 1.17	42.93 ± 2.34	6.57 ± 2.43	98.01 ± 1.26	90.45 ± 1.35	95.67 ± 1.44
0.3 - 0.2	94.23 ± 1.8	88.29 ± 1.89	81.63 ± 1.08	88.11 ± 1.08	97.11 ± 1.08	98.19 ± 1.17
0.2 - 0.1	105.03 ± 1.62	101.97 ± 1.71	112.05 ± 1.98	108.45 ± 0.9	101.07 ± 0.9	129.69 ± 0.99
0.1 - 0.0	108.09 ± 1.17	100.53 ± 1.17	142.29 ± 1.35	104.49 ± 0.36	99.27 ± 0.72	129.51 ± 0.81

Table 6.4: Comparison of the three track reconstruction methods. The values are the 68% containment radii in degrees. The uncertainties reflect the precision with which the values could be determined given the number of events generated and the binning of the PSF histograms. For all tested energies, Method II outperforms Method I in most angular bins, reported in terms of the cosine of the angle as measured from normal incidence ($cos(\theta) = 1$ corresponds to LAT zenith). The Hough Transform performs better than MI or MII as the deviation from zenith increases. See Figures 6.5 and 6.6 for corresponding plots.

Chapter 7

Conclusion

The research described in this dissertation began with the desire to explore the possibility of detecting high-energy emission from gamma-ray bursts. The search through EGRET TASC data led to the discovery of high-energy emission from a burst with a long quiescent period. Appendix B shows that the sensitivity of the search was such that it would have detected burst emission with $\sim 1 - 250$ MeV fluence of $4 \times 10^{-5} \frac{ergs}{cm^2}$.

GLAST will provide data of a much higher quality than previously available in its energy range, and analysis of the data will lead to a wide range of high-energy burst emission, in addition to other gamma-ray phenomena. The flight software event filter was embedded in the standard science analysis environment for detailed event filtering studies. Work was done to develop and refine methods to allow the GLAST LAT to distinguish the charged particle background and Earth albedo photons from celestial gamma-rays that the LAT was designed to detect. These methods are implemented as onboard software algorithms that must run with efficiency and accuracy if the LAT is to satisfy the mission requirements. It was shown that the LAT will not only meet these requirements; it will exceed them.

After it was found that it is possible to reduce the background rate to an acceptable level for normal LAT operation, attention was turned to the possibility of onboard, real-time, GRB detection in the LAT. A GRB detection algorithm had already been developed and successfully tested, but the ground-based circumstances in which they tested were insufficiently realistic. A goal was to determine whether it would be possible to achieve a satisfactory background level, and to provide quality onboard track reconstruction – two necessities for onboard GRB detection – that were more realistic. This goal was achieved, and several methods of reducing the background rate to acceptable levels were provided. GRB detection with simulated bursts were tested for two background filters, and two track reconstruction methods were developed that allow the GRB detection algorithm to find simulated bursts with realistic light curves and spectral characteristics. Even with prototype background cuts, track reconstruction, and burst detection algorithms, the LAT burst detection requirements are exceeded. Finally, some suggestions were offered about how to enhance burst detection performance in the coming months before GLAST is launched.

Questions regarding high-energy emission from gamma-ray bursts, especially delayed emission, are still largely unanswered, even while theoretical speculation on the topic increases. GLAST will have the capability to detect high-energy photons in space with unprecedented sensitivity, and many questions should be answered, even as new ones emerge. The science community should anticipate great discoveries from this observatory.

Appendix A

Possible Evidence of Delayed, High-Energy Emission

A.1 The Detection of a Flare

In the Chapter 3 search, there was at least one detection of a peak that went over threshold because of a solar flare. GRB 000302 had three intervals over threshold, and after subtracting background, power-law emission was not visible (see Figure A.1). The strongest of the peaks had an accumulation interval that nearly coincided with a solar flare that was identified in BATSE notes about the burst. The BATSE log reports that there was a flare at about 540 s after the burst trigger, while the strongest TASC-data peak was from 501 to 533 s after the BATSE trigger. Ninety percent of the BATSE-detected emission fell within less than 23 s, so the flare started about 8 minutes after lower-energy emission had ended. Given the shape of the spectrum and that the emission nearly coincides with the flare as described in the BATSE notes, it was concluded that the rise in rates was most likely due to a flare. The EGRET spark chamber was not taking data at this time.

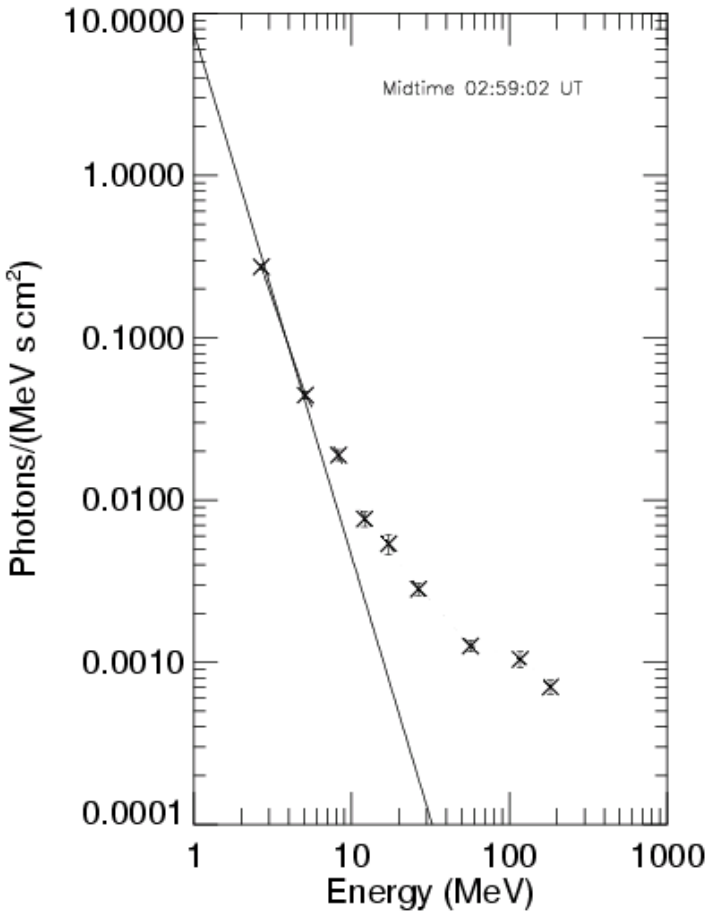

Figure A.1: Spectrum of a GRB 000302 interval near a known solar flare. The straight line is an attempted fit over 1-10 MeV.

A.2 Two Possible Detections of Delayed Burst Emission

One TASC-detected burst, previously reported (Schneid et al., 1995), also had peaks in the spectral rates following the initial burst emission. This burst was number 41 in the Table 3.1 list of most fluent bursts, with a BATSE >300 keV fluence of $(7.6 \pm 0.1) \times 10^{-5}\ ergs/s$. The published analysis of this burst's prompt TASC-detected emission described one high-energy spectrum with an index of 2.48 ± 0.10 for a fit up to 10 MeV. Photons of up to 160 MeV were also detected in the spark

chamber during the TASC accumulation interval, and the flux for the spark chamber photons was consistent with the TASC spectrum. No delayed photons were found, and there is no mention of any rise in lower-energy light curves after the burst, even though the EGRET anticoincidence dome rate does show an obvious rise (Figure A.3).

A similar rise in rates is visible in the TASC spectral rates light curve (Figure A.2). The rise begins about 5 minutes after the 45 s of BATSE T_{90} emission. It was during the rise in rates that three significant peaks (σ = 3.3, 4.5, and 2.6) were detected by the peak finding program. A peak of σ = 4.9 corresponding to the prompt burst emission was also over the 95% confidence threshold. It is apparent from Figure A.2 that the background selection used for the prompt burst emission was good, but for the peaks found later, the background intervals overlapped with the rise in rates. If the intervals had been chosen to be before and after the rise instead, the detected significance of the three peaks would have been higher, with σ = 5.5, 6.2, and 5.0. After recalculating the significance of the peaks, there appeared an additional peak of $sigma$ =2.9 preceding the original three periods. The rise in spectral rates following the T_{90} period was higher than the rise during the prompt burst emission.

Both the spectral rates light curve and the curve generated from anticoincidence dome rate could be consistent with a solar flare or burst emission. However, there is nothing in the BATSE notes about emission that occurs about 5 minutes after the initial emission episode of the BATSE-detected burst, and no indication

in the GOES data of a solar flare. Neither is this period reported in the catalogs of untriggered BATSE bursts or the IPN data. It is also possible that the rise was a fluctuation in the cosmic-ray background. However, this emission cannot be easily dismissed, because there is one EGRET spark chamber photon consistent with the burst direction (as determined by BATSE) close to the height of the broad peak. See Table A.1 for the list of photons. Other photons during the time of the rise appear to be randomly distributed, and it is not possible to conclude whether the photon came from the burst, was just a diffuse gamma-ray background event, or came from another source on the sky.

To investigate further, energy spectra were calculated for the three original periods over threshold. Because the initial background interval selection was poor, a selection of intervals before and after the rise was used. Attempted power-law fits to the spectra associated with the peak intervals had varying success. Figure A.4 shows the spectrum corresponding to the first peak over threshold. The fit was over 3-10 MeV, but extrapolated over the entire energy range on the plot. The resulting power-law index was 1.32 ± 0.56, which is harder than, but not inconsistent with a typical burst. Another fit was possible over 5-20 MeV, and its index was 1.73 ± 0.35, which is consistent with the first fit. Fits over higher energy ranges were attempted, but would not converge. For the spectrum in Figure A.5, a single power-law fit was not possible over 1-100 MeV, but it was possible to fit two power-laws over 3-10 MeV and 10-100 MeV, respectively. The 3-10 MeV fit does not appear to well represent the data points, but fits to a larger energy range were not possible. The index was

1.82 ± 0.25, with a normalization constant of $0.16 \pm 0.07\ photons/(MeV\ s\ cm^2)$. The 10-100 MeV fit better represents the data points, and its index of 1.46 ± 0.11 is harder. The two fits cannot be successfully joined at 10 MeV even when the uncertainties are taken into account. In Figures A.4 and A.5, the first data point is a 1σ upper limit, and may be due to bad background subtraction or could be a sign of a lower-energy spectral break. The third spectrum, shown in Figure A.6, is best fit by a single power-law from 1-100 MeV. Fits of two power-laws over 3-10 MeV and 10-100 MeV were less successful. The index for the 1-100 MeV fit is 1.35 ± 0.049. The final spectrum, in Figure A.7, can also be fit by a single power-law over 1-100 MeV, and it also has a hard spectrum with index 1.33 ± 0.06.

Each of the spectra plotted show visible deviations from simple power-law emission, though it was possible to fit the latter two over a wide energy range. It was only possible to fit one of the spectra with a broken power-law. Deviations from a power-law may be due to the background selection, because the background spectra had to be chosen from before and after the long rise in rates corresponding to the spectra. Other combinations of fits may be possible to the complex spectra, but the shape of the spectra do not immediately suggest that the production mechanism for the emission is that same as that for a gamma-ray burst. The more likely possibility is that these spectra correspond to a fluctuation in the background rate that may or may not have been caused by a solar flare. Still, the possibility of an unknown delayed emission production mechanism cannot be eliminated, and the rise in rates may or may not have been due to the GRB that preceded it.

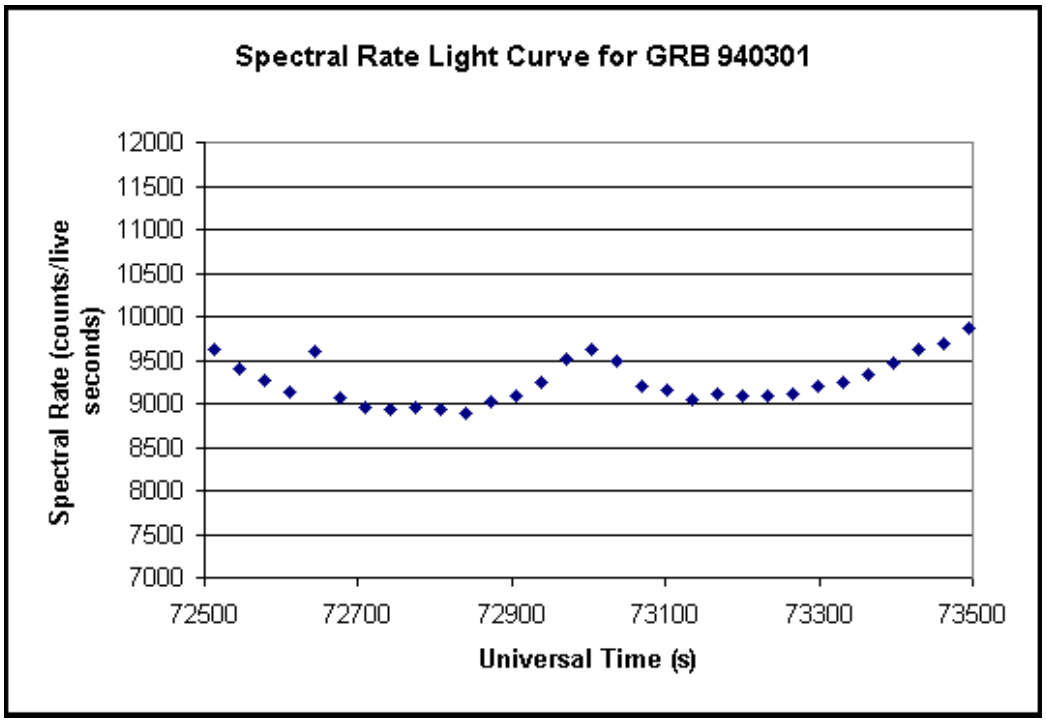

Figure A.2: Spectral rates light curve for GRB 940301. The initial rise in rates due to the burst is visible, as is a slow rise and decay a few minutes later. The cause of the second rise is unknown, but one photon from the burst direction was detected in the spark chamber during the second rise.

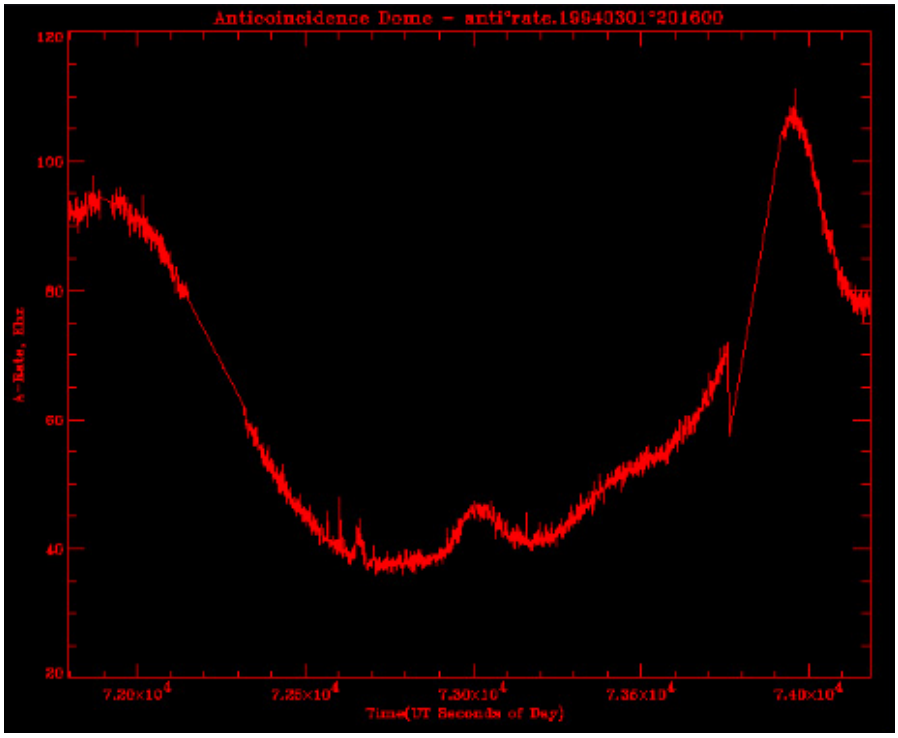

Figure A.3: EGRET anticoincidence dome discriminator rates for the time periods surrounding GRB 940301. The A-rates show a pattern also visible in the TASC spectral rates.

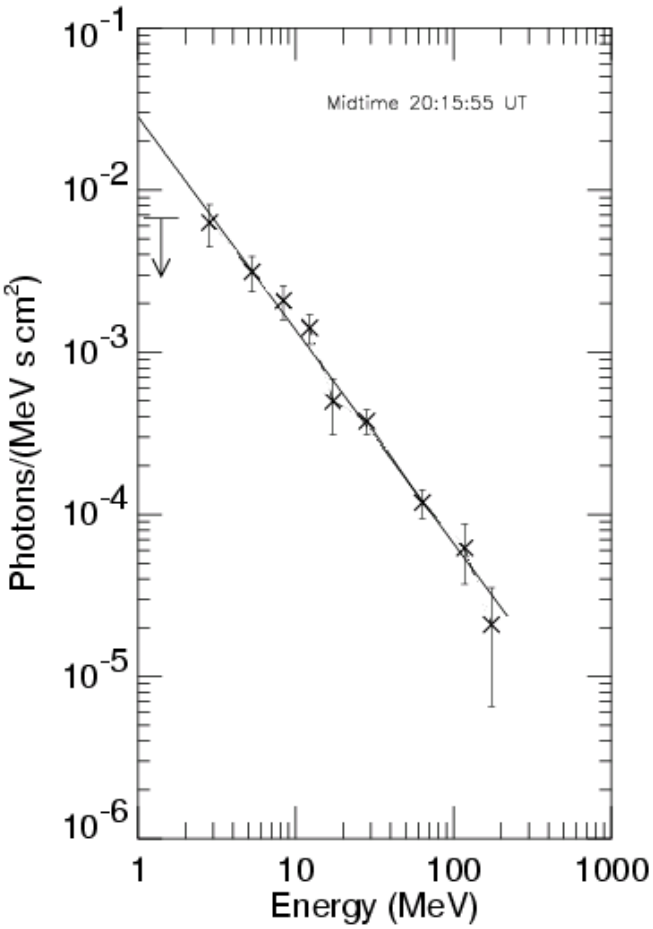

Figure A.4: First spectrum during a rise in rates following GRB 940301. The accumulation interval for this spectrum was centered 318 s after the BATSE trigger. A power-law fit was possible over two attempted energy ranges: 3-10 MeV, and 5-20 MeV. The 3-10 MeV fit is shown, with the line extrapolated to cover the entire energy range. The index for the 3-10 MeV fit was 1.32 ± 0.56, with a normalization constant of $0.028 \pm 0.036\, photons/(MeV\ s\ cm^2)$. The 5-20 MeV fit was consistent with the other fit, with an index of 1.73 ± 0.35, and a normalization constant of $0.083 \pm 0.072\, photons/(MeV\ s\ cm^2)$. The upper limit in the first energy bin may be due to the background subtraction or could be evidence of a lower-energy spectral break.

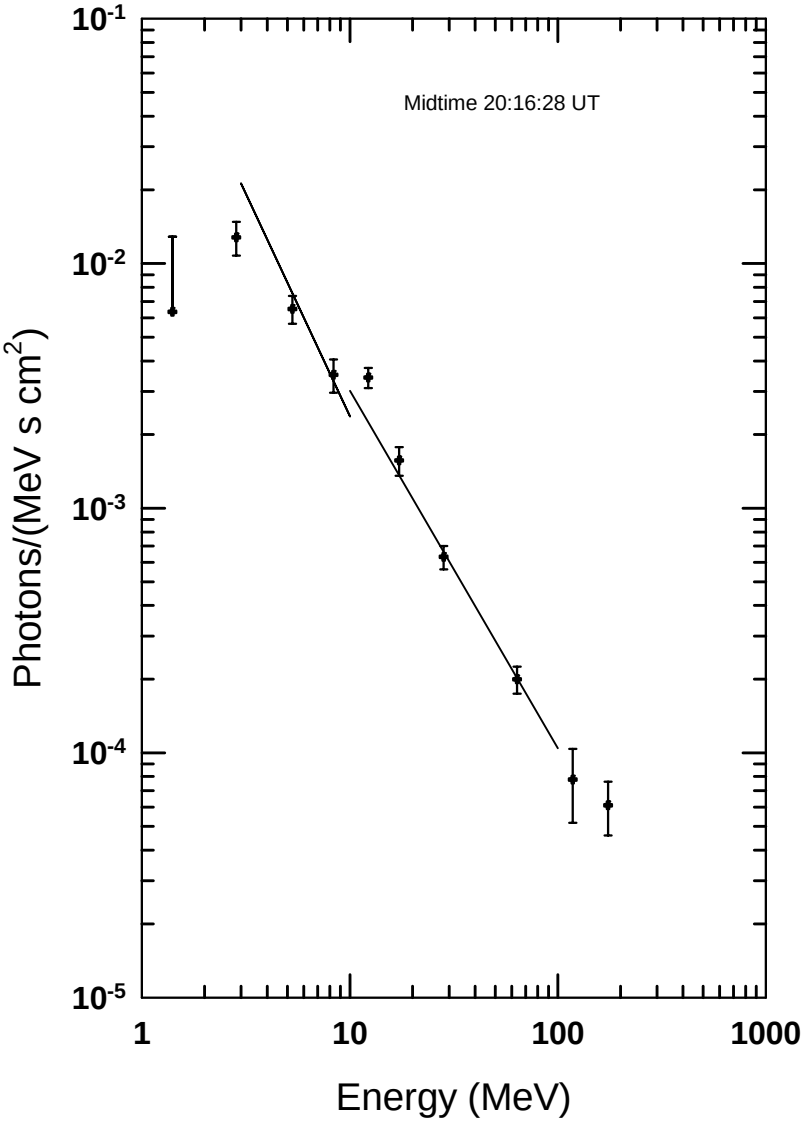

Figure A.5: Second spectrum during a rise in rates following GRB 940301. The accumulation interval for this spectrum was centered 351 s after the BATSE trigger. A single power-law fit was not possible, but a broken power-law was somewhat successful. The first fit is over 3-10 MeV, and does not seem to well represent the initial data point. Its index is 1.82 ± 0.25, with a normalization constant of $0.16 \pm 0.07\, photons/(MeV\ s\ cm^2)$. The second fit is over 10-100 MeV, and it had an index of 1.46 ± 0.11, and a normalization of $0.087 \pm 0.035\, photons/(MeV\, s\, cm^2)$. Even when the 1σ errors are accounted for, the two power-laws cannot be successfully joined. The upper limit in the first energy bin may be due to the background subtraction or could be evidence of a lower-energy spectral break.

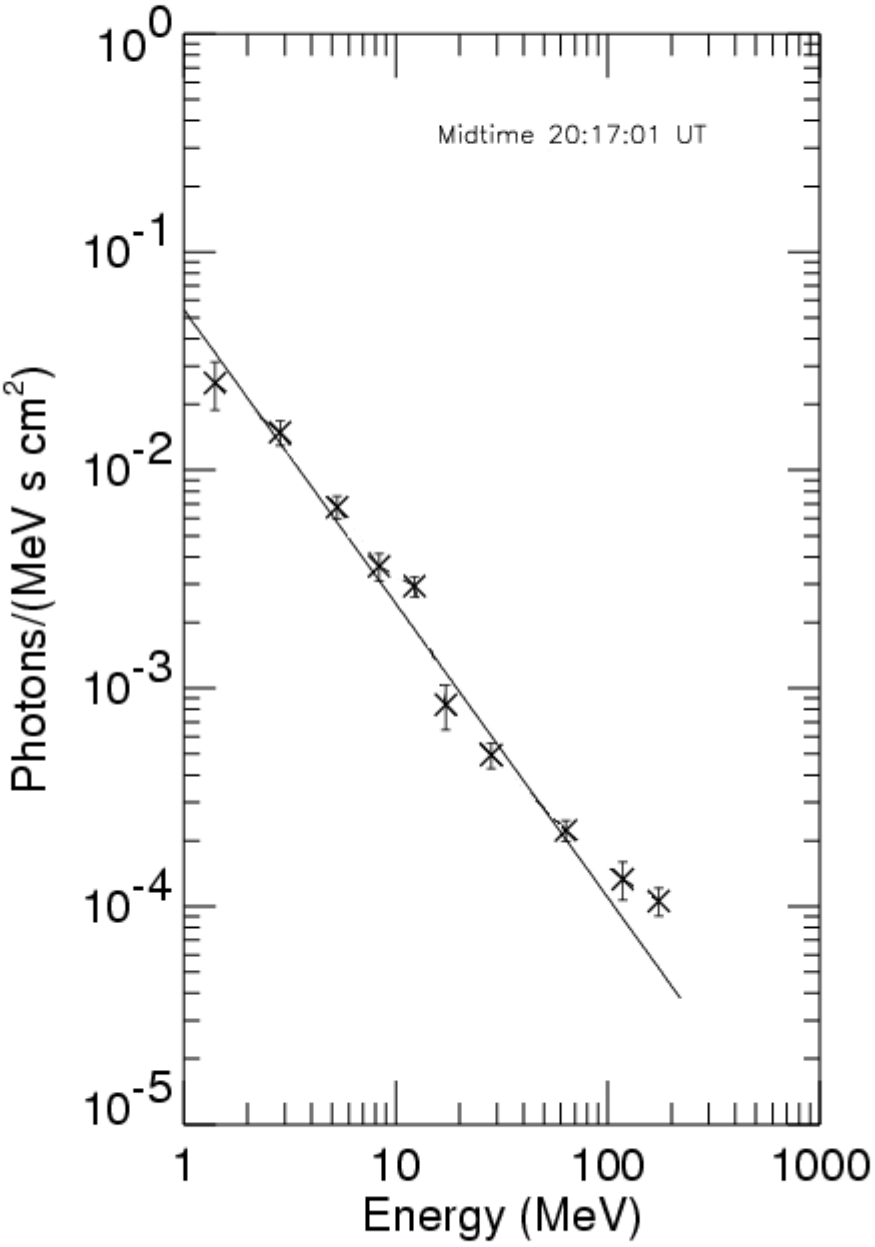

Figure A.6: Third spectrum during a rise in rates following GRB 940301. The accumulation interval for this spectrum was centered 384 s after the BATSE trigger. A 1-100 MeV fit was possible for this spectrum. It had an index of 1.35±0.05, with a normalization of $0.054 \pm 0.008 photons/(MeV\, s cm^2)$. It is possible that fits of two different power-laws may better represent the data points, but it is clear that they could not be joined near 10 MeV.

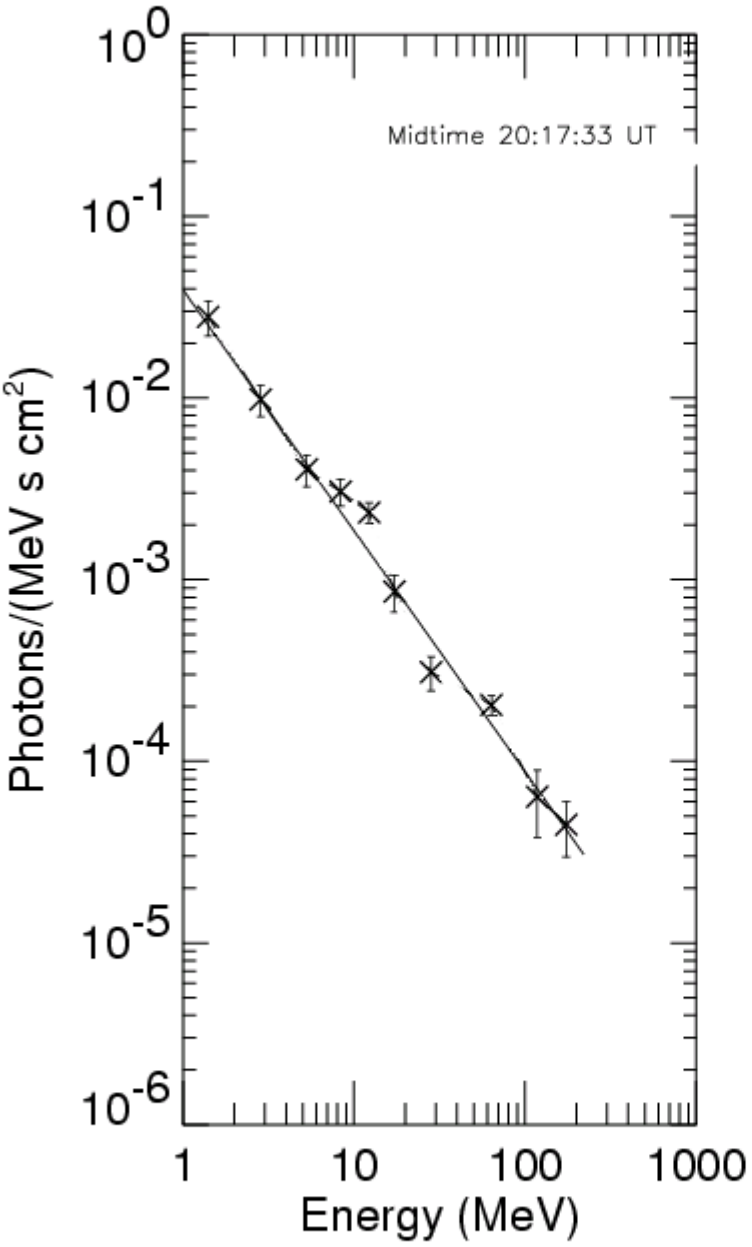

Figure A.7: Fourth spectrum during a rise in rates following GRB 940301. The accumulation interval for this spectrum was centered about 417 s after the BATSE trigger. A 1-100 MeV fit was possible for this spectrum. It had an index of 1.33 ± 0.06, with a normalization of $0.039 \pm 0.008\, photons/(MeV\ s\, cm^2)$. Statistically significant deviations from the fit are easily visible.

Table A.1: EGRET spark chamber photons near the time of GRB 940301 burst-time and post-burst emission. Events highlighted in light grey are photons that occurred during a peak in the spectral rates. Events highlighted in darker grey are those that may be consistent with the BATSE determined burst direction.

BATSE burst direction: RA 103.51^o DEC 64.35^o				
Energy (MeV)	RA (deg)	DEC (deg)	Time (UT s)	Time (Before) or After Burst (s)
58.2±26.5	236.2	46.2	72494.703	(142.375)
50.2±16.3	170.6	38.3	72519.795	(117.283)
90.6±14.4	19.2	67	72528.664	(108.414)
187.4±21.4	49	54.6	72565.932	(71.146)
41.8±10.0	43.2	65.8	72567.841	(69.237)
930.3±96	97.3	58.6	72616.346	(20.732)
244.4±61.3	210.8	55	72617.206	(19.872)
123.8±15.9	108.3	65.4	72653.996	16.918
92.4±13.6	112.5	68.1	72655.698	18.62
135.1±16.9	112.6	57.2	72660.365	23.287
155.6±44.1	167.1	21.8	72660.773	23.695
92.1±42.3	108.7	63.5	72661.847	24.769
516.9±51.9	38.6	74.5	72662.872	25.794
134.6±16.7	103.8	66.1	72665.495	28.417
132.3±16.5	108.3	65.6	72665.611	28.533
72.3±16.4	104.6	60.3	72674.812	37.734
193.4±51.1 6	206.8	49.9	72685.52	48.442
74.3±39.6	54.7	73.5	72704.737	67.659
385.6±93.1	207.6	52.5	72760.484	123.406
279.4±68.7	193.2	47.1	72764.434	127.356
645.6±153.6	259.5	61.2	72792.959	155.881
61.2±27.3	116	42.4	72816.495	179.417
92.0±33.5	204.8	50.4	72825.826	188.748
160.8±45.1	189.8	32.4	72871.241	234.163
683.2±69.9	58.3	61.6	72883.866	246.788
215.9±55.5	279	67	72892.079	255.001

Continued on Next Page...

Table A.1 – Continued

BATSE burst direction: RA 103.51^o DEC 64.35^o				
Energy	RA (deg)	DEC (deg)	Time (UT s)	Time (Before) or After Burst (s)
330.3±80.1	69	47.4	72910.799	273.721
93.6±33.8	81.5	42.3	72931.282	294.204
170.7±46.9	234.7	66.4	72940.196	303.118
77.8±31.3	19.4	59.1	72956.5	319.422
197.8±52	104.8	62.5	72969.225	332.147
472.3±114.7	-50.3	65.2	73004.331	367.253
71.8±17.2	206.9	65.3	73047.796	410.718
45.7±23.5	-50.5	69.6	73123.166	486.088
40.5±9.5	225.6	69	73131.36	494.282
96.4±14.3	121.4	54.8	73136.765	499.687
35.5±13.2	188.2	63.3	73176.006	538.928
117.9±45.2	279.5	71.7	73186.34	549.262
101.8±34.6	121.5	71.2	73198.876	561.798
277.2±28.9	82.4	62.6	73208.327	571.249
76.9±31.2	250.2	51.1	73209.669	572.591
115.8±29.5	261.3	70.6	73213.704	576.626
357.2±86.3	217.4	60.3	73221.068	583.99

Another possibility of delayed emission that cannot be entirely ruled out by any of the typical reasons are the peaks 4 hrs 24 min after GRB 981203 (Figure A.8). These peaks occurred as the background rate was decreasing rapidly after the telescope had exited the SAA, and background subtraction in these regions is often unreliable due to the rapidly changing background rate and spectra. There are no spark chamber photons at the time of the peaks, and there is no sign of a flare in GOES data or any untriggered burst in those catalogs. For the spectrum

accumulated from 19378–19411 s UT, the strong data point near 50 MeV could be interpreted as an artifact from an unideal background spectrum. Instrumental effects sometimes contributed to problematic background spectra.. However, the spectrum is relatively well fit (Figure A.9), with an index of 2.75 ± 0.30 and an error of less than 11% of the value. The normalization constant is also relatively well defined at $1.39 \pm 0.48\, photons/(MeV\ s\ cm^2)$ so the possibility of burst-related emission cannot be ruled out. If this spectrum were measured during known BATSE-detected emission, it would be likely regarded as a good measurement of high-energy burst emission.

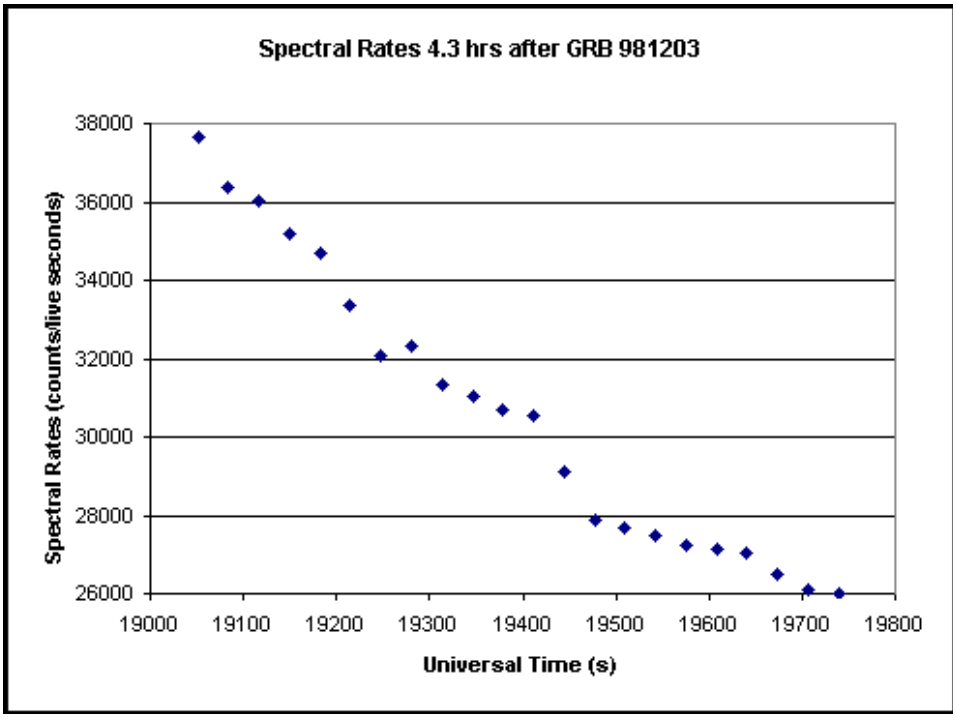

Figure A.8: Spectral rate light curve 4.3 hours after GRB 981203. The interval beginning at 19378 s UT was identified by the automated peak finding program as being over threshold, as were some other intervals nearby.

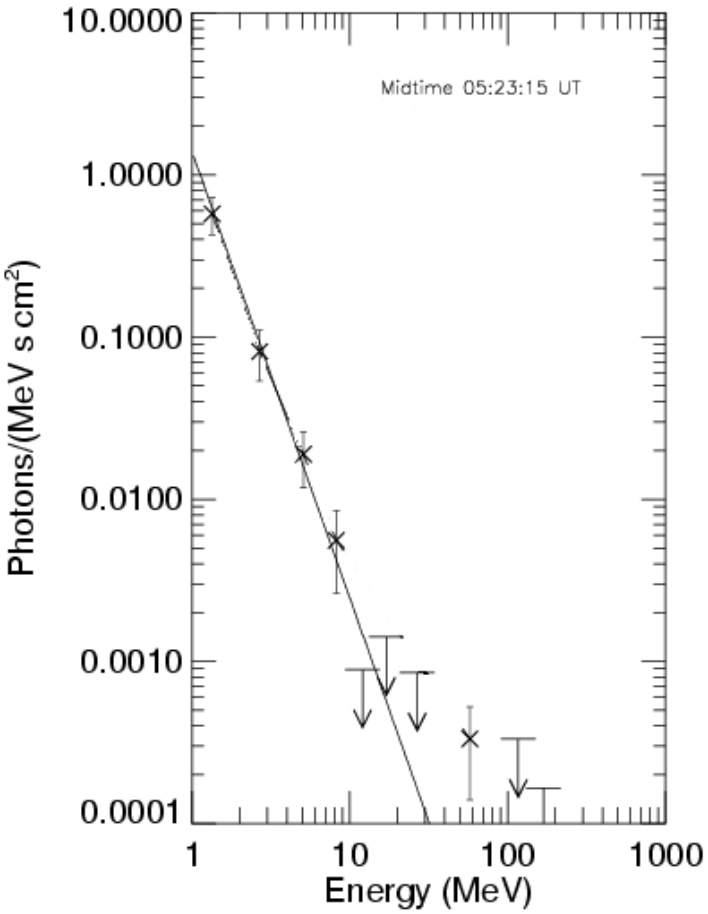

Figure A.9: Spectrum accumulated from 19378–19411 s UT, 4.4 hrs after the GRB 981203 trigger. This spectrum may be consistent with burst emission, but features at higher energies may be artifacts of an unideal background subtraction.

However, because there is no way of associating this emission with gamma-rays or a gamma-ray burst, other possibilities must be considered. When background subtraction is difficult due to fluctuations or a rapidly increasing or decreasing rate, as is the case here, it is not uncommon for lower energy excess emission to appear to follow a power-law, only to deviate from it at higher energies. The spectrum shown in Figure A.10 is softer than the first, with an index of 3.43 ± 0.24, and it shows an excess of emission at higher energies. The same behavior may also be

visible in the preceding spectrum, which may suggest that the first spectrum is also more consistent with background than burst emission. Without spark chamber photons that indicate that the possible emission is due to gamma rays from the burst direction, it is not possible to conclusively determine the cause of the rise in spectral rates.

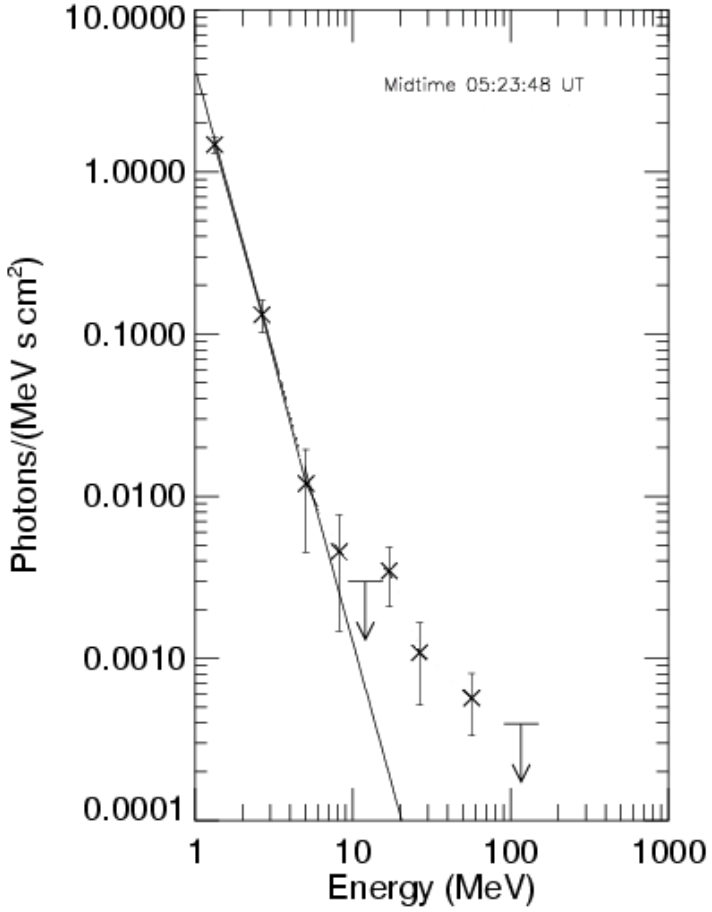

Figure A.10: Spectrum accumulated from 19411–19444 s UT, 4.4 hrs after the GRB 981203 trigger. This spectrum may show evidence of artifacts from the background subtraction.

Appendix B

Estimating an Upper Limit on TASC-Detected, Delayed, High-Energy Emission

The two cases of possible detections of delayed, high-energy emission described in Appendix A cannot be definitively linked to a gamma-ray burst, and may simply be due to fluctuations in background or solar flares. High-energy emission in which more confidence can be placed was also detected in the TASC for 16 of 18 the bursts that had peaks over threshold during the BATSE-detected emission period. Some of the 16 had more than one burst interval that was over threshold, so there are a total of 22 prompt phase spectra available for study.

A conservative description of the results in Chapter 3 and Appendix A must assume that no conclusive evidence of delayed emission was detected. If this is the case, it is desirable to know how sensitive the search was, so that an upper limit can be placed on the magnitude of emission that might have been present yet not detected by this search method. Two methods of determining an upper limit are presented in this appendix. One is more conservative, one is more speculative, The two are compared and a discussion follows about what conclusions one can

reasonably draw from the results.

B.1 Limitations and Sources of Uncertainty

This search in Chapter 3 was designed to be sensitive to the detection of high-energy emission that lasted on the order of a few 10s of seconds, yet could occur minutes or hours before or after a burst. The search was restricted to peaks in spectral rates that were no less than 95% significant when compared to a local background selection.

The upper limit calculated here is that of emission that is approximately in the 0.84-234 MeV range, where those boundaries are the average lower bound and upper bound of the TASC energy range for the bursts that were searched. The boundaries differ for each search period because of fluctuations in the TACS phototube gain, but the lower limit never went below 0.75 MeV, and the upper limit never went above 260 MeV.

Burst emission is commonly described in terms of the fluence, which is the total energy falling on a given area normal to the incident direction of the photons. The fluence, in units of $ergs\,cm^{-2}$, is not normalized for time. However, because it is known that each TASC spectrum was accumulated over the same time periods, if the fluence is known, we can divide by 32.768 s to get an average energy flux with units of $ergs\,cm^{-2}\,s^{-2}$. Upper limits are calculated and reported in both of these units below.

B.2 Calculating Burst Fluence

Determining the fluence of TASC detected emission is difficult because instrument deadtime can mask fluctuations in incident burst emission. Only if the emission is assumed to be smooth can one integrate the spectrum to get a fluence. One method of smoothing the spectrum is to do a fit over the appropriate energy range, and acknowledge that there is a calculable uncertainty due to known deviations from the fit, and an incalculable uncertainty due to possible unknown fluctuations not seen because of instrument deadtime. Because of the latter, order of magnitude estimations of fluence and flux for TASC bursts may be all that can be reasonably quoted.

Another source of error when calculating fluence is in determining the energy range over which to integrate the fit. For a TASC spectrum, the range can be determined from the gain during the period of the spectrum's integration. One cannot know with certainty over what energy range the power-law is valid, but some idea can be obtained from a plot of the spectrum, because one can see when the value in a bin can only be determined as an upper limit. The cutoff was typically judged to be between 5 MeV and 50 MeV, usually towards the lower end of that range. When computing fluence, one set of fluences was calculated over a restricted energy range as determined by a look spectral plots, another set was calculated using the entire energy range of the TASC for that burst period as determined from the gain. Tables B.1 and B.2 contain the list of spectra, the energy ranges, and the corresponding fluences for the 32.768 s periods. The encouraging result is that

the average difference between the fluence for the entire energy range and that of the restricted range is only a factor of 2.1, with a range between 1.1x to 5.5x. The relatively weak dependence on integration limits suggests that an order of magnitude fluence estimate is possible.

Calculating the fluence and an averaged flux is mechanically simple. Because the upper limit calculated in this appendix corresponds to a search using the standard background selection described in Chapter 3, spectra and fits corresponding to that background selection were used to calculate the fluence. The lower and upper energy limits used are found in Tables B.1 and B.2. (As explained later, two sets of limits were tried for each spectrum.) The fit parameters and energy limits were used to integrate the spectrum as follows. The differential gamma-ray flux (y-axis of the spectrum plots) is given by:

$$\frac{dN}{dE} = \alpha \left(\frac{E}{MeV} \right)^{-\beta} \frac{photons}{cm^2\ s\ MeV} \tag{B.1}$$

Where α is the normalization constant from the fit in units of $(\frac{photons}{cm^2\ s\ MeV})$ and β is the power-law spectral index. The differential flux can be integrated over energy to get the fluence:

$$fluence \left(\frac{MeV}{cm^2} \right) = \Delta T \int_{E_1}^{E_2} \frac{dN}{dE} E dE \tag{B.2}$$

where ΔT is the period over which the differential flux is integrated. To convert this to $\frac{ergs}{cm^2}$ we multiply by a conversion factor and substitute in the right hand side of formula 3.1:

$$fluence\left(\frac{ergs}{cm^2}\right) = \alpha\left(1.602\times10^{-6}\frac{ergs}{MeV}\right)(32.768\text{ s})\int_{E_1}^{E_2}\left(\frac{E}{E_o}\right)^{\beta}EdE \qquad \text{(B.3)}$$

where $E_o = 1\,MeV$. The analytic solution to this equation is:

$$fluence\left(\frac{ergs}{cm^2}\right) = \alpha\left(1.602\times10^{-6}\right)(32.768)\left(\frac{{E_2}^{2-\beta}}{2-\beta} - \frac{{E_1}^{2-\beta}}{2-\beta}\right) \qquad \text{(B.4)}$$

To instead look at the average flux (over energy and time), one can just divide by 32.768 s. Computing a highly reliable uncertainty in the fluence is not possible due to reasons described above, but it is possible to get some idea of what the uncertainty is from parameters that can be computed.

These parameters are the uncertainty in the gain and the error in the spectral fit. Determining the error in the gain is straightforward. When fitting a parabola to the peak in the spectrum's counts, the results of three fits were averaged. The first fit used a total of five data points: the point closest to the peak, and two points to either side. The second fit used seven points, with three points on either side. The third fit used nine points, with four points on either side. After fitting each set of points, the uncertainty in the fit parameters were propagated through the calculation, the three uncertainties were added in quadrature to get the uncertainty in the average gain value. For the spectra examined, the average uncertainty in the gain was about 11%. This uncertainty translates directly to an uncertainty in the energy bins of the TASC spectra, and therefore to the limits of the integral.

However, we have already seen that large changes in the energy range over which one integrates does not have a large impact on the final result. Indeed, the uncertainty in the gain only contributes 4.0% to the total uncertainty for fluence calculated over the entire energy range, and only 5.3% of the total uncertainty calculated over the restricted energy range. Relatively small changes due to uncertainty in the gain have a small impact in the final result.

The error in the spectral fit also has to be propagated through the fluence calculation, and for this the 1σ uncertainties in the normalization constant and the spectral index were used. The uncertainty in the $\delta\alpha$ and $\delta\beta$ terms in the fluence formula contribute more to the total uncertainty than anything else, and these were calculated by the Levenberg-Marquardt based fitting routine. The general formula for error propagation is:

$$\delta fluence = \sqrt{\left(\frac{\partial fluence}{\partial \alpha}\delta\alpha\right)^2 + \left(\frac{\partial fluence}{\partial \beta}\delta\beta\right)^2 + \left(\frac{\partial fluence}{\partial E_1}\delta E_1\right)^2 + \left(\frac{\partial fluence}{\partial E_2}\delta E_2\right)^2} \tag{B.5}$$

Where the individual terms are:

$$\frac{\partial fluence}{\partial \alpha} = (32.768 \times 1.602 \times 10^{-6})\left(\frac{E_2^{2-\beta}}{2-\beta} - \frac{E_1^{2-\beta}}{2-\beta}\right) \tag{B.6}$$

$$\frac{\partial fluence}{\partial \beta} = (32.768 \times 1.602 \times 10^{-6}) \times \left(\frac{E_2^{2-\beta}}{2-\beta} - \frac{E_1^{2-\beta}}{2-\beta} - \frac{E_2^{2-\beta} ln(E_2)}{2-\beta} + \frac{E_1^{2-\beta} ln(E_1)}{2-\beta} \right) \quad \text{(B.7)}$$

$$\frac{\partial fluence}{\partial E_2} = \alpha(32.768 \times 1.602 \times 10^{-6}) E_2^{1-\beta} \quad \text{(B.8)}$$

$$\frac{\partial fluence}{\partial E_1} = \alpha(32.768 \times 1.602 \times 10^{-6}) E_1^{1-\beta} \quad \text{(B.9)}$$

$\delta\alpha$ and $\delta\beta$ are known from the spectral fit, and δE_2 and δE_3 are computed directly from the fractional uncertainty in the gain. The result is a single value for the 1σ uncertainty in each spectrum's fluence.

An additional uncertainty in the energy spectra due to the response matrix remains as an unknown, and is only as reliable as the BATSE determination of direction and the accuracy of the EGRET Monte Carlo and mass model. The EGRET mass model was tested in beam tests, and the response function is considered to be reliable. There exists a possibility that small changes in direction (a few degrees) may sometimes alter a matrix such that there are detectable changes in the resulting energy spectra, but creating multiple response matrices for different positions within the BATSE error box for each burst is not feasible. These potential uncertainties would be more of a concern if the attempt was to calculate a highly accurate upper limit, but it has already been argued that the fluence calculation limits us to order

of magnitude arguments.

After calculating the fluence, the values range from about $1.6 \times 10^{-5} \frac{ergs}{cm^2}$ to $6.4 \times 10^{-4} \frac{ergs}{cm^2}$ over the entire energy range, and $7.6 \times 10^{-6} \frac{ergs}{cm^2}$ to $2.4 \times 10^{-4} \frac{ergs}{cm^2}$ over the restricted energy range. The uncertainty in these values ranged from less than 7% to over 240%, as evident in the error bars in Figures B.1 through B.8. These figures were the result of two programs written to perform a weighted fit to the fluence plotted as a function of spectral rate (where the weights were $\frac{\sigma^2}{\text{uncertainty}_i{}^2}$) and to compute the confidence and prediction intervals. The straight line is the fit to the data, the inner set of dashed lines are the 95% confidence intervals, and the outer set of dashed lines are the 95% prediction intervals. A description of how to use those intervals is presented in the next section.

B.3 Using the Weakest Burst Spectrum

After computing the fluence for each spectrum, there are two ways of determining an upper limit on emission. The most straightforward method is to simply look at the weakest spectral rate strength (the weakest peak) and say that any burst with a 33 s fluence greater than that value would have likely produced a >=95% confidence spectral rate peak. Therefore, the fluence corresponding to the weakest peak could be used as a measure of the search sensitivity.

There is not a perfect linear relationship between spectral rate strength and fluence, but for the fluence values computed by integrating over the entire energy range, the lowest value is $(1.62 \pm 0.83) \times 10^{-5} \frac{ergs}{cm^2}$, which corresponds to a spectral rate

strength of 2.58σ. The uncertainties reported here are 1σ. If we instead look first at the lowest spectral rate significance of 2.32σ and then at the corresponding fluence, it is apparent that it is larger at $(4.69 \pm 6.27) \times 10^{-5} \frac{ergs}{cm^2}$; it has a large uncertainty. If we instead look at the restricted energy range, the lowest fluence is $(1.47 \pm 0.28) \times 10^{-5} \frac{ergs}{cm^2}$ and corresponds to a rate strength of 6.74σ significance, while the fluence corresponding to the lowest rate strength of 2.32σ is $(1.81 \pm 3.16) \times 10^{-5} \frac{ergs}{cm^2}$. These four values range between $(1.47 \pm 0.28) \times 10^{-5}$ to $(4.69 \pm 6.27) \times 10^{-5} \frac{ergs}{cm^2}$, so at the very least, it can be stated that the weakest fluence detected was no more than $(4.69 + 6.27) \times 10^{-4} = 1.1 \times 10^{-4} \frac{ergs}{cm^2}$, which translates into an average flux of $3.34 \times 10^{-6} \frac{ergs}{cm^2\, s}$. If one instead wants to know this limit at the 95% confidence level, it is necessary to use the 1.96σ uncertainty, which gives the highest fluence a value of $(4.69 + 12.3) \times 10^{-5} = 1.7 \times 10^{-4} \frac{ergs}{cm^2}$, for an upper limit on average flux of $5.18 \times 10^{-6} \frac{ergs}{cm^2\, s}$.

B.4 Fluence vs. Spectral Rates

The weakest fluence detected is not necessarily the weakest fluence that the search was sensitive to, however. Instead, one can forecast from the data by looking at the fit at the point at which the spectral rate is equal to 1.96σ (95% confidence) above the local background. The uncertainty for this point is derived from the 95% prediction intervals on the same plots used above. This method is also complicated, in that there are not only two sets of fluences for the different energy ranges, but also two ways in which the data can be fit. The data were fit both with a forced

zero intercept and without.

When the fluence is calculated using the entire energy range and the intercept is not forced through zero, the fluence plus prediction interval value is $2.24 \times 10^{-5} \frac{ergs}{cm^2}$. When it is forced through zero, it is $3.83 \times 10^{-5} \frac{ergs}{cm^2}$. When the fluence is calculated with the restricted energy range and the intercept is not forced, the fluence plus prediction interval value is $1.24 \times 10^{-5} \frac{ergs}{cm^2}$. When forced through zero, the value is $2.50 \times 10^{-5} \frac{ergs}{cm^2}$. Because it is better to err on the conservative side, the largest of these values is chosen as the upper limit as derived from the fit to fluence vs. spectral rates.

However, the most conservative estimate of an upper limit on detectable fluence is still the large $1.7 \times 10^{-4} \frac{ergs}{cm^2}$ that was calculated by looking at the fluence corresponding to the weakest burst-time spectral rate strength. The problem with this is that the uncertainty in that estimate is based only on a single value, rather than on the combined errors taken into account by the weighted fit to the data. The highest of the values derived from the prediction intervals should be considered a more reliable indicator of a conservative upper limit fluence detection. This value is $3.83 \times 10^{-5} \frac{ergs}{cm^2}$, which corresponds to an average flux of $1.17 \times 10^{-6} \frac{ergs}{cm^2\, s}$ in the nominal 1-250 MeV energy range. Given that the uncertainties inherent in the calculations are large, it is better to state this as an order of magnitude figure of $\sim 10^{-6} \frac{ergs}{cm^2\, s}$. Any TASC spectrum due to a an average flux (over 33 s) of that value would have a 95% chance of being detected by the search method used for this chapter's work.

B.5 Downtime

The one problem not yet addressed is the instrument downtime. Because it was only possible to search the spectral rates for an average of 3.65 hours, it is not possible to comment on what happened during the remaining average period of 3.33 hours that had no searchable data. The upper limits on fluence and flux are only valid for the searchable periods when the TASC was taking data, the possibility that a sustained flux greater than $\sim 10^{-6} \frac{ergs}{cm^2\, s}$ was present after a burst cannot be excluded. It can only be argued that for the total of 117 hours that were searched before and after 32 bursts, beginning 1 hour before, and extending 6 hours after, a 95% confidence can be attached to the statement that no fluence greater than $\sim 4 \times 10^{-5} \frac{ergs}{cm^2}$ was detected in the 1-250 MeV energy range.

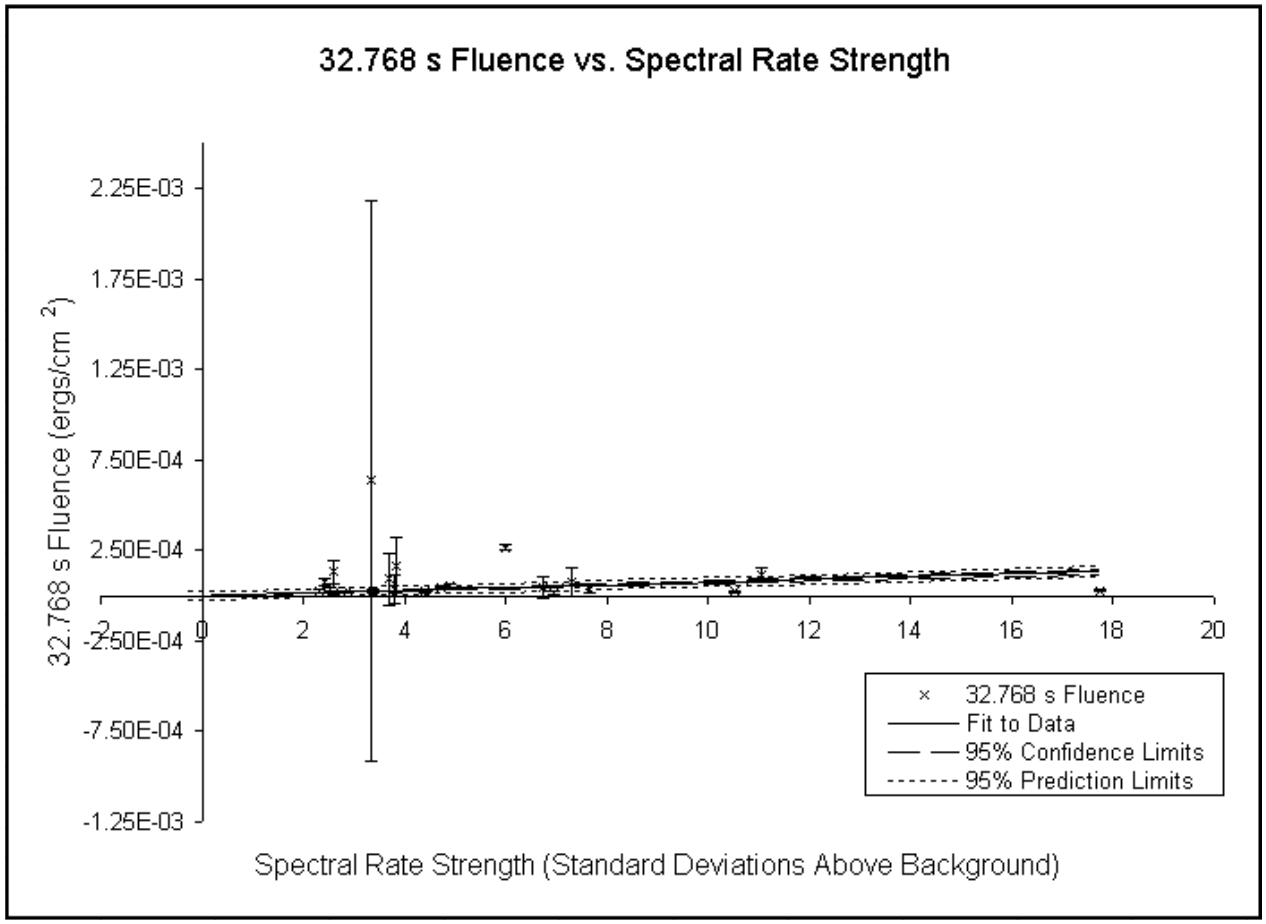

Figure B.1: Fluence vs. spectral rates for entire energy range, forced zero intercept.

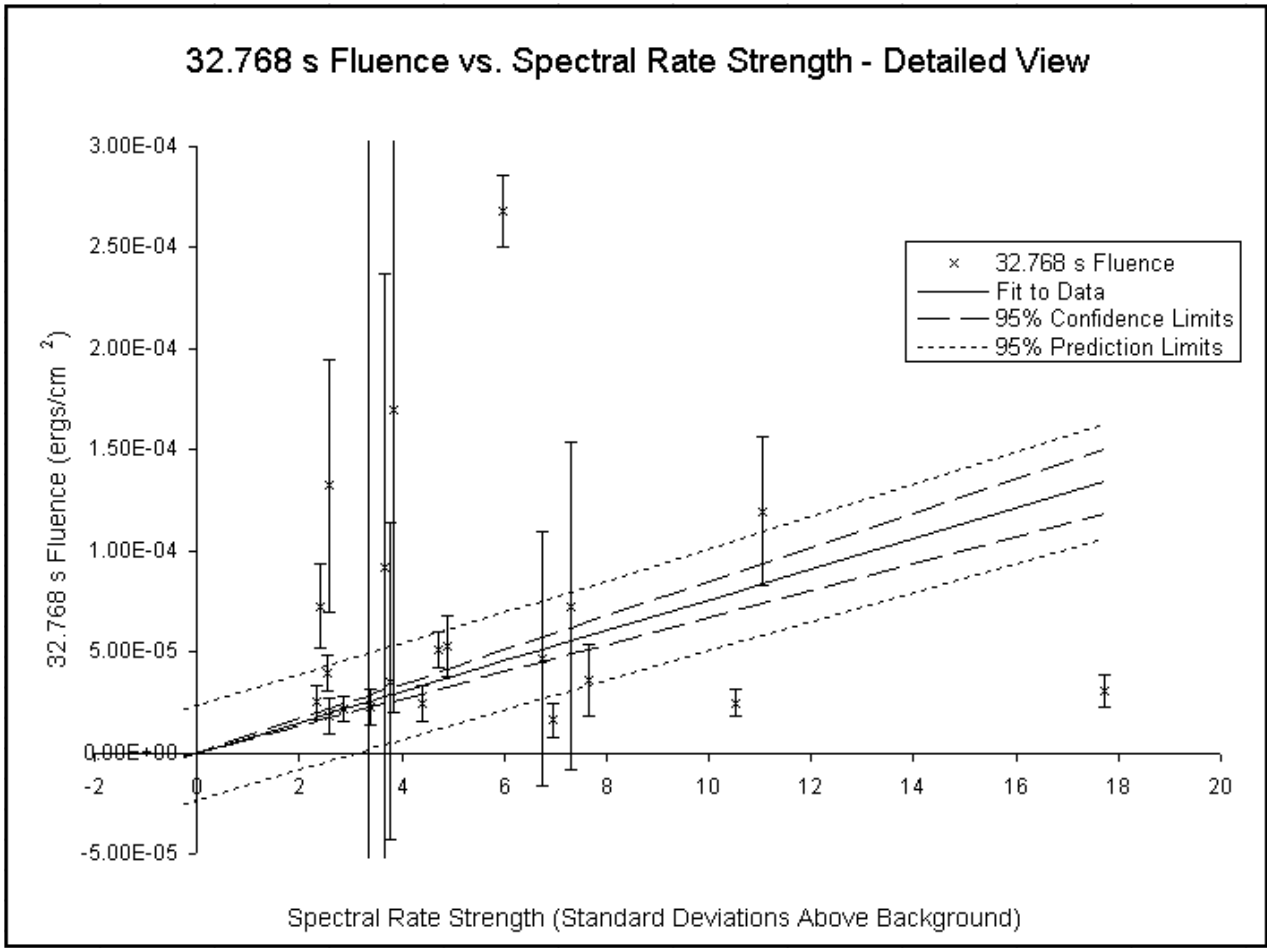

Figure B.2: Fluence vs. spectral rates for entire energy range, forced zero intercept detail.

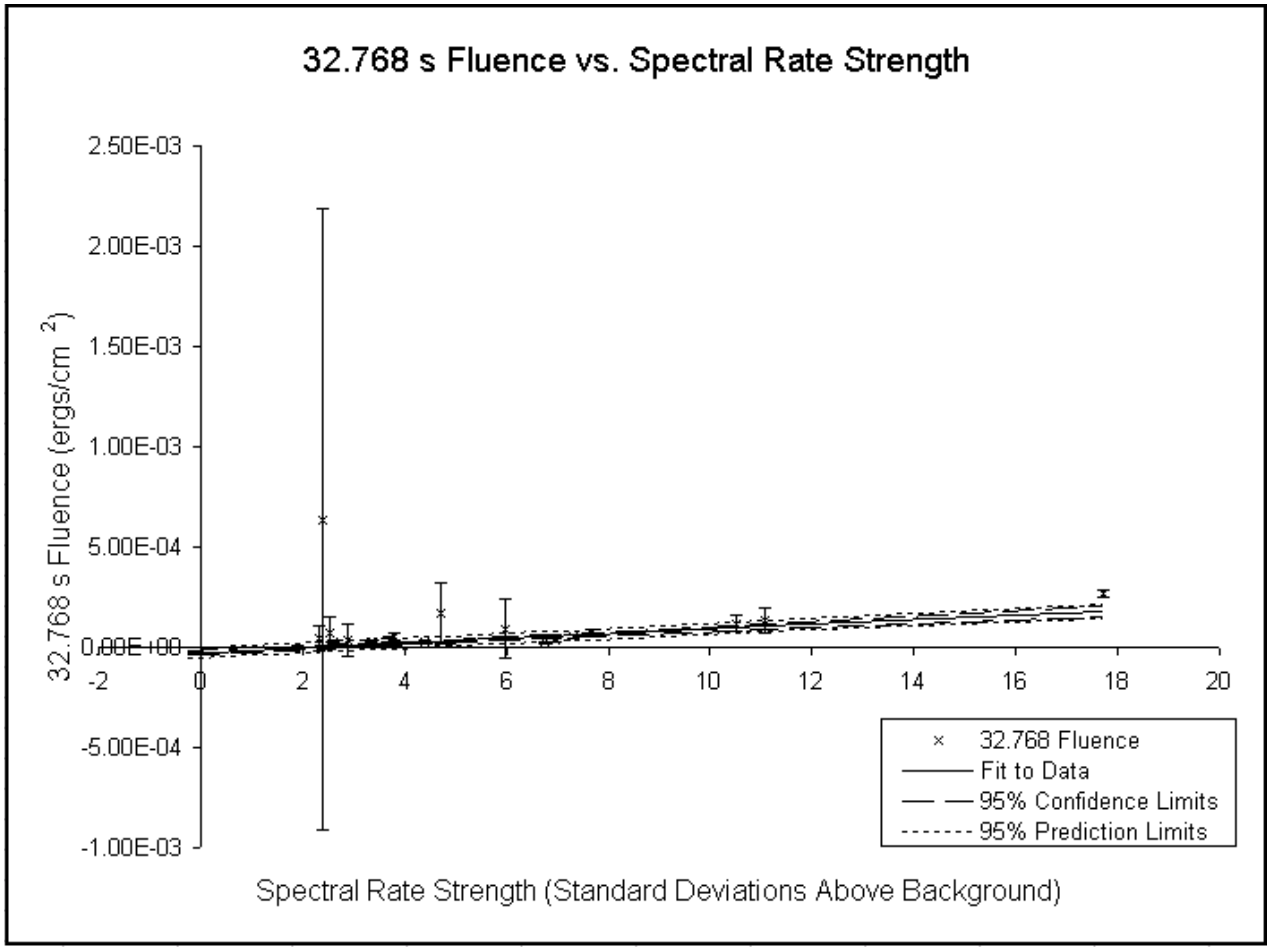

Figure B.3: Fluence vs. spectral rates, entire energy range. Intercept not forced.

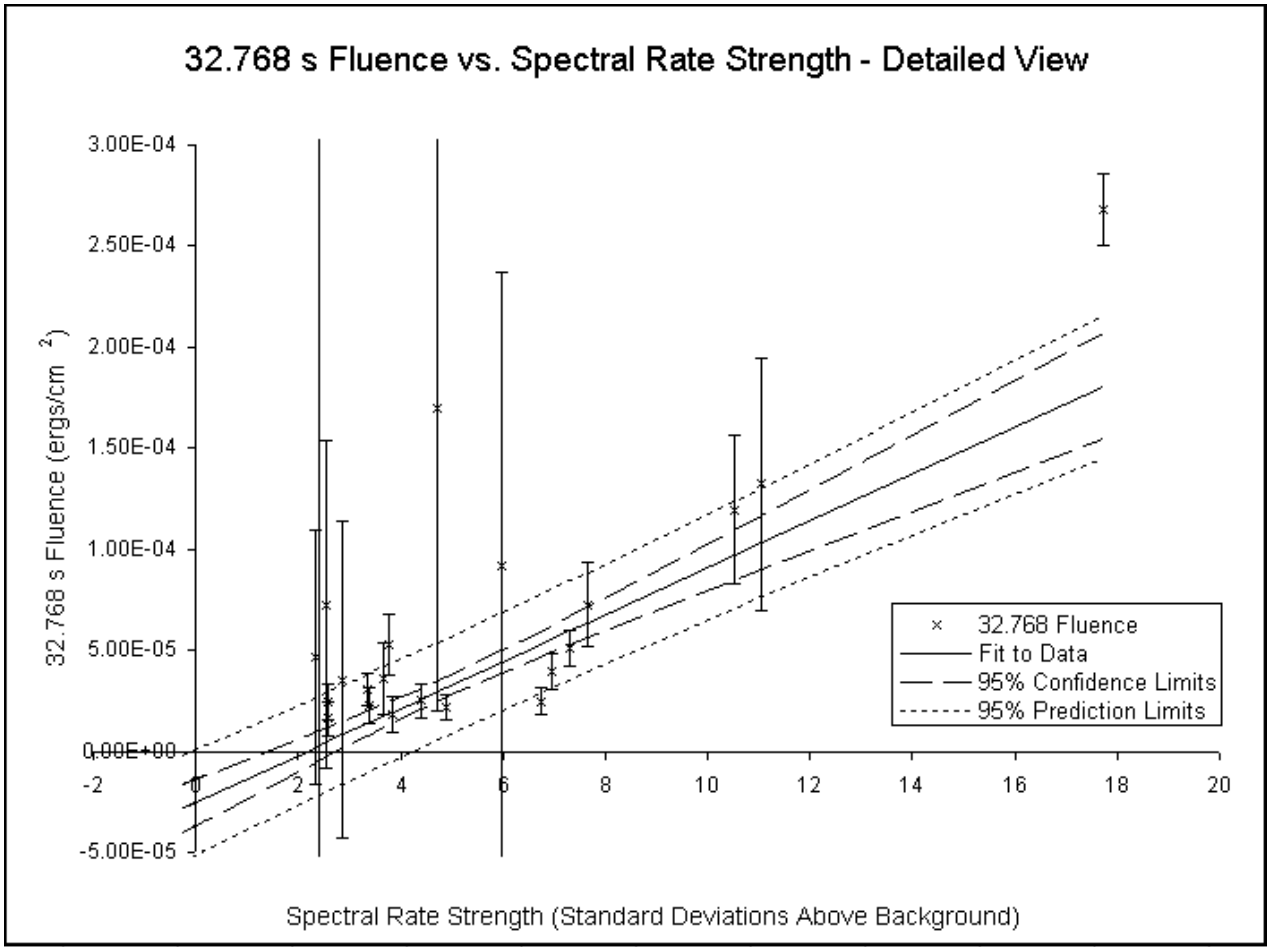

Figure B.4: Fluence vs. spectral rates, entire energy range detail. Intercept not forced.

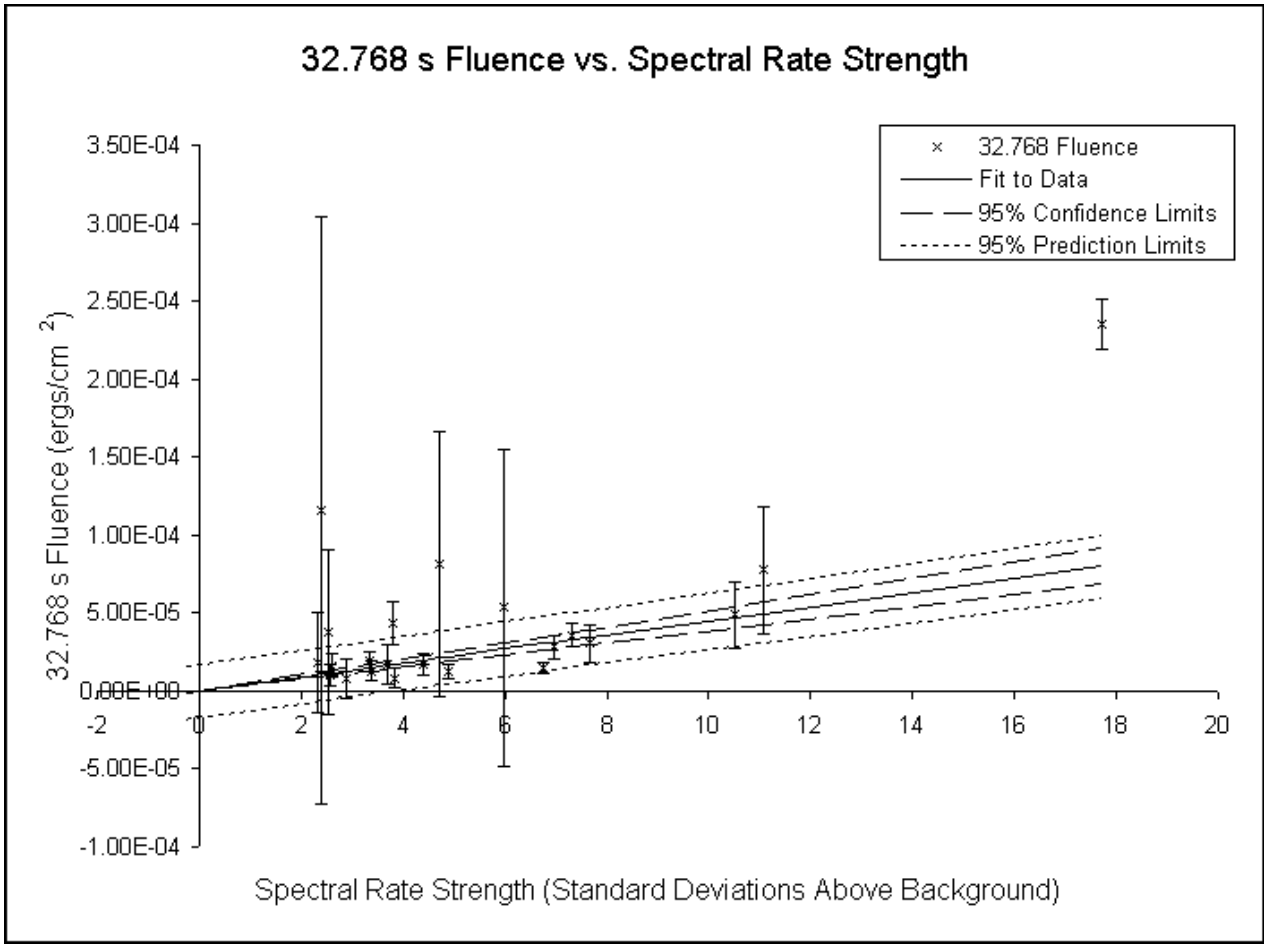

Figure B.5: Fluence vs. spectral rates, restricted energy range, forced zero intercept

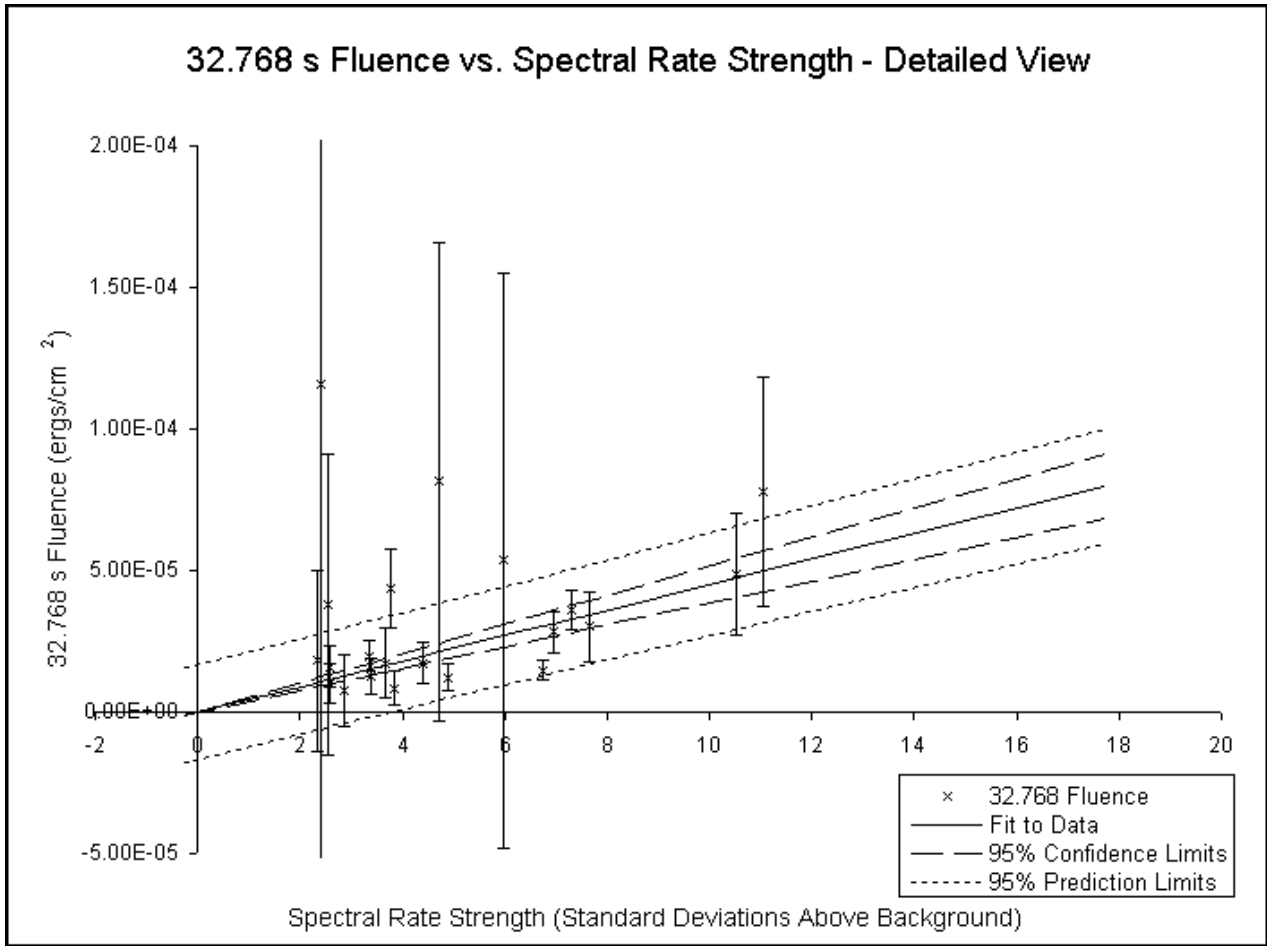

Figure B.6: Fluence vs. spectral rates, restricted energy range, forced zero intercept detail

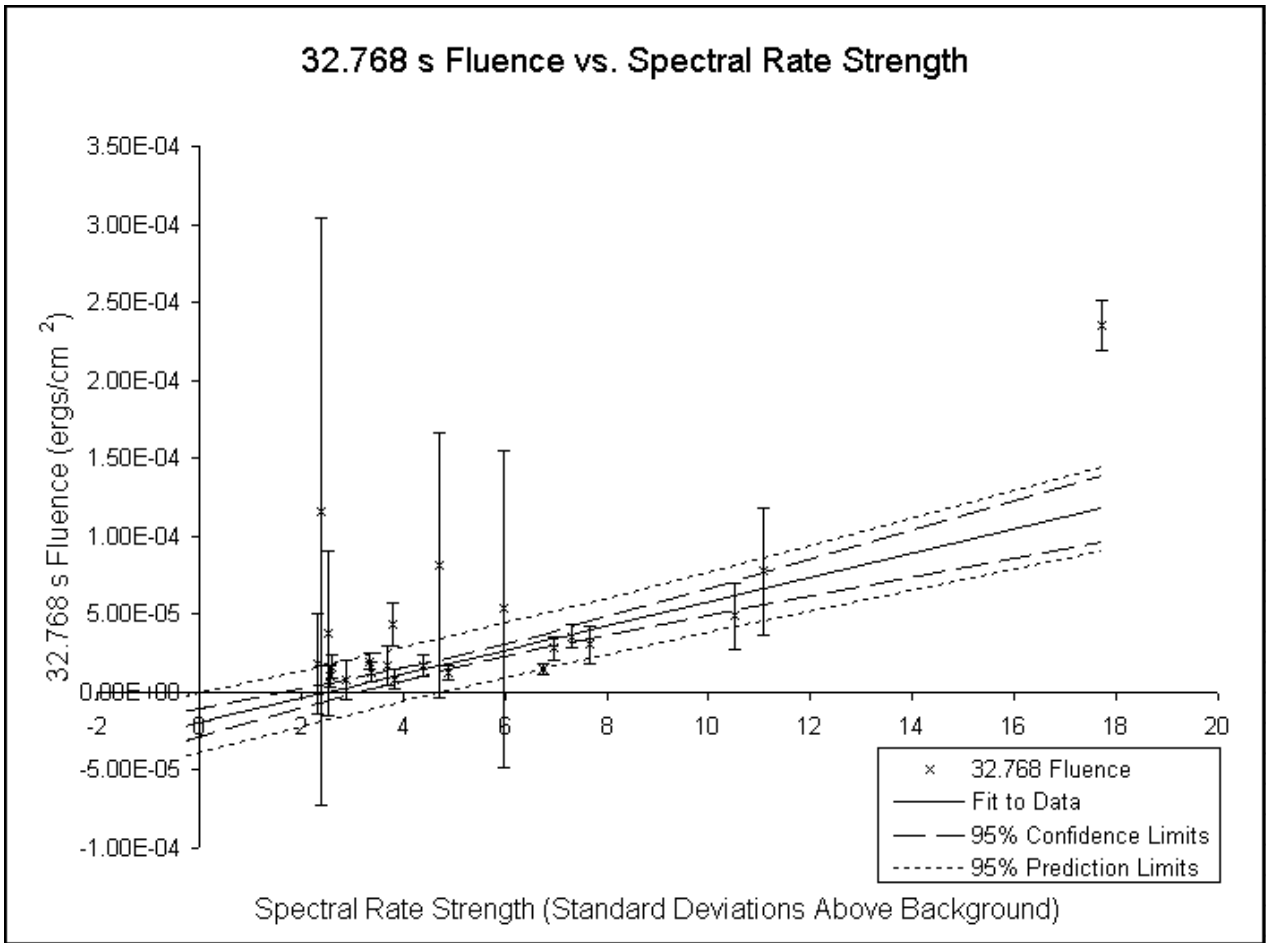

Figure B.7: Fluence vs. spectral rates, restricted energy range. Intercept not forced.

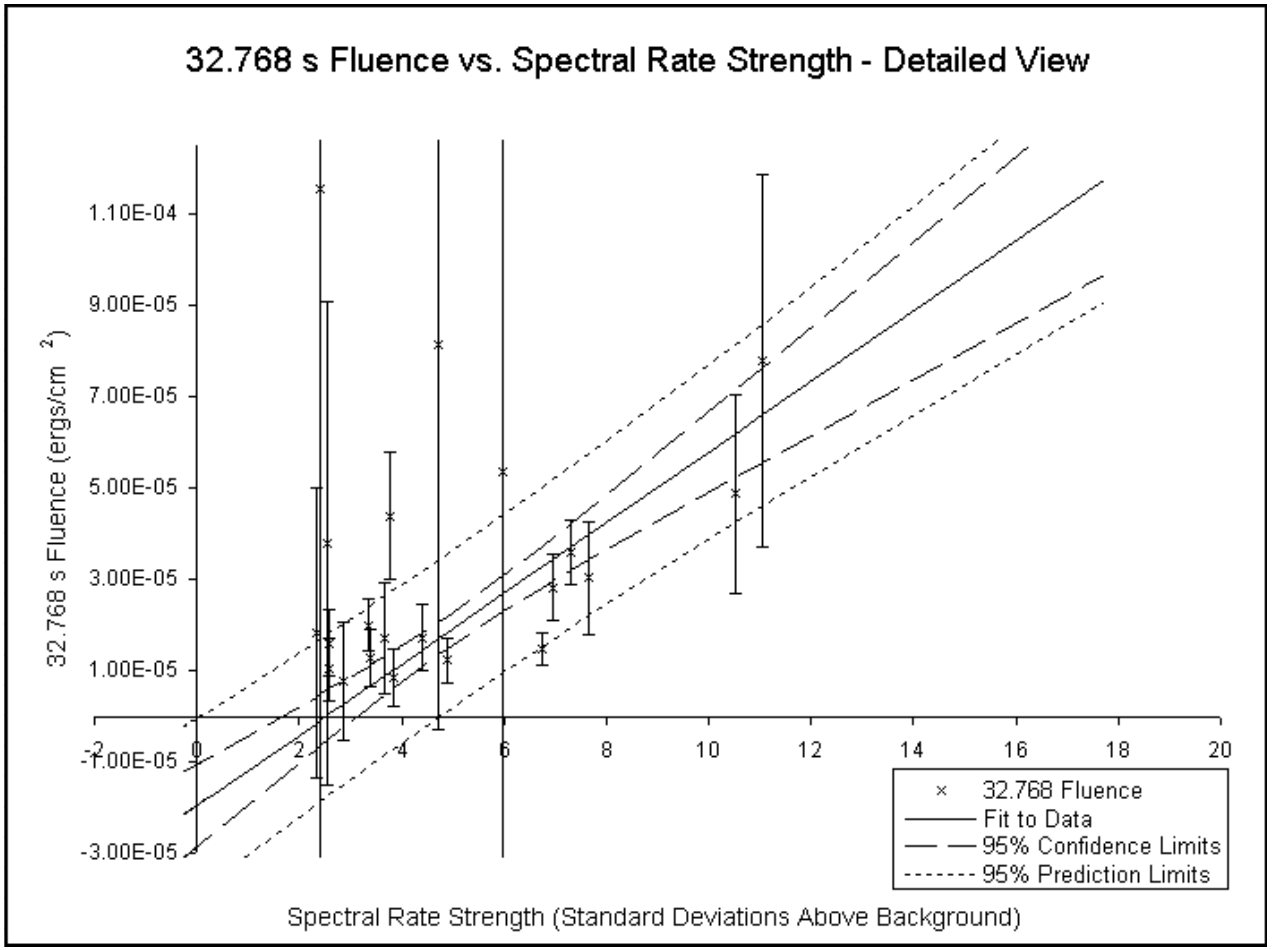

Figure B.8: Fluence vs. spectral rates, restricted energy range detail. Intercept not forced.

Table B.1: Fluence vs. spectral rates for burst-time normal mode spectra. The integration is over the entire TASC energy range for each spectrum.

Burst	BATSE Trigger	Spectrum Midtime (UT s)	Spectral Rate Strength (σ)	Normalization Const. from Fit ($\frac{photons}{cm^2\ s\ MeV}$)	Spectral Index from Fit	Lower Energy Limit (MeV)	Upper Energy Limit (MeV)	Fluence $\frac{ergs}{cm^2}$	δ Fluence $\frac{ergs}{cm^2}$
910601	249	69766.742	6.74	0.48	3.587	0.76	212.16	2.47E-05	6.4E-06
940217	2831	82970.242	3.35	0.56	3.284	0.80	222.62	3.05E-05	8.2E-06
940217	2831	83068.492	7.32	0.66	2.82	0.80	222.62	5.06E-05	8.9E-06
990123	7343	35232.43	6.96	0.67	3	0.89	248.21	3.96E-05	8.6E-06
990123	7343	35265.242	4.39	0.38	2.866	0.89	248.21	2.52E-05	8.3E-06
990104	7301	57896.68	3.79	0.64	2.66	0.92	255.97	5.26E-05	1.5E-05
990104	7301	57929.43	17.72	2.68	2.52	0.92	255.97	0.000268	1.8E-05
910814	678	69299.805	3.38	0.25	2.715	0.74	205.69	2.26E-05	9.2E-06
910814	678	69266.992	7.66	0.45	2.278	0.74	205.69	7.24E-05	2.1E-05
940301	2855	72660.617	4.90	0.23	2.632	0.79	220.83	2.16E-05	6.2E-06
980124	6576	23686.865	2.58	0.22	2.79	0.85	236.03	1.62E-05	8.5E-06
960529	5477	43656.867	2.32	0.25	2.203	0.77	212.83	4.69E-05	6.3E-05
990728	7678	39830.242	3.84	0.13	2.358	0.83	231.02	1.79E-05	8.9E-06
990728	7678	39862.992	2.87	0.08	1.858	0.83	231.02	3.54E-05	7.9E-05
941017	3245	37204.617	3.68	0.27	2.37	0.83	231.02	3.59E-05	1.8E-05
991216	7906	58037.992	10.52	0.68	2.211	0.93	258.81	0.000120	3.7E-05

Continued on Next Page...

Table B.1 – Continued

Burst	BATSE Trigger	Spectrum Midtime (UT s)	Spectral Rate Strength (σ)	Normalization Const. from Fit ($\frac{photons}{cm^2\ s\ MeV}$)	Spectral Index from Fit	Lower Energy Limit (MeV)	Upper Energy Limit (MeV)	Fluence $\frac{ergs}{cm^2}$	δ Fluence $\frac{ergs}{cm^2}$
981203	7247	3601.054	2.54	0.39	2.181	0.91	253.41	7.26E-05	8.1E-05
981203	7247	3568.304	4.73	0.76	2.112	0.91	253.41	0.000169	0.000150
970411	6168	35568.305	2.41	1.14	1.779	0.80	223.74	0.000637	0.001550
950425	3523	911.991	11.05	0.56	2.079	0.94	244.66	0.000132	6.3E-05
920902	1886	1726.045	2.60	0.36	2.9	0.86	239.26	2.46E-05	9.1E-06
980923	7113	72677	5.99	0.42	2.113	0.90	252.63	9.20E-05	0.000145

Table B.2: Fluence vs. spectral rates for burst-time normal mode spectra. The integration is over a restricted TASC energy range for each spectrum.

Burst	BATSE Trigger	Spectrum Midtime (UT s)	Spectral Rate Strength (σ)	Normalization Const. from Fit ($\frac{photons}{cm^2\ s\ MeV}$)	Spectral Index from Fit	Lower Energy Limit (MeV)	Upper Energy Limit (MeV)	Fluence $\frac{ergs}{cm^2}$	δ Fluence $\frac{ergs}{cm^2}$
910601	249	69766.742	6.74	0.48	3.59	1	5	1.47E-05	3.6E-06
940217	2831	82970.242	3.35	0.56	3.28	1	5	1.99E-05	5.6E-06
940217	2831	83068.492	7.32	0.66	2.82	1	10	3.60E-05	7.0E-06
990123	7343	35232.43	6.96	0.67	3.00	1	5	2.82E-05	7.3E-06
990123	7343	35265.242	4.39	0.38	2.87	1	5	1.72E-05	7.2E-06
990104	7301	57896.68	3.79	0.64	2.66	1	20	4.39E-05	1.4E-05
990104	7301	57929.43	17.72	2.68	2.52	1	50	0.000235	1.7E-05
910814	678	69299.805	3.38	0.25	2.73	1	5	1.265E-05	6.3E-06
910814	678	69266.992	7.66	0.45	2.28	1	5	3.03E-05	1.2E-05
940301	2855	72660.617	4.90	0.23	2.63	1	5	1.22E-05	4.8E-06
980124	6576	23686.865	2.58	0.22	2.79	1	5	1.03E-05	6.9E-06
960529	5477	43656.867	2.32	0.25	2.20	1	5	1.81E-05	3.2E-05
990728	7678	39830.242	3.84	0.13	2.36	1	5	8.47E-06	6.1E-06
990728	7678	39862.992	2.87	0.08	1.89	1	5	7.62E-06	1.3E-05
941017	3245	37204.617	3.68	0.27	2.37	1	5	1.71E-05	1.2E-05
991216	7906	58037.992	10.52	0.68	2.21	1	5	4.87E-05	2.2E-05

Continued on Next Page...

Table B.2 – Continued

Burst	BATSE Trigger	Spectrum Midtime (UT s)	Spectral Rate Strength (σ)	Normalization Const. from Fit ($\frac{photons}{cm^2\ s\ MeV}$)	Spectral Index from Fit	Lower Energy Limit (MeV)	Upper Energy Limit (MeV)	Fluence $\frac{ergs}{cm^2}$	δ Fluence $\frac{ergs}{cm^2}$
981203	7247	3601.054	2.54	0.38	2.18	1	10	3.80E-05	5.3E-05
981203	7247	3568.304	4.73	0.76	2.11	1	10	8.14E-05	8.4E-05
970411	6168	35568.305	2.41	1.14	1.78	1	5	0.000116	0.00019
950425	3523	911.991	11.05	0.56	2.08	1	20	7.79E-05	4.1E-05
920902	1886	1726.045	2.60	0.36	2.90	1	5	1.61E-05	7.4E-06
980923	7113	72677	5.99	0.42	2.11	1	20	5.37E-05	0.00010

Appendix C

Tower Alignment, and the Impact of Tower or Layer Failures

An understanding of trigger rates and reduction methods could rendered useless if there are unknown problems with the LAT, or if the collaboration does not know how to respond to different types of instrument failures. For this reason, contributions were made to the understanding of how GlastSim could be used to study tracker tower alignment and what the impact of hardware failures would be.

C.1 Aligning Towers on the Ground

One issue that is faced by the LAT collaboration is how to determine how well the 16 towers are aligned relative to each other and the spacecraft once they are assembled into a unit. If the towers are misaligned by any amount, the misalignment needs to be well understood in order to correct for it when doing track reconstruction on the ground. Track reconstruction done onboard (in flight) will not be able to correct for this complication, but onboard reconstruction is not so precise that this will be a problem.

It was agreed that the best way to study tower alignment was to pass a known source through the LAT from different angles, and study the resulting tracks. One possibility was to model muons at sea level, and then turn the LAT on its side to maximize the number of muons that would create tracks that crossed the boundaries between towers. Any misalignment would be along these boundaries, so the problem could be characterized this way.

The collaboration developed a "surface muon" source based on ground muon data (from the CAPRICE experiment (Kremer et al., 1999)) and integrated it into GlastSim. For comparison, the following plots of the surface muon source were generated; when units are adjusted, the plots agree with experimental data. Figure C.1 is a plot of the surface muon flux at sea level, and Figure C.2 is the corresponding flux when generated by the Monte Carlo (the x-axis is log(Energy) in MeV, the y-axis is just the number in each energy bin). Figures C.3 and C.4 are the flux as a function of the cosine of the angle from anti-zenith. When the cosine of the angle is minus one, that corresponds to 180^o, which is "up" in the LAT coordinate system.

Once the source was defined, it was possible to tell GlastSim to orient the LAT such that it was on its side (rotated 90 degrees), and generate a large sample of surface muon events. With the muons generated at a rate of 735 ± 2 Hz, the trigger rate was 175 ± 1 Hz for all three Level 1 Triggers, and 171 ± 1 Hz for the tracker trigger alone, such that about 23% of the muons caused the tracker to trigger. The goal was not to measure the tracker trigger rate, however. The goal was to measure the rate at which muons crossed from one tower to another. This information was

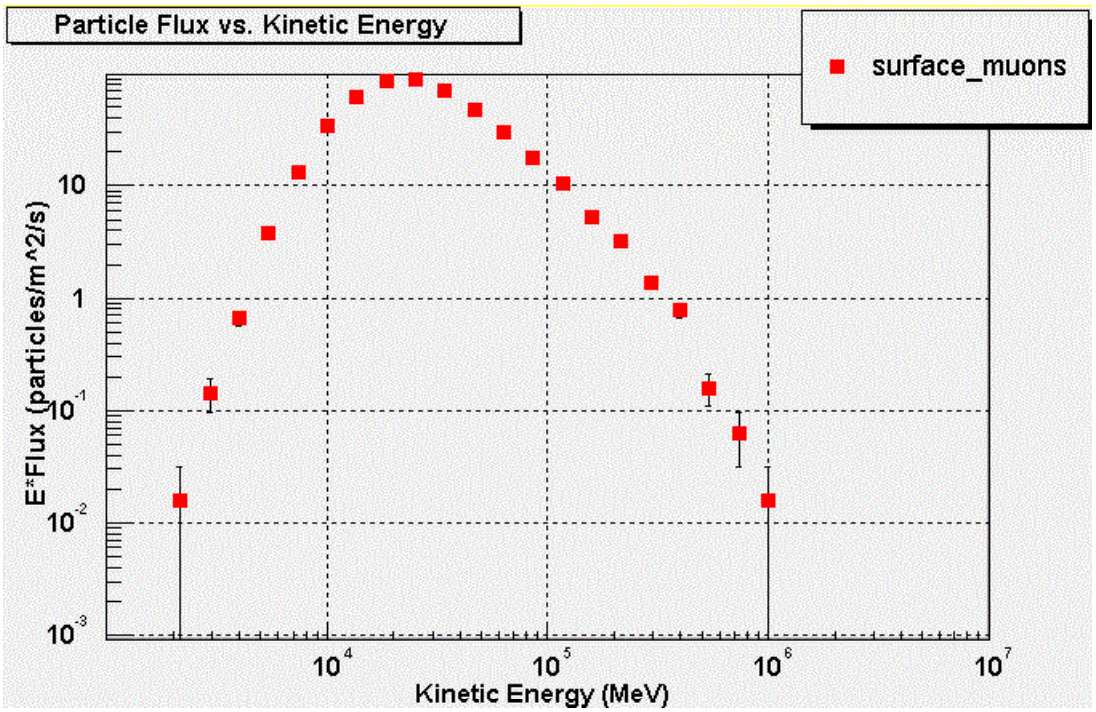

Figure C.1: The energy distribution of the surface muon source in GlastSim. This source was used to simulate and design ground-based LAT tower alignment studies.

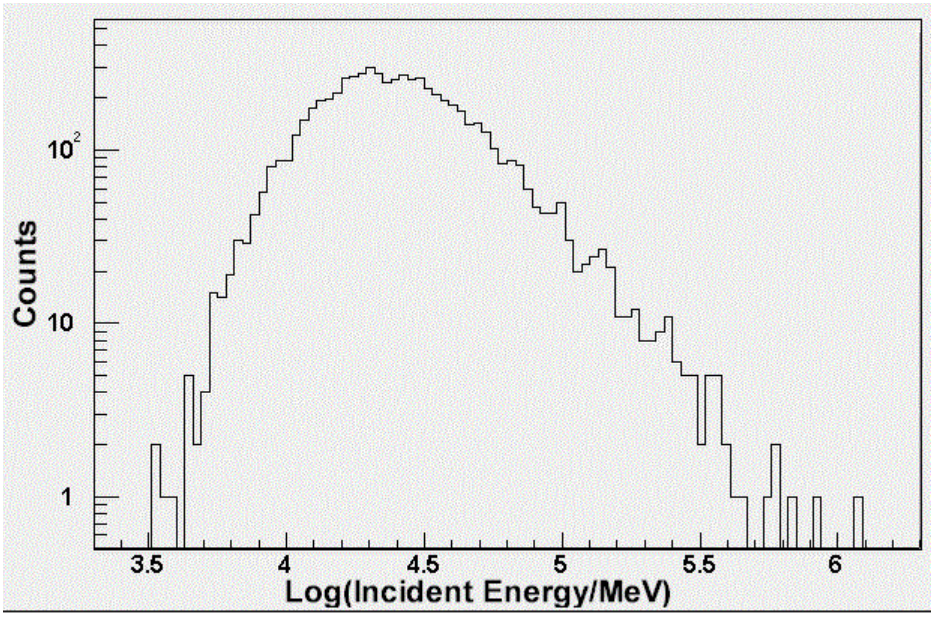

Figure C.2: A histogram of the surface muon energy distribution as generated by the GlastSim Monte Carlo.

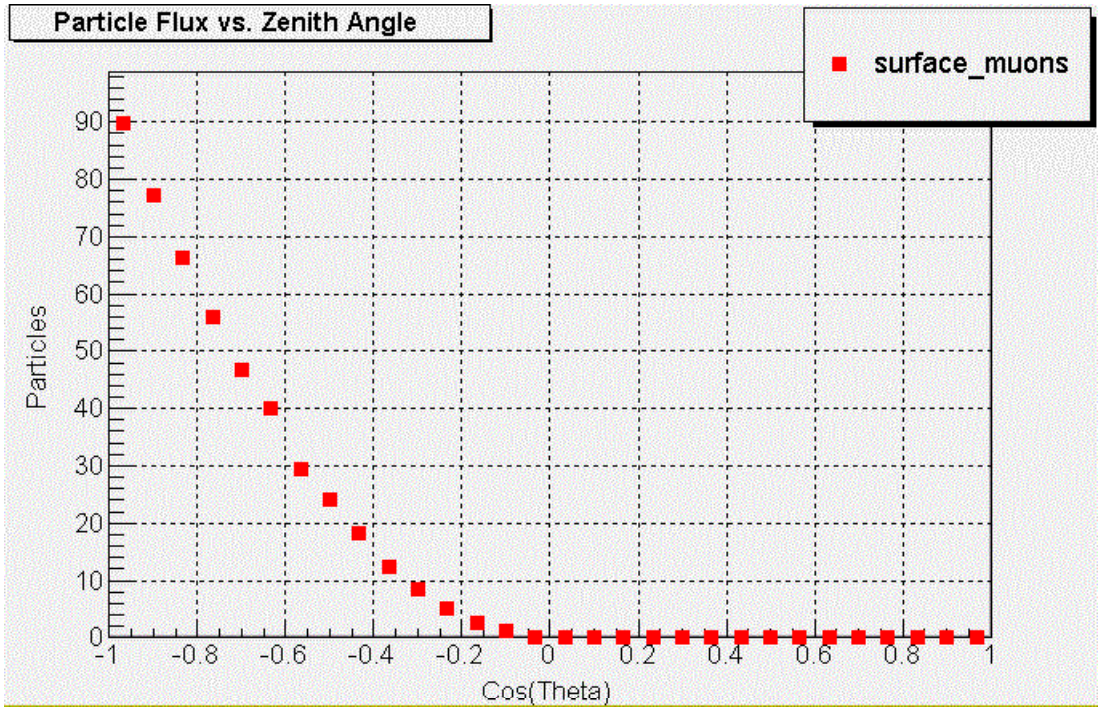

Figure C.3: The angular distribution of the surface muon source in GlastSim. Cos(θ) = -1 corresponds to "up" or "zenith" in LAT coordinates.

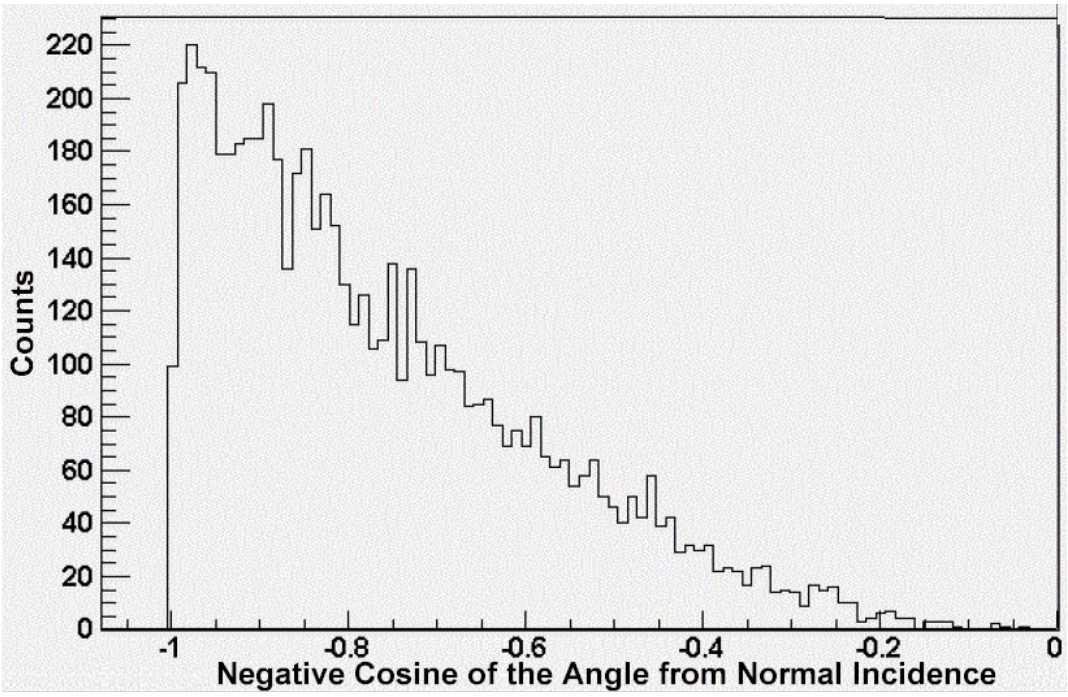

Figure C.4: A histogram of the surface muon angular distribution as generated by the GlastSim Monte Carlo.

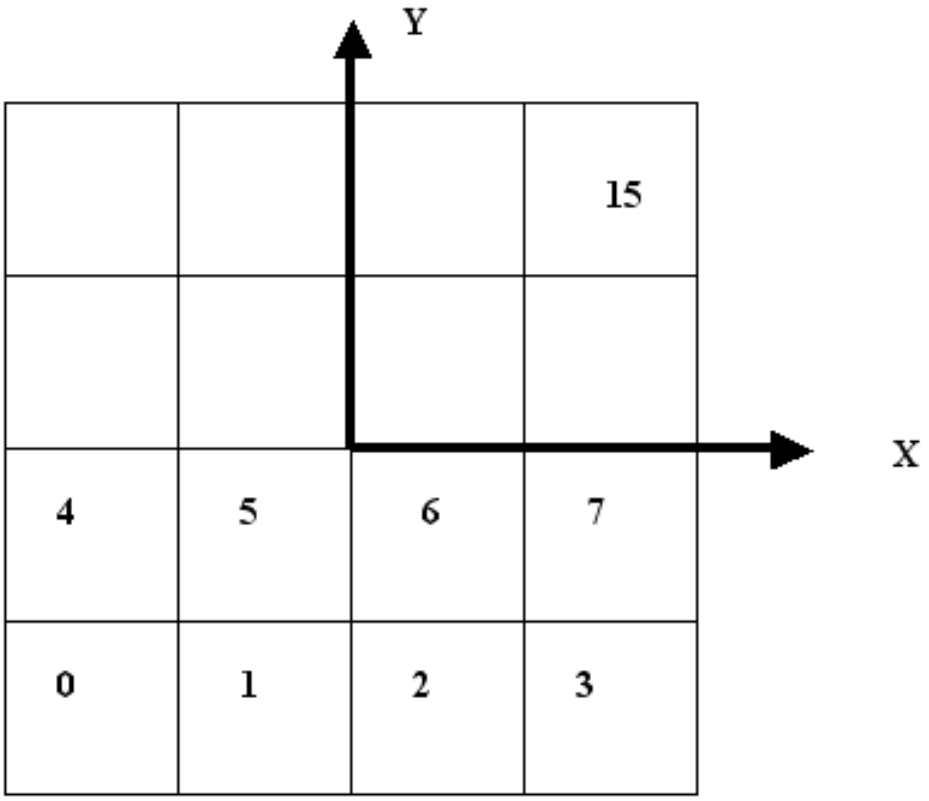

Figure C.5: A top-down view of the LAT tower numbering convention, taken from "LAT Coordinate System" (Ritz, 2000). The Z-axis points out of the page. When the LAT was tilted on its side for the tower crossing studies, the Y+ side was on the ground.

required in order for a Tower Alignment team to determine how long it would be necessary to take data.

In order to determine the "tower crossing rate," as it is called here, it was necessary to check every possible combination of pairs of towers between which a muon could pass. For example, if it passed from tower 0 to tower 1, the towers can be designated as "Pair 0." The standard analysis environment used for the LAT allows the user to program macros, and a custom macro was used to examine the rate at which each pair was active (the rate at which a muon triggered both towers in that pair). Table C.1 lists the frequency of tower crossings for each pair, and Figure C.5 is a diagram of the tower numbering convention. One result that is useful as verification that the simulation is working correctly is that the vertically oriented pairs are more likely to occur than horizontal pairs, which is what one would expect for a source that is most intense at zenith. This difference in pair frequency is easily observed in Figure C.6, a plot of the frequency in Hz for each of the 24 possible pairs. Figure C.7 shows the LAT tilted to its side.

The overall frequency of tower crossings is greater than 80 Hz, but it is less than 15 Hz for horizontally oriented pairs, which suggests that the LAT may need to be rotated by 90^o in order to put those horizontal pairs into a vertical orientation in order to get high statistics. However, it is not necessary to put the LAT onto each of its 4 sides, because the frequency of crossings as a function of how high the pair was located in the stack of pairs was about the same regardless of height: a combined 22.6 ± 0.4 Hz for the top pairs, 21.6 ± 0.4 Hz for the middle, and 22.1 ± 0.4

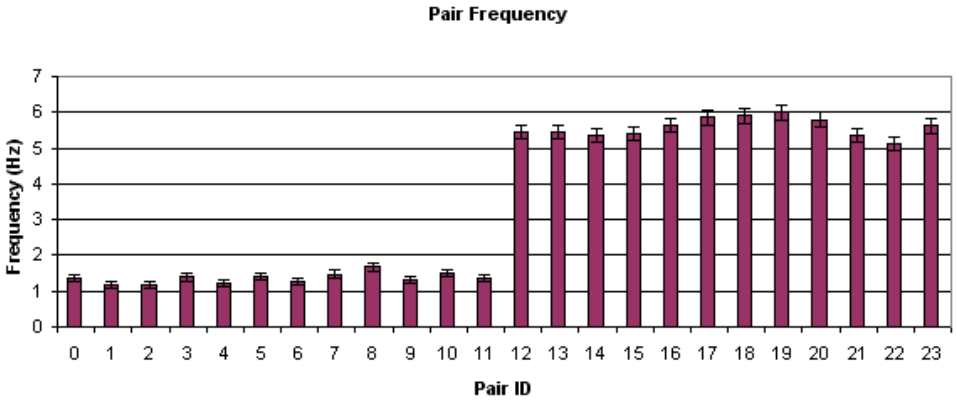

Figure C.6: Rate (Hz) of muon tower crossings. GlastSim was used to simulate the LAT tilted on its side for a ground-based study of the surface muon flux. The vertical axis is the rate at which simulated muons crossed from one LAT tower to the next. Vertically oriented tower pairs show a greater frequency of tower crossings than horizontally oriented pairs. Errors are statistical.

Horizontal Pairs			Vertical Pairs		
Pair ID	Pair	Frequency (Hz)	Pair ID	Pair	Frequency (Hz)
0	0-1	1.37 ± 0.10	12	0-4	5.44 ± 0.20
1	1-2	1.18 ± 0.09	13	4-8	5.44 ± 0.20
2	2-3	1.15 ± 0.09	14	8-12	5.35 ± 0.20
3	4-5	1.39 ± 0.10	15	1-5	5.41 ± 0.20
4	5-6	1.24 ± 0.10	16	5-9	$4.99 \pm 0.0.19$
5	6-7	1.41 ± 0.10	17	9-13	5.87 ± 0.21
6	8-9	1.28 ± 0.10	18	2-6	5.90 ± 0.21
7	9-10	1.47 ± 0.10	19	6-10	6.01 ± 0.21
8	10-11	1.67 ± 0.11	20	10-14	5.80 ± 0.21
9	12-13	1.33 ± 0.10	21	3-7	5.35 ± 0.20
10	13-14	1.49 ± 0.10	22	7-11	5.12 ± 0.19
11	14-15	1.35 ± 0.10	23	11-15	5.62 ± 0.20

Table C.1: Frequencies of muon tower crossings. GlastSim was used to simulate the LAT tilted on its side for a ground-based study of the surface muon flux. The first column is a pair ID number used to identify the tower pair that the surface muon passed between. Towers are in a 4x4 array, numbered from 0 to 15, so there are 24 possible pairs. The frequency is how many times a second a muon passed from one tower to the next. Errors are statistical.

Hz for the bottom. This means it is sufficient to take data with the LAT rotated such that one of the side faces is parallel to the ground, and then turn it about its Z-axis such that one other side face is parallel to the ground. The amount of data to take is a decision made by the Tower Alignment Team, but this study gives them a starting point.

C.2 Impacts of Potential Failures of Tracker Layers or Towers

Because hardware failures are known to happen in space, it is important to study what the impact would be on mission objectives. One possible failure that could impact the triggering is the loss of a plane of silicon in one of the towers. To study this effect, the simulation was used to turn off layers at the bottom and the middle

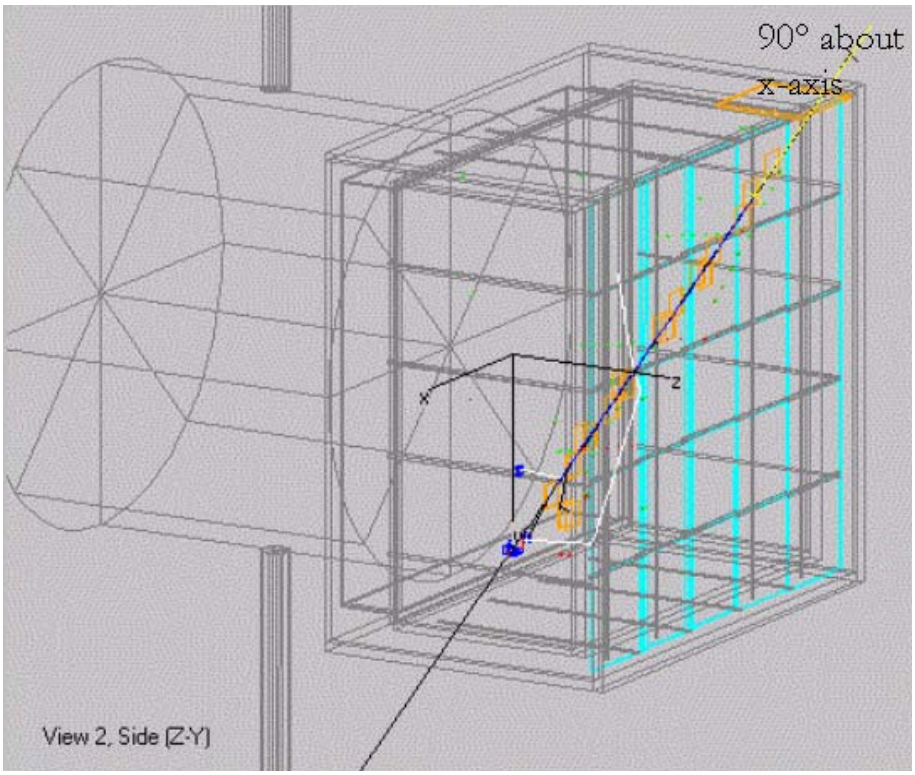

Figure C.7: The LAT rotated to be on its side with a "surface muon" passing through. The level of visible detail was reduced for easier visualization.

of a core tower of the LAT, and then the tracker trigger rate was calculated for the entire LAT. The bottom layers of tracker have the thickest converter, so the trigger rate was expected to decrease the most of those layers were removed. In addition to removing one layer, several X-oriented planes of silicon in the bottom and middle of a tower were turned off to see what kind of effect this would have. Because 3 X-Y pairs in a row are required for a trigger, this only allowed a trigger to occur in the top 3 layers of the tower, effectively shutting down most of the tower.

Two input sources were used for this study, a beam of 1 GeV gammas coming in from LAT zenith, and another beam coming in at 40 degrees from LAT zenith, over all 360^o about the Z-axis. The peak sensitivity of the LAT is around 1 GeV for a typical astrophysical spectrum, so this is an appropriate energy choice. When the very bottom X plane of silicon was turned off, the next X plane up from the calorimeter was turned off, or a plane in the middle of the tracker was turned off, there was no statistically significant change in the trigger rate. This was true regardless of whether gammas were normally incident or incident from 40 degrees off axis.

Things start to change when one looks at what happens when most of a tower is damaged. If only the top three layers of a core tower are active, the trigger rate for the entire LAT drops by $5.7 \pm 1.9\%$ for zenith gammas. Considering that each tower is responsible for 6.25% of LAT triggers (the flux of gammas through each tower is the same except for random Monte Carlo fluctuations), a drop in trigger rate of 5.7% is equivalent to losing over 91% of that tower's effectiveness. In fact, if the

entire tower is lost, the simulation gives a rate reduction of $6.1 \pm 1.9\%$, which is only $0.15(\pm 1.9)\%$, or 8 triggered events different than what is expected for a situation with no statistical fluctuations. For this run that generated 5547 ± 75 triggers, the statistical fluctuation is 9 times greater than the difference observed. This is only a validation that the simulation works as expected. The important result is that the overall trigger rate would drop by about $6 \pm 2\%$. However, the decrease is not as great if the gammas come in at an angle. For the 40^o source, the reduction in rate after losing a tower was $3.9 \pm 2.0\%$. The LAT mission can expect to a drop in effective area of about $6 \pm 2\%$ or less at 1 GeV. If the effective area is above 9000 cm^2, as was the stated projection in Chapter 2, a drop of 6% still keeps it above 8000 cm^2, which is the performance requirement. A loss of one tower should not jeopardize the mission.

Appendix D

Tabulation of Chapter 6 Track Reconstruction and Burst Detection Results

In this appendix, the performance of the track reconstruction methods and the burst detection study in Chapter 6 are tabulated. Tables D.1 through D.12 contain data on the 68% and 95% containment radii for the track reconstruction point spread functions. Tables D.13 and D.14 have the results of the burst detection study.

100 MeV Gamma Rays			
Ch 5 Onboard Filter All Triggers Not Vetoed			
Corresponding background rate: 367 ± 7 Hz			
Range $cos(\theta)$	Filt MII	Hough	Ground
68% containment radius (degrees)			
1.0 - 0.9	7.47 ± 0.09	9.09 ± 0.09	5.85 ± 0.09
0.9 - 0.8	6.93 ± 0.09	10.89 ± 0.27	6.39 ± 0.09
0.8 - 0.7	8.01 ± 0.27	11.25 ± 0.18	6.93 ± 0.09
0.7 - 0.6	8.37 ± 0.18	13.05 ± 0.18	8.01 ± 0.18
0.6 - 0.5	11.97 ± 0.09	15.03 ± 0.27	8.91 ± 0.18
0.5 - 0.4	10.71 ± 0.18	21.33 ± 0.18	9.81 ± 0.18
0.4 - 0.3	23.49 ± 0.18	43.29 ± 0.36	14.67 ± 0.36
0.3 - 0.2	33.39 ± 0.27	61.47 ± 0.36	16.47 ± 0.36
0.2 - 0.1	78.75 ± 0.18	77.31 ± 0.27	49.05 ± 0.27
0.1 - 0.0	104.67 ± 0.18	103.41 ± 0.27	114.03 ± 0.27
95% containment radius (degrees)			
1.0 - 0.9	23.31 ± 0.09	27.27 ± 0.09	24.93 ± 0.09
0.9 - 0.8	26.01 ± 0.09	32.85 ± 0.27	23.31 ± 0.09
0.8 - 0.7	26.55 ± 0.27	38.43 ± 0.18	26.73 ± 0.09
0.7 - 0.6	28.53 ± 0.18	44.73 ± 0.18	34.11 ± 0.18
0.6 - 0.5	45.81 ± 0.09	57.69 ± 0.27	52.29 ± 0.18
0.5 - 0.4	69.57 ± 0.18	78.03 ± 0.18	51.57 ± 0.18
0.4 - 0.3	113.67 ± 0.18	105.39 ± 0.36	115.47 ± 0.36
0.3 - 0.2	96.93 ± 0.27	124.65 ± 0.36	130.41 ± 0.36
0.2 - 0.1	113.67 ± 0.18	128.25 ± 0.27	147.15 ± 0.27
0.1 - 0.0	140.85 ± 0.18	146.43 ± 0.27	152.19 ± 0.27
	Triggered events: 112225		
Reconstructed:	71707	86925	87717

Table D.1: The 68% and 95% containment point spread function for 100 MeV gamma rays incident on the LAT. These photons triggered the LAT and passed the Onboard Filter cuts. Their directions were reconstructed with the MII and Hough track reconstruction methods, and the ground based track reconstruction results are provided for comparison. At this energy, MII outperforms the Hough transform. The uncertainties reflect the precision with which the values could be determined given the number of events generated and the binning of the PSF histograms.

100 MeV Gamma Rays			
Filter 9 All Triggers Not Vetoed & Passed Layer Cut			
Corresponding background rate: 76 ± 5 Hz			
Range $cos(\theta)$	Filt MII	Hough	Ground
68% containment radius (degrees)			
1.0 - 0.9	6.57 ± 0.09	6.93 ± 0.09	4.77 ± 0.18
0.9 - 0.8	7.11 ± 0.09	11.43 ± 0.18	6.03 ± 0.09
0.8 - 0.7	8.73 ± 0.27	9.45 ± 0.18	6.75 ± 0.09
0.7 - 0.6	8.55 ± 0.09	13.59 ± 0.09	7.29 ± 0.18
0.6 - 0.5	11.97 ± 0.18	10.89 ± 0.09	8.73 ± 0.09
0.5 - 0.4	9.09 ± 0.09	17.73 ± 0.09	5.31 ± 0.09
0.4 - 0.3	19.17 ± 0.09	32.85 ± 0.09	9.99 ± 0.09
0.3 - 0.2	20.97 ± 0.18	33.21 ± 0.18	11.61 ± 0.18
0.2 - 0.1	31.77 ± 0.09	76.23 ± 0.09	25.83 ± 0.09
0.1 - 0.0	99.81 ± 0.09	79.47 ± 0.09	114.03 ± 0.09
95% containment radius (degrees)			
1.0 - 0.9	22.59 ± 0.09	26.91 ± 0.09	20.43 ± 0.18
0.9 - 0.8	33.57 ± 0.09	30.33 ± 0.18	20.07 ± 0.09
0.8 - 0.7	33.93 ± 0.27	28.71 ± 0.18	26.91 ± 0.09
0.7 - 0.6	24.93 ± 0.09	48.51 ± 0.09	27.45 ± 0.18
0.6 - 0.5	38.07 ± 0.18	41.85 ± 0.09	42.57 ± 0.09
0.5 - 0.4	43.65 ± 0.09	85.05 ± 0.09	13.95 ± 0.09
0.4 - 0.3	113.67 ± 0.09	98.55 ± 0.09	129.87 ± 0.09
0.3 - 0.2	58.05 ± 0.18	97.65 ± 0.18	136.17 ± 0.18
0.2 - 0.1	96.03 ± 0.09	110.43 ± 0.09	148.23 ± 0.09
0.1 - 0.0	117.81 ± 0.09	156.69 ± 0.09	152.37 ± 0.09
	Triggered events: 75720		
Reconstructed:	30440	31820	32480

Table D.2: The 68% and 95% containment point spread function for 100 MeV gamma rays incident on the LAT. These photons triggered the LAT and passed the Filter 9 and projection-layer albedo cuts. Their directions were reconstructed with the MII and Hough track reconstruction methods, and the ground based track reconstruction results are provided for comparison. At this energy, MII outperforms the Hough transform. The uncertainties reflect the precision with which the values could be determined given the number of events generated and the binning of the PSF histograms.

100 MeV Gamma Rays			
Filter 9 All Triggers Not Vetoed & Passed Layer and Direction Cuts			
Corresponding background rate: 33 ± 4 Hz			
Range $cos(\theta)$	Filt MII	Hough	Ground
68% containment radius (degrees)			
1.0 - 0.9	6.57 ± 0.09	7.11 ± 0.09	4.77 ± 0.18
0.9 - 0.8	7.29 ± 0.09	10.71 ± 0.09	6.21 ± 0.09
0.8 - 0.7	8.73 ± 0.27	9.45 ± 0.18	6.93 ± 0.18
0.7 - 0.6	8.55 ± 0.09	15.21 ± 0.09	7.29 ± 0.18
0.6 - 0.5	11.07 ± 0.09	11.07 ± 0.18	8.37 ± 0.18
0.5 - 0.4	9.27 ± 0.18	17.73 ± 0.09	5.31 ± 0.09
0.4 - 0.3	19.17 ± 0.09	32.85 ± 0.09	8.55 ± 0.09
0.3 - 0.2	30.51 ± 0.18	40.59 ± 0.18	13.05 ± 0.18
0.2 - 0.1	33.57 ± 0.09	77.31 ± 0.09	25.83 ± 0.09
0.1 - 0.0	99.81 ± 0.09	79.47 ± 0.09	114.03 ± 0.09
95% containment radius (degrees)			
1.0 - 0.9	22.59 ± 0.09	26.91 ± 0.09	20.43 ± 0.18
0.9 - 0.8	33.57 ± 0.09	27.81 ± 0.09	17.91 ± 0.09
0.8 - 0.7	27.45 ± 0.27	28.71 ± 0.18	26.91 ± 0.18
0.7 - 0.6	28.53 ± 0.09	48.51 ± 0.09	27.45 ± 0.18
0.6 - 0.5	31.77 ± 0.09	36.27 ± 0.18	42.57 ± 0.18
0.5 - 0.4	43.65 ± 0.18	85.05 ± 0.09	13.95 ± 0.09
0.4 - 0.3	113.67 ± 0.09	98.55 ± 0.09	129.87 ± 0.09
0.3 - 0.2	135.99 ± 0.18	97.65 ± 0.18	136.17 ± 0.18
0.2 - 0.1	96.03 ± 0.09	110.43 ± 0.09	148.23 ± 0.09
0.1 - 0.0	117.81 ± 0.09	156.69 ± 0.09	152.37 ± 0.09
	Triggered events: 75720		
Reconstructed:	28100	29480	29660

Table D.3: The 68% and 95% containment point spread function for 100 MeV gamma rays incident on the LAT. These photons triggered the LAT and passed the Filter 9 and the projection-layer and directional albedo cuts. Their directions were reconstructed with the MII and Hough track reconstruction methods, and the ground based track reconstruction results are provided for comparison. At this energy, MII outperforms the Hough transform. The uncertainties reflect the precision with which the values could be determined given the number of events generated and the binning of the PSF histograms.

1 GeV Gamma Rays			
Ch 5 Filter All Triggers Not Vetoed			
Corresponding background rate: 367 ± 7 Hz			
Range $cos(\theta)$	Filt MII	Hough	Ground
68% containment radius (degrees)			
1.0 - 0.9	1.89 ± 0.09	2.25 ± 0.09	0.81 ± 0.09
0.9 - 0.8	1.89 ± 0.09	2.07 ± 0.09	0.81 ± 0.09
0.8 - 0.7	2.25 ± 0.09	2.43 ± 0.09	0.99 ± 0.09
0.7 - 0.6	2.97 ± 0.09	2.61 ± 0.09	1.35 ± 0.09
0.6 - 0.5	3.69 ± 0.09	2.79 ± 0.09	1.71 ± 0.09
0.5 - 0.4	4.41 ± 0.18	3.51 ± 0.09	1.89 ± 0.09
0.4 - 0.3	8.55 ± 0.18	5.85 ± 0.18	2.97 ± 0.09
0.3 - 0.2	26.37 ± 0.36	17.37 ± 0.18	3.51 ± 0.09
0.2 - 0.1	94.77 ± 0.27	56.25 ± 0.27	38.97 ± 0.27
0.1 - 0.0	126.09 ± 0.18	91.71 ± 0.09	126.99 ± 0.18
95% containment radius (degrees)			
1.0 - 0.9	13.77 ± 0.09	14.85 ± 0.09	3.15 ± 0.09
0.9 - 0.8	18.81 ± 0.09	17.37 ± 0.09	3.51 ± 0.09
0.8 - 0.7	11.61 ± 0.09	12.51 ± 0.09	5.49 ± 0.09
0.7 - 0.6	11.43 ± 0.09	11.07 ± 0.09	10.71 ± 0.09
0.6 - 0.5	19.53 ± 0.09	9.09 ± 0.09	7.29 ± 0.09
0.5 - 0.4	51.39 ± 0.18	12.69 ± 0.09	11.61 ± 0.09
0.4 - 0.3	81.45 ± 0.18	52.83 ± 0.18	17.91 ± 0.09
0.3 - 0.2	104.31 ± 0.36	91.17 ± 0.18	43.47 ± 0.09
0.2 - 0.1	138.87 ± 0.27	134.01 ± 0.27	140.85 ± 0.27
0.1 - 0.0	145.89 ± 0.18	153.09 ± 0.09	152.01 ± 0.18
	Triggered events: 261709		
Reconstructed:	105903	109627	108990

Table D.4: The 68% and 95% containment point spread function for 1 GeV gamma rays incident on the LAT. These photons triggered the LAT and passed the Onboard Filter cuts. Their directions were reconstructed with the MII and Hough track reconstruction methods, and the ground based track reconstruction results are provided for comparison. The Hough transform begins to outperform MII when the angle from zenith reaches 45^o. The uncertainties reflect the precision with which the values could be determined given the number of events generated and the binning of the PSF histograms.

1 GeV Gamma Rays			
Filter 9 All Triggers Not Vetoed & Passed Layer Cut			
Corresponding background rate: 76 ± 5 Hz			
Range $cos(\theta)$	Filt MII	Hough	Ground
68% containment radius (degrees)			
1.0 - 0.9	1.71 ± 0.09	1.71 ± 0.09	0.81 ± 0.09
0.9 - 0.8	1.89 ± 0.09	1.89 ± 0.09	0.81 ± 0.09
0.8 - 0.7	2.61 ± 0.27	2.79 ± 0.09	0.99 ± 0.09
0.7 - 0.6	2.61 ± 0.09	1.89 ± 0.09	1.89 ± 0.09
0.6 - 0.5	3.51 ± 0.18	3.33 ± 0.09	1.53 ± 0.09
0.5 - 0.4	4.23 ± 0.09	2.61 ± 0.09	1.35 ± 0.09
0.4 - 0.3	13.05 ± 0.18	10.53 ± 0.18	2.61 ± 0.09
0.3 - 0.2	20.79 ± 0.18	9.63 ± 0.09	1.89 ± 0.18
0.2 - 0.1	97.11 ± 0.09	94.05 ± 0.09	19.71 ± 0.09
0.1 - 0.0	129.15 ± 0.09	118.71 ± 0.09	120.51 ± 0.09
95% containment radius (degrees)			
1.0 - 0.9	8.01 ± 0.09	9.27 ± 0.09	2.97 ± 0.09
0.9 - 0.8	15.21 ± 0.09	7.47 ± 0.09	3.15 ± 0.09
0.8 - 0.7	19.53 ± 0.27	17.01 ± 0.09	4.59 ± 0.09
0.7 - 0.6	11.25 ± 0.09	7.83 ± 0.09	12.33 ± 0.09
0.6 - 0.5	19.17 ± 0.18	16.83 ± 0.09	22.05 ± 0.09
0.5 - 0.4	71.55 ± 0.09	6.93 ± 0.09	6.75 ± 0.09
0.4 - 0.3	82.89 ± 0.18	52.83 ± 0.18	27.27 ± 0.09
0.3 - 0.2	102.69 ± 0.18	40.05 ± 0.09	9.27 ± 0.18
0.2 - 0.1	141.03 ± 0.09	137.43 ± 0.09	137.43 ± 0.09
0.1 - 0.0	141.57 ± 0.09	159.57 ± 0.09	160.65 ± 0.09
	Triggered events: 94824		
Reconstructed:	35712	37008	36648

Table D.5: The 68% and 95% containment point spread function for 1 GeV gamma rays incident on the LAT. These photons triggered the LAT and passed the Filter 9 and projection-layer albedo cuts. Their directions were reconstructed with the MII and Hough track reconstruction methods, and the ground based track reconstruction results are provided for comparison. The Hough transform begins to outperform MII when the angle from zenith reaches 45^o. The uncertainties reflect the precision with which the values could be determined given the number of events generated and the binning of the PSF histograms.

1 GeV Gamma Rays			
Filter 9 All Triggers Not Vetoed & Passed Layer and Direction Cuts			
Corresponding background rate: 33 ± 4 Hz			
Range $cos(\theta)$	Filt MII	Hough	Ground
68% containment radius (degrees)			
1.0 - 0.9	1.71 ± 0.09	1.71 ± 0.09	0.81 ± 0.09
0.9 - 0.8	1.89 ± 0.09	1.89 ± 0.09	0.81 ± 0.09
0.8 - 0.7	2.61 ± 0.27	2.79 ± 0.09	0.99 ± 0.09
0.7 - 0.6	2.61 ± 0.09	1.89 ± 0.09	1.89 ± 0.09
0.6 - 0.5	3.51 ± 0.18	3.33 ± 0.09	1.53 ± 0.09
0.5 - 0.4	4.23 ± 0.09	2.61 ± 0.09	1.35 ± 0.09
0.4 - 0.3	10.53 ± 0.18	10.53 ± 0.18	2.61 ± 0.09
0.3 - 0.2	20.79 ± 0.18	9.63 ± 0.09	1.89 ± 0.18
0.2 - 0.1	97.11 ± 0.09	94.05 ± 0.09	19.71 ± 0.09
0.1 - 0.0	129.15 ± 0.09	118.71 ± 0.09	120.51 ± 0.09
95% containment radius (degrees)			
1.0 - 0.9	8.01 ± 0.09	9.27 ± 0.09	2.97 ± 0.09
0.9 - 0.8	15.21 ± 0.09	7.47 ± 0.09	3.15 ± 0.09
0.8 - 0.7	19.53 ± 0.27	17.01 ± 0.09	4.59 ± 0.09
0.7 - 0.6	11.25 ± 0.09	7.83 ± 0.09	12.33 ± 0.09
0.6 - 0.5	19.17 ± 0.18	16.83 ± 0.09	22.05 ± 0.09
0.5 - 0.4	71.55 ± 0.09	6.93 ± 0.09	6.75 ± 0.09
0.4 - 0.3	82.89 ± 0.18	52.83 ± 0.18	27.27 ± 0.09
0.3 - 0.2	102.69 ± 0.18	40.05 ± 0.09	9.27 ± 0.18
0.2 - 0.1	141.03 ± 0.09	137.43 ± 0.09	137.43 ± 0.09
0.1 - 0.0	141.57 ± 0.09	159.57 ± 0.09	160.65 ± 0.09
	Triggered events: 94824		
Reconstructed:	35064	36432	36000

Table D.6: The 68% and 95% containment point spread function for 1 GeV gamma rays incident on the LAT. These photons triggered the LAT and passed the Filter 9 and the projection-layer and directional albedo cuts. Their directions were reconstructed with the MII and Hough track reconstruction methods, and the ground based track reconstruction results are provided for comparison. At this energy, MII outperforms the Hough transform. The uncertainties reflect the precision with which the values could be determined given the number of events generated and the binning of the PSF histograms.

10 GeV Gamma Rays			
Ch 5 Filter All Triggers Not Vetoed			
Corresponding background rate: 367 ± 7 Hz			
Range $cos(\theta)$	Filt MII	Hough	Ground
68% containment radius (degrees)			
1.0 - 0.9	0.45 ± 0.09	0.63 ± 0.09	0.09 ± 0.09
0.9 - 0.8	0.45 ± 0.09	0.63 ± 0.09	0.09 ± 0.09
0.8 - 0.7	1.17 ± 0.09	1.17 ± 0.09	0.27 ± 0.09
0.7 - 0.6	1.89 ± 0.09	1.35 ± 0.09	0.27 ± 0.09
0.6 - 0.5	2.25 ± 0.09	1.53 ± 0.09	0.45 ± 0.09
0.5 - 0.4	5.31 ± 0.18	2.97 ± 0.09	0.63 ± 0.09
0.4 - 0.3	30.15 ± 0.36	4.95 ± 0.09	2.43 ± 0.18
0.3 - 0.2	77.49 ± 0.18	60.03 ± 0.18	7.83 ± 0.18
0.2 - 0.1	103.95 ± 0.27	109.71 ± 0.27	120.33 ± 0.27
0.1 - 0.0	107.73 ± 0.09	123.93 ± 0.18	144.45 ± 0.18
95% containment radius (degrees)			
1.0 - 0.9	20.43 ± 0.09	15.03 ± 0.09	0.99 ± 0.09
0.9 - 0.8	14.67 ± 0.09	9.99 ± 0.09	1.17 ± 0.09
0.8 - 0.7	18.99 ± 0.09	14.13 ± 0.09	1.35 ± 0.09
0.7 - 0.6	38.25 ± 0.09	19.71 ± 0.09	4.05 ± 0.09
0.6 - 0.5	31.05 ± 0.09	11.61 ± 0.09	9.63 ± 0.09
0.5 - 0.4	54.81 ± 0.18	59.67 ± 0.09	31.23 ± 0.09
0.4 - 0.3	110.79 ± 0.36	118.53 ± 0.09	47.25 ± 0.18
0.3 - 0.2	124.29 ± 0.18	131.67 ± 0.18	142.11 ± 0.18
0.2 - 0.1	144.99 ± 0.27	148.77 ± 0.27	157.59 ± 0.27
0.1 - 0.0	155.61 ± 0.09	154.71 ± 0.18	158.85 ± 0.18
	Triggered events: 264474		
Reconstructed:	104354	107179	104578

Table D.7: The 68% and 95% containment point spread function for 10 GeV gamma rays incident on the LAT. These photons triggered the LAT and passed the Onboard Filter cuts. Their directions were reconstructed with the MII and Hough track reconstruction methods, and the ground based track reconstruction results are provided for comparison. The Hough transform begins to outperform MII when the angle from zenith reaches 45^o. The uncertainties reflect the precision with which the values could be determined given the number of events generated and the binning of the PSF histograms.

10 GeV Gamma Rays			
Filter 9 All Triggers Not Vetoed & Passed Layer Cut			
Corresponding background rate: 76 ± 5 Hz			
Range $cos(\theta)$	Filt MII	Hough	Ground
68% containment radius (degrees)			
1.0 - 0.9	0.45 ± 0.09	0.45 ± 0.09	0.09 ± 0.09
0.9 - 0.8	0.45 ± 0.09	0.63 ± 0.18	0.09 ± 0.09
0.8 - 0.7	0.63 ± 0.09	0.63 ± 0.09	0.09 ± 0.09
0.7 - 0.6	1.53 ± 0.27	1.53 ± 0.09	0.27 ± 0.09
0.6 - 0.5	3.51 ± 0.27	1.53 ± 0.09	0.27 ± 0.09
0.5 - 0.4	4.23 ± 0.18	3.87 ± 0.18	0.63 ± 0.09
0.4 - 0.3	21.33 ± 0.18	4.95 ± 0.18	1.53 ± 0.09
0.3 - 0.2	69.75 ± 0.18	59.49 ± 0.18	7.65 ± 0.18
0.2 - 0.1	111.69 ± 0.18	117.99 ± 0.18	110.43 ± 0.09
0.1 - 0.0	105.21 ± 0.09	119.79 ± 0.09	138.51 ± 0.09
95% containment radius (degrees)			
1.0 - 0.9	11.79 ± 0.09	8.37 ± 0.09	0.63 ± 0.09
0.9 - 0.8	17.91 ± 0.09	11.43 ± 0.18	0.63 ± 0.09
0.8 - 0.7	17.01 ± 0.09	13.77 ± 0.09	1.35 ± 0.09
0.7 - 0.6	20.97 ± 0.27	9.99 ± 0.09	1.35 ± 0.09
0.6 - 0.5	47.43 ± 0.27	44.19 ± 0.09	3.15 ± 0.09
0.5 - 0.4	81.27 ± 0.18	63.09 ± 0.18	5.67 ± 0.09
0.4 - 0.3	94.59 ± 0.18	103.41 ± 0.18	6.21 ± 0.09
0.3 - 0.2	114.93 ± 0.18	115.29 ± 0.18	115.11 ± 0.18
0.2 - 0.1	141.39 ± 0.18	144.81 ± 0.18	138.87 ± 0.09
0.1 - 0.0	137.79 ± 0.09	153.27 ± 0.09	140.49 ± 0.09
	Triggered events: 150720		
Reconstructed:	54060	56040	53280

Table D.8: The 68% and 95% containment point spread function for 10 GeV gamma rays incident on the LAT. These photons triggered the LAT and passed the Filter 9 and projection-layer albedo cuts. Their directions were reconstructed with the MII and Hough track reconstruction methods, and the ground based track reconstruction results are provided for comparison. The Hough transform begins to outperform MII when the angle from zenith reaches 53^o. The uncertainties reflect the precision with which the values could be determined given the number of events generated and the binning of the PSF histograms.

10 GeV Gamma Rays			
Filter 9 All Triggers Not Vetoed & Passed Layer and Direction Cuts			
Corresponding background rate: 33 ± 4 Hz			
Range $cos(\theta)$	Filt MII	Hough	Ground
68% containment radius (degrees)			
1.0 - 0.9	0.45 ± 0.09	0.45 ± 0.09	0.09 ± 0.09
0.9 - 0.8	0.45 ± 0.09	0.63 ± 0.18	0.09 ± 0.09
0.8 - 0.7	0.63 ± 0.09	0.63 ± 0.09	0.09 ± 0.09
0.7 - 0.6	1.53 ± 0.27	1.53 ± 0.09	0.27 ± 0.09
0.6 - 0.5	3.51 ± 0.27	1.53 ± 0.09	0.27 ± 0.09
0.5 - 0.4	4.23 ± 0.18	3.87 ± 0.18	0.63 ± 0.09
0.4 - 0.3	21.33 ± 0.18	4.95 ± 0.18	1.53 ± 0.09
0.3 - 0.2	69.75 ± 0.18	59.49 ± 0.18	7.65 ± 0.18
0.2 - 0.1	111.69 ± 0.18	117.99 ± 0.18	110.43 ± 0.09
0.1 - 0.0	105.21 ± 0.09	119.79 ± 0.09	138.51 ± 0.09
95% containment radius (degrees)			
1.0 - 0.9	11.79 ± 0.09	8.37 ± 0.09	0.63 ± 0.09
0.9 - 0.8	17.91 ± 0.09	11.43 ± 0.18	0.63 ± 0.09
0.8 - 0.7	17.01 ± 0.09	13.77 ± 0.09	1.35 ± 0.09
0.7 - 0.6	20.97 ± 0.27	9.99 ± 0.09	1.35 ± 0.09
0.6 - 0.5	47.43 ± 0.27	44.19 ± 0.09	3.15 ± 0.09
0.5 - 0.4	81.27 ± 0.18	63.09 ± 0.18	5.67 ± 0.09
0.4 - 0.3	94.59 ± 0.18	103.41 ± 0.18	6.21 ± 0.09
0.3 - 0.2	114.93 ± 0.18	115.29 ± 0.18	115.11 ± 0.18
0.2 - 0.1	141.39 ± 0.18	144.81 ± 0.18	138.87 ± 0.09
0.1 - 0.0	137.79 ± 0.09	153.27 ± 0.09	140.49 ± 0.09
	Triggered events: 150720		
Reconstructed:	54060	56040	53280

Table D.9: The 68% and 95% containment point spread function for 10 GeV gamma rays incident on the LAT. These photons triggered the LAT and passed the Filter 9 and the projection-layer and directional albedo cuts. Their directions were reconstructed with the MII and Hough track reconstruction methods, and the ground based track reconstruction results are provided for comparison. The Hough transform begins to outperform MII at 53^o from zenith. The uncertainties reflect the precision with which the values could be determined given the number of events generated and the binning of the PSF histograms.

100 GeV Gamma Rays			
Ch 5 Filter All Triggers Not Vetoed			
Corresponding background rate: 367 ± 7 Hz			
Range $cos(\theta)$	Filt MII	Hough	Ground
68% containment radius (degrees)			
1.0 - 0.9	0.27 ± 0.09	0.45 ± 0.09	0.09 ± 0.09
0.9 - 0.8	0.45 ± 0.09	1.89 ± 0.18	0.09 ± 0.09
0.8 - 0.7	0.99 ± 0.18	3.87 ± 0.36	0.09 ± 0.09
0.7 - 0.6	10.17 ± 0.09	7.83 ± 0.18	0.09 ± 0.09
0.6 - 0.5	29.07 ± 1.53	43.47 ± 1.71	0.09 ± 0.09
0.5 - 0.4	75.69 ± 0.27	56.25 ± 0.36	20.97 ± 0.27
0.4 - 0.3	93.33 ± 1.44	85.41 ± 0.27	83.79 ± 0.27
0.3 - 0.2	96.21 ± 0.09	116.91 ± 1.44	108.45 ± 0.27
0.2 - 0.1	108.99 ± 0.27	129.15 ± 0.27	98.37 ± 0.27
0.1 - 0.0	103.77 ± 0.18	137.79 ± 0.18	114.93 ± 0.18
95% containment radius (degrees)			
1.0 - 0.9	42.21 ± 0.09	17.01 ± 0.09	0.27 ± 0.09
0.9 - 0.8	43.11 ± 0.09	52.83 ± 0.18	0.63 ± 0.09
0.8 - 0.7	80.37 ± 0.18	72.09 ± 0.36	2.43 ± 0.09
0.7 - 0.6	91.17 ± 0.09	93.15 ± 0.18	13.59 ± 0.09
0.6 - 0.5	113.13 ± 1.53	110.61 ± 1.71	95.13 ± 0.09
0.5 - 0.4	121.77 ± 0.27	130.23 ± 0.36	133.65 ± 0.27
0.4 - 0.3	136.35 ± 1.44	140.31 ± 0.27	139.59 ± 0.27
0.3 - 0.2	140.49 ± 0.09	147.51 ± 1.44	152.37 ± 0.27
0.2 - 0.1	150.03 ± 0.27	153.27 ± 0.27	142.65 ± 0.27
0.1 - 0.0	150.93 ± 0.18	157.05 ± 0.18	160.11 ± 0.18
	Triggered events: 104256		
Reconstructed:	50536	56444	50564

Table D.10: The 68% and 95% containment point spread function for 100 GeV gamma rays incident on the LAT. These photons triggered the LAT and passed the Onboard Filter cuts. Their directions were reconstructed with the MII and Hough track reconstruction methods, and the ground based track reconstruction results are provided for comparison. Neither method performs well beyond 45^o from zenith, and MII is better than the Hough on axis to 45^o. The uncertainties reflect the precision with which the values could be determined given the number of events generated and the binning of the PSF histograms.

100 GeV Gamma Rays			
Filter 9 All Triggers Not Vetoed & Passed Layer Cut			
Corresponding background rate: 76 ± 5 Hz			
Range $cos(\theta)$	Filt MII	Hough	Ground
68% containment radius (degrees)			
1.0 - 0.9	0.27 ± 0.09	0.45 ± 0.09	0.09 ± 0.09
0.9 - 0.8	0.45 ± 0.09	1.89 ± 0.18	0.09 ± 0.09
0.8 - 0.7	0.99 ± 0.18	4.77 ± 0.18	0.09 ± 0.09
0.7 - 0.6	10.53 ± 0.36	11.43 ± 0.63	0.09 ± 0.09
0.6 - 0.5	19.89 ± 0.63	40.77 ± 0.72	0.09 ± 0.09
0.5 - 0.4	74.61 ± 1.17	61.83 ± 0.36	27.63 ± 0.27
0.4 - 0.3	93.87 ± 0.99	85.77 ± 0.18	80.91 ± 0.18
0.3 - 0.2	99.27 ± 0.27	103.77 ± 0.81	108.45 ± 0.27
0.2 - 0.1	108.99 ± 0.18	120.69 ± 0.36	115.47 ± 0.27
0.1 - 0.0	95.85 ± 0.27	132.03 ± 0.54	114.93 ± 0.18
95% containment radius (degrees)			
1.0 - 0.9	42.21 ± 0.09	41.85 ± 0.09	0.27 ± 0.09
0.9 - 0.8	44.19 ± 0.09	47.61 ± 0.18	0.45 ± 0.09
0.8 - 0.7	71.55 ± 0.18	72.27 ± 0.18	1.35 ± 0.09
0.7 - 0.6	98.91 ± 0.36	100.35 ± 0.63	15.75 ± 0.09
0.6 - 0.5	112.05 ± 0.63	110.97 ± 0.72	76.05 ± 0.09
0.5 - 0.4	126.09 ± 1.17	131.49 ± 0.36	126.09 ± 0.27
0.4 - 0.3	132.03 ± 0.99	140.31 ± 0.18	139.59 ± 0.18
0.3 - 0.2	130.77 ± 0.27	142.83 ± 0.81	147.15 ± 0.27
0.2 - 0.1	150.03 ± 0.18	148.05 ± 0.36	148.95 ± 0.27
0.1 - 0.0	150.39 ± 0.27	156.69 ± 0.54	166.05 ± 0.18
	Triggered events: 97606		
Reconstructed:	35839	40119	35331

Table D.11: The 68% and 95% containment point spread function for 100 GeV gamma rays incident on the LAT. These photons triggered the LAT and passed the Filter 9 and projection-layer albedo cuts. Their directions were reconstructed with the MII and Hough track reconstruction methods, and the ground based track reconstruction results are provided for comparison. Neither method performs well beyond 45^o from zenith, and MII is better than the Hough on axis to 45^o. The uncertainties reflect the precision with which the values could be determined given the number of events generated and the binning of the PSF histograms.

100 GeV Gamma Rays			
Filter 9 All Triggers Not Vetoed & Passed Layer and Direction Cuts			
Corresponding background rate: 33 ± 4 Hz			
Range $cos(\theta)$	Filt MII	Hough	Ground
68% containment radius (degrees)			
1.0 - 0.9	0.27 ± 0.09	0.45 ± 0.09	0.09 ± 0.09
0.9 - 0.8	0.45 ± 0.09	1.89 ± 0.18	0.09 ± 0.09
0.8 - 0.7	0.63 ± 0.72	4.77 ± 0.18	0.09 ± 0.09
0.7 - 0.6	10.53 ± 0.36	13.41 ± 1.26	0.09 ± 0.09
0.6 - 0.5	19.89 ± 0.63	40.77 ± 0.63	0.09 ± 0.09
0.5 - 0.4	74.61 ± 1.17	61.83 ± 0.36	27.63 ± 0.27
0.4 - 0.3	93.87 ± 0.99	85.77 ± 0.18	80.91 ± 0.18
0.3 - 0.2	99.27 ± 0.27	105.39 ± 0.18	108.81 ± 0.81
0.2 - 0.1	108.99 ± 0.18	120.69 ± 0.36	115.47 ± 0.27
0.1 - 0.0	95.85 ± 0.27	132.03 ± 0.54	114.93 ± 0.18
95% containment radius (degrees)			
1.0 - 0.9	42.21 ± 0.09	41.85 ± 0.09	0.27 ± 0.09
0.9 - 0.8	44.19 ± 0.09	47.61 ± 0.18	0.45 ± 0.09
0.8 - 0.7	71.55 ± 0.72	74.43 ± 0.18	1.17 ± 0.09
0.7 - 0.6	98.91 ± 0.36	100.35 ± 1.26	15.75 ± 0.09
0.6 - 0.5	112.05 ± 0.63	110.97 ± 0.63	76.05 ± 0.09
0.5 - 0.4	126.09 ± 1.17	131.49 ± 0.36	126.09 ± 0.27
0.4 - 0.3	132.03 ± 0.99	140.31 ± 0.18	139.59 ± 0.18
0.3 - 0.2	130.77 ± 0.27	142.83 ± 0.18	147.15 ± 0.81
0.2 - 0.1	150.03 ± 0.18	148.05 ± 0.36	148.95 ± 0.27
0.1 - 0.0	150.39 ± 0.27	156.69 ± 0.54	166.05 ± 0.18
	Triggered events: 97606		
Reconstructed:	35602	39882	35094

Table D.12: The 68% and 95% containment point spread function for 100 GeV gamma rays incident on the LAT. These photons triggered the LAT and passed the Filter 9 and the projection-layer and directional albedo cuts. Their directions were reconstructed with the MII and Hough track reconstruction methods, and the ground based track reconstruction results are provided for comparison. Neither method performs well beyond 45^o from zenith, and MII is better than the Hough on axis to 45^o. The uncertainties reflect the precision with which the values could be determined given the number of events generated and the binning of the PSF histograms.

Table D.13: Results of the onboard burst detection study corresponding to a 30 Hz background. The five bursts in the previous table were generated for three incident directions while the background remained at an average rate of 30 Hz. This background rate corresponds to the use of Filter 9 with both albedo cuts. Both track reconstruction methods were tried, as were different GRB detection algorithm parameters. The window width is the number of events that the algorithm examined at any one time, and the window incrementation is the number of events by which the window would advance. The time of arrival of the first burst photon is listed after the number of gamma rays that were not rejected by the filtering method, and that the onboard track reconstruction was able to reconstruct. Trigger times are listed for when the algorithm determined that a burst had occurred. The methods used were the combined spatial and temporal likelihoods, the spatial likelihood alone, the temporal likelihood alone, and the simple count rate above background.

Burst Label	Incident θ from zenith	Track Recon Method	γ's Passing Filter and Reconstructed	Time of 1st photon (s)	Time of Combined Trigger	Time of Spatial Trigger	Time of Temporal Trigger	Time of Rate Trigger(events)	Window Width	Window Incrementation (events)
A	7.5	MII	656	399.959	400.000	400.009	375.583	400.500	10	2
A	7.5	Hough	654	399.984	400.027	400.039	400.021	400.500	10	2

Continued on Next Page...

Burst Label	Incident θ from zenith	Track Recon Method	γ's Passing Filter and Reconstructed	Time of 1st photon (s)	Time of Combined Trigger	Time of Spatial Trigger	Time of Temporal Trigger	Time of Rate Trigger(events)	Window Width	Window Incrementation (events)
A	37.5	MII	544	399.977	400.035	400.035	400.020	400.500	10	2
A	37.5	Hough	540	399.942	399.985	400.045	399.985	400.500	10	2
A	70.0	MII	194	399.953	403.605	403.605	400.168	400.500	10	2
A	70.0	Hough	187	399.988	no trig	403.676	403.641	400.500	10	2
B	7.5	MII	345	399.959	400.008	400.008	399.992	400.500	10	2
B	7.5	Hough	345	400.000	400.023	400.023	400.023	400.008	10	2
B	37.5	MII	272	399.961	399.984	399.992	399.984	400.500	10	2
B	37.5	Hough	270	399.980	400.012	400.012	399.992	400.500	10	2
B	70.0	MII	106	399.953	no trig	no trig	120.617	no trig	10	2
B	70.0	MII	106	399.953	400.031	400.031	400.000	no trig	20	4
B	70.0	Hough	102	399.984	400.035	no trig	400.035	no trig	10	2
B	70.0	Hough	102	399.984	400.035	400.035	400.035	no trig	20	4
C	7.5	MII	113	399.961	400.005	400.064	400.005	404.500	10	2
C	7.5	Hough	113	399.961	400.016	400.086	400.016	no trig	10	2
C	37.5	MII	117	399.965	400.059	400.059	400.059	404.500	10	2
C	37.5	Hough	117	399.969	400.105	400.105	400.086	no trig	10	2
C	70.0	MII	35	399.994	no trig	no trig	no trig	no trig	10	2
C	70.0	MII	35	399.994	708.000	50.0137	no trig	no trig	80	16
C	70.0	Hough	35	399.981	no trig	no trig	158.393	no trig	10	2
C	70.0	Hough	35	399.981	no trig	no trig	158.393	no trig	20	4

Continued on Next Page...

Burst Label	Incident θ from zenith	Track Recon Method	γ's Passing Filter and Reconstructed	Time of 1st photon (s)	Time of Combined Trigger	Time of Spatial Trigger	Time of Temporal Trigger	Time of Rate Trigger(events)	Window Width	Window Incrementation (events)
C	70.0	Hough	35	399.981	817.467	162.879	no trig	no trig	40	8
C	70.0	Hough	35	399.981	107.118	18.1104	no trig	no trig	80	16
D	7.5	MII	83	399.959	399.988	400.660	400.164	400.129	10	2
D	7.5	Hough	83	400.000	400.176	400.281	400.176	no trig	10	2
D	37.5	MII	63	399.961	no trig	404.289	400.848	no trig	10	2
D	37.5	Hough	63	399.980	400.816	400.816	403.590	no trig	10	2
D	70.0	MII	14	399.953	no trig	no trig	no trig	no trig	10	2
D	70.0	MII	14	399.953	no trig	no trig	63.6016	no trig	20	4
D	70.0	MII	14	399.953	no trig	531.406	63.6016	no trig	40	8
D	70.0	Hough	13	399.984	no trig	no trig	585.363	no trig	10	2
D	70.0	Hough	13	399.984	no trig	no trig	585.363	no trig	20	4
D	70.0	Hough	13	399.984	no trig	272.992	no trig	no trig	40	8
E	7.5	MII	49	399.988	400.621	400.621	400.621	no trig	10	2
E	7.5	MII	49	399.988	359.602	359.508	359.836	no trig	40	8
E	7.5	Hough	48	400.000	400.672	400.672	400.672	no trig	10	2
E	7.5	Hough	48	400.000	400.625	400.625	330.320	no trig	20	4
E	7.5	Hough	48	400.000	400.730	207.707	400.730	no trig	40	8
E	37.5	MII	41	399.961	no trig	no trig	400.688	no trig	10	2
E	37.5	MII	41	399.988	400.738	400.738	400.738	no trig	20	4
E	37.5	Hough	41	399.980	no trig	no trig	no trig	no trig	10	2

Continued on Next Page...

Burst Label	Incident θ from zenith	Track Recon Method	γ's Passing Filter and Reconstructed	Time of 1st photon (s)	Time of Combined Trigger	Time of Spatial Trigger	Time of Temporal Trigger	Time of Rate Trigger(events)	Window Width	Window Incrementation (events)
E	37.5	Hough	41	399.980	400.707	400.707	273.598	no trig	20	4
E	70.0	MII	12	399.953	no trig	no trig	63.6016	no trig	20	4
E	70.0	Hough	12	399.953	no trig	916.844	63.6016	no trig	40	8

Continued from Previous Page.

Table D.14: Results of onboard burst detection study corresponding to a 75 Hz background. The five bursts were generated for three incident directions while the background remained at an average rate of 75 Hz. This background rate corresponds to the use of Filter 9 with the projection-layer albedo cut. The columns are the same as in the previous table.

Burst Label	Incident θ from zenith	Track Recon Method	γ's Passing Filter and Reconstructed	Time of 1st photon (s)	Time of Combined Trigger	Time of Spatial Trigger	Time of Temporal Trigger	Time of Rate Trigger(events)	Window Width	Window Incrementation (events)
A	7.5	MII	1125	399.988	400.035	400.035	400.035	400.500	20	4
A	7.5	Hough	1119	399.973	399.994	399.994	399.994	400.500	20	4
A	37.5	MII	845	399.988	400.035	400.035	400.035	400.500	20	4
A	37.5	Hough	840	399.999	400.031	400.031	400.031	400.500	20	4
A	70.0	MII	258	400.000	400.182	400.182	400.182	400.500	20	4
A	70.0	Hough	249	399.996	400.789	400.707	400.221	400.500	20	4
B	7.5	MII	577	399.969	399.973	399.973	399.973	400.500	20	4
B	7.5	Hough	576	400.000	400.012	400.012	400.012	400.500	20	4
B	37.5	MII	409	399.988	400.016	400.016	400.016	400.500	20	4
B	37.5	Hough	407	399.986	400.008	400.008	162.773	400.500	20	4
B	70.0	MII	144	399.969	400.008	400.031	400.000	no trig	20	4
B	70.0	Hough	140	399.953	400.031	400.031	400.000	no trig	20	4
C	7.5	MII	206	399.963	400.010	400.010	400.010	406.500	20	4

Continued on Next Page...

Burst Label	Incident θ from zenith	Track Recon Method	γ's Passing Filter and Reconstructed	Time of 1st photon (s)	Time of Combined Trigger	Time of Spatial Trigger	Time of Temporal Trigger	Time of Rate Trigger(events)	Window Width	Window Incrementation (events)
C	7.5	Hough	206	399.992	400.027	400.027	400.027	400.500	20	4
C	37.5	MII	184	399.988	400.059	400.059	400.059	404.500	20	4
C	37.5	Hough	184	399.986	400.104	400.104	400.104	no trig	20	4
C	70.0	MII	51	399.992	no trig	400.117	439.982	no trig	20	4
C	70.0	Hough	51	399.996	400.141	400.141	400.141	no trig	20	4
D	7.5	MII	142	399.969	400.082	400.082	400.082	400.500	20	4
D	7.5	Hough	142	400.000	400.078	400.078	400.078	400.500	20	4
D	37.5	MII	102	399.988	400.652	400.652	400.766	no trig	20	4
D	37.5	Hough	102	399.986	400.670	400.611	162.773	no trig	20	4
D	37.5	Hough	102	399.986	400.232	43.3242	403.676	no trig	40	8
D	70.0	MII	21	399.969	no trig	no trig	no trig	no trig	20	4
D	70.0	MII	21	399.969	651.125	98.8672	no trig	no trig	40	8
D	70.0	Hough	20	399.996	no trig	no trig	no trig	no trig	20	4
E	7.5	MII	84	399.969	400.621	400.133	400.621	no trig	20	4
E	7.5	Hough	83	400.000	400.637	400.637	400.648	no trig	20	4
E	37.5	MII	64	399.988	400.672	400.652	403.770	no trig	20	4
E	37.5	Hough	64	399.986	400.688	400.660	162.773	no trig	20	4
E	70.0	MII	18	399.969	no trig	no trig	no trig	no trig	20	4
E	70.0	MII	18	399.969	no trig	98.8672	no trig	no trig	40	8
E	70.0	Hough	17	399.996	no trig	no trig	no trig	no trig	20	4

Continued on Next Page...

Burst Label	Incident θ from zenith	Track Recon Method	γ's Passing Filter and Reconstructed	Time of 1st photon (s)	Time of Combined Trigger	Time of Spatial Trigger	Time of Temporal Trigger	Time of Rate Trigger(events)	Window Width	Window Incrementation (events)
E	70.0	Hough	17	399.996	no trig	7.91992	no trig	no trig	20	4

Continued from Previous Page.

BIBLIOGRAPHY

Akerlof, C., et al. 1999, Nature, 398, 400

Alcaraz, J., et al. 2000, Physics Letters B, 472, 215

Alcaraz, J., et al. 2000, Physics Letters B, 494, 193

Alfaro, J., Morales-Técotl, H. A., & Urrutia, L. F. 2002, Phys. Rev. D, 65, 103509

Aloy, M. A., Ibáñez, J. M., Miralles, J. A., & Urpin, V. 2002, Astron. Astrophys. 396, 693

Alvarez, L., & Compton, A. H. 1933, Phys. Rev., 43, 835

Amati, L., et al. 2000, Science, 290, 953

Amati, L., et al. 2002, Astron. Astrophys, 390, 81

Amelino-Camelia, G. et al. 1998, Nature, 393, 319

Antonelli, L. A., et al. 2000, ApJ, 533, L119

Atkins, R., et al. 2000a, Nucl. Instrum. Methods Phys. Res. A, 449, 478

Atkins, R., et al. 2000b, ApJ, 533, L119

ATLAS Collaboration, Retrieved December 2004, from `http://hepwww.rl.ac.uk/OpenDays98/Detectors/Silicon.htm`

Atwood, W. B., 1993, *Applying Silicon Strip Detector Technology to the Detection of Gamma Rays in Space*, SLAC-PUB-6267

Atwood, W. B., et al. 2000, NIM, A446, 444

Atwood, W. B. 2002, GLAST Internal Document, Retrieved December 2004, from `http://glast.gsfc.nasa.gov/science/lat/oct02/`, GLAST LAT IDT & Test Collaboration Meeting

Baldini, L., et al. 2003, in IEEE Nuclear Science Symposium Record, 3, 1535

Band, D. L. et al. 1992, Exp. Astro., 2, 307

Band, D. L., et al. 1993, ApJ, 413, 663

Baring, M. G. 1999, preprint (astro-ph/9911061)

Barnett, R. M., et al. 1996, Phys. Rev. D54, 118

Barraud, C. 2003, Astron. Astrophys., 400, 1021

Barwick, S. W. 1998, ApJ, 498, 779

Berger, E. et al. 2003, Nature 426, 154B

Bersier, D., et al. 2003, ApJ, 583, L63

Bethe, H., & Heitler, W. 1934, Proc. Roy. Soc., 146, 90

Bicron Inc. 1998, Spec Sheet: *BC-400/BC-404/BC-408/BC-412/BC-416 Premium Plastic Scintillators*, Retrieved December 2004, from `www.detectors.saint-gobain.com`

Bicron Inc. 2003, Technical Note: *Charged Particle Detection*, SaintGobain Crystals and Detectors, Retrieved December 2004, from `www.detectors.saint-gobain.com`

Bloom, J. S., et al. 1999, Nature, 401, 453

Bloom, E., Johnson, R.P., Tune, T., Ritz, S., Sadrozinski, H., Thurston, T.S. 2001, GLAST Technical Document, LAT–TD–00070–01, Retrieved December 2004, from `https://oraweb.slac.stanford.edu:8080/pls/slacquery/DOCUMENTS.STARTUP?PROJECT=GLAST`

Bloom, J. S., et al. 2002, ApJ, 572, L45

Bloom, J. S., Frail, D. A., & sari, R. 2003, ApJ, 594, 674

Bloom, J. S., et al. 2005, preprint (astro-ph/0505480 v1)

Bonnell, J. T., & Norris, J. P. 2004, unpublished memo, *GRB Trigger and Localization Algorithms Applied to GLAST Data Challenge One*, Retrieved February 2005, from `http://glast.gsfc.nasa.gov/science/grbst/pubs/`

Breakstone, A. 1994, in Computing in High Energy Physics 1994 — Proc., ed. S. C. Loken, LBL-35822, 41

Brigida, M., et al. 2002, GLAST Technical Document, LAT–TD–1058, Retrieved December 2004, from https://oraweb.slac.stanford.edu:8080/pls/slacquery/DOCUMENTS.STARTUP?PROJECT=GLAST

Bulik, T., Rudak, B., & Dyks, J. 2000, Mon. Not. Roy. Astro. Soc., 317, 97

Burenin, R. A., et al. 1999, Astron. Astrophys., 344, L53

Catelli, J. R. et al. 1996, AIP Conf. Proc. 384, ed. C. Kouveliotou, M. S. Briggs, & G. J. Fishman (New York: AIP), 158

Catelli, J. R., Dingus, G. L., & Schneid, E. J. 1998, in AIP Conf. Proc. 428, Fourth Huntsville Symp. on Gamma-Ray Bursts, ed. C. A. Meegan, R. D. Preece, & T. M. Koshut (New York: AIP), 309

CERN Web Page: http://rd11.web.cern.ch/RD11/rkb/PH14pp/node153.html

Cavallo, G., & Rees, M. J. 1978, Mon. Not. Roy. Astron. Soc., 183, 359

Chenette, D. L., et al. 1994, IEEE Trans. Nucl. Sci., 41, no. 6, 2332

Cheng, L. X., & Cheng, K. S. 1996, ApJ, 459, L79

Cheng, K. S., & Lu, T. 2001, Chin. J. Astron. Astrophys., 1, 1, 1

Ciprini, S. 2003, Memorie della Societa Astronomica Italiana Supplement, 3, 238

Cline, D. B., Matthey, C., & Otwinowski, S. 2003, Astropart. Phys., 18, 531

Cohen, E., Katz, J. I., Piran, T., Sari, R., Preece, R. D., and Band, D. L. 1997, ApJ, 488, 330

Connaughton, V. 2002, ApJ, 567, 1028

Costa, E., et al. 1997, Nature, 387, 783

Covino, S., et al. 1999, Astron. Astrophys., 348, L1

Covino, S., et al. 2002, GRB Circular Network, 1214, 1

CREME96 web page: `https://creme96.nrl.navy.mil/`

Dai, Z. G., & Lu, T. 2002, ApJ, 580, 1013

Dai, Z. G., Zhang, B., Gou, L. J., Mészáros, P., Waxman, E. 2002, ApJ, 580, L7

de Jager, O. C., & Stecker, F. W. 2002, 566, 738

Dermer, C. D., Chiang, J., & Mitman, K. E. 2000, ApJ, 537, 785

Dermer, C. D., & Atoyan, A. 2004, AIP Conf. Proc. 727: Gamma-Ray Bursts: 30 Years of Discovery, 727, 557

Dingus, B. L., et al. 1994 in AIP Conf. Proc. 307, ed. G. J. Fishman (New York: AIP), 22

Dingus, B. L., Catelli, J. R., & Schneid, E. J. 1998, in AIP Conf. Proc. 428, ed. C. A. Meegan, R. D. Preece, & T. M. Koshut (New York: AIP),349

do Couto e Silva, E., & GLAST Collaboration 2000, Bulletin of the American Astronomical Society, 32, 1262

Edwards, H. L., et al. 1991, IEEE Trans. on Nuc. Sci., 38, 2, 553

EGRET ACD Preliminary Design Review internal document, unpublished. 1982

Eichler, D., Livio, M., Piran, T., & Schramm, D. N. 1989, Nature, 340, 126

Fan, Y. Z., Wei, D. M., & Wang, C. F. 2004, Astron. and Astrophys., 424, 477

Fenimore, E. E., & Ramirez-Ruiz, E. 2000, preprint (astro-ph/0004176)

Fenimore, E. E., Ricker, G., Atteia, J-L., Kawai, N., Lamb, D., & Woosley, S. 2004, GRB Circular Network, 2735, 1

Fichtel, C. E., & Trombka, J. I. 1997, *Gamma-Ray Astrophysics: New Insight Into the Universe* (2nd ed; Washington, DC: NASA Reference publication 1386)

Fichtel, C. E., Hartman, R. C., Kniffen, D. A., Thompson, D. J., Bignami, G. F., Ogelman, H., Ozel, M. E., & Tumer, T. 1975, ApJ, 198, 163.

Fishman, G. J., & Meegan, C. A. 1995, Annu. Rev. Astron. Astrophys. 33, 415

Ford, L. A., et al. 2995, ApJ, 439, 307

Fox, D. B, & Moon, D. S. 2004, GRB Circular Network, 2734, 1

Fox, D. W., et al. 2003, Nature, 422, 284

Frail, D. A., Kulkarni, S. R., Nicastro, S. R., Feroci, M., & Taylor, G. B. 1997, Nature, 389, 261

Frail, D. A., et al. 2000, ApJ, 538, L129

Frail, D. A., et al. 2001, Apj, 562, L55

Freedman, D. L., & Waxman, E., ApJ, 547, 922

Fruchter, D. L. et al. 1998, in AIP Conf. Proc. No. 428, ed. C. A. Meegan, T. M. Koshut, & R. D. Preece (New York,: AIP), 509

Fruchter, A. S., 1999, ApJ, 516, 683

Fruhwirth, R. 2000, *Data Analysis Techniques for High-Energy Physics*, (2nd ed; Cambridge, UK; Cambridge University Press)

Fryer, C. L., Woosley, S. E. 1998, ApJ, 502, L9

Fryer, C. L., Woosley, S. E., Herant, M., & Davies, M. B. 1999, ApJ, 520, 650

Fynbo, J. P. U., Hornstrup, A., Hjorth, J., Jensen, B. L., & Andersen, M. I. 2004, GRB Circular Network, 2747, 1

Garnavich, P. M., et al. 2003, ApJ, 582, 924

GEANT4 Web Page: `http://wwwasd.web.cern.ch/wwwasd/geant4/geant4.html`

Gehrels, N. et al. 2004, ApJ, 611, 1005G

Gehrels, N. et al. 2005, preprint (astro-ph 0505630)

Ghiselliini, G., Lazzati, D., Rossi, E., & Rees, M. J. 2002, Astron. Astrophys., 389, L33

Giblin, T. W., van Paradijs, J., Kouveliotou, C., Connaughton, V., Wijers, R. A. M. J., Briggs, M. S., Preece, R. D., & Fishman, G. J. 1999, ApJ, 524, L47

GLAST Flight Software Group Web Page: http://www-glast.slac.stanford.edu/Elec_DAQ/Elec_DAQ_home.htm

GLAST Proposal Study, Retrieved December 2004, from http://www-glast.stanford.edu/studyprop/overview.html

ACD CDR Review documents 2003, Retrieved December 2004, from http://lhea-glast.gsfc.nasa.gov/acd/cdr/index.html

Golenetskii, S., Aptekar, R., Mazets, E., Pal'shin, V., & Frederiks, D. 2004, GRB Curicular Network, 2754, 1

González, M. M., Dingus, B. L., Kaneko, Y., Preece, Dermer, C. D., R. D., Briggs, M. S. 2004, Nature, 424, 749

Greiner, J. 2003, Nature, 426, 157

Greiner, J. 2005, http://www.mpe.mpg.de/~jcg/grbgen.html

Grove, E. J., 1997, *Particle Background Estimates for GLAST*, Unpublished Memo, Retrieved November 16, 2004 from http://heseweb.nrl.navy.mil/glast/tech_memos/Particle_Background.PDF

Guetta, D., & Granot, J. 2002, Mon. Not. R. Astron. Soc., 336, 803

Granot, J., & Guetta, D. 2003, ApJ, 598, L11

Guetta, D., Piran, T., & Waxman, E. 2005, ApJ, 619, 412

Hakkila, J., & Giblin, T. W. 2004, ApJ, 610, 361

Haller, G. 2003, GLAST Technical Document, LAT–PR–1967, DAQ Subsystem, Retrieved December 2004, from https://oraweb.slac.stanford.edu:8080/pls/slacquery/DOCUMENTS.STARTUP?PROJECT=GLAST

Handa, T., & GLAST Collaboration 2000, Bulletin of the American Astronomical Society, 32, 1262

Harrison, F. A., et al. 1999, ApJ, 523, L121

Harrison, F. A., et al. 2001, ApJ, 559, 123

Higdon, J. C., & Lingenfelter, R. E., 1998, AIP Conference Proceedings No. 428, ed. C. A. Meegan, T. M. Koshut, & R. D. Preece, (New York: AIP), 40

Hjorth, J., et al. 2003, 423, 847

Hough, P. V. C. 1959, *Machine Analysis of Bubble Chamber Pictures*, International Conference on High Energy Accelerators and Instrumentation, CERN

Hu, J. H., et al. 1004, GRB Circular Network, 2744, 1

Hurley, K., et al. 1994, Nature, 372, 652

Hurley, K., et al. 2005, *The Interplanetary Network Supplement to the BATSE Catalogs of Untriggered Cosmic Gamma-Ray Bursts*, ApJS, 156, 217

Hurley, K. 1994, Nature, 372, 652

Hurley, K., Sari, R., & Djorgovski, S. G. 2002, preprint (astro-ph/0211620)

Inoue, S., Guetta, D., & Pacini, F. 2003, ApJ, 583, 379

Johnson, W. N., et al. 2000, *The Construction and Performance of the CsI Hodoscopic Calorimeter for the GLAST Beam Test Engineering Module*, American Astronomical Society, HEAD Meeting #5, #43.22; Bulletin of the American Astronomical Society, 32, 1263

Johnson, T. H. 1933, Phys. Rev. 43, 307; 43, 381

Johnson, R. P. 2000, GLAST Internal Document, *The GLAST Silicon-Strip Tracking System*, Retrieved December 2004, from `scipp.ucsc.edu/~nora/preprint/2000/scipp-00-01.pdf`

Johnson, W. N., Grove, J. E., Phlips, B. F., Ampe, J., Singh, S., & Ponslet, E. 2000, Bulletin of the American Astronomical Society, 32, 1263

Johnson, R. P. 2001, GLAST Technical Document, LAT–SS–00017, Retrieved December 2004, from `https://oraweb.slac.stanford.edu:8080/pls/slacquery/DOCUMENTS.STARTUP?PROJECT=GLAST`

Johnson, R. P. 2003, GLAST Technical Document, LAT–PR–1967, Tkr Subsystem, Retrieved December 2004, from `https://oraweb.slac.stanford.edu:8080/pls/slacquery/DOCUMENTS.STARTUP?PROJECT=GLAST`

Johnson, W. N. 2003, GLAST Technical Document, LAT–PR–1967, CAL Subsystem, Retrieved December 2004, from `https://oraweb.slac.stanford.edu:8080/pls/slacquery/DOCUMENTS.STARTUP?PROJECT=GLAST`

Jones, B. B., et al. 1996, ApJ, 463, 565

Kalman, R. E. 1960, Transactions of the ASME–Journal of Basic Engineering, 82D, 35

Kaluzienski, L., Point of Contact, Research Program Management Division., *Appendix G., COMPTON GAMMA RAY OBSERVATORY GUEST INVESTIGATOR PROGRAM, CYCLE 9 SOL NRA-99-OSS-02 DUE 050699*, Retrieved 5 November 2004, from `http://cossc.gsfc.nasa.gov/cossc/nra/appendix_g.html`

Kamae, T., Ohsugi, T., Thompson, D. J., & Watanabe, K. 2000, Advances in Space Research, 25, 905

Kanbach, G., et al. 1988, *Space Sci. rev.*, 49, 69

Katz, J. I., 1994, ApJ, 432, L27

Katz, J. I., & Piran, T., 1997, ApJ, 490, 772

Katz, J. I. 1997, ApJ, 490, 772

Kharnitov, I., et al. 2004a, GRB Circular Network, 2740, 1

Kharnitov, I., et al. 2004b, GRB Circular Network, 2749, 1

Kharnitov, I., et al. 2004c, GRB Circular Network, 2752, 1

Klebesadel, R., Strong, I., & Olson. R. 1973, ApJ 182, L85

Kommers, J. M., et al. 2001, ApJS, 134, 385

Koshut, T. M., Kouveliotou, C., Paciesas, W. S., van Paradijs, J., Pendleton, G. N., Briggs, M. S., Fishman, G. J., Meegan, C. A. 1995, ApJ, 452, 145

Kouveliotou, C., et al. 1993, ApJ, 413, L101

Kremer, J., et al. 1999, Phys. Rev. Lett., 83, 21, 4241

Kulkarni, S. R., et al. 1998, Nature, 393, 35

Kulkarni, S. R., et al. 1999, ApJ, 522, L97

Kwok, P. W., et al. 1993, in AIP Conf. Proc. 304, ed. Edited by N. Gehrels, J. P. Norris, & C. E. Fichtel (New York: AIP)

Lemaitre, G., & Vallarta, M. S. 1933, Phys. Rev., 43, 87

Li, W., Filippenko, A. V., Chornock, R., & Jha, S. 2003, ApJ, 576, L923

Li, W.,Filippenko, R., Chornock, R., & Jha, S. 2004, GRB Circular Network, 2748, 1

Liang, E., & Kargatis, V. 1996, 381, 49

Lithwick, Y., & Sari, R. 2001, ApJ, 555, 540

Lloyd, N. M, & Petrosian, V. 1999, ApJ, 511, 550

Lloyd-Ronning, N. M., Fryer, C. L., Ramirez-Ruiz, E. 2002, ApJ, 574, 554

Mészáros, P., Rees, M. J., & Papathanassiou, H. 1994, ApJ, 432, 181

Mészáros, A., Bagoly, Z., Horváth, I., Balázs, G. G., & Vavrek, R. 2000a, ApJ, 539, 98

Mészáros, A., Bagoly, Z., & Vavrek, R. 2000b, Astron. Astrophys., 354, 1

Mészáros, P., et al. 2002, ApJ, 578, 812

MacFadyen, A. I. & Woosley, S. E. 1999, ApJ, 524, 262

Magliocchetti, M., Ghirlanda, G., & Celotti, A. 2003, Mon. Not. R. Astron. Soc., 343, 255

Mallozzi, R. S., Paciesas, W. S., Pendleton, G. N., Briggs, M. S., Preece, R. D., Meegan, C. A., & Fishman, G. J. 1995, ApJ, 454, 597

Mallozzi, R. S., Pendleton, G. N., Paciesas, W. S., Preece, R. D., & Briggs, M. S. 1998, AIP conference Proceedings No. 428, ed. by C. A. Meegan, T. M. Koshut, & R. D. Preece, (New York: AIP), 279

Marshall, S., et al. 1999, 191st AAS Meeting, No. 48.15; Bulletin of the American Astronomical Society, 29, 1290

Martin, E. 1999, S&T, 98b, 44

Mazets, E. P., Golenetskii, S. V., & Illinskii, V. N. 1974, JETP Lett. 19, 77

McEnery, J. E. 2003, American Astronomical Society Meeting Abstracts, 202, 3503

Meegan, C. A., Fishman, G. J., Wilson, R. B., Horack, J. M., Brock, M., N., Paciesas, W. S., Pendleton, G. N., & Kouveliotou, C. 1992, Nature, 355, 143

Mészáros, P., & Rees, M. J. 1993, ApJ, 405, 278

Mészáros, P., & Rees, M. J. 1994, Mon. Not. Roy. Astro. Soc., 269, L49

Metzger, M. R., et al. 1997, Nature, 387, 878

Mizuno, T. et al. 2004, preprint (astro-ph/0405490), accepted for publication in ApJ

Moiseev, A. A., Ormes, J. F., Hartman, R. C., Johnson, T. E., Mitchell, J. W., & Thompson, D.J. 2004, Astropart. Phys., 22, 34, 275

Moiseev, A. A 1999a, GLAST ACD Document, Retrieved December 2004, from `http://lhea-glast.gsfc.nasa.gov/acd/pubs/`

Moiseev, A. 1999b, Proceedings of the 26th International Cosmic Ray Conference. August 17-25, 1999. Salt Lake City, Utah, USA. Under the auspices of the International Union of Pure and Applied Physics (IUPAP). Volume 2. Edited by D. Kieda, M. Salamon, and B. Dingus, 2, 273

MT Berlin web page: `http://www.mt-berlin.com/frames_cryst/crystals_frameset1.htm`

Nakar, E., & Piran, T., 2002, Mon. Not. Royal. Astro. Soc., 331, 40

Narayan, R., Paczynski, B., & Piran, T. 1992, ApJ, 395, L83

Narayan, R., Piran, T., & Kumar, P. 2001, ApJ, 557, 949

National Geophysics Data Center: *GOES Space Environment Monitor data*, online at `http://goes.ngdc.noaa.gov/data/plots/`

Norris, J. P., Nemiroff, R. J., Bonnell, J. T., Scargle, J. D., Kouveliotou, C., Paciesas, W. S., Meegan C. A., & Fishman, G. J. 1996, ApJ, 459, 393

Norris, J. P., Marani, G. F., & Bonnell, J. T. 2000, ApJ, 534, 248

Norris, J. P. 2004, unpublished memo, *GRB Observation-bsed Simulator*, Retrieved February 2005, from `http://glast.gsfc.nasa.gov/ssc/dev/SU_GRB_040929/`

Omodei, N. 2002, unpublished memo, *GRB Spectrum, Transient Source Simulations*, Retrieved February 2005 from, `http://glast.gsfc.nasa.gov/science/grbst/present/`

Ormes, J. F. 2002, GLAST Technical Document LAT–SS–00352–01–D6, Retrieved December 2004, from `https://oraweb.slac.stanford.edu:8080/pls/slacquery/DOCUMENTS.STARTUP?PROJECT=GLAST`

Paciesas, W. S., et al. 1999, ApJS, 122, 465

Paciesas, W. S., et al. 2000, *The Current BATSE Burst Catalog*, online at `http://cossc.gsfc.nasa.gov/batse/BATSE_Ctlg/index.html`

Paczynski, B. 1991, Acta Astron., 41, 257

Paczynski, B. 1998, ApJ, 494, L45

Panaitescu, A., & Kumar, P., 2000, ApJ, 543, 66

Panaitescu, A., & Kumar, P., 2001, ApJ, 560, L49

Panaitescu, A., & Mésáros, P. 1999, ApJ, 526, 707

Perkins, D. H. 1987, *Introduction to High Energy Physics* (3rd ed; Menlo Park, CA: AddisonWesley),

Pilla, R. P., & Loeb, A. 1998, ApJ, 494, L167

Piran, T., Kumar, P., Panaitescu, A., & Piro, L. 2001, ApJ, 560, L167

Piran, T., & Narayan, R. 1996, AIP Converence Proceedings No. 384, ed. C. Kouvekiotou, M. F. Briggs, & G. J. Fishman, (New York: AIP), 233

Piran, T. 2005, Rev. Mod. Phys., 76, 1143

Piro, L., et al. 1999, Astron. Astrophys. Suppl. Ser., 138, 431

Piro, L., et al. 2000, Science, 290, 955

Piro, L. 1997, 191st AAS Meeting, #55.01; Bulletin of the American Astronomical Society, 29, 1303

Plaga, R., 1995, Nature, 374, 430

Preece, R. D., Briggs, M. S., Mallozzi, R. S., Pendleton, G. N., Paciesas, W. S., & Band, D. L. 2000, ApJS, 126, 19

Price, P. A. 2003, Nature, 423, 844

Ramirez-Ruiz, E., & Merloni, A. 2001, Mon. Not. R. Astron. Soc., 320L, 25

Ramirez-Ruiz, E., Merloni, A., & Rees, M. J., 2001, Mon. Not. R. Astron. Soc. 324, 1147

Ramirez-Ruiz, E., Celotti, A., Rees, M. J. 2002, Mon. Not. R. Astron. Soc., 337, 1349

Rees, M. J., & Mészáros, P. 1992, Mon. Not. R. Astron. Soc., 258, 41P

Reeves, J. N., et al. 2002, Nature, 416, 512

Reichart, D. E., Lamb, D. Q., Fenimore, E. E., Ramirez-Ruiz, E., Cline, T. L., & Hurley, K. 2001, ApJ, 552, 57

Reichart, D. E. 1999, ApJ, 521, L111

Rhoads, J. E. 1998, ApJ, 487, L1

Rhoads, J. E. 1999, ApJ, 525, 737

Ritz, S. 2000, GLAST Technical Document, LAT–SS–00035, Retrieved December 2004, from `https://oraweb.slac.stanford.edu:8080/pls/slacquery/DOCUMENTS.STARTUP?PROJECT=GLAST`

Ritz, S. 2002, GLAST Technical Document, LAT–PR–00660–00, Retrieved 15 November 2004, from `https://oraweb.slac.stanford.edu:8080/pls/slacquery/DOCUMENTS.STARTUP?PROJECT=GLAST`

Ritz, S. 2003, GLAST Technical Document, LAT–PR–01967–01, Science Requirements, Retrieved November 2004, from `https://oraweb.slac.stanford.edu:8080/pls/slacquery/DOCUMENTS.STARTUP?PROJECT=GLAST`

Rol, E., et al. 2000, ApJ, 544, 707

ROOT Web Page: http://root.cern.ch

Rudak, B. 2001, LNP Vol. 576: Physics and Astrophysics of Ultra-High-Energy Cosmic Rays, 576, 90

Ruderman, M. 1975, in 7th Texas Symposium on Relativisitc Astrophysics, Dallas, Tx., Ann. N. Y. Acad. Sci., 262, 164

Russell, J. J. 2001, GLAST Technical Document, LAT–TD–00286, Retrieved December 2004, from https://oraweb.slac.stanford.edu:8080/pls/slacquery/DOCUMENTS.STARTUP?PROJECT=GLAST

Rutledge, R. E., & Sako, M. 2003, Mon. Not. R. Astron. Soc., 339, 600

Salmonson, J. D., & Galama, T. J. 2002, ApJ, 569, 682

Sanuki, T., et al. 2000, ApJ, 545, 1135

Sari, R., & Piran, T. 1999, ApJ, 517, L109

Sari, R., Piran, T., & Halpern, J. P. 1999, ApJ, 519, L17

Schaefer, B. E., et al. 1998, ApJ, 492, 696

Schneid, E. J. et al. 1992, Astron. Astrophys., 255, L13

Schneid, E. J., et al. 1995, ApJ, 453, 95

Soderberg, A. M. et al. 2002, GRB Circular Network 1554

Stanek, K. Z., Garnavich, P. M., Kaluzny, J., Pych, W., & Thompson, I. 1999, ApJ, 522, L39

Stanek, K. Z., et al. 2003, ApJ, 591, L17

Stecker F. W., et al. 1993, ApJ, 410, L71

Stecker, F. W. 1999, Proceedings of the 26th International Cosmic Ray Conference. August 17-25, 1999. Salt Lake City, Utah, USA. Under the auspices of the International Union of Pure and Applied Physics (IUPAP). Volume 3. Edited by D. Kieda, M. Salamon, and B. Dingus, p.313, 3, 313

Stern, B. E. & Tikhomirova, Ya. 2002, *The GRB Catalog of Stern and Tikhomirova*, online at `http://www.astro.su.se/groups/head/grb_archive.html`

Taylor, G. B., Frail, D. A., & Fox, D. 2001, GRB Circular Newtork, 1122, 1

Terada, H., & Akiyama, M. 2004, GRB Circular Ntework, 2742, 1

Terada, H., Akiyama, M., & Kawaii, N. 2004, GRB Circular Network, 2750, 1

Thompson, D. J., et al. 1981, JGR, 86, 1265

Thompson, D. J, et al. 1993, *Calibration of the Energetic Gamma-Ray Experiment Telescope (EGRET) for the Compton Gamma-Ray Observatory*, ApJS, 86, 629

Thompson, C. 1994, Mon. Not. R. Astron. Soc., 270, 480

Thompson, D. J., Simpson, G. A., and & Oumlzel, M. E., 1981, JGR, 86, 1265

Thompson, D. J, & Thompson, T. E. 2003, GLAST Technical Document, LAT–PR–1967, ACD Subsystem, Retrieved December 2004, from https://oraweb.slac.stanford.edu:8080/pls/slacquery/DOCUMENTS.STARTUP?PROJECT=GLAST

Thurston, T. S. 2001, GLAST Technical Document, LAT–TD–0012501, Retrieved December 2004, from https://oraweb.slac.stanford.edu:8080/pls/slacquery/DOCUMENTS.STARTUP?PROJECT=GLAST

Totani, T., 1998a, ApJ, 502, L13

Totani, T., 1998b, ApJ, 509, L81

Totani, T., & Kitayama, T. 2000, ApJ, 545, 572

Treiman, S. B. 1953, Phys. Rev., 91, 957

Tylka, A. J. et al. 1997, IEEE Trans. on Nuc. Sci., 44, 2150

Tylka, A.J. 2000, *A Review of Cosmic-Ray Albedo Studies: 1949-1970*, NRL SEM 2000-03 Unpublished Memo

Usher, T., 2003, GLAST Internal Document, Retrieved December 2004, from http://www-glast.slac.stanford.edu/software/Workshops/July03Workshop/agenda.htm, GLAST Ground Software Workshop

Usov, V. V. 1992, Nature, 357, 472

Usov, V. V. 1994, Mon. Not. R. Astron. Soc. 267, 1035

van der Horst, A. J., Rol, E., & Wijers, R. A. M. J. 2004, GRB Circular Network, 2746, 1

van Paradijs, J., et al. 1997, Nature, 386, 686

Vietri, M., 1997, ApJ, 478, L9

Vietri, M., & Stella, L. 1998, ApJ, 507, L45

Wang, X. Y., Dai, Z. G., & Lu, T. 2001, ApJ, 556, 1010

Wang, X. Y., Dai, Z. G., & Lu, T. 2002, Mon. Not R. Astro. Soc., 336, 803W

Watts, R. N. 1971, S&T, 41, 281W

Waxman, E., & Mészáros, P. 2003, ApJ, 584, 390

Waxman, E. Kulkarni, S. R., & Frail, D. A. 1998, ApJ, 497, 288

Wiersema, K., Starling, R. L. C., Rol, E., Vreeswijk, P., Wijers, R. A. M. J. 2004, GRB Circular Network, 2800, 1

Wijers, R. A. M. I., Rees, M. J., Mészáros, P. 1997, Mon. Not. R. Astron. Soc., 288, L51

Wijers, R. A. M. I., et al. 1999, ApJ, 523, L33

Winkler, C., et al. 1992, Astron. & Astrophys., 255, L9

Woosley, S. E. 1993, ApJ, 405, 273

Wren, D. N., Bertsch, D. L., & Ritz, S. 2002, ApJ, 547, L47

Wren, D. N. 2004a, Glast Technical Document, LAT–TD–02979, Retrieved February 2004, from https://oraweb.slac.stanford.edu:8080/pls/slacquery/DOCUMENTS.STARTUP?PROJECT=GLAST

Wren, D. N. 2004b, unpublished memo, *FilterAlg Description and User's Guide*, Retrieved June 2004, from http://www-glast.slac.stanford.edu/software/AnaGroup/

Zhang, B., & Mészáros, P. 2001, ApJ, 559, 110

Zhang, B., & Mészáros, P. 2002, ApJ, 581, 1236

Zhang, B., & Mészáros, P. 2004, IJMPA, 19, 15, 2385

Zhang, L., Zhang, Y. J., & Cheng, K. S. 2000, Astron. & Astroph., 357, 957

Zhang, W., Woosley, S. E., & MacFadyen, A. I. 2003, ApJ, 586, 356